Bepalen van persoonlijke blootstelling aan radiofrequente straling in realistische omgevingen

Assessment of Personal Exposure to Radio Frequency Radiation in Realistic Environments

Arno Thielens

Promotoren: prof. dr. ir. W. Joseph, prof. dr. ir. L. Martens
Proefschrift ingediend tot het behalen van de graad van
Doctor in de Ingenieurswetenschappen: Toegepaste Natuurkunde

Vakgroep Informatietechnologie
Voorzitter: prof. dr. ir. D. De Zutter
Faculteit Ingenieurswetenschappen en Architectuur
Academiejaar 2014 - 2015

UNIVERSITEIT GENT

ISBN 978-90-8578-801-0
NUR 926
Wettelijk depot: D/2015/10.500/45

Dankwoord

"To understand the actual world as it is, not as we should wish it to be, is the beginning of wisdom."

—Bertrand Russell, *Mortals and Others*

Ondanks dat er maar een auteur op de voorpagina van dit boek staat, moge het duidelijk zijn dat dit werk niet tot stand gekomen was zonder de hulp van velen in mijn omgeving zowel op professioneel als op persoonlijk vlak. Ik wil hen daarom met dit dankwoord in de bloemetjes zetten. Voor zij die niet bij naam vermeld worden: u ligt even nauw aan mijn hart dan zij die wel vermeld zijn, echter iets verder weg van mijn verstand tijdens het schrijven van dit stuk. Ik beloof dat u, indien dit boek een bestseller wordt, met naam en toenaam vermeld wordt in de tweede oplage.

Vooreerst zou ik mijn promotoren, Wout en Luc, willen bedanken. Dankzij de middelen en de omkadering van het onderzoek die zij voorzien hebben, is dit proefschrift er gekomen. Ik wil Wout bedanken voor het enthousiasme en de motivatie die hij mij de afgelopen jaren heeft gegeven. Samen hebben we ondertussen de halve wereld - van Canada tot Australië - afgereisd, om op conferenties (succesvol) te leuren met onze exposimeter. Hopelijk is nu de tijd aangebroken om daar de vruchten van te plukken. Luc wil ik bedanken voor zijn begeleiding en kritische blik op mijn wetenschappelijk werk en ideeën. Mijn onderzoek zou niet aan dezelfde standaarden voldoen zonder hem.

Naast mijn promotoren zijn er natuurlijk nog andere mensen die tijd en moeite in mij en mijn onderzoek geïnvesteerd hebben. Günter heeft mij in de eerste jaren van mijn doctoraat geweldig geholpen met het aanleren van de benodigde simulatietechnieken. Graag wil ik hem bedanken voor zijn geduld en inzicht. Emmeric wil ik bedanken voor de discussies omtrent de verwerking van mijn meet- en kalibratiedata. Het is zeer aangenaam om met een erudiet persoon als hem te overleggen over mijn werk, maar zeker even leuk om over minder serieuze onderwerpen te praten.

Ik wil bij deze ook de leden van de jury bedanken voor hun suggesties en de verbeteringen die ze aan dit boek aangebracht hebben n.a.v. de eerste verdediging van dit proefschrift.

Daarnaast heb ik bij mijn onderzoek behoorlijk wat hulp nodig gehad van verschillende mensen, die ik hier dan ook in het bijzonder wil bedanken. Aliou, Hans, Jeroen, Leen, Peter, Sam Aerts en Sam Agneessens hebben ofwel vele uurtjes moeten doorbrengen in de kooi van Faraday, terwijl ik rondjes aan het draaien was in de anechoïsche kamer, ofwel met mij de reis naar het verre Rijsel moeten maken om die laatste beetjes meetdata te kunnen vergaren. Hans, Jeroen, Matthias, Patrick, Peter en Sam Agneessens hebben voor mijn onderzoek onmisbaar werk verricht door de geschikte antennes en bijpassende elektronica aan te maken. Leen en Matthias hebben mij op technisch vlak geholpen en met veel optimisme ter zijde gestaan tijdens de metingen die we samen gedaan hebben. Isabelle en Kris hebben me geholpen bij mogelijk wel mijn twee zwakste punten: administratief en computergerelateerd werk. Jullie hebben allemaal mijn dank.

Mijn collega's bij WiCa (waar staat dit tegenwoordig voor?): Aliou, Amine, Brecht, David, Emmeric, Frederic, Günter, Jens, Kris, Leen, Margot, Matthias, Michel, Toon, Reza, Roel, Said, Sam en Xu; maar ook zij die andere oorden opgezocht hebben: Adrian, Damiano, Divya, Karen, Mikel, Mostafa, Ning, Quentin en Simon, wil ik bedanken voor de aangename werksfeer. Een speciale vermelding gaat naar Sam, die op vier jaar tijd is uitgegroeid van langharig tuig dat te laat voor mijn les aankwam op zijn sandalen, tot een van de meest competente onderzoekers in onze groep en tevens mijn compagnon waarmee ik al zeer aangename momenten beleefd heb in binnen- en buitenland.

During my doctoral research, I have had the chance to collaborate with some pleasant and interesting colleagues from foreign research institutes and universities. I would like to thank my co-workers from the University of Lille 1, Ericsson Sweden, TPH Basel, IT'IS Zürich, and Monash University for the fruitful collaborations. In particular, I would like to thank Marie-Christine and Milena, with whom I have spent more time after a conference than during the actual scientific meetings.

Daarmee zijn we naadloos aanbeland bij het gedeelte waarin ik overschakel van het professionele naar het persoonlijke. De bijdrage van kennissen, vrienden en familie aan een doctoraat is misschien niet direct te kwantificeren, maar naar mijn mening minstens even belangrijk dan de bijdrage geleverd door collega's en begeleiders.

Ik heb de afgelopen jaren een aanzienlijk deel van mijn vrije tijd al tafeltennissend gespendeerd en wil zeker de leden en het bestuur van TTC Gent bedanken voor de aangename sfeer tijdens de training en competitie. In het bijzonder Michiel, met wie ik wekelijks nog een extra trainingssessie inleg, inclusief filosofische nabespreking.

Met mijn vriendengroep heb ik tijdens deze doctorale periode leuke momen-

ten beleefd en dat verdient zeker een bedankje. Sommigen ken ik al van op de middelbare school (Derek, Gert, Tom), anderen uit het bruisende nachtleven van Brasschaat (Dimi, Eliane, Raph), sommigen leerde ik pas kennen aan de universiteit (Chloé, Koen, Luc, Michiel, Sam W., Sofie, Stefanie, Stijn), anderen leerde ik kennen tijdens mijn uitwisseling in Porto (Liesa) en een enkeling leerde ik kennen in de Ekerse pingpongscne (Domien). Gelukkig hebben jullie een goede smaak en hebben jullie onze vriendengroep uitgebreid met (nog?) toffe(re) vriendjes en vriendinnetjes (Ben, Elien, Eline, Emma, Joan, Pauline, Sarah, Tine). Ik wil al mijn vrienden, ook zij die hier niet met naam vermeld staan (sorry), bedanken voor deze zeer aangename periode.

Toen ik begon te studeren aan de UGent, was ik de enige telg uit onze familie die in Gent vertoefde. De afgelopen jaren zijn, tot mijn grote tevredenheid, Zino, Nomi en Levi gevolgd. Ik ben bevoorrecht om hun studieperiode van dichtbij mee te maken en wil hen bedanken voor de leuke tijd die we samen doorgebracht hebben. JP wil ik bedanken om mij al die jaren op sleeptouw te nemen, eerst op rolschaatsen, later op ons snowboard. Tanja voor de vele wandelingen met de hondjes en zoveel meer. Mijn grootouders wil ik bedanken voor hun steun en voor alle leuke momenten die ik met hen beleefd heb. In het bijzonder wil ik mijn ouders bedanken om mij alle kansen te geven om mezelf te ontwikkelen en mij te steunen met mijn (studie)keuzes en levenswandel. De overige leden van mijn familie wil ik eveneens bedanken voor alles wat zij voor mij gedaan hebben.

De laatste paragraaf van dit dankwoord is vanzelfsprekend gereserveerd voor Gloria. Zij heeft de totstandkoming van dit boek vanop de eerste rij meegemaakt en heeft zonder twijfel bijgedragen aan de kwaliteit ervan. Het is leuk om een doctoraat te ontvangen, maar zij is het beste dat mij de afgelopen jaren overkomen is. Ongetwijfeld worden de komende jaren voor ons beide even leuk dan de voorbije.

Arno Thielens
Gent, mei 2015

Table of Contents

List of Figures

List of Tables

List of Acronyms

0-9

2G Second Generation

3G Third Generation

3GPP Third Generation Partnership Project

4G Fourth Generation

5G Fifth Generation

A

AA Antenna Aperture

ASTRID All-round Semi-cellular Trunking Radio communication system with Integrated Dispatching

B

BB Bounding Box

BFD Basic Field Distribution

BIPT Belgian Institute for Postal services and Telecommunications

BMI Body Mass Index

BSA Base Station Antenna

C

CAD Computer-Aided Design

CDF Cumulative Distribution Function

CENELEC European Committee for Electrotechnical Standardization

CEPT European Conference of Postal and Telecommunications Administrations

D

DAB Digital Audio Broadcasting

DCS Digital Cellular Service

DECT Digital Enhanced Cordless Telecommunication

DL Down-Link

DMC Diffuse Multipath Components

DVB-H Digital Video Broadcasting - Hand held

DVB-NGH Digital Video Broadcasting - Next Generation Hand held

DVB-T Digital Video Broadcasting - Terrestrial

E

ECC Electronic Communications Committee

ECDF Experimental Cumulative Distribution Function

EDGE Enhanced Data rates for GSM Evolution

EMF Electromagnetic Field

EU European Union

F

FDTD Finite-Difference Time-Domain

FF Far Field

FM Frequency Modulated radio

G

GHB Generalized Huygens Box

GPRS General Packet Radio Service

GPU Graphics Processing Unit

GSM Global System for Mobile communications

H

HPC High-Performance Computing

HSPA High Speed Packet Access

I

ICNIRP International Commission on Non-Ionizing Radiation Protection

IEC International Electrotechnical Commission

IEEE Institute of Electrical and Electronics Engineers

ISM Industrial, Scientific, and Medical

L

LTE Long Term Evolution

N

NLOS Non Line Of Sight

O

OSA Organ-Specific Average

P

PEC Perfect Electric Conductor

PIFA Planar Inverted F-Antenna

PML Perfectly Matched Layer

Q

QQ Quantile-Quantile

R

R Response

RAM Random-Access Memory

RMS Root Mean Square

RF Radio-Frequency

S

SA Spectrum Analyzer

SAR Specific Absorption Rate

SAR_{10g} 10 g averaged Specific Absorption Rate

SAR_{osa} organ-specific averaged Specific Absorption Rate

SAR_{wb} Specific Absorption Rate

SIW Substrate Integrated Waveguide

SPW Single Plane Wave

T

TETRA TErrestrial Trunked RAdio

U

UL Up-Link

UMTS Universal Mobile Telecommunications System

V

VFB Virtual Family Boy

VFM Virtual Family Male

VNA Vector Network Analyzer

W

WiFi Wireless Fidelity

WIMAX Worldwide Interoperability for Microwave Access

Nederlandstalige samenvatting

Draadloze communicatie wordt wereldwijd door miljarden mensen gebruikt. Om deze communicatie mogelijk te maken, worden radiofrequente (RF) elektromagnetische (EM) velden met een bepaalde frequentie uitgewisseld tussen verschillende antennes. Deze antennes kunnen enerzijds deel uitmaken van een draadloos netwerk dat uitgebaat wordt door een telecomoperator of kunnen anderzijds ingebouwd zijn in een persoonlijk toestel dat bestuurd wordt door een gebruiker van het netwerk. Er bestaan verschillende draadloze technologieën die aan bepaalde specifieke frequentiebanden in the RF spectrum toegewezen zijn. Enkele gekende voorbeelden zijn *Global System for Mobile communications* (GSM), *Wireless Fidelity* (WiFi), and *Long Term Evolution* (LTE).

Dit intensieve gebruik van draadloze technologieën heeft een maatschappelijke bezorgdheid doen ontstaan over potentiële gezondheidseffecten die mogelijk veroorzaakt worden door RF straling. Een reeds bewezen gezondheidseffect is de opwarming van biologische, diëlektrische media door de absorptie van RF straling. Dit effect werd gebruikt als wetenschappelijke basis voor het uitvaardigen van (inter)nationale limieten op de absorptie van RF straling. Deze absorptie wordt gekwantificeerd door het specifiek absorptietempo oftewel de *specific absorption rate* (SAR). Deze grootheid is gedefiniëerd als de verhouding van het geabsorbeerde RF vermogen en de diëlektrische massa waarin dit vermogen gebasorbeerd wordt. De SAR dient uitgemiddeld te worden over een bepaald volume of massa. De SAR uitgemiddeld over het hele lichaam (*whole-body averaged SAR* of SAR_{wb}) en het maximale SAR uitgemiddeld over 10 g aaneensluitende massa (SAR_{10g}) zijn voorbeelden van courante uitmiddelingen. De SAR kan echter niet opgemeten worden in het lichaam van een levende mens. Daarom werden er referentieniveaus gedefiniëerd voor de amplitude van invallende EM velden of de grootte van de invallende vermogensdichtheid. Deze kunnen wel opgemeten worden en SAR waarden kunnen van deze metingen afgeleid worden. Dit is echter niet vanzelfsprekend in realistische omgevingen, aangezien er verschillende onzekerheden optreden tijdens de metingen. Bijgevolg is het doel van dit proefschrift om de schatting en meting van bovenstaande grootheden te verbeteren in realistische blootstellingsscenario's.

Het studiedomein dat deze grootheden onderzoekt wordt RF dosimetrie genoemd. Een deel van het onderzoek in dit domein bepaalt of uitgezonden of geabsorbeerde RF EM velden in overeenstemming zijn met de uitgevaardigde wetten of richtlijnen. De richtlijnen met het grootste draagvlak, die ook het meest geïmplementeerd worden, zijn deze uitgegeven door de internationale commissie

voor de bescherming tegen niet-ioniserende straling (ICNIRP).

Rondom een antenne die RF EM velden uitzendt met een bepaald vermogen, kan er een zone zijn waar de SAR of de invallende EM velden te hoog zijn in vergelijking met de geldende richtlijnen. Indien het uitgezonden vermogen lager zou zijn, dan zou de blootstelling lager zijn. Wij hebben de maximaal toegelaten vermogens bestudeerd in vergelijking met de richtlijnen van de ICNIRP rondom LTE, multifrequente basisstations (BSs). We maken hierbij gebruik van de basisrestricties op de SAR_{wb} en het maximum van de SAR_{10g}, en referentieniveaus op de invallende veldsterkte, gedefiniëerd zijn door de ICNIRP. Dit is, tot zover onze kennis reikt, de eerste studie die dergelijke toegelaten vermogens bepaalt voor LTE, multifrequente BSs.

Invallende EM velden kunnen enerzijds opgemeten worden in de vrije ruimte, zonder dat er een menselijk subject aanwezig is, anderzijds kunnen ze opgemeten worden op het lichaam van het subject. Hierbij wordt er gebruik gemaakt van persoonlijke exposimeters (PEMs). Deze instrumenten hebben het voordeel dat ze draagbaar zijn op het lichaam en dus meten op dezelfde locatie als het subject. PEMs meten echter de veldsterktes op het lichaam en niet de invallende veldsterktes, waarvoor de richtlijnen gedefiniëerd zijn en die als agent beschouwd worden in epidemiologische onderzoeken. De kwadratische verhouding tussen de opgemeten en de invallende veldsterkte wordt het antwoord van een PEM genoemd. In hoofdstuk 3 van dit proefschrift wordt deze grootheid bestudeerd in verschillende blootstellingsscenario's. Eerst wordt het antwoord bepaald van een PEM die gedragen wordt op het lichaam van een subject in de nabijheid van een multifrequente BS. In een tweede deel van dit hoofdstuk wordt dit antwoord bestudeerd in realistische, verre-veld omgevingen, gebruik makend van numerieke simulaties. Het antwoord van een PEM heeft een bepaalde distributie, waaruit verschillende predictie-intervallen bepaald kunnen worden. Deze laten ons toe om de meetonzekerheid, die schaalt met de grootte van de overeenkomstige predictie-intervallen, van een PEM in te schatten. Deze studie toont aan dat PEMs de invallende velden onderschatten en dat de predictie-intervallen op metingen met een PEM relatief groot zijn t.o.v. metingen in de vrije ruimte. Bijgevolg hebben PEMs een onaanvaardbaar grote meetonzekerheid op de invallende veldsterktes.

Het antwoord van een PEM kan ook bestudeerd worden met kalibratiemetingen. Er wordt daarom een simultane kalibratie uitgevoerd van twee RF PEMs die gedragen worden op beide heupen van een menselijk subject in een anechoïsche kamer. Deze metingen tonen aan dat individuele PEMs de invallende EM velden onderschatten en een relatief grote variatie hebben op hun antwoord. Deze variatie kan gereduceerd worden indien er uitgemiddeld wordt over de twee PEMs op beide heupen. Daaropvolgend worden de kalibratiemetingen gebruikt om metingen met de PEMs te corrigeren voor de aanwezigheid van het lichaam. Tijdens de kalibratiemetingen werd een significante overspraak opgemeten tussen de verschillende frequentiebanden. Dit is een indicatie dat metingen met een PEM in een reële omgeving ook beïnvloed zullen zijn door overspraak.

Een persoonlijke, gedistribueerde exposimeter (*personal, distributed exposimeter* of PDE) is een meetinstrument dat bestaat uit verschillende sensoren voor

RF EM velden. Dit toestel heeft het potentiëel om de meetonzekerheid, die veroorzaakt wordt door de aanwezigheid van het menselijke lichaam, op de invallende vermogensdichtheid te reduceren. Er worden verschillende numerieke ontwerpmogelijkheden beschouwd om dit potentieel te onderzoeken. Deze numerieke simulaties tonen aan dat de meetonzekerheid op de invallende vermogensdichtheid gereduceerd kan worden, wanneer er een combinatie van meerdere RF sensoren op het lichaam gedragen worden. Dit wordt ook bevestigd door kalibratiemetingen. Zowel in de GSM 900 *downlink* (DL), d.i. de communicatie van het basisstation naar de gebruiker, als in de WiFi bij 2.4 GHz (2G) frequentieband, toont een kalibratie aan dat de meetonzekerheid op de invallende vermogensdichtheid gereduceerd kan worden indien de blootstelling opgemeten wordt met meerdere sensoren. De kalibratiemetingen worden ook gebruikt om een multifrequente PDE te ontwerpen. Dit toestel meet simultaan de blootstelling in elf frequentiebanden, gebruik makend van zes antennetypes. Metingen tonen aan dat de meetonzekerheid in alle beschouwde banden gereduceerd kan worden, indien er meerdere RF sensoren gebruikt worden om de blootstelling in de betreffende banden op te meten. Een optimale plaatsing van de verschillende antennetypes op twaalf potentiële locaties op het bovenlichaam wordt onderzocht. Deze studie toont aan dat een combinatie van twee antennes van elk van de zes onderzochte types op beide zijden van het bovenlichaam zal resulteren in de laagste gecombineerde meetonzekerheid op de totale blootstelling.

Na een kalibratie van de PDE op het lichaam, worden er metingen uitgevoerd met het toestel in verschillende omgevingen. Deze worden uitgevoerd te Gent in zowel de GSM 900 DL als de WiFi 2G band. De meetresultaten worden dan statistisch verwerkt, gebruik makend van de kalibratie. Andere factoren die kunnen bijdragen aan de meetonzekerheid worden eveneens onderzocht en gecombineerd.

Conventionele PEMs meten enkel invallende veldsterktes en vermogensdichtheden. Dit onderzoek stelt zich ook als doel om de SAR te bepalen uit metingen met een PDE. Twee uitmiddelingen van de SAR worden in dit opzicht bestudeerd: de SAR_{wb} en de orgaan-specifieke SAR (SAR_{osa}). Eerst wordt er een methode, die zowel op kalibratiemetingen als op numerieke simulaties gebaseerd is, uitgewerkt en toegepast om de SAR_{wb} te schatten uit metingen met een PDE. Daarna wordt er onderzocht of het mogelijk is om de SAR_{osa} te bepalen in heterogene, numerieke fantomen (of mensmodellen) die blootgesteld worden aan RF EM velden in een realistische omgeving. Dit leidt tot een stochastische methode, gebaseerd op een vlakke-golf benadering van de verre-veld blootstelling en de lineariteit van de vergelijkingen van Maxwell, om de SAR_{osa} te bepalen in een volwassen man in de GSM 900 DL band. Een validatie toont de bruikbaarheid van de methode aan, die bijgevolg gebruikt kan worden om de SAR_{osa} in te schatten tijdens metingen met een PDE. Dit onderzoek staat toe om de PDE niet enkel als RF exposimeter, maar ook als SAR-meter te gebruiken.

Het bovenstaande onderzoek resulteerde in tien publicaties in internationale tijdschriften, onderworpen aan collegiale toetsing, tien bijdragen op internationale conferenties en seminaries, en twee internationale wetenschappelijke onderscheidingen.

English Summary

Wireless communication is used by billions worldwide. This interaction is enabled by radio-frequency (RF) electromagnetic fields (EMFs) with a certain frequency, which are interchanged between antennas. These are either part of a network operated by a telecommunication company or embedded in a personal device operated by the user. Different technologies for wireless communication, assigned to specific frequency bands, exist. Popular examples of RF telecommunication technologies are the Global System for Mobile communications (GSM), Wireless Fidelity (WiFi), and Long Term Evolution (LTE).

The usage of RF technologies is accompanied by a concern about potential health effects that may be caused by RF radiation. The heating of dielectric tissues by the absorption of RF radiation is a proven health effect. This is used as a basis for (inter)national limits on the absorption of RF EMFs, quantified using the specific absorption rate (SAR). The SAR is defined as the rate of power absorbed in a certain mass and is usually averaged over a mass or volume. The most commonly studied quantities are the whole-body averaged SAR (SAR_{wb}) and the (peak) 10 g-averaged SAR (SAR_{10g}). These quantities cannot be measured inside the body of a living human. Therefore, reference levels have been defined on the amplitude of the incident EMFs or the magnitude of the incident power density. The goal of this dissertation is to improve the assessment of these dosimetric quantities in realistic exposure scenarios.

Part of the research in RF dosimetry focuses on compliance assessment to certain guidelines or restrictions on the emission or absorption of RF EMFs. The most commonly implemented guidelines are those issued by the International Commission on Non-Ionizing Radiation Protection (ICNIRP). There can be a zone around an antenna emitting RF EMFs where the SAR or the incident EMFs are too high in comparison to those guidelines, while further away from the antenna the exposure will be lower. The distance from the antenna at which the SAR or the incident RF EMFs are in compliance with the considered guidelines are called compliance distances or boundaries. We have numerically studied compliance boundaries around multi-band, LTE base station antennas (BSAs), based on the ICNIRP basic restrictions on the SAR_{wb} and peak SAR_{10g}, and based on the ICNIRP reference levels on the incident field strength. To the author's knowledge, these are the first compliance boundaries for LTE BSAs.

Incident EMFs are either measured using free-space measurements, without a human subject present, or on the body, using devices called personal exposimeters (PEMs). These devices have the advantage that they can be worn on the body

and thus allow for a measurement of the EMFs on the same location as the subject wearing the device. However, PEMs will measure field strengths on the body rather than the incident field strengths. The quadratic ratio of both quantities is called a PEM's response. In Chapter 3, the response of a PEM is studied in different exposure situations. First, the response of a body-worn PEM near a multi-band, base station antenna is determined. Second, a PEM's response in realistic, far-field environments is determined numerically. The response of a PEM has a certain statistical distribution, from which prediction intervals on PEM measurements of the incident field strengths can be obtained. These prediction intervals are proportional to a PEM's measurement uncertainty. This study shows that PEMs underestimate the incident fields and that their prediction intervals are relatively large. PEM measurements are consequently confronted with unacceptably large measurement uncertainties on the incident electric field strength.

The response of PEMs can also be studied using calibration measurements. Therefore, a pair of RF PEMs worn simultaneously on both hips of a male human subject is calibrated in an anechoic chamber. The calibration measurements show that single PEMs generally underestimate the incident electric field and show a relatively large variation on their response. This variation can be reduced when an average over the two PEMs is used. The calibration measurements are used to correct measurements for the influence of the body. Significant crosstalk is measured during the calibration, indicating that measurements in the individual bands with the PEMs will be obfuscated by crosstalk.

A personal, distributed exposimeter (PDE) is a device consisting of multiple on-body RF sensors, which has a potential for the reduction of the measurement uncertainty caused by the presence of the human body on the incident power density. To investigate this potential, different design approaches of a PDE are investigated using numerical simulations. These numerical designs show that using multiple RF sensors placed on the human torso, can reduce the uncertainty on measurements of the incident power density. Using calibration measurements, it is demonstrated that a PDE for measurements with good accuracy and low uncertainty in the GSM 900 downlink (DL) band can be constructed using a limited number of antennas. A PDE for the detection of WiFi around 2450 MHz is calibrated as well. A calibration of the PDE shows that the uncertainty, in terms of the 50% prediction interval, on the measured incident electric-field strength can be reduced significantly. A third, multi-band PDE, consisting of six types of antennas that measure in eleven frequency bands between 0.7 and 3 GHz, is calibrated in an anechoic chamber. The calibration measurements show that the measurement uncertainty in the different frequency bands, in terms of the 68% prediction interval, can be reduced when multiple antennas are placed on the body. An optimal placement to measure simultaneously on the 12 potential locations on the body in the eleven different frequency bands is determined. A combination of two antennas of each type placed on opposite sides of the body leads to the lowest combined 68% prediction interval.

Measurements are executed with the different PDEs in real environments, following an on-body calibration. Measurements using a PDE in the GSM 900 DL

band and the WiFi 2G band are executed and summary statistics are provided for the measured power densities. A study to determine the combined measurement uncertainty on these power densities is executed.

Conventional PEMs only measure the incident field strengths or power densities. This research also aims at estimating the SAR from PDE measurements. Two quantities are studied: the SAR_{wb} and the organ-specific averaged SAR (SAR_{osa}). First, a method, based on calibration measurements and numerical simulations, to estimate the SAR_{wb} from PDE measurements is presented and applied. Second, a method to numerically investigate the SAR_{osa} in heterogeneous phantoms in realistic environments is presented. A stochastic method based on a plane-wave approximation of far-field exposure, environmentally dependent distributions for these plane-wave exposure conditions, and the linearity of Maxwell's equations, is used in order to determine the SAR_{osa} in an adult human phantom at 950 MHz. These SAR_{osa} values are then used to determine the SAR_{osa} during measurements using a PDE, converting it to an SAR_{osa}-meter.

This research outlined above has led to ten publications in international, peer-reviewed journals, ten contributions at international conferences or workshops, and two international scientific awards.

1 Introduction

1.1 Context and motivation

Electromagnetic Fields (EMFs) are omnipresent on earth, as electromagnetism is one of the four fundamental forces of nature. EMFs are characterized by their frequency and corresponding energy. The carriers of EMFs are called photons, which have a frequency dependent energy. Photons with a higher frequency have more energy and are able to break molecular bonds. Therefore, the EMFs associated with these photons are called ionizing radiation. The EMFs with a lower energy are consequently classified as non-ionizing radiation. These fields might not carry enough energy to ionize radiation, but can be absorbed by dielectric, conductive media. This absorption in its turn can lead to dielectric relaxation and consequently tissue heating. An example of non-ionizing radiation are Radio-Frequency (RF) EMFs. These are located at frequencies ranging from several kHz up to 300 GHz and are mainly used for wireless communication.

This wireless communication using RF EMFs has become more important in the past decades and its usage will increase even more in the future [1]. Consequently the number of sources that emit RF electromagnetic radiation has considerably risen in the past decades and will increase even further. RF wireless communication uses signals that are emitted and received by antennas. This communication usually takes place between different users of the wireless network with one or more intermediate network providers. The providers operate a wireless network of several antennas connected to a (wired) backbone network. The antennas that make up the wireless network range from the large Base Station Antennas (BSAs)

(or macro-cell antennas), which are (arrays) of antennas typically mounted on towers or tall buildings, that can cover areas of several square kilometers and emit dozens of Watts of power, to femto-cell antennas, which are smaller antennas that cover areas of several square meters, emit lower RF power, and can be placed in a home or office environment. The users communicate with the network using antennas embedded in their mobile devices such as smart phones, cellular phones, or tablets. In some cases the users only receive signals from the network and are not able to return any. This kind of communication, using a limited set of antennas on high towers that emit hundreds to thousands of Watts of power, is referred to as broadcasting. In other scenarios users can communicate wirelessly with one another without using a network. Therefore, different frequency bands and technical standards have been defined to enable these different applications.

1.1.1 Frequency Bands

The usage of the RF spectrum is regulated on a national level. In Belgium this is the responsibility of the Belgian Institute for Postal services and Telecommunications (BIPT) [2]. On a European scale, the Electronic Communications Committee (ECC) within the European Conference of Postal and Telecommunications Administrations (CEPT) is responsible for the registration, future planning, and harmonization of the RF spectrum in the European Union (EU) [3]. This harmonization is an ongoing process and up to date there still exist differences between the different EU member states [3]. The ECC informs the general public on all the allocated frequencies on their website [4] and through reports such as [3]. In our research, we focused on the frequency bands as defined by the BIPT [2].

The main frequency bands that contribute to personal exposure are either broadcast bands (such as Frequency Modulated radio (FM)), in which a signal is (mainly) emitted from a central base station to the users, but no signal is emitted by the users towards the base station, or telecommunication bands (such as the Global System for Mobile communications (GSM) 900), in which both the base stations and the users exchange signals. Table 1.1 lists the most common RF bands and their allocated frequencies in Belgium. The different communication bands are briefly described below.

Frequency Modulation (**FM**) is used for radio transmissions around 100 MHz. This band is named after the modulation technique used to broadcast public and commercial radio to the listeners.

A second frequency band designated to broadcasting is located around 200 MHz. This frequency band, denoted **TV/DAB**, is used for digital television and audio: Digital Video Broadcasting - Terrestrial (DVB-T) [5], Digital Video Broadcasting - Hand held (DVB-H) [6], and Digital Video Broadcasting - Next Generation Hand held (DVB-NGH) [7], and Digital Audio Broadcasting (DAB) [8].

Name	Frequency Range (MHz)
FM	87.5-108
TV/DAB	174-230
TETRA	380-400
TV	470-862
Lower 3GPP LTE	791-821 832-862
GSM-R UL	876-880
GSM 900 UL	880-915
GSM-R DL	921-925
GSM 900 DL	925-960
DCS UL/ GSM 1800 UL	1710-1785
DCS DL/ GSM 1800 DL	1805-1880
DECT	1880-1900
UMTS/HSPA	1900-1920
UMTS UL / HSUPA	1920-1980
UMTS DL / HSDPA	2110-2170
WiFi 2G	2400-2483.5
Upper 3GPP LTE	2500-2570 2575-2620 2620-2690
WIMAX	3400-3600
WiFi 5G	5150-5350 5470-5725 5725-5875

Table 1.1: Name and frequency band of the most used RF frequency bands in Belgium [2].

TETRA or Terrestrial Trunked Radio is a telecommunication band around 400 MHz. It was standardized in order to achieve a common wireless network for the public sector (government agencies, emergency services) across Europe [9, 10]. In Belgium the system is commonly known as ASTRID: All-round Semi-cellular Trunking Radio communication system with Integrated Dispatching, which is used by public services such as the police, the army, hospitals, and the fire department for their telecommunication.

A third frequency band designated to broadcasting is located between 400 and 900 MHz. This frequency band, denoted **TV** in Table 1.1, is used predominantly for digital (and analogue) television broadcasts, including: DVB-T [5], DVB-H [6], and DVB-NGH [7]. The upper part of this frequency band (above 791 MHz) is now used for telecommunication as well.

The newest of the studied technologies is **Third Generation Partnership Project (3GPP) Long Term Evolution (LTE)** [11]. This technology is used in two different frequency bands: a lower band around 800 MHz and an upper band around 2600 MHz (see Table 1.1). This communication band is mainly used for fast data (and voice) transmission between users and base stations [11] and is widely known as 4G.

Global System for Mobile Communications (GSM), also known as 2G, is

a technology which is divided over 4 frequency bands: two Up-Link (UL) bands, for communication from the user to the base station, around 900 and 1750 MHz, and two Down-Link (DL) bands, used for communication from the base station to the users, around 950 MHz and 1845 MHz. The upper bands are also known as **Digital Cellular Service (DCS)** UL and DL. GSM was the first technology that enabled digital wireless communication [12] and at that time caused an improved connectivity and higher quality of service in comparison to the older, analogue systems. Two separate GSM bands, an UL and a DL band, are used for communications in the European railway system (GSM-R). The GSM frequency bands listed in Table 1.1 are nowadays also used for other technologies such as General Packet Radio Service (GPRS) [13], Enhanced Data rates for GSM Evolution (EDGE) [14], Universal Mobile Telecommunications System (UMTS), High Speed Packet Access (HSPA) [15], and LTE, that allow for short message services, data transfer, or internet browsing.

Digital Enhanced Cordless Telecommunication (DECT) [16] is a telecommunication channel used for domestic or professional communication between a small base station and (multiple) cordless phones around 1800 MHz.

Universal Mobile Telecommunications System (UMTS) and High Speed Packet Access (HSPA), also known as 3G, are telecommunication technologies used for transmitting data and voice messages between a BSA and a user [15, 17]. These technologies are used in the lower GSM band and also have three dedicated frequency bands in Belgium (see Table 1.1).

Wireless Fidelity (WiFi) is a technology used for wireless internet access, usually in indoor environments, but recently also in outdoor environments. The standard is defined by the Institute of Electrical and Electronics Engineers (IEEE) in standards IEEE.802.11a-u [18]. The technology shares the Industrial, Scientific, and Medical (ISM) frequency bands around 2.4 and 5 GHz with other applications. This license free ISM band is used for a large amount of medical, industrial, scientific, and commercial applications, such as microwave heating, communication between devices, and tissue heating. The frequency bands listed in Table 1.1 are those assigned in Belgium. However, this is the frequency band with the largest differences in assigned bandwidth across Europe [4].

Worldwide Interoperability for Microwave Access (WIMAX) operating in the 3.5 GHz band, is a not so commonly used telecommunication frequency band defined by IEEE in the IEEE 802.16 standard [19]. This technology for data communication promises higher bit rates and flexibility in terms of used bandwidth and has both a fixed and a mobile version.

1.1.2 Fields of Study Concerning RF Radiation

The increase in the use of RF radiation is accompanied by an increasing number of studies [20–26] that aim at quantifying exposure of the human body to RF ra-

diation. This is motivated by the potential adverse health effects associated with this radiation. Three different types of studies exist in this research area: a first type investigates the different physical quantities involved in human exposure to RF EMFs, such as the incident electric or magnetic field strengths, the incident power densities, but also the power absorbed in dielectric tissues [27–29], and even the potential temperature increases [30]. This line of research is named **RF dosimetry** and the studied quantities are consequently referred to as dosimetric quantities. Numerical dosimetry uses simulations to study the exposure to and absorption of RF EMFs [27–30]. Another line of research within RF dosimetry, called RF exposure assessment, focuses on the development and execution of methods and protocols for assessing or measuring these quantities [21, 31]. **RF Epidemiology** is a second type of study that uses RF dosimetry to statistically correlate (human) exposure to potential (adverse) health effects [20, 25, 26]. In a final line of study either **in-vivo or in-vitro RF exposures** are used to determine potential (adverse) biological effects of exposure to RF radiation [32–34]. These studies also rely heavily on dosimetry and exposure assessment in order to obtain a reliable dose-response in their studies. Other related fields of study are: computational electromagnetism, where techniques are developed to simulate the behavior of EMFs in different situations, antenna studies, where the sources and receivers of EMFs are studied, and hyperthermia, where curing cancer through RF tumor tissue heating is studied clinically. This dissertation is situated primarily in the field of RF dosimetry.

1.1.3 ICNIRP Basic Restrictions and Reference Levels

RF EMFs can cause tissue heating and therefore have to be regulated. The most widely accepted and adopted exposure limits are issued by the International Commission on Non-Ionizing Radiation Protection (ICNIRP) [35]. For frequencies between 10 MHz and 10 GHz, including the frequency range used for mobile communications, the fundamental dosimetric quantity is the Specific Absorption Rate (SAR), which is the rate at which energy is absorbed in a certain mass (unit: W/kg). This quantity is to be averaged over a certain volume or mass. ICNIRP defines two different averaging methods in its guidelines [35]: the whole-body averaged SAR (SAR_{wb}) and the 10 g averaged SAR (SAR_{10g}). There exist other averaging methods such as organ-specific averaged SAR (SAR_{osa}) [36] or 1 g averaged SAR [37], but these are not considered in the ICNIRP guidelines.

In order to limit the SAR, the ICNIRP defines basic restrictions, these are SAR values that may not be exceeded, even in worst-case conditions. Different basic restrictions exist for the general public and occupational exposure. In case of the SAR_{10g}, two different basic restrictions are issued: one for the peak value of the SAR_{10g} in the head and trunk of an individual, and one for the peak value of the SAR_{10g} in the limbs. However, these SAR values cannot be measured in living

humans. Therefore, the ICNIRP has determined reference levels, derived from the basic restrictions, that limit the incident electric and magnetic field strengths (without the presence of a human). Table 1.2 lists the different basic restrictions and reference levels applicable to the research presented in this book.

Basic restrictions	General Public	Occupational
SAR_{wb} (10 MHz-10 GHz)	0.08 W/kg	0.4 W/kg
peak SAR_{10g} in head and trunk (10 MHz-10 GHz)	2 W/kg	10 W/kg
peak SAR_{10g} in limbs (10 MHz-10 GHz)	4 W/kg	20 W/kg
Reference Levels	General Public	Occupational
Electric Field Strength (0.4-2 GHz)	$1.375 \times f^{1/2}$ V/m	$3 \times f^{1/2}$ V/m
Electric Field Strength (2-300 GHz)	61 V/m	137 V/m
Magnetic Field Strength (0.4-2 GHz)	$0.0037 \times f^{1/2}$ A/m	$0.008 \times f^{1/2}$ A/m
Magnetic Field Strength (2-300 GHz)	0.16 A/m	0.36 A/m

Table 1.2: ICNIRP basic restrictions and reference levels [35]. f is the frequency in MHz.

1.1.4 Compliance Assessment

Some studies [38–40] in RF dosimetry focus on compliance assessment to the ICNIRP guidelines [35]. An antenna emitting RF EMFs with a certain output power will cause a certain SAR in a person near this antenna. This SAR can exceed the basic restrictions (see Table 1.2) close to the antenna, while the SAR can be in compliance with the ICNIRP basic restrictions at larger distances from the antenna. The distance at which the SAR induced in the subject's body equals the ICNIRP basic restrictions is called a compliance distance or compliance boundary. This distance depends on the antenna's characteristics and the antenna's input (or emitted) power. Since there are different basic restrictions, there are also different compliance boundaries for each basic restriction. There might exist distances from an antenna where the SAR_{wb} is in compliance with the basic restriction, but the peak SAR_{10g} is not in compliance. In order to ensure full compliance with all basic restrictions, the maximal compliance boundary determined for a given output power of the antenna should be considered. Similar compliance distances can be determined using the reference levels instead of the basic restrictions.

1.1.5 Personal Exposure Assessment

Dosimetry mainly uses numerical simulations or measurements in phantoms, which are objects used to represent the human body (often a shell filled with a tissue simulating liquid [41]), to assess the different dosimetric quantities in certain RF exposure situations. Exposure assessment will use different RF measurement equipment to assess the different dosimetric quantities. Personal exposimeters (PEMs)

are commonly used devices to measure one's exposure to RF EMFs. These devices have the advantage that they can be worn on the body and thus allow for a measurement of the electric fields on the same location as that of the subject wearing the device. The reference levels (see Tabel 1.2) hold for incident field strengths (without the presence of the body) while a PEM measures on the body. The ratio of both quantities is called a PEM's response. This quantity is studied throughout this dissertation.

1.2 Outline

The general topic of this dissertation is personal exposure assessment to RF electromagnetic fields. The following subjects are described in the chapters of this thesis:

In Chapter 2, a numerical study of compliance boundaries around multi-band BSAs based on the whole-body averaged SAR (SAR_{wb}), peak 10 g averaged SAR (SAR_{10g}) in head and trunk or in the limbs, and on the E_{rms} using the ICNIRP basic restrictions and reference levels for the general public and occupational exposure is executed. Two different approaches are followed: first, a compliance assessment using detailed antenna models of the studied multi-band BSAs and a realistic phantom is executed. Second, a compliance assessment in front of a generic model for one of the multi-band antennas is executed using standardized procedures.

The same simulations are used in Chapter 3 to determine the response of a personal exposimeter (PEM) near a multi-band, base station antenna. Additional numerical simulations are executed to determine a PEM's response in five realistic, far-field environments. This response is a quantity which provides the relationship between the electrical field strengths measured by a PEM and the incident field strengths. The response of a PEM is studied as a statistical variable, with a certain distribution, from which prediction intervals can be obtained. These prediction intervals are proportional to a PEM's measurement uncertainty.

In Chapter 4, the response of conventional PEMs is studied using calibration measurements. Two RF PEMs worn simultaneously on both hips are calibrated on a male human subject in an anechoic chamber for 880 MHz-5.58 GHz and used for actual measurements. Besides the response, the crosstalk is determined during the calibration as well. The calibration data are used to correct PEM measurement data for the influence on the body and determine the uncertainty on the summary statistics of these data.

A personal, distributed exposimeter (PDE) is a device, consisting of body-worn antennas, which is used to measure one's personal exposure to RF incident power density. Chapter 5 investigates the potential of a PDE for the reduction of the measurement uncertainty caused by the presence of the human body on the

incident power density. To this end, different design approaches are investigated using numerical simulations.

Following this numerical design, calibration measurements of PDEs are executed in Chapter 6. A method for calibration measurements of on-body antennas is introduced. This method is then used to calibrate two PDEs designed using numerical simulations: one for the GSM 900 DL band and one for the WiFi 2G band. In a second part of the chapter, the same calibration method is used for the design of another PDE in the GSM 900 DL band. In a final part of the chapter, a multi-band PDE is designed, based on calibration measurements.

In Chapter 7, the PDE is used for measurements in a real environment. Measurements using a PDE in the GSM 900 DL band and the WiFi 2G band are presented and discussed. These measurements will have an uncertainty which is estimated using both measurements and numerical simulations. In a final part of the chapter, it is investigated whether the SAR_{wb} can be estimated from PDE measurements.

Chapter 8 investigates whether the organ-specific averaged SAR (SAR_{osa}) can be estimated from PDE measurements as well. To this aim, a method to numerically investigate the SAR_{osa} in heterogeneous phantoms in realistic environments is introduced. This method is used to determine the SAR_{osa} of the virtual family male (VFM) in the 'Urban Macro-cell' scenario in the GSM 900 DL band. A method to estimate the SAR_{osa} from PDE measurements is investigated in the final part of the chapter.

A summary of the results obtained in this work and some potential areas of future research are presented in Chapter 9.

1.3 Publications

The following list provides an overview of the publications produced by the author during his PhD. This PhD research has led to twelve publications in international, peer-reviewed journals and eleven contributions at international conferences or workshops.

1.3.1 A1

(peer-reviewed publications in journals listed in the ISI Web of Science)

1.3.1.1 As first author

[AT1] **A. Thielens**, G. Vermeeren, D. Kurup, W. Joseph, and L. Martens, "Compliance Boundaries for Multiple-Frequency Base Station Antennas in Three Directions," *Bioelectromagnetics*, vol. 34, no. 7, pp. 563-567, 2013.

[AT2] **A. Thielens**, G. Vermeeren, W. Joseph, and L. Martens, "Stochastic Method for Determination of the Organ-Specific Averaged SAR in Realistic Environments at 950 MHz," *Bioelectromagnetics*, vol. 34, no. 7, pp. 549-562, 2013.

[AT3] **A. Thielens**, H. De Clercq, S. Agneessens, J. Lecoutere, L. Verloock, F. Declercq, G. Vermeeren, E. Tanghe, H. Rogier, R. Puers, L. Martens, and W. Joseph, "Personal Distributed Exposimeter for Radio Frequency Exposure Assessment in Real Environments," *Bioelectromagnetics*, vol. 34, no. 7, pp. 563-567, 2013.

[AT4] **A. Thielens**, P. Vanveerdeghem, S. Agneessens, P. Van Torre, G. Vermeeren, H. Rogier, L. Martens, and W. Joseph, "Whole-Body Averaged Specific Absorption Rate Estimation using a Personal, Distributed Exposimeter" *IEEE Antennas and Wireless Propagation Letters*, published online, November 2014, doi:10.1109/LAWP.2014.2368597.

[AT5] **A. Thielens**, S. Agneessens, L., Verloock, E. Tanghe, H. Rogier, L. Martens, and W. Joseph, "On-body Calibration and Processing for a Combination of Two Radio Frequency Personal Exposimeters," *Radiation Protection Dosimetry*, vol. 163, no. 1, pp. 58-69, 2015.

[AT6] **A. Thielens**, S. Agneessens, H. De Clercq, J. Lecoutere, L. Verloock, E. Tanghe, S. Aerts, R. Puers, H. Rogier, L. Martens, and W. Joseph, "On-body Calibration and Measurements using a Personal, Distributed Exposimeter for Wireless Fidelity," *Health Physics*, vol. 108, no. 4, pp. 407-418, 2015.

1.3.1.2 As co-author

[AT7] K. LL Roman, G. Vermeeren, **A. Thielens**, W. Joseph, and L. Martens, "Characterization of path loss and absorption for a wireless radio frequency link between an in-body endoscopy capsule and a receiver outside the body," *EURASIP Journal on Wireless Communications and Networking*, vol. 2014, no. 1, pp. 21, 2014.

[AT8] B. Thors, **A. Thielens**, D. Colombi, C. Törnevik, G. Vermeeren, L. Martens, and W. Joseph, "Radio frequency electromagnetic field compliance assessment of multi-band and MIMO equipped radio base stations," *Bioelectromagnetics*, vol. 35, no. 4, pp. 296-308, 2014.

[AT9] A. Bamba, W. Joseph, G. Vermeeren, **A. Thielens**, E. Tanghe, and L. Martens, "A Formula for Human Whole-body averaged SAR under Single Plane Wave and Diffuse Fields Exposure in the GHz region," *Physics in Medicine and Biology*, vol. 59, no. 23, pp. 7435-7456, 2014.

[AT10] S. Aerts, D. Plets, **A. Thielens**, L. Martens, and W. Joseph, "Impact of a small cell on the RF-EMF exposure in a train," *International Journal of Environmental Research and Public Health*, vol. 12, no. 3, pp. 2639-2652, 2015.

[AT11] M. Marinova, **A. Thielens**, E. Tanghe, L. Vallozzi, G. Vermeeren, W. Joseph, H. Rogier, and L. Martens, "Diversity Performance of Off-body MB-OFDM UWB-MIMO ," *IEEE Transactions on Antennas and Propagation*, published online, doi:10.1109/TAP.2015.2422353, 2015.

[AT12] P. Vanveerdeghem, P. Vantorre, **A. Thielens**, J. Knockaert, W. Joseph, and H. Rogier, "Compact Personal Distributed Wearable Exposimeter," *IEEE Sensors Journal*, published online, doi:10.1109/JSEN.2015.2420583, 2015.

1.3.2 Conference

(peer-reviewed publications presented at international conferences or workshops)

1.3.2.1 As first author

[AT13] **A. Thielens**, G. Vermeeren, W. Joseph, and L. Martens, "Organ specific averaged SAR in a realistic environment at 950 MHz," in *33th Ann. Meeting of the Bioelectromagnetics Soc.*, Halifax, Nova Scotia, Canada, June 2011.

[AT14] **A. Thielens**, G. Vermeeren, D. Kurup, W. Joseph, and L. Martens, "Compliance Boundaries for LTE Base Station Antennas," in *6th European Conference on Antennas and Propagation*, Prague, Czech Republic, March 2012.

[AT15] **A. Thielens**, G. Vermeeren, W. Joseph, and L. Martens, "Organ specific averaged SAR for the central nervous system," in *7th International Workshop on Non Ionizing Radiation*, Edinburgh, Scotland, UK, May 2012.

[AT16] **A. Thielens**, G. Vermeeren, D. Kurup, W. Joseph, and L. Martens, "Organ specific averaged SAR near multiple-frequency base station antennas," in *34th Ann. Meeting of the Bioelectromagnetics Soc*, Brisbane, Australia, June 2012.

[AT17] **A. Thielens**, G. Vermeeren, W. Joseph, and L. Martens, "Influence of the incident angle of single plane-waves on the organ specific SAR at 950 MHz," in *34th Ann. Meeting of the Bioelectromagnetics Soc*, Brisbane, Australia, June 2012.

[AT18] **A. Thielens**, H. De Clercq, S. Agneessens, J. Lecoutere, L. Verloock, F. Declerq, G. Vermeeren, E. Tanghe, H. Rogier, R. Puers, L. Martens and W. Joseph, "Personal Distributed Exposimeter for Radio Frequency Electromagnetic Field Assessment," in *BioEM2013 Joint Meeting of The Bioelectromagnetics Society (BEMS) and the European BioElectromagnetics Association (EBEA)*, Thessaloniki, Greece, June 2013, **Awarded with the Joseph James Morrissey Memorial Award**.

[AT19] **A. Thielens**, S. Agneessens, G. Vermeeren, H. Rogier, L. Martens, and W. Joseph, "Response of Personal Exposimeters for Exposure Assessment in the GSM900 Down-link Band," in *International Conference on Electromagnetic Fields, Health and Environment*, Porto, Portugal, April 2014.

[AT20] **A. Thielens**, P. Vanveerdeghem, S. Agneessens, P. Vantorre, G. Vermeeren, H. Rogier, L. Martens, and W. Joseph, "Whole-body Averaged SAR Assessment Using a Personal, Distributed Exposimeter," in *BioEM2014 Joint Meeting of The Bioelectromagnetics Society (BEMS) and the European BioElectromagnetics Association (EBEA)*, Cape Town, South Africa, June 2014.

[AT21] **A. Thielens**, S. Agneessens, J. Lecoutere, L. Verloock, E. Tanghe, S. Aerts, R. Puers, H. Rogier, L. Martens, and W. Joseph, "On-Body Calibration of a Personal Distributed Exposimeter for Wireless Fidelity for Indoor and Outdoor Measurements," in *URSI AT-RASC 2015*, Gran Canaria, Spain, May 2015.

1.3.2.2 As co-author

[AT22] J. Lecoutere, H. De Clercq, **A. Thielens**, S. Agneessens, H. Rogier, W. Joseph, and R. Puers, "Assessing radio frequency electromagnetic field exposure with a wearable network of dosimeters," in *20th Symposium of the International Society on Biotelemetry (ISOB 2014)*, Kyoto, Japan, 2014.

[AT23] H. De Clercq, **A. Thielens**, J. Lecoutere, S. Agneessens, H. Rogier, W. Joseph, and R. Puers, "A distributed wearable EM field recorder for RF exposure assessment in real environments," in *20th Symposium of the International Society on Biotelemetry (ISOB 2014)*, Kyoto, Japan, 2014.

1.3.3 Other publications

1.3.3.1 As first author

[AT24] **A. Thielens**, W. Joseph, and L. Martens, "How much Radio Frequency Radiation is absorbed in our bodies?," in *13th FEA PhD Symposium*, Ghent, Belgium, December 2012, session: It's alive.

[AT25] **A. Thielens**, G. Vermeeren, D. Kurup, W. Joseph, and L. Martens, "Compliance Boundaries for LTE Base Station Antennas at 2600 MHz," in *COST IC 1400 6th Management Committee Meeting*, Malaga, Spain, February 2013, ref.: TD(13)06002.

[AT26] **A. Thielens**, H. De Clercq, S. Agneessens, J. Lecoutere, L. Verloock, F. Declerq, G. Vermeeren, E. Tanghe, H. Rogier, R. Puers, L. Martens, and W. Joseph, "Design and Calibration of a Personal, Distributed Exposimeter for Radio Frequency Electromagnetic Field Assessment," in *COST IC 1400 8th Management Committee Meeting*, Ghent, Belgium, September 2013, ref.: TD(13)08033.

[AT27] **A. Thielens**, "2013 Best Student Platform Presentation: Joseph James Morrissey Memorial Award - Arno Thielens," in *The Bioelectromagnetics Society's newsletter*, volume: 233, October 2013.

[AT28] **A. Thielens**, "A Personal, On-Body Distributed Exposimeter," in *The Bioelectromagnetics Society's news*, April 2014, ref: https://www.bems.org/node/14323.

1.3.3.2 As co-author

[AT29] M. Marinova, E. Tanghe, **A. Thielens**, L. Vallozzi, G. Vermeeren, W. Joseph, H. Rogier, and L. Martens, "Diversity Performance of Off-body UWB-MIMO," in *COST IC 1400 8th Management Committee Meeting*, Ghent, Belgium, September 2013, ref.: TD(13)08032.

1.4 Awards

This PhD research has led to two scientific awards [AT18] and [AT21]. The author received the Joseph James Morrissey Memorial Award issued by the Bioelectromagnetics Society (BEMS) and the European BioElectromagnetics Association (EBEA) in June 2013. He also received the URSI Young Scientist Award 2015 issued by the International Union of Radio Science (Union Radio-Scientifique Internationale or URSI) in May 2015.

References

[1] Cisco. *Cisco Visual Networking Index: Global Mobile Data Traffic Forecast Update, 20132018.* White paper, Technical report, 2013.

[2] Belgian Institute for Postal services and Telecommunications (BIPT). *www.bipt.be*.

[3] Electronic Communications Committee (ECC). *The European Table of Frequency Allocations and Applications in the frequency range 8.3 kHz to 3000 GHz (ECA Table).* ERC REPORT 25, 2013.

[4] Electronic Communications Committee (ECC). *http://www.efis.dk/.*

[5] ETSI. *Digital Video Broadcasting (DVB); Framing structure, channel coding and modulation for digital terrestrial television.* EN 300 744 v1.6.1, January 2009.

[6] ETSI. *Digital Video Broadcasting (DVB); Transmission System for Handheld Terminals (DVB-H).* EN 302 304 v1.1.1, November 2004.

[7] ETSI. *Next Generation broadcasting system to Handheld, physical layer specification (DVB-NGH).* DVB Bluebook A160, November 2012.

[8] ETSI. *Radio Broadcasting Systems; Digital Audio Broadcasting (DAB) to mobile, portable and fixed receivers.* EN 300 401 v1.4.1, June 2006.

[9] ETSI. *Terrestrial Trunked Radio (TETRA), Voice plus Data (V+D).* ETS 300 392 series of standards., 1995-2015.

[10] ETSI. *Terrestrial Trunked Radio (TETRA), Packet Data Optimized (DPO).* ETS 300 392 series of standards., 1995-2015.

[11] 3rd Generation Partnership Project (3GPP). *LTE; Technical Specification Group Radio Access Network; Evolved Universal Terrestrial Radio Access (E-UTRA); User Equipment (UE) Radio Transmission and Reception (TS 36.101 v 9.1.0 Release 9).* 2009.

[12] ETSI. *Digital cellular telecommunications system (Phase 2+); GSM Cordless Telephony System (CTS), Phase 1; CTS radio interface layer 3 specification (GSM 04.56 version 7.1.1 Release 1998).* ETSI EN 302 406 v7.1.1, 2000.

[13] ETSI. *Digital cellular communications system (Phase 2+); General Packet Radio Service (GPRS); Overall description of the GPRS radio interface; Stage 2 (3GPP TS 03.64 version 8.12.0 Release 1999).* ETSI TS 101 350 v8.12.0, 2004.

[14] ETSI. *Digital cellular telecommunications system (Phase 2+); Physical Layer on the Radio Path (General Description) (3GPP TS 45.001 version 4.0.1 Release 4).* ETSI TS 145 001 v4.0.1, 2000.

[15] 3rd Generation Partnership Project 3GPP. *Technical Specification Group Radio Access Network: Physical Layer Aspects of UTRA High Speed Downlink Packet Access (Release 4).* TR 25.848 v4.0.0, 2000.

[16] ETSI. *Digital Enhanced Cordless Telecommunications (DECT); DECT Packet Radio Service (DPRS).* ETSI EN 301 649 v1.4.1, 2004.

[17] 3rd Generation Partnership Project 3GPP. *Technical Specification Group Radio Access Network, UE Radio Transmission and Reception (TDD) Release 1999.* TR 25.102 v3.13.0, 2006.

[18] LAN/MAN Standards Committee of the IEEE Computer Society. *Supplement to IEEE Standard for Information technology - Telecommunications and information exchange between systems - Local and metropolitan area networks - Specific requirements - Part 11: Wireless LAN Medium Access Control (MAC) and Physical Layer (PHY) specifications: Higher-speed Physical Layer Extension in the 2.4 GHz band.* 1999.

[19] IEEE Computer Society, the IEEE Microwave Theory, and Techniques Society. *Air interface for Fixed Broadband Wireless Access Systems.* 1999.

[20] P Frei, E Mohler, G Neubauer, G Theis, A Bürgi, J Frölich, C Braun-Fährländer, J Bolte, M Egger, and M Röösli. *Temporal and spatial variability of personal exposure to radio frequency electromagnetic fields.* Environmental research, 109(6):779–85, August 2009.

[21] W Joseph, G Vermeeren, L Verloock, M Masache Heredia, and L Martens. *Characterization of personal RF electromagnetic field exposure and actual absorption for the general public.* Health physics, 95(3):317–30, September 2008.

[22] W Joseph, P Frei, M Roösli, G Thuróczy, P Gajsek, T Trcek, J Bolte, G Vermeeren, E Mohler, P Juhász, V Finta, and L Martens. *Comparison of personal radio frequency electromagnetic field exposure in different urban areas across Europe.* Environmental research, 110(7):658–63, October 2010.

[23] U Knafl, H Lehmann, and M Riederer. *Electromagnetic field measurements using personal exposimeters.* Bioelectromagnetics, 29(2):160–2, February 2008.

[24] G Neubauer, M Feychting, Y Hamnerius, L Kheifets, N Kuster, Io Ruiz, J Schüz, R Uberbacher, J Wiart, and M Röösli. *Feasibility of future epidemiological studies on possible health effects of mobile phone base stations.* Bioelectromagnetics, 28(3):224–30, April 2007.

[25] M Röösli, P Frei, E Mohler, C Braun-Fahrländer, A Bürgi, J Fröhlich, G Neubauer, G Theis, and M Egger. *Statistical analysis of personal radiofrequency electromagnetic field measurements with nondetects.* Bioelectromagnetics, 29(6):471–8, September 2008.

[26] J F Viel, E Cardis, M Moissonnier, R de Seze, and M Hours. *Radiofrequency exposure in the French general population: band, time, location and activity variability.* Environment international, 35(8):1150–4, November 2009.

[27] G Vermeeren, W Joseph, and L Martens. *Whole-body SAR in spheroidal adult and child phantoms in realistic exposure environment*. Health Physics, 94(June):345–354, 2008.

[28] J F Bakker, M M Paulides, A Christ, N Kuster, and G C van Rhoon. *Assessment of induced SAR in children exposed to electromagnetic plane waves between 10 MHz and 5.6 GHz.* Physics in medicine and biology, 55(11):3115–3130, 2010.

[29] S Iskra, R McKenzie, and I Cosic. *Monte Carlo simulations of the electric field close to the body in realistic environments for application in personal radiofrequency dosimetry.* Radiation Protection Dosimetry, 147(4):517–27, 2011.

[30] J F Bakker, M M Paulides, E Neufeld, A Christ, N Küster, and G C van Rhoon. *Children and adults exposed to electromagnetic fields at the ICNIRP reference levels: Theoretical assessment of the induced peek temperature increase.* Physics in medicine and biology, 56:4967–4989, 2011.

[31] L Verloock, W Joseph, G Vermeeren, and L Martens. *Procedure for assessment of general public exposure from WLAN in offices and in wireless sensor network testbed.* Health Phys., 98(4):628–638, 2010.

[32] E Brillaud, A Piotrowski, and R de Seze. *Effect of an acute 900 MHz GSM exposure on glia in the rat brain: A time-dependent study*. Toxicology, 238(1):23–33, August 2007.

[33] E van Rongen, R Croft, J Juutilainen, I Lagroye, J Miyakoshi, R Saunders, R de Seze, T Tenforde, L Verschaeve, B Veyret, and Z Xu. *Effects of Radiofrequency Electromagnetic Fields on the Human Nervous System*. Journal of Toxicology and Environmental Health-Part B-Critical Reviews, 12(8):572–597, 2009.

[34] Q Balzano, CK Chou, R Cicchetti, A Faraone, and RYS Tay. *An efficient RF exposure system with precise whole-body average SAR determination for in vivo animal studies at 900 MHz*. IEEE Transactions on Microwave Theory and Techniques, 48(11, 2):2040–2049, NOV 2000.

[35] ICNIRP International Commission on Non-Ionizing Radiation Protection. *Guidelines for limiting exposure to time-varying electric, magnetic, and electromagnetic fields (up to 300 GHz).* Health physics, 74:494–522, 1998.

[36] A Thielens, G Vermeeren, W Joseph, and L Martens. *Stochastic Method for the Determination of the Organ-specific Averages SAR in Realistic Environments at 950 MHz.* Bioelectromagentics, 34(7):549–562, 2013.

[37] IEEE Institute of Electrical and Electronics Engineers. *IEEE Standard for safety levels with respect to human exposure to radio frequency electromagnetic fields, 3 kHz to 300 GHz Std C95.1*. New York: IEEE, 2005.

[38] Paolo Bernardi, Marta Cavagnaro, Stefano Pisa, and Emanuele Piuzzi. *Human Exposure to Radio Base-Station Antennas in Urban Environment*. IEEE Trans Microw Theory Tech, 48:1996–2002, November 2000.

[39] Björn Thors, Marie L Strydom, Frans J C Meyer, and K Kimmo. *On the Estimation of SAR and Compliance Distance Related to RF Exposure From Mobile Communication Base Station Antennas*. IEEE Trans Electromagn Compat, 50(4):837–848, November 2008.

[40] Marie-Christine Gosselin, Andreas Christ, Sven Kühn, and Niels Kuster. *Dependence of the Occupational Exposure to Mobile Phone Base Stations on the Properties of the Antenna and the Human Body*. IEEE Transactions on Electromagnetic Compatibility, 51(2):227–235, May 2009.

[41] CENELEC (European Committee for Electrotechnical Standardization). *Basic standard for the calculation and measurement of electromagnetic field strength and SAR related to human exposure from radio base stations and fixed terminal stations for wireless telecommunication systems (110 MHz40 GHz). CENELEC EN 50383:2010. Brussels, Belgium*. 2010.

2

Personal Exposure Assessment Near Base Station Antennas

2.1 Introduction

Exposure of a human to radio frequency (RF) electromagnetic fields (EMFs) may induce health effects such as tissue heating [1]. In order to prevent the general public and workers from this tissue heating, the International Commission on Non-Ionizing Radiation Protection (ICNIRP) has issued certain limits (basic restrictions and reference levels, see Table 1.2) on the specific absorption rate (SAR) and incident electric fields. RF EMFs are for example emitted by base station antennas (BSAs), which are large antenna (arrays) used by telecom operators to enable communication between their clients using RF signals. These BSAs can be approached by the general population and instructed workers, whose exposure has to be in compliance with the ICNIRP guidelines [1] and other (inter)national legislations, which are usually based on the former. Therefore, these guidelines are used to determine compliance distances or allowed BSA output powers. Standards for the evaluation of RF compliance near BSAs have also been issued by the International Electrotechnical Commission (IEC) [2, 3] and the European Committee for Electrotechnical Standardization (CENELEC) [4].

Earlier studies [5–10] aim at evaluating the SAR and electric fields in the proximity of a BSA. In those studies, compliance distances are determined in the direction of the antenna's main lobe, using measurements or simulations of electric fields. More recent studies also consider other directions towards the an-

tenna [11] and use the Virtual Family for compliance simulations [12, 13]. The former study also presents formulas to estimate SAR values or compliance distances using parameters of the antenna. A large study has determined the SAR at different sides (front and back) of the antenna for several generic antenna types (modeled as dipole arrays) and single frequency exposure conditions in the region of 0.3 - 5 GHz [12, 14]. The influence of a reflective environment around the phantom is also studied in [5] and [14]. Recently, Long Term Evolution (LTE) BSAs, emitting at 800 and 2600 MHz, and multiple-frequency BSAs are developed and are now in use [15]. Yet a full assessment of the compliance boundaries around these antennas did not exist. The exposure caused by these BSAs is already studied by [16] but only for one direction and single-frequency operation. Two different approaches are currently pursued in the research on compliance assessment, namely a first approach where very detailed antenna models and human phantoms are used or a second approach where simplified generic antenna models and standardized procedures are preferred. Some studies use detailed antenna models, that are constructed by replicating the fine geometrical structures of the corresponding physical antennas, in order to produce results with high accuracy. However, a disadvantage of this approach is that the creation of the numerical antenna model and the simulations using the highly detailed models are time-consuming. Furthermore, in the reported studies, different types of anatomical human phantom models have been used. This reduces the general applicability of these studies, since SAR depends on the size and shape of the considered phantoms. Although the obtained results are very accurate, one could argue that they are only valid for a subset of the human population. For product compliance tests on the other hand, it is important that the assessments are conducted using standardized procedures to obtain repeatable and conservative results with a quantified uncertainty. However, the quality of a more generic and generally applicable compliance assessment can only be evaluated in comparison with more detailed studies. Both approaches thus remain necessary and complementary.

The goal of this chapter is to determine compliance distances and allowed output powers for different directions near multi band, LTE BSAs. To this aim, numerical simulations are carried out, using a heterogeneous phantom near detailed models of multi-band BSAs. The compliance distances are then compared to those that can be obtained using a generic model for one of the BSAs and standardized compliance assessment techniques. More specific, we will use the IEC 62232 standard [3] to assess compliance with the basic restrictions and use the CENELEC EN-50383 standard to assess compliance with the reference levels.

This chapter presents a numerical investigation and comparison of compliance boundaries based on the ICNIRP basic restrictions on the whole-body averaged SAR and peak 10 g localized SAR and electric field reference levels [1]. In Section 2.2, the methodology, simulation, and modeling techniques used to determine

compliance boundaries for LTE BSAs are described. Two different approaches to study compliance are presented in this chapter: in Section 2.3 the simulated compliance distances using detailed models of the BSA and a realistic human phantom are presented and compared for the different used frequencies and antennas, while in Section 2.4 compliance distances are presented using a generic model for the BSA and standardized techniques for compliance assessment. Section 2.5 discusses the compliance distances and compares these two different approaches. Finally, conclusions are drawn in Section 2.6.

These results are important for wireless operators that wish to use similar antennas and are looking for compliance boundaries when installing them. Not only the network providers but also local authorities that wish to protect the general public can benefit from these results. Workers that have to perform maintenance on these antennas are also of major concern to the operators, who need to know whether an RF worker can approach a BSA from the back or side without exceeding the ICNIRP basic restrictions.

2.2 Materials and Method

2.2.1 Studied Quantities and Technologies

An antenna emitting RF EMFs with a certain output power will cause a certain SAR in a human near this antenna. This SAR can exceed the basic restrictions (see Table 1.2 in Chapter 1) close to the antenna, while the SAR can be in compliance with the ICNIRP basic restrictions at larger distances from the antenna. The distance at which the SAR induced in the subject's body equals the ICNIRP basic restrictions is called a compliance distance or compliance boundary. This distance depends on the antenna's characteristics and the antenna's input (or emitted) power. In this chapter, compliance boundaries are determined, based on the ICNIRP basic restrictions on the whole-body averaged SAR (SAR_{wb}), the peak 10 g averaged SAR (SAR_{10g}), and the reference levels on the electric field strength (E_{rms}) [1]. Compliance with the magnetic field strengths is not mentioned in this chapter, due to the dominant electric fields emitted by the BSAs, it suffices to study the electric field strengths. The compliance boundaries are determined for both the general public and occupational exposure in the vicinity of typical multiple-frequency BSAs. The multiband antennas are operated at four frequencies (800, 900, 1800, and 2600 MHz), where both single-frequency and cumulative exposure are considered. These four frequencies correspond to four communication technologies: the lower LTE band around 800 MHz, the Global System for Mobile communications (GSM) band around 900 MHz, the GSM band around 1800 MHz, and the upper LTE band around 2600 MHz. The BSAs are placed either in free space, near the heterogeneous Virtual Family Male (VFM) [17], or near the stan-

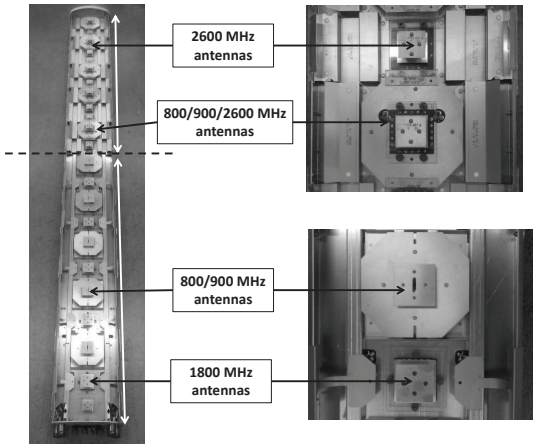

Figure 2.1: Antenna 3 shown from a perspective (left). Details of the 2600 MHz antennas and the 800/900/2600 MHz multi-band antennas (top right) located on top of the antenna array and details of the 1800 MHz antenna and the 800/900 MHz antennas (bottom right), located on the bottom of the antenna array.

dardized IEC phantom [3]. We consider three directions for the VFMs placement with respect to the BSAs, namely, at the front, back and side of the BSA.

2.2.2 Studied Base Station Antennas

Three base station antennas (1 to 3) operating at frequencies of 800 MHz, 900 MHz, 1800 MHz, and 2600 MHz are considered. The three BSAs consist of arrays of patch antennas. The whole of the BSA can be considered to be an assembly of two (upper and lower) parts. The antennas operating at 1800 MHz are placed in the lower half of the antenna, while the antennas that operate at 2600 MHz, are placed in the upper half of the antenna. The antennas operating at 800 and 900 MHz are distributed over both the upper and the lower part of the BSA. Fig. 2.1 shows an image of antenna 3 and details of the patch antennas that constitute the BSA. There are four kinds of patch antennas: the bottom of the BSA consists of patch antennas with a resonance around 1800 MHz and antennas that operate around 800 and 900 MHz, see Fig. 2.1 bottom right, while the top part of the BSA consists of an array of patch antennas that resonate around 2600 MHz and patch antennas that operate around 800 and 900 MHz and are covered with an extra 2600 MHz patch antenna, see Fig. 2.1 top right.

Antennas 1 and 2 have a similar structure to antenna 3, but contain less patch antennas and are consequently shorter. Table 2.1 shows an overview of the most important characteristics of the three BSAs. All the antennas are cross polarized.

Antennas with different lengths, gains, vertical and horizontal beam widths are considered to provide generally usable results.

Antenna	Frequency (MHz)	Gain (dBi)	Horizontal beam width -3dB (°)	Vertical beam width -3dB (°)	Length (m)	Operational output Power (W)	Number of patch antennas
Antenna 1 [18]	800	13.9	73	14.9	1.4	0 to 120	5
	900	14.5	67	13.9		0 to 300	5
	1800	14.2	68	13.3		0 to 240	3
	2600	14.6	60	12.0		0 to 120	5
Antenna 2 [19]	800	15.6	73	9.6	2.2	0 to 120	8
	900	16.0	67	8.6		0 to 300	8
	1800	15.8	68	10.0		0 to 240	4
	2600	16.5	60	8.7		0 to 120	8
Antenna 3 [20]	800	16.8	73	7.4	2.8	0 to 120	10
	900	17.4	67	7.2		0 to 300	10
	1800	17.2	68	7.0		0 to 240	5
	2600	17.9	60	5.8		0 to 120	12

Table 2.1: Characteristics of the studied BSAs obtained from the manufacturer's data sheets.

2.2.3 Detailed Base Station Antenna models

Antenna	Frequency (MHz)	Gain (dBi)	Horizontal beam width -3dB (°)	Vertical beam width -3dB (°)
Antenna 1	800	12.2	73	14.9
	900	12.9	67	13.9
	1800	14.1	68	13.3
	2600	14.2	84	12.0
Antenna 2	800	13.2	73	9.6
	900	13.9	67	8.6
	1800	16.3	68	10.0
	2600	16.3	82	8.7
Antenna 3	800	14.5	73	7.4
	900	15.5	67	7.2
	1800	18.9	68	7.0
	2600	17.5	74	5.8

Table 2.2: Characteristics of the detailed numerical models of the studied BSAs.

In a first approach, detailed models are made for three real multiple-frequency BSAs. In the modeling approach, firstly, antennas working at their respective frequency are modeled. Secondly, they are assembled to create the whole BSA. An antenna consists of various antenna components (such as the feeds, substrate, and reflectors) and the specifications of these components are described as follows. For

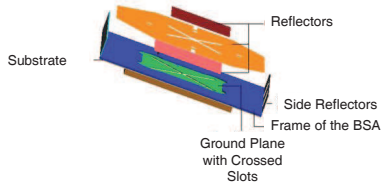

(a) 800/900 MHz antenna

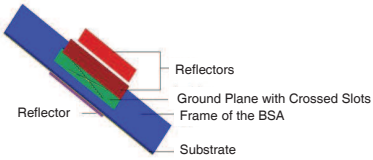

(b) 1800 MHz antenna

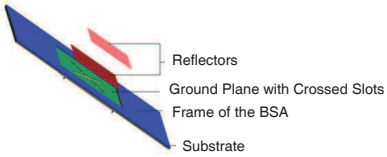

(c) 2600 MHz antenna

Figure 2.2: Models of the individual patch antennas.

each antenna, there exist four feeds. These are perfectly conducting transmission lines fed by a voltage source. The feeds are on top of a layer of substrate with a relative permittivity, $\epsilon_r = 2$ and a conductivity, σ = 0 S/m, with a thickness of 0.75 mm. The substrate is covered with a Perfectly Electric Conducting (PEC) ground plane with a crossed slot. The dimensions of these layers are equal to that of the measured dimensions of layers on the antenna. The planar antenna is then fixed to a perfectly conducting frame with a thickness of 1.5 mm. The reflectors are separated from the frame by means of plastic separators. The frame of the antenna is modeled differently from the one of the original antenna to obtain an optimized gain. There are additional reflectors present on the side and the back of the antenna. The structure of the side reflectors has been simplified for the ease of modeling. The ground planes, planar feed lines, and reflectors are modeled as two dimensional objects in FDTD. The models of the various patch antennas are shown in Fig.2.2.

The goal of the detailed antenna modeling is to obtain a high physical resemblance with the original model and have similar far-field characteristics of the radiation pattern, i.e., a similar gain as the real antennas with only small deviations in the vertical and horizontal beam widths. Table 2.2 lists the properties of the antenna models. The antennas length, polarization, number of used patch antennas, and the emitted powers are those listed in Table 2.1. Figure 2.3 shows the complete base station antenna 3 after the different antenna components are assembled.

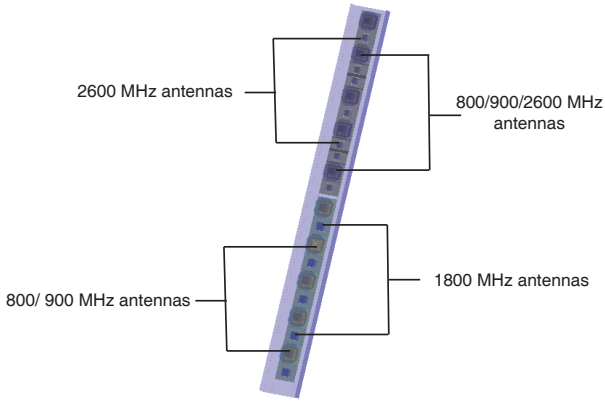

Figure 2.3: Detailed model used for FDTD simulations of antenna 3.

2.2.4 Generic Base Station Antenna model

In order to conduct a numerical product compliance assessment of a BSA, a model of the corresponding BSA that can be used the employed numerical algorithm, in this case FDTD, has to be created. Computer-Aided Design (CAD) files of the antenna are usually considered as proprietary information by the antenna manufacturer and therefore these are seldom available. Making a detailed model of the antenna thus requires a lot of effort. The BSA has to be disassembled and measured manually. This can often lead to the destruction of the BSA. The detailed models may also come with a significant computational cost since they may contain very small components. Moreover, a trained engineer or electromagnetic expert is needed to correctly model these antennas due to their complexity. Consequently simplified antenna models have to be created using the modeling tools of the used FDTD software.

In this subsection a generic numerical model is created for antenna 1. The number of antenna elements, polarizations, and antenna ground plane dimensions of the model are the same as those of the real antennas. For simplicity, the feed networks and the detailed antenna element structures are replaced by arrays of simple wire dipoles fed with voltage sources at the center of each element. This simplification should provide accurate results for SAR simulations when the separation distance between the antenna and the phantom is larger than 1-2 wavelengths [21, 22]. The dimensions of the antenna elements and the reflectors are adapted to obtain a good free-space impedance match and fulfill the set tolerance specifications on the vertical and horizontal half-power beam widths (VHPBW and

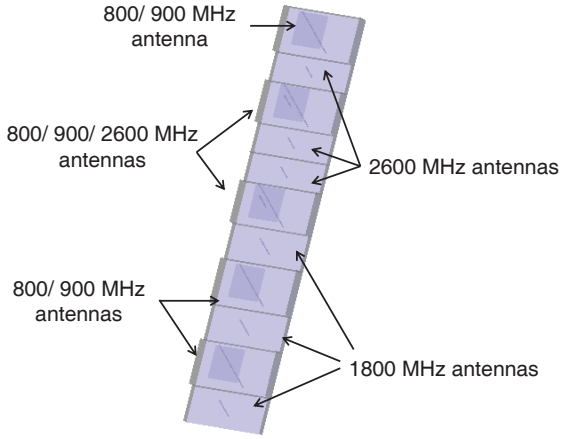

Figure 2.4: Generic model used for FDTD simulations of antenna 1.

HHPBW). More specifically, the standing wave ratio (SWR) is kept below 2 at the considered frequencies (800, 900 , 1800, and 2600 MHz) and the VHPBW and HHPBW are within 1° and 5° from the nominal values of the real antennas (see Table 2.1), respectively. Figure 2.4 shows the generic model of antenna 1, while Table 2.3 lists some of its far-field parameters.

Antenna	Frequency (MHz)	Gain (dBi)	Horizontal beam width -3dB (°)	Vertical beam width -3dB (°)	Length (m)	Number of patch antennas
Antenna 1	800	14.7	74.8	15.2	1.3	5
	900	15.2	71.8	13.7		5
	1800	12.8	72.3	12.6		3
	2600	12.0	58.6	11.4		5

Table 2.3: Characteristics of the generic numerical model of antenna 1.

The differences with the detailed antenna model of antenna 1 are: the use of dipoles instead of patch antennas and the adaptation of the reflectors and the separation between the reflectors, the dipoles, and the ground plane of the antenna.

2.2.5 Configuration of Numerical Simulations near Base Station Antennas

The compliance boundaries are assessed numerically using the FDTD method. When compared to other numerical techniques, the FDTD method easily mod-

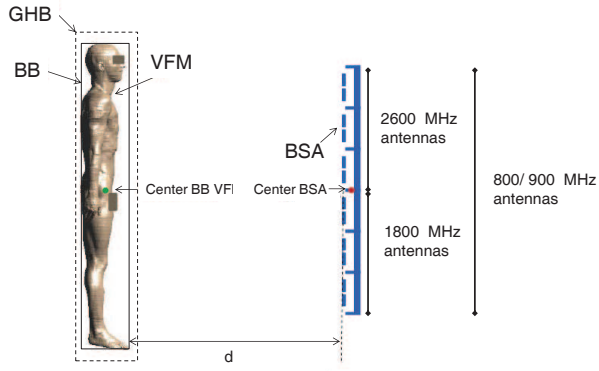

Figure 2.5: Scheme of the VFM in the vicinity of a BSA, indicating the vertical alignment and distance between the VFM's bounding box (BB) and the BSA. The position of the generalized Huygens Box (GHB) and the VFM's Bounding Box are also shown.

els bodies with complex material distributions, such as large inhomogeneous human body models, without largely increasing the computational expenses [23]. We have selected the commercially available tool SEMCAD-X (SPEAG, Zürich, Switzerland) for the FDTD computations. The simulation domain is discretized according to the FDTD algorithm using a grid-step smaller than 7% of the smallest wavelength in the media. Uniaxial perfectly matched layers (UPML) [24] are used to truncate the simulation domain and to prevent non-physical reflections. Two different approaches are used to determine compliance distances. First, a realistic phantom is placed in the vicinity of the detailled models of the BSAs. Second, a standardized approach is followed using the IEC phantom [3] (following IEC 62232) and CENELEC plane [4] (following CENELEC EN-50383), near the generic BSA. The IEC phantom is an homogeneous box-shaped phantom with dimensions $1.54\times0.339\times0.15\ m^3$ and dielectric parameters corresponding to the tissue-equivalent liquid for the considered frequencies [3].

In both approaches, two types of simulations are carried out. First, electric fields surrounding the antennas are calculated using FDTD simulations with only the selected BSA present. The root-mean-square (RMS) electric field E_{rms} surrounding the antenna is then recorded. Secondly, the SAR in the phantom is determined with FDTD simulations using the configurations shown in Figures 2.5 to 2.7, where both the BSA and the used phantoms are present.

In the first approach, the phantom selected to carry out the FDTD simulations, is the VFM [17]. This is a three-dimensional human-body model or phantom, based on magnetic resonance images (MRI) of a healthy volunteer. This adult

model has a mass of 72.2 kg, a height of 1.80 m and consists of 81 different tissues. The dielectric properties of the body tissues have been taken from the Gabriel database [25]. The maximum grid step inside the VFM is chosen to be 2 mm in order to ensure accurate SAR results. We found deviations smaller than 5% for the SAR_{wb} and peak SAR_{10g} values at a grid step of 2 mm, compared to a grid step of 1 mm at 2600 MHz. These small deviations are acceptable, taking into account that a grid step of 1 mm at 2600 MHz leads to an enormous amount ($> 10^9$) of grid cells in the simulation domain. The VFM is placed in the proximity of the BSAs, where the horizontal distance between the VFM and a BSA is measured between the anterior face of the bounding box (BB) of the VFM (a cuboid surrounding the VFM, with each face perpendicular to the main axes and tangential to the VFM in the extreme point of the VFM in that direction, with dimensions 282 x 540 x 1804 mm^3) and the proximal face of the BB of the BSA, as shown in Figure 2.5.

A separation of 0 mm is defined as the distance where the anterior face of the VFM's bounding box is at 16 mm distance of the proximal face of the BSA's BB, this to ensure that there is no contact between the VFM and the BSA. Figure 2.5 shows that the center of the VFM's BB box is vertically aligned to the center of the whole BSA. Although some frequencies only use a part of the BSA to be emitted from, this alignment is chosen for all frequencies. Figure 2.6 shows the three different configurations that have been studied. The VFM is always facing the BSA and is placed in front of the BSA, at the side of the BSA or behind the BSA. The VFM is then moved away from the BSA along the respective directions over distances d_{front}, d_{side} and d_{back}.

After determination of the SAR values in the phantom, values for the SAR_{wb} and the maximum of the SAR_{10g}, both in the limbs ($SAR_{10g,limbs}$) and in the trunk and head ($SAR_{10g,trunk}$), can be calculated. As the output power (P_n) of the antenna at frequency f_n is known and the phantom is moved from the front, side and back of the antenna, this leads to relationships $E_{rms}(d_i, f_n, P_n)$, $SAR_{wb}(d_i, f_n, P_n)$, and $SAR_{10g}(d_i, f_n, P_n)$, Where d is distance, i is either front, side, or back, and f_n and P_n are the n^{th} studied frequency band (with n=1..4, see Table 2.1) and the output power in this frequency band. The maximal P_n under realistic operating conditions are frequency-dependent and are listed in Table 2.1.

In the second approach, the IEC box-shaped phantom [3] is placed in front of a generic model of antenna 1 at several separation distances. The density of the phantom is set to 1000 kg/m^3 as required by the IEC 62232 standard. With the phantom centered in front of the antenna, a part of the transmitted power will be absorbed inside it. This absorption is studied using the SAR_{wb} and the peak SAR_{10g}, which both may be expressed as a function of the phantom-antenna separation distance, d_{front}, the frequency, f_n, and the transmitted power, P_n. In order to determine the SAR_{wb}, according to the standard [3], the absorbed power in a

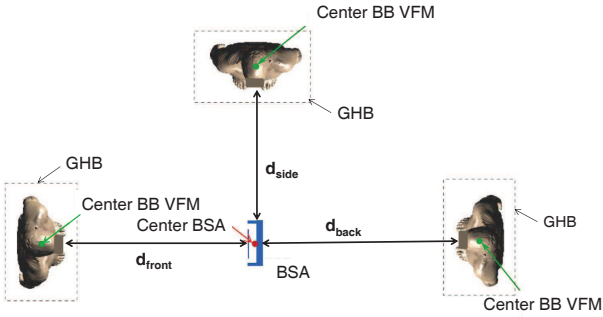

Figure 2.6: Top view illustrating the different possible orientations and horizontal alignment of the VFM with respect to the BSA. The contour of the GHB is also shown.

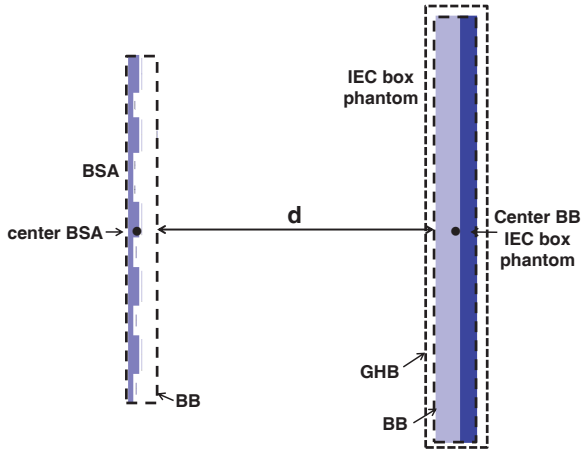

Figure 2.7: Side view illustrating the alignment of the IEC box phantom with respect to the generic BSA. The contour of the GHB is also shown. The part of the IEC phantom colored in a lighter shade of blue, indicates the volume of $1.54\times0.339\times0.09\ m^3$ which is used for the SAR_{wb} calculations.

sub-volume of the phantom with dimensions $1.54\times0.339\times0.09\ m^3$ is determined and divided by a mass of 46 kg for adults and a mass of 12.5 kg for children [3]. The cuboid of $1.54\times0.339\times0.09\ m^3$ corresponds to a conservative SAR_{wb} for 95% of the human population [12]. Correction factors to account for the tissue layering effect and varying element load conditions were also used as required by the procedure in IEC 62232 to obtain conservative results. Figure 2.7 shows the

generic antenna and the IEC box shaped phantom.

If there is a large separation between the phantom and the BSA, the FDTD algorithm will assign an enormous amount of cells to the air between the antenna and the body. Running such a simulation is very time consuming and poses high memory requirements on the hardware that is used for the computations. Therefore, a hybrid technique called the Generalized Huygens Box Method (GHBM) is used for the larger configurations (separation $> 2m$) [12, 14]. The GHBM is a two-step method where in a first step, the incident fields on a closed cuboid (GHB) with dimensions $300 \times 568 \times 1832\ mm^3$, surrounding the phantom are computed, and in a second step, FDTD is used to simulate the SAR inside a human body model using the complex incident field vectors on the GHB around the human body model as excitation. The placement of the GHB is illustrated in Figures 2.5 to 2.7. The GHBM is based on the assumption that the influence of the coupling between the human body and the BSA on the SAR_{wb} and peak SAR_{10g} can be neglected. This assumption has been verified in [26] where it is found that for separation distances larger than two times the wavelength the differences in SAR_{wb} and SAR_{10g} determined in the VFM or the virtual family boy [17] using either the GHBM or a full FDTD simulation are smaller than 6%. We have also executed full FDTD simulations of the VFM in front of the detailed model of antenna 1 at the four studied frequencies in order to validate the usage of the GHB. The results of this validation are described in Subsection 2.3.5.1.

In this study the phantoms are placed near a BSA without considering a reflective ground or wall near the phantoms. These configurations have been studied in [14], where it is found that a wall placed next to the VFM can increase the SAR_{wb} and peak SAR_{10g} at the frequencies studied in this chapter, while a reflective ground was found to not lead to an increase in SAR values at the frequencies studied in this chapter. Therefore, it should be noted that the compliance boundaries presented in this chapter are valid for the configurations shown in Figures 2.5 to 2.7, but that the presence of a reflective wall in the vicinity of the BSA might yield larger compliance distances.

2.2.6 Determining Compliance Boundaries

The reference levels for the electric fields and the basic restrictions for SAR_{wb} and SAR_{10g} (for the general public and occupational exposure) defined by the ICNIRP [1] are used to determine compliance boundaries for the BSAs.

Compliance distances $d_{compl}^{SAR_x}(f_n, P_n)$ are defined as the distance from the antenna where for a certain power P_n and frequency f_n, the SAR_x values (x = whole-body averaged (wb) or 10 g) equal the basic restrictions. A similar compliance distance can also be defined by comparing E_{rms} averaged over a volume (the volume of the BB of the VFM or the IEC phantom, while the phantoms are not present in the calculations of the E_{rms}) with the reference levels, that

is, $d_{compl}^{E_{rms}}(f_n, P_n)$. In our first approach using the detailed antenna models, we have chosen to average E_{rms} over a volume surrounding the VFM because the reference levels should be averaged over the entire body according to [1]. Other publications use a surface to calculate compliance boundaries based on the reference levels [8]. In order to also study this averaging method, the E_{rms} averaged over the CENELEC plane [4] is studied in the vicinity of the generic BSA antenna 1. In this second approach, E_{rms} is averaged over a plane of $0.4 \times 0.6\ m^2$ [4], centered and placed at a distance d_{front} in front of the antenna, see Fig. 2.7. This averaging results in values $E_{rms}(d_{front}, f_n, P_n)$. Moreover, we have also studied compliance distances $d_{compl}^{E_{rms}^{peak}}$, based on the peak of the E_{rms} in this plane. These E_{rms} values are compared with the reference levels [1].

Compliance with the magnetic field strengths is studied, but not mentioned in this chapter. The reference levels on the electric and magnetic fields have to be determined separately [1]. Due to the dominant electric fields emitted by the BSAs, the electric field strengths are always closer to the reference levels than the magnetic field strengths and consequently the compliance distances are higher.

The antennas under consideration emit at multiple frequencies simultaneously. Table 2.1 lists the typical maximal operational output powers per frequency for each antenna. The maximum powers range from 120 to 300 W. Since the antennas radiate electric fields at multiple frequencies, comparison of the fields and SAR values at an individual frequency with the ICNIRP basic restrictions and reference levels at that frequency does not suffice. To check compliance with the basic restrictions and reference levels, one has to use following formulas [1]:

$$\sum_{n=1}^{4} \left(\frac{E_x^2(d_i, f_n, P_n)}{E_{ref}^2(f_n)}\right) \leq 1 \tag{2.1}$$

$$\sum_{n=1}^{4} \frac{SAR_x(d_i, f_n, P_n)}{SAR_{BR}(f_n)} \leq 1 \tag{2.2}$$

where the index n denotes the four different frequencies, d_i the distance in three directions from the antenna, f_n and P_n the emitted frequency and power, and $E_{ref}(f_n)$ and $SAR_{BR}(f_n)$ are the ICNIRP reference levels and basic restrictions, respectively, at frequency f_n. it should be noted that for the frequencies studied in this chapter $SAR_{BR}(f_n)$ is a constant value, see Table 1.2. SAR_x can either be SAR_{wb} or peak SAR_{10g}. E_x can either be an averaged over a volume (E_{rms}^{volume}), a plane E_{rms}^{plane}, or a peak E_{rms}^{peak} value in a volume or plane.

To check compliance with the basic restrictions for the peak SAR_{10g}, Equation 2.2 should be fulfilled in every grid cell of the human body phantom. It is a computationally heavy task to check this. We used a worst-case approximation for all cases, in accordance with the ICNIRP 1998 guidelines, which are used to determine the compliance boundaries in this study where all the maximal SAR_{10g}

at different frequencies (f_n) are assumed to be located at the same point in the body. Therefore, we use:

$$\sum_{n=1}^{4} \frac{peak\ SAR_{10g}(d_i, f_n, P_n)}{SAR_{BR,10g}(f_n)} \leq 1 \tag{2.3}$$

with $SAR_{BR,10g}(f_n)$ the relevant basic restriction at frequency f_n, see Table 1.2 in Chapter 1, and $peak\ SAR_{10g}(d_i, f_n, P_n)$ the maximum SAR_{10g} found in the VFM for frequency f_n, output power P_n at distance d_i from the antenna. Equation 2.3 will provide a conservative estimation of the cumulative peak SAR_{10g} according to ICNIRP [1].

In [13] the peak SAR_{10g} values in the VFM near a multi-band antenna are calculated using this approach and compared to the exact value under cumulative exposure of GSM 900, GSM 1800, and UMTS at 2100 MHz. A maximal overestimation of 46% is found for one particular combination of output power ratios (1/5 of the total emitted power in the GSM 900 band, 3/10 in the GSM 1800 band, and 1/2 in the UMTS band). Averaged over 10 different exposure scenarios (distances of the phantom from the antenna) and 8 different ratios of multi-band output powers, the overestimation is only $17\% \pm 10\%$ [13] .

Using Equations 2.1, 2.2, and 2.3, compliance boundaries $d_{compl}^{SAR_x}(P_1, P_2, P_3, P_4)$ and $d_{compl}^{E_x}(P_1, P_2, P_3, P_4)$ can be estimated. The final compliance distance will be determined by the maximum of all the different compliance distances. Equivalently, maximally allowed powers $P_{compl}^{E_x}(d)$ and $P_{compl}^{SAR_x}(d)$, which are the powers needed to obtain the basic restrictions or reference levels at a certain distance (d) from the antenna, can be determined, both for individual frequencies and cumulative exposure.

In order to show how compliance boundaries are determined, a case study of compliance distances based on SAR_{wb} for the detailed model of antenna 1 is shown in Figure 2.8. In the example shown in Figure 2.8, 30 W is emitted at 800 and 900 MHz and 70 W is emitted at 1800 and 2600 MHz. Figure 2.8 shows that at short distances (for example distances smaller than 560 mm for 30 W at 800 MHz) from the antenna, the ICNIRP basic restrictions for the general public are not satisfied. With increasing separation, SAR_{wb} decreases and finally becomes smaller than the basic restriction for the general public. If radiation would only be present at the single frequencies, the compliance distances for SAR_{wb} would be located where the blue, black, green and pink curves intersect with the horizontal dashed lines, e.g., 560 mm for 30 W at 800 MHz, 610 mm for 30 W at 900 MHz, 1280 mm for 70 W at 1800 MHz and 1420 mm for 70 W at 2600 MHz for the general public. In these points the SAR_{wb} will equal the basic restriction at these frequencies. The red curve in Figure 2.8 ("all frequencies") shows the summation of the different SAR_{wb} as a function of distance from the antenna 1. Note that according to

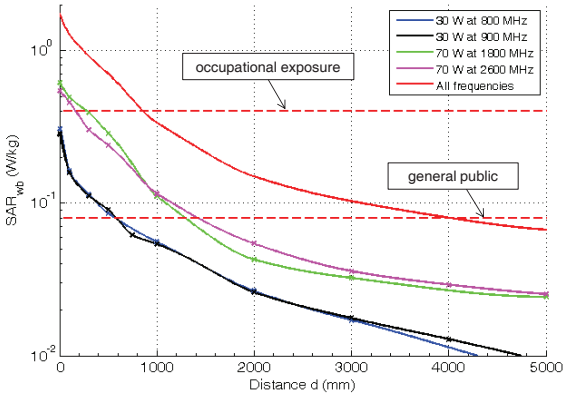

Figure 2.8: SAR_{wb} as a function of distance in front of antenna 1, for 30 W at 800 and 900 MHz and 70 W at 1800 and 2600 MHz.

Equation 2.2 the ratios of the SAR_{wb} values over the basic restrictions should be summed and not the SAR_{wb} values. However, the basic restrictions are the same here for all frequencies, so it is allowed to sum the SAR_{wb} values in this example.

Where this curve intersects with the horizontal dashed black line, the actual compliance distance for these output powers can be found, i.e., 4010 mm for the general public and 860 mm for occupational exposure. Also note that for 800 and 900 MHz at 30 W, no individual compliance boundaries exist for occupational exposure (because the basic restrictions are not exceeded), but due to the cumulative exposure, a compliance distance does exist. For other output powers the curves at the individual frequencies can be rescaled. The curve corresponding to the sum of the SAR_{wb} values (in red) should then be recalculated.

2.3 Results using detailed modeling of the BSA and a realistic phantom

In order to determine compliance distances, E_{rms}, SAR_{wb}, and SAR_{10g} are determined in front of, at the side, and at the back of the three studied BSAs.

2.3.1 Compliance Boundaries Based on the ICNIRP Basic Restrictions on SAR_{wb} and Peak SAR_{10g}

Figure 2.9 shows the maximally allowed output power the three antennas can emit frontally in order to induce SAR values in the VFM human body model equal to the ICNIRP basic restriction for general public (left axis) and occupational exposure (right axis). The allowed powers and compliance distances in front of the three

antennas based on the different averaged SAR values are shown. For instance, for antenna 1 at 800 MHz, the ICNIRP basic restriction for SAR_{wb} and the general public is exceeded at a distance of 2 m in front of the antenna for output powers larger than 91.2 W (Fig. 2.9 (a)). We have chosen not to show the compliance boundaries at the side and back of the antennas for the individual frequencies, since they are located at unrealistically high output powers.

At close distances in front of the antenna, the $SAR_{10g,trunk}$ is more restrictive than the SAR_{wb} and thus determines the compliance distance, as shown in Figure 2.9. This holds for all frequencies and antennas and can be seen by investigating Figure 2.9 at a constant allowed output power and determining the curve that provides the highest safety distance, e.g., at 800 MHz and 31.6 W of output power: the compliance distances for the general public based on SAR_{wb} are 610, 560, and 350 mm for antenna 1 to 3 respectively, while based on the peak $SAR_{10g,trunk}$ these are 850, 680, and 850 mm. At higher distances the SAR_{wb} or the peak $SAR_{10g,limbs}$ can become the most stringent basic restriction.

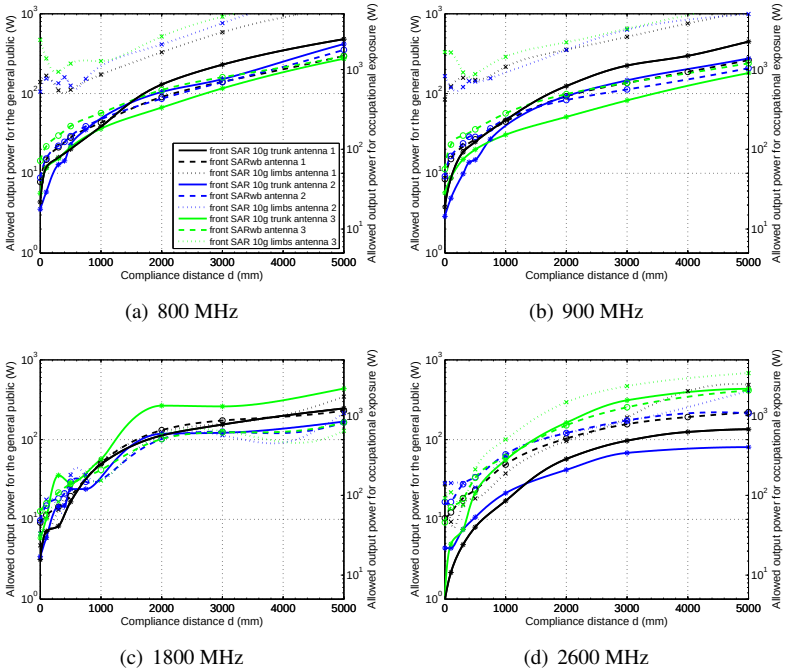

(a) 800 MHz (b) 900 MHz

(c) 1800 MHz (d) 2600 MHz

Figure 2.9: Compliance distances for the general public and occupational exposure in front of the three studied antennas based on the SAR_{wb} and peak SAR_{10g}. The markers show the simulated values, while the lines show a spline interpolation.

The results presented in this section show an excellent agreement with the ones presented in [11]. The values for compliance boundaries based on SAR_{wb} and SAR_{10g} presented in that paper (for the VFM near an antenna emitting at 900 MHz with a horizontal beam width of $70°$, a vertical beam width of $12°$, a length of 1.3 m, and a gain of 14 dBi) are within the error margin (see Sections 2.3.5 and 2.3.6) of the results shown in Figure 2.9 (b). The values presented in [6] (for a BSA of length 1.14 m consisting of an array of 4 dipoles emitting at 935 MHz and simulations using the visible human) correspond well with the values in Figure 2.9 (b) for occupational exposure, i.e., at 350 mm, [6] determined an allowed power of 100 W, while for the 3 antennas in this study this allowed power is 155 W, 135 W and 115 W. The SAR_{10g} values presented in [7] (for a BSA with a gain of 15.5 dBi, a horizontal beam width of $90°$, a vertical beam width of $8.5°$ and a length of 1.9 m, that emits at 947.5 MHz) increase up to an allowed power of 27.5 W at 60 mm. This is comparable to our values for allowed output powers based on the $SAR_{10g,trunk}$ at 60 mm: 20.4 W and 38 W at 900 MHz found for antennas 1 and 3. The phantom used in the study [7] emulates the trunk of a human body so an agreement between the allowed powers based on the $SAR_{10g,trunk}$ was expected. The allowed output power found for antenna 2 based on the $SAR_{10g,trunk}$ at 60 mm is 135 W, which is higher than the value found in [7]. The considered antennas, which are arrays of patch antennas in this section and an array of dipoles in [7], and the used phantoms will also have an influence on the value and the location of the peak SAR_{10g}.

In [13] the SAR_{10g} and SAR_{wb} are determined for a tri-band antenna in the VFM, who is aligned to the bottom of the BSA. At a distance of 1000 mm from the BSA, the allowed output powers for occupational exposure are 170 W and 323 W for GSM 900, based on the SAR_{wb} and peak $SAR_{10g,trunk}$, respectively, while for 1800 MHz these allowed power at 1000 mm are 159 W and 222 W, based on the SAR_{wb} and peak $SAR_{10g,trunk}$, respectively. In this section the occupational allowed output powers at 900 MHz are 225, 240, and 280 W for antennas 1 to 3 based on the SAR_{wb} and 230, 200, and 150 W based on the $SAR_{10g,trunk}$. The allowed output powers based on SAR_{wb} are thus higher in this section, while those based on the SAR_{10g} are lower. However, the deviations are still within the uncertainty on the simulations (see Section 2.3.6). At 1800 MHz the allowed output powers for occupational exposure are 254, 157, and 209 W for antennas 1 to 3 based on the SAR_{wb} and 245, 168, and 285 for antennas 1 to 3 based on the peak $SAR_{10g,trunk}$ at 1000 mm from the BSAs. These results are in agreement with those found in [13].

The comparison between the different studied antennas in this section and the antennas studied in literature shows that a general agreement between the allowed output powers at a certain (compliance) distance from a BSA based on SAR simulations can be found. However, significant differences, in particular for the values

obtained for the peak SAR_{10g}, might exist. The studied type of antennas (arrays of patch antennas, dipoles,..) and the used phantoms will have an influence on the absorption, especially for small distances of the phantom to the antenna, and the location of the peak SAR_{10g}.

2.3.2 Compliance Boundaries Based on the ICNIRP Reference Levels on the Electric Field strengths

The reference levels on the electric fields, see Table 1.2, are also used to define compliance boundaries. Figure 2.10 shows the allowed power of the antennas (front, side, and back) in order to comply with the reference levels for the general public (left axis) and occupational exposure (right axis), averaged over the bounding box (BB) surrounding the VFM at a certain distance from the antenna. The corresponding compliance distances can be determined for any realistic output power using this figure. For example, at an operating frequency of 800 MHz, the ICNIRP reference level for the general public is exceeded at a distance of 1.5 m in front of antenna 2 for input powers larger than 31.6 W (Fig. 2.10 (a)). The three antennas show the same behaviour. Clearly, the highest compliance distances are obtained in front of the antennas, as the antennas' main lobes are in this direction.

The allowed powers can be compared to the maximal operational output powers listed in Table 2.1. At 1800 and 2600 MHz (Fig. 2.10 (c) and (d)) no compliance distances based on the electric field need to be defined for the general public at the side and back of the antenna, since the power that is necessary to obtain E_{rms} values equal to the reference levels is higher than the maximal operational power (see Table 2.1). At 800 and 900 MHz, compliance boundaries for the general public also exist at the side and back of the antennas for high operational powers. For occupational exposure, compliance distances only exist in front of the antenna for these allowed output powers.

At the largest distance (200 mm) considered in [7] the results for the compliance distances for occupational exposure based on the electric field in front of their BSA (with a gain of 15.5 dBi, a horizontal beam width of 90°, a vertical beam width of 8.5° and a length of 1.9 m) emitting at 947.5 MHz are comparable (differences smaller than a factor of 2) to the ones that are presented in this study. At closer distances to the antennas the values in [7] are more conservative.

2.3.3 Actual Compliance Boundaries Based on the ICNIRP Reference Levels and Basic Restrictions

The actual compliance distances are combined compliance distances where all quantities - the ICNIRP reference levels and basic restrictions - are met at a single

frequency. In terms of the allowed powers this is calculated as $min_x(P^x_{compl}(f_n, d))$, where x can be E_{rms}, SAR_{wb}, $SAR_{10g,trunk}$ or $SAR_{10g,limbs}$.

The actual compliance distances for the general public and occupational exposure should be determined separately, since the ratios between the ICNIRP reference levels and the basic restrictions are not the same at each frequency [1]. For 800, 900, and 1800 MHz, the ratio of the reference levels for occupational exposure and those defined for the general public is 4.8, while at 2600 MHz this ratio is 5.04. For the basic restrictions the ratio between those defined for occupational exposure and the general public is exactly 5 at all considered frequencies.

Figure 2.11 shows the actual compliance distances and allowed powers for the three antennas, based on the ICNIRP guidelines for occupational exposure. The green dashed lines show the maximal operational output powers from Table 2.1. We have chosen to only show the allowed powers for occupational exposure. The allowed powers for the general public will be a factor of 5 lower, where a deviation of 4% is possible at the lower three frequencies, if the reference levels are the most restrictive quantity at a certain distance d. From Figure 2.11, it should be clear

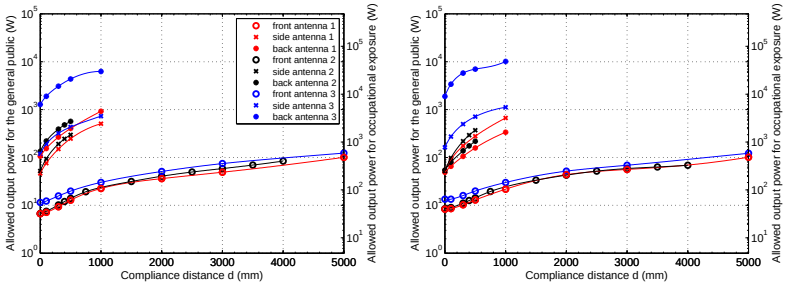

(a) 800 MHz (b) 900 MHz

(c) 1800 MHz (d) 2600 MHz

Figure 2.10: Compliance distances for the general public and occupational exposure of the three studied antennas, based on E^{volume}_{rms} averaged over the VFM's BB. The markers show the simulated values, while the lines show a spline interpolation.

that restrictions on the output power exist in front of the antennas for occupational exposure using the operating powers given in Table 2.1. At the side and back of the antenna, restrictions only exist at 900 MHz, where an output power of 300 W induces a compliance distance of 5 cm at the side of antennas 1 and 2 and around 10 cm at the back of antennas 1 and 2. An RF worker can approach the BSAs in compliance with the ICNIRP reference levels and basic restrictions if an output power smaller than 158 W is emitted at one of the studied frequencies. A cumulative compliance distance is needed to study multiple-frequency exposure situations.

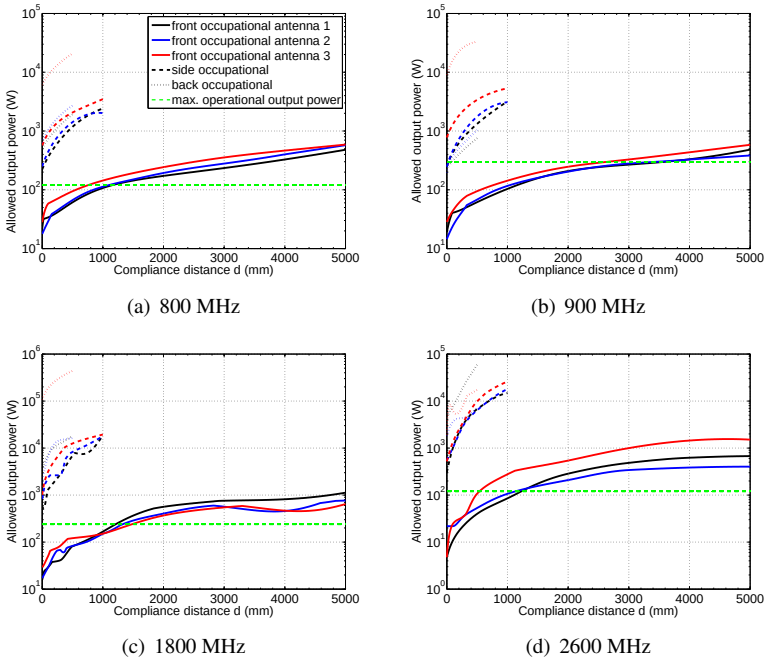

(a) 800 MHz (b) 900 MHz

(c) 1800 MHz (d) 2600 MHz

Figure 2.11: Actual compliance distances for occupational exposure for three orientations around the three studied antennas.

The results that are presented in [16] for the lowest allowed powers for BSAs with a horizontal beam width $> 60^\circ$ based on any basic restriction for occupational exposure, are comparable to the worst-case results for the combined compliance distances in Figure 2.11.

2.3.4 Cumulative Compliance Boundaries

In reality the BSAs will emit at multiple frequencies f_n with output powers P_n. A cumulative compliance distance can be determined for every combination of output powers P_n, distance d from the antenna, and basic restriction or reference level. The cumulative compliance distances and corresponding allowed powers can be calculated from the allowed powers presented in the previous sections using:

$$\sum_{n=1}^{4} \frac{P_n}{P^x_{compl}(f_n, d)} \leq 1 \tag{2.4}$$

with $P^x_{compl}(f_n, d)$ the allowed power which complies with the basic restrictions (x = SAR_{wb} or SAR_{10g}) or reference levels (x = E_{rms}) at frequency f_n and distance d from the antenna. P_n is the output power at frequency f_n. This can be calculated for both the general public and occupational exposure and any set of output powers P_n. The exact compliance distance for a specific power distribution can be calculated by inserting the output powers P_n and the combined allowed powers $P^x_{compl}(f_n, d)$ from Figures 2.9 and 2.10 in Equation 2.4.

A total output power of $P = \sum_{n=1}^{4} P_n$ can be obtained using different combinations of P_n and will thus also lead to a different compliance distance. Since a compliance boundary should be a constant distance for a given output power, the largest distances that can be found for a total output power P have been determined. Equivalently, one can estimate the lowest P at a given distance, which complies with the basic restrictions and reference levels at all frequencies, regardless the distribution of the powers amongst the frequencies. It is this P that is shown in Figure 2.12.

Figure 2.12 thus shows the worst-case cumulative compliance distances for the general public based on the individual basic restrictions (red, blue and green markers) for the three studied antennas at the points where an FDTD simulation has been carried out. The markers show the values obtained from numerical simulations. The solid lines are fitted lines to the compliance distances for the individual basic restrictions and reference levels. An exponential fit for the power as a function of the compliance distance is applied:

$$P(W) = A \times (\frac{d(mm)}{1mm} + C)^B \tag{2.5}$$

with A, B, and C the parameters of the fit and d the cumulative compliance distance. The fit is carried out for distances larger than a quarter wavelength. Table 2.4 summarizes the values for A, B, and C for the 3 antennas. Figure 2.12 shows that at distances close to the antennas ($<$ 1 m), the basic restrictions for $SAR_{10g,trunk}$ will be the most conservative, while at larger distances from the antenna, the reference levels can be the most conservative.

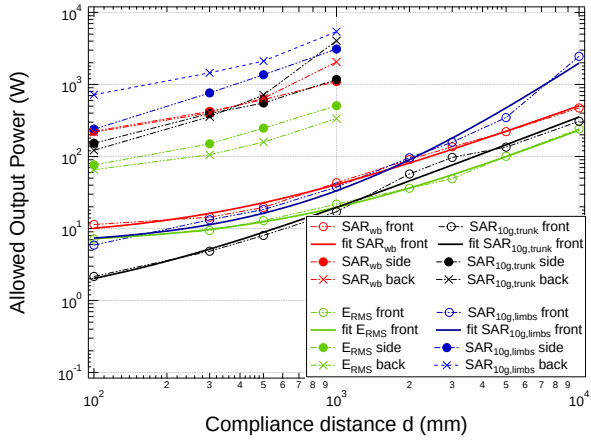

(a) antenna 1

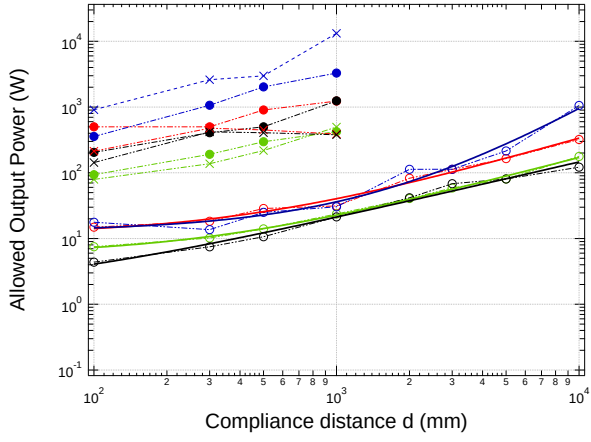

(b) antenna 2

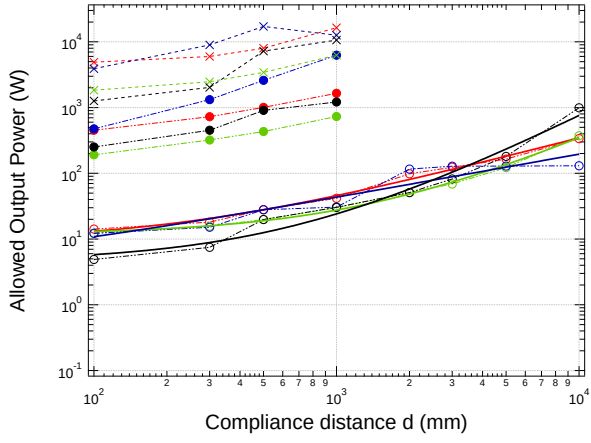

(c) antenna 3

Figure 2.12: Allowed total output power as a function of distance for the *general public* along three directions around the three studied antennas. The solid lines show a fit to the data in front of the antennas.

	Quantity	A(W)	B	C
Antenna 1				
	E_{rms}	8.3×10^{-4}	1.4	7.3×10^{2}
	SAR_{wb}	6.1×10^{-3}	1.2	3.2×10^{2}
	$SAR_{10g,trunk}$	4.4×10^{-2}	1.3	8.9×10^{1}
	$SAR_{10g,limbs}$	8.4×10^{-7}	2.3	8.8×10^{2}
Antenna 2				
	E_{rms}	2.0×10^{-2}	9.8×10^{-1}	3.1×10^{2}
	SAR_{wb}	1.7×10^{-2}	1.1	4.4×10^{2}
	$SAR_{10g,trunk}$	5.5×10^{-2}	8.6×10^{-1}	5.4×10^{1}
	$SAR_{10g,limbs}$	9.2×10^{-7}	2.2	1.7×10^{3}
Antenna 3				
	E_{rms}	7.0×10^{-5}	1.7	1.5×10^{3}
	SAR_{wb}	5.1×10^{-2}	9.5×10^{-1}	2.3×10^{2}
	$SAR_{10g,trunk}$	2.3×10^{-5}	1.9	6.8×10^{2}
	$SAR_{10g,limbs}$	4.4×10^{-1}	6.6×10^{-1}	2.6×10^{1}

Table 2.4: Values for fit coefficients A, B, and C in Equation 2.5 for the three studied antennas and the different studied dosimetric quantities.

The allowed power presented in Figure 2.12 (for the *general public*) can be extended to the worst-case scenario for *occupational exposure* if the allowed power is multiplied by a factor of 5. The aforementioned deviation of 4% due to a difference in ratio between reference levels and basic restrictions has to be taken into account. From Figure 2.12, one can conclude that antennas 1, 2, and 3 can be approached up till 0.1 m from the back and side by an informed RF worker, if the total output power is smaller than 316 W, 398 W, and 1 kW, respectively.

2.3.5 Simulation Errors at Large Distances (> 2 m) from the BSA

FDTD discretizes the full simulation domain and calculation times can thus become too long at large distances from the antenna. To investigate compliance with the basic restrictions at these distances we have used the Generalized Huygens' Box Method [14] and an extrapolation of the simulation results at even larger distances.

2.3.5.1 Error due to the use of the Generalized Huygens' Box Method

The GHBM is used for separations between the VFM and the BSAs larger than 2 m. In these simulations, the GHB is a cuboid of $310 \times 568 \times 1832\ mm^3$ surrounding the VFM. The validity of this method has been tested at the four studied frequencies, using the VFM placed at 2 m from antenna 1. The SAR_{wb} and peak SAR_{10g} values obtained using the GHBM deviate 8.9% and 9.3% on average

from the values obtained using FDTD simulations. The error is smaller at larger distances from the BSA, as the antenna-phantom coupling decreases.

2.3.5.2 Extrapolation error on allowed powers at large distances from the antennas

As can be seen in Figure 2.8, the cumulative compliance boundaries can be quite larger than the compliance boundaries for the individual frequencies. In order to limit the number of far-field simulations, an extrapolation is used at larger distances.

To determine the different SAR values at the back orientation, we extrapolate beyond 30 cm. This gives rise to an average error of 12% at 50 cm. The extrapolation for the SAR values at the face of the antenna (beyond 5 m) is checked for antenna 2 at 10 m with an average error of 40%. These errors are acceptable when compared to the worst-case correlated error associated with FDTD with heterogeneous human body models (i.e., order of 64% [27]).

For the E_{rms} values, we also use an extrapolation beyond 500 cm in front of the antennas, this is checked for antenna 3 at 1000 cm and gives rise to an average error of 15%. At the side and back of the antennas we extrapolated the electric fields beyond 50 cm, this is associated with an average error of 35% at 100 cm.

2.3.6 Uncertainty Analysis

Every measurement or numerical computation induces uncertainties on the obtained results. These are discussed in this section.

2.3.6.1 Uncertainty on the Allowed Power

The results for the allowed power: $P_{compl}^{SAR_x}(d)$ (x= wb or 10g), are directly calculated from values from the SAR_{wb} and peak $SAR_{10g,trunk}$. The uncertainty on the SAR_{wb} and peak $SAR_{10g,trunk}$ has already been investigated in previous studies [14, 24, 27, 28]. Because the selected FDTD settings are similar and for some parameters even better than in the referenced papers, the estimated uncertainty is not larger than the overall uncertainty presented in these studies. The overall worst-case expanded uncertainty U (k = 2) with 95% confidence interval is 59% and 64% for SAR_{wb} and SAR_{10g}, respectively and will be the same for allowed powers associated with these SAR values [27].

2.3.6.2 Uncertainty on the compliance distance

The uncertainties on SAR_{wb} and SAR_{10g} [27] can be used to determine uncertainties on the compliance distances. The performed FDTD computations provide

relationships $SAR_{wb}(d)$ and peak $SAR_{10g}(d)$, such as the ones shown in Figure 2.13. The distance d at which the SAR value is equal to SAR_{BR} is the compliance distance. Upper and lower boundaries for the 95% confidence interval on the SAR can be determined, using the expanded uncertainty on the SAR values. The distances d_1 and d_2 where these lower and upper boundaries equal the basic restrictions can be determined using Equations 2.6 and 2.7:

$$SAR_x(d_1) - SAR_x(d_1) \times U = SAR_{BR} \tag{2.6}$$

$$SAR_x(d_2) + SAR_x(d_2) \times U = SAR_{BR} \tag{2.7}$$

where x = wb or 10g and U the overall worst-case expanded uncertainty on SAR_x. The interval [d_1,d_2] corresponds to the 95% confidence interval for the compliance distance. Figure 2.13 shows the simulated $SAR_{wb}(d)$ and $SAR_{10g,trunk}(d)$ for antenna 1 at 800 MHz (the black and blue circles in Fig. 2.13), for an antenna input power of 120 W. The solid lines show the used inter- and extrapolation, while the dashed curves show the upper and lower limits of the 95% confidence intervals. The distances d_1 and d_2, the boundaries of the 95% confidence interval of d, are indicated in this figure. The red lines are the respective basic restrictions on SAR_{wb} (0.08 W/kg) and $SAR_{10g,trunk}$ (2 W/kg) for the general public. The complaince distance d is the distance where the solid black or blue curves intersect with the red lines. The confidence interval for the compliance distance (d) can be found where the red lines intersect with the dashed curves. In the example of Figure 2.13: d = 2570 mm, while d_1 = 1210 mm and d_2 = 3770 mm for SAR_{wb} = 0.08 W/kg.

To estimate a power averaged uncertainty of the compliance distances, one has to determine the relationships $d(P_n)$, $d_1(P_n)$ and $d_2(P_n)$. The average relative upper (err_{up}) and lower boundaries (err_{low}) of the 95% confidence interval can be determined by calculating following integrals:

$$err_{up}(f) = \frac{1}{P_{max}(f) - P_{min}(f)} \int_{P_{min}(f)}^{P_{max}(f)} (d_2(P) - d(P))/d(P)dP \tag{2.8}$$

$$err_{low}(f) = \frac{1}{P_{max}(f) - P_{min}(f)} \int_{P_{min}(f)}^{P_{max}(f)} (d(P) - d_1(P))/d(P)dP \tag{2.9}$$

with $P_{min}(f)$ and $P_{max}(f)$ the minimum and maximum input powers taken from Table 2.1. Table 2.5 summarizes the power averaged relative errors that determine the 95% confidence interval for the individual frequencies in front of the antenna. The errors range from 56 - 122% for the SAR_{wb} and from 41 - 78% for the $SAR_{10g,trunk}$. The orientation in front of the antenna has been chosen to estimate the errors, because it has the most non-zero values for the compliance

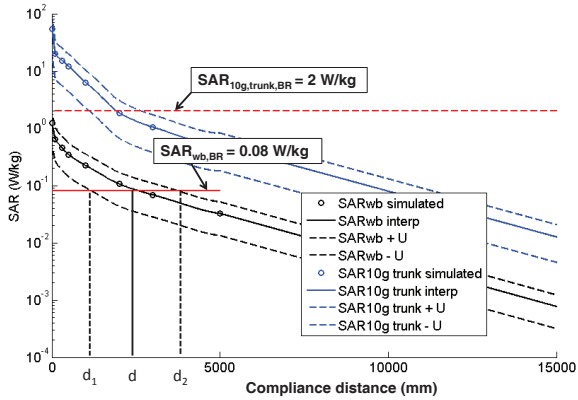

Figure 2.13: SAR_{wb} and $SAR_{10g,trunk}$, with the corresponding uncertainty intervals, as a function of distance from antenna 1 at 800 MHz for 120 W output power. The red lines indicate the ICNIRP basic restrictions for the general public SAR_{wb} (solid) and $SAR_{10g,trunk}$ (dashed).

distances. The values for the $SAR_{10g,trunk}$ are representative for the error on $SAR_{10g,limbs}$ because there are no differences in the calculation methods.

	Frequency (MHz)	err_{low}, err_{up} using $SAR_{wb}(\%)$	err_{low}, err_{up} using $SAR_{10g,trunk}(\%)$
Antenna 1			
	800	68.0, 81.5	62.9, 57.5
	900	60.4, 56.2	56.5, 48.8
	1800	55.1, 81.7	59.7, 64.5
	2600	60.4, 71.1	50.5, 62.0
Antenna 2			
	800	69.8, 84.0	62.7, 62.5
	900	62.7, 59.0	57.4, 45.3
	1800	63.0, 89.3	62.0, 75.5
	2600	63.6, 74.3	68.5, 95.2
Antenna 3			
	800	72.5, 122.2	70.6, 69.1
	900	66.5, 71.1	57.4, 44.1
	1800	67.1, 93.8	50.8, 78.0
	2600	62.2, 81.5	52.0, 40.6

Table 2.5: Relative power averaged lower and upper errors for the compliance distances, as defined in Equations 2.8 and 2.9, for the general public, in front of the antennas. The first column lists the different antennas and frequencies. The second and third column list err_{low} and err_{up} on the compliance distances based on SAR_{wb} and peak $SAR_{10g,trunk}$, respectively.

2.4 Results using a generic BSA and standardized compliance assessment

The previous section provided a detailed assessment of compliance boundaries and allowed output powers, using realistic models for both the used phantom and the antennas. In this section, the compliance boundaries are determined for a generic model of antenna 1, see Fig. 2.4, and standardized methods to determine compliance distances. Subsection 2.4.1 presents compliance boundaries based on the IEC 62232 directive [3] and the CENELEC EN-50383 standard [4] for the individual frequency bands. Subsection 2.4.2 presents cumulative compliance boundaries using the aforementioned standards in front of antenna 1.

2.4.1 Compliance Distances using the IEC 62232 and CENELEC EN-50383 standards

Figure 2.14 shows the obtained compliance boundaries and the corresponding maximum allowed output powers in front of the studied multi-band BSA using single-band transmission. Five different compliance distances are shown at every studied frequency for phantom-antenna separation distances up to 2.5 m. The black and blue curves indicate the compliance boundaries based on the ICNIRP basic restrictions [1] for SAR_{wb} and peak $SAR_{10g,trunk}$, respectively, using the scale factors (to take into account the tissue layering effect and varying element load conditions) and phantom described in IEC 62232 [3]. The SAR_{wb} is calculated using masses of 46 kg (black dashed curve) and 12.5 kg (blue dashed curve), corresponding to a SAR_{wb} value for an adult and a child respectively [3]. The red curves indicate the compliance distances for the studied antenna, based on the averaged electric and magnetic field strengths over a centered surface of 0.4×0.6 m^2 [4] and the corresponding maxima in that plane.

The maximally allowed output powers based on the peak SAR_{10g}, $P_{compl}^{SAR_{10g}}$, are in very good agreement with those found in Figure 2.9 (see Section 2.3.1) for the peak $SAR_{10g,trunk}$ of the VFM for the detailed model of the same antenna. The $P_{compl}^{SAR_{wb}}$ values determined for the adult phantom in this section are about a factor of 2 lower than those shown in Figure 2.9 (see Section 2.3.1), which was to be expected since the IEC phantom is designed to have a SAR that is higher than the SARs found in 95% of all adult humans [12]. For example, using the VFM at 1 m from the detailed model of antenna 1, a $P_{compl}^{SAR_{wb}}$ of 43 W is found at 800 MHz, while for the generic model and the IEC phantom the $P_{compl}^{SAR_{wb}}$ at the same distance and frequency is 19 W. The $P_{compl}^{E_{rms}}$ values at 800 MHz and 900 MHz are lower in this section compared to the allowed powers shown in Figure 2.9 (see Section 2.3.1). This can be attributed to the fact that the electric field is averaged

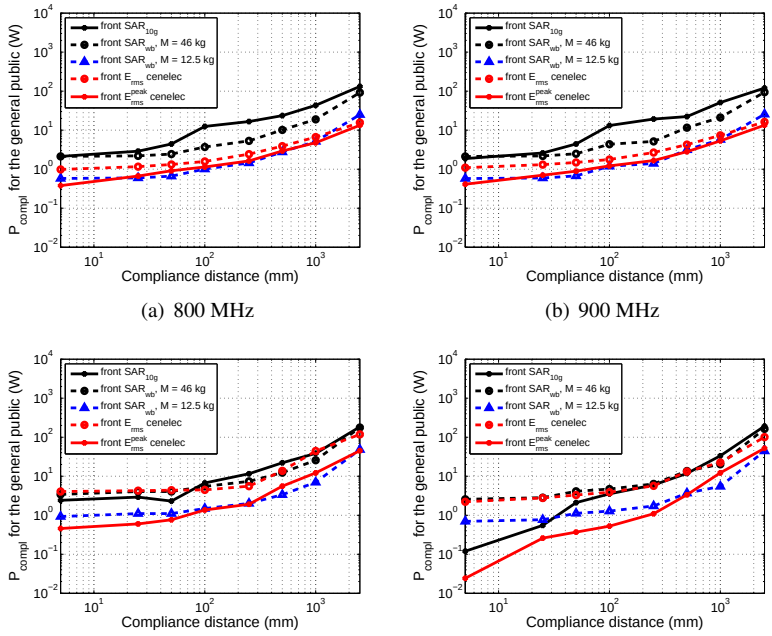

(a) 800 MHz (b) 900 MHz

(c) 1800 MHz (d) 2600 MHz

Figure 2.14: Compliance distances for the studied multi-band antenna based on the ICNIRP basic restrictions using the IEC box phantom [3] and reference levels for the electric field averaged over the CENELEC plane [4] and the peak value (maximum) in that plane.

over a $40 \times 60\ cm^2$ plane centered with respect to the antenna, whereas the electric field in Figure 2.9 (see Section 2.3.1) are averaged over a box with dimensions $28 \times 54 \times 180\ cm^3$. With the frontal plane of the box placed at the same distance from the antenna as the CENELEC averaging plane, the box averaging will obviously result in lower averaged field values. At 1800 MHz and 2600 MHz, $P_{compl}^{E_{rms}}$ are comparable to those shown in Figure 2.9 (see Section 2.3.1). The results obtained for $P_{compl}^{SAR_{wb}}$ and $P_{compl}^{SAR_{10g}}$ are also compared with the allowed powers obtained from the compact form of the SAR_{wb} and peak SAR_{10g} estimation formulas, determined in [12] and intended to provide conservative estimates of SAR values near base station antennas. The allowed powers using our simulations are on average a factor of 2.7 and 3.6 higher than those based on the estimation formulas for SAR_{wb} and SAR_{10g}, respectively.

2.4.2 Cumulative Compliance Boundaries

Figure 2.15 shows the worst-case cumulative compliance distances based on the exposure assessment quantities considered in this section. The cumulative compliance distances are higher than those shown in Figure 2.12 (Section 2.3.4), which is expected, as P_{compl} at the individual frequencies, shown in Fig. 2.14 (Section 2.4.1), are comparable or lower than those shown in Figure 2.9 (Section 2.3.1). For example, for a total output power of 10 W, compliance distances of 0.45 m, 0.75 m, and 1.6 m are obtained based upon the SAR_{10g}, SAR_{wb} in the adult phantom, and E_{rms}, see Figure 2.14, while in Figure 2.12 these compliance distances are 0.54 m, 0.10 m, and 0.30 m, respectively.

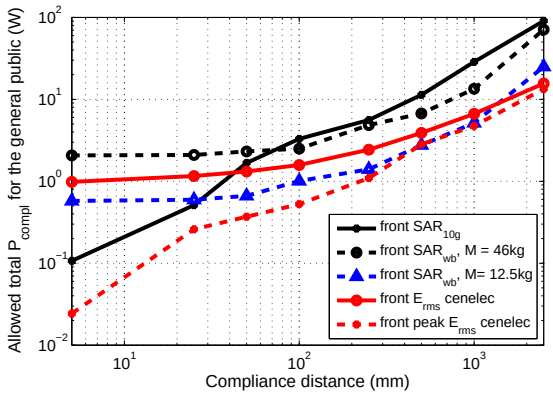

Figure 2.15: Cumulative Compliance distances for the studied multi-band antenna based on the ICNIRP basic restrictions using the IEC box phantom [3] and reference levels for the electric field averaged over the CENELEC plane [4] and the maximum in that plane for cumulative exposure.

2.5 Discussion

The results presented in sections 2.3 and 2.4 and the different modeling techniques used to obtain those results are discussed here.

2.5.1 Modeling of the antenna

As mentioned before, two different modeling techniques are used in this chapter. The goal of the first technique is to model both the physical details of the antennas and have similar far-field characteristics as the real antennas. In the second approach, the goal is to obtain a generic antenna and that has similar far-field characteristics as antenna 1. Therefore, the BSA is modeled as an array of dipoles with resonance around the frequencies of interest.

In the detailed modeling approach, all individual components of the patch antennas (see Fig. 2.2) are measured physically and recreated in the CAD software. These patch antennas are fed with transmission lines printed on the substrate, denoted as feeds. These are modeled with the same physical dimensions, but whereas the real antenna is fed by a coaxial wire, the antenna model is fed by a voltage source. The position of the voltage source is chosen so that the source is matched to the transmission line, i.e. the power reflection coefficient is lower than 0.1 at the simulated frequencies. The patch antennas are then assembled in the same order as the real antenna. The far-field characteristics of the antenna models are listed in Table 2.2. The realized gains are close to the ones listed in the data sheet of the antennas, with differences smaller than 2.4 dB. The vertical beam widths are the same as those listed in the data sheets of the antenna. For the lower three bands (800 MHz, 900 MHz, and 1800 MHz), the horizontal beam widths are recreated within the round-off error. However, for the highest LTE band (2600 MHz) the horizontal beam width is larger than listed in the data sheets, while the gains are very similar (differences smaller than 0.4 dB). Given the good resemblance in antenna gain and physical resemblance, these antenna models are used for simulations.

Table 2.6 lists the required number of grid cells for an FDTD simulation at the listed frequencies with the detailed model of antenna 1, both without a subject present (just the antenna) and with the VFM placed at 1 m distance. The BSA requires between 50 $\times 10^6$ and 54 $\times 10^6$ cells. The number of cells decreases as a function of frequency when just the BSA is considered. This is because the absorbing boundaries require a certain frequency-dependent separation distance from the BSA, which is smaller if the wavelength of the emitted radiation is smaller. If the VFM is placed at 1 m from the BSA, this number of cells increases to 292 $\times 10^6$ at 800 MHz up to 832 $\times 10^6$ at 2600 MHz. Due to the presence of the VFM, the number of cells increases with frequency. This is due to the discretization of the space in between the VFM and the BSA. The spatial steps that can be taken in this zone, are frequency-dependent and are smaller for smaller wavelengths. Table 2.6 lists two different values for the simulations with the VFM present: one with all the antenna feeds included in the simulation and one where only the feeds of the antennas that emit at the listed frequency are used. As Table 2.6 shows, this can drastically reduce the number of required cells. The feeds are not aligned with the FDTD grid, because the antennas are cross-polarized and therefore require a large number of cells. Moreover, the fine resolution of the feeds (sometimes < 1 mm) is automatically extended throughout the full simulation domain in the relevant dimensions, due to the properties of the FDTD algorithm, which also increases the number of cells. Both effects are reduced if some of the feeds at unused frequencies are not used in FDTD. The omission of the unused antenna feeds has no effect on the antennas' far-field properties.

Note that in order to obtain this physical and far-field resemblance of the an-

tennas with relatively low amount of grid cells needed for the simulations using these antennas, three months of work by a trained engineer are required. This is a cost that is reasonable for research purposes, but cannot be justified for some commercial parties that are involved in compliance assessment. Therefore, a generic approach to model the antennas is also investigated.

		Number of cells ($\times 10^6$)		
Antenna	Frequency (MHz)	BSA	BSA and phantom at 1 m	
			with feeds	without feeds
Detailed antenna 1	800	54	292	200
	900	54	293	221
	1800	50.1	464	179
	2600	51.9	832	288
Generic Antenna 1	800	66	144	
	900	66	153	
	1800	61	262	
	2600	59	402	

Table 2.6: Number of cells ($\times 10^6$) necessary to run an FDTD simulation with the detailed and the generic antenna models. (with and without feeds concerns the feeds at frequencies other than the considered frequency)

In the second approach, the goal is to produce a generic model of the BSA, which has the same number of radiating elements and similar far-field characteristics, but not the same physical structure as the original antenna. We have chosen to work with arrays of dipoles. The advantage of this approach is that the dimensions of the dipoles can be readily obtained from standard works on electromagnetism such as [29]. The dipoles are modeled as two cylinders fed by a voltage source and are rotated 45° around the normal vector to the front surface of the BSA, in order to have the correct polarization. The dimensions of the dipoles are chosen so that the power reflection coefficient is below 0.1 at the frequencies used in the simulations. Figure 2.4 shows the antenna and its components. The dimensions of the side reflectors and the separation between the different dipoles are adapted in order to approximate the far-field characteristics of the real antennas. The resulting horizontal beam width is within 5° of that of the real antennas and the vertical beam width is within 1° of that of the antenna. The gain was not chosen as a design specification, but the gain values are within 3 dB of those listed in the data sheets of the real antennas. Due to the simple approach, the design of the BSA can be finished within a weeks work, even by a person with limited knowledge of antenna design. This is a considerable gain in cost and time compared to the modeling of the detailed antenna. Moreover, since standard dipole antennas are used, no antenna design and adaptations are necessary.

Table 2.6 also lists the number of cells necessary to perform the simulations with the generic BSA with and without the IEC phantom [3] at 1 m from the BSA.

The configuration with just the BSA shows the same frequency dependence as the other antenna. The number of cells decreases from 66×10^6 cells at 800 MHz to 59×10^6 cells at 2600 MHz. There are more cells needed at higher wavelengths, due to the separation between the antenna model and the absorbing boundaries. The number of cells is higher than the number of cells needed for the detailed antenna model, because the dipoles require a relatively large amount of cells, in comparison to the patch antennas. The dipoles are cylinders, volumes rotated over 45° around the normal to the BSAs frontal surface, that require a large number of cells to be sufficiently refined for accurate simulation results, whereas in the detailed antennas the feed networks are also rotated over the same 45°, but these are surface objects that require less grid cells to resolve. Although the antenna requires less time to construct and is easily understandable in design, it comes with a computational cost. The number of cells increases With the IEC phantom present. The number of cells is higher at higher frequencies, due to the smaller steps in between the BSA and the phantom. No optimization is applied to this antenna, as it is the goal to perform simulations with a generic, "textbook" antenna, that could be made by obtaining information from literature. However, at the two higher frequencies this leads to a larger number of grid cells than the simulations of the detailed BSA and the VFM, without the feeds of the non-radiating elements resolved.

2.5.2 Detailed modeling of the BSA and a realistic phantom

This section consists out of four parts: first, the differences between SAR_{wb}, the peak SAR_{10g} and E_{rms} are discussed. Second, the conservativeness of the ICNIRP reference levels is investigated. Third, the cumulative compliance distances are treated. Finally, an assessment of the methods to determine the actual compliance distances is made.

Figure 2.10 shows that the curves based on E_{rms} generally follow the same trend for the three antennas. The same holds for the SAR_{wb}, see Figure 2.9. Due to the whole-body averaging (SAR_{wb}) and the averaging over a volume surrounding the phantom (E_{rms}), differences in antenna design are not that significant. For the other compliance distances based on the peak $SAR_{10g,trunk}$ and $SAR_{10g,limbs}$ more variation exists in the position and value of the maxima as the phantom moves away from the antenna. The location and value of the peak SAR_{10g} are dependent on the exposure conditions and on the heterogeneity and shape of the used phantom. The differences in the value of the peak SAR_{10g} for the different antennas at the same phantom position relative to the antennas, are due to differences in antenna design, length, and number of radiating antennas at a certain frequency (see Table 2.1), which can cause other locations and values of the peak SAR_{10g} in the VFM. The positioning of the phantom with respect to the antenna can have an influence as well [13].

The reference levels for E_{rms} are deduced from the basic restrictions on SAR_{wb} for plane-wave exposure (in the far field) of a spheroid phantom [1]. The reference levels ought to be more conservative, meaning that when the reference levels are exceeded, the basic restrictions are not exceeded. This is not always the case for a heterogeneous human in the near field of a BSA.

In this study we used a realistic human body phantom which is exposed to a BSA. When comparing Figures 2.9 and 2.10, one can see that the reference levels are not always conservative, i.e., sometimes $P_{compl}^{E_{rms}}(f_n, d) > P_{compl}^{SAR_{wb}}(f_n, d)$. For the lower frequencies 800 and 900 MHz $P_{compl}^{E_{rms}}(f_n, d)$ is always smaller than $P_{compl}^{SAR_{wb}}(f_n, d)$, while for the higher frequencies 1800 and 2600 MHz, this is not always true. We attribute this to both the localized nature of the exposure and the quadratic relationship between incident power and electric fields. At the lower frequencies (800 and 900 MHz) the full antenna is emitting, while at the higher frequencies (1800 and 2600 MHz) only one half of the antenna is emitting. Since the E_{rms} is calculated as a volume average, the spatial distribution of the electric fields will play a role. Areas in the volume with a lower coverage by the antenna will lower the overall average E_{rms} field and thus increase the power needed to obtain the reference levels. The number of patch antennas will also influence the SAR_{wb} values, since a heterogeneous phantom is used. To investigate this, we have performed simulations where antenna 1 is adapted to have 11 patch antennas emitting at 2600 MHz spread over the full length of the antenna, instead of 5 over half the length of the antenna as in the original antenna 1. Table 2.7 lists the differences in allowed powers at 2600 MHz for the same antenna with different numbers of radiating patch antennas. The table shows that when all 11 patch antennas are emitting, the allowed power based on the electric fields is indeed more conservative than the one based on SAR_{wb}. While when only 5 patch antennas are emitting, the reference levels allow for higher powers.

Number of Radiating Patch Antennas	$P_{compl}^{SAR_{wb}}(2600\ MHz,$ 300 mm) (W)	$P_{compl}^{E_{rms}}(2600\ MHz,$ 300 mm) (W)
5	18.12	20.71
11	21.22	19.69

Table 2.7: Allowed powers at 300 mm from antenna 1, when only the upper half of the antenna is radiating and when the full antenna is radiating.

To gain more insight in the curves $P_{compl}^{x}(d)$ (with $x = SAR_{wb}$, $SAR_{10g,limbs}$, $SAR_{10g,trunk}$, or E_{rms}) of the cumulative compliance distances, a fit using Equation 2.5 is carried out, see Figure 2.12. A linear decay of the SAR values due to the cylindrical nature of wave propagation is expected in the region close to a linear array of antennas, while further away from the antenna spherical propagation is ex-

pected, leading to a quadratic decay of SAR values with distance [11, 12, 30]. The different simulation results used to determine the cumulative compliance distance are situated in both the region of cylindrical propagation and the spherical propagation region, depending on the frequency and distance from the antenna [11]. An average value of 1.4 ± 0.5 is estimated for the exponent B, as shown in Table 2.4, which implies an increase of the allowed power with $d^{1.4\pm0.5}$ confirming the interplay between cylindrical (B=1) and spherical (B=2) propagation.

The goal of any base station antenna compliance assessment is to determine an actual compliance distance, d_{tot}, at which the exposure is below relevant limits on both localized and whole-body exposure. Obviously, a d_{tot} solely based on one exposure quantity would require the least computational effort. However, as Figures 2.9 and 2.10 show, there exists no quantity which is most conservative for all the studied antennas and frequencies. Therefore, quantities have to be combined in order to determine d_{tot}. Using the notation employed before, d_{tot} can be determined using any of the approaches listed below in order of increasing computational demands:

$$d_{tot} = max(d_{compl}^{SAR_{wb}}, d_{compl}^{SAR_{10g,limbs}}) \tag{2.10}$$

$$d_{tot} = max(d_{compl}^{SAR_{wb}}, d_{compl}^{SAR_{10g,trunk}}) \tag{2.11}$$

$$d_{tot} = max(d_{compl}^{SAR_{wb}}, d_{compl}^{SAR_{10g,trunk}}, d_{compl}^{SAR_{10g,limbs}}) \tag{2.12}$$

$$d_{tot} = max(d_{compl}^{E_{rms}^{av}}, d_{compl}^{SAR_{wb}}) \tag{2.13}$$

$$d_{tot} = max(d_{compl}^{E_{rms}^{av}}, d_{compl}^{SAR_{10g,limbs}}) \tag{2.14}$$

$$d_{tot} = max(d_{compl}^{E_{rms}^{av}}, d_{compl}^{SAR_{10g,trunk}}) \tag{2.15}$$

$$d_{tot} = max(d_{compl}^{E_{rms}^{av}}, d_{compl}^{SAR_{wb}}, d_{compl}^{SAR_{10g,limbs}}) \tag{2.16}$$

$$d_{tot} = max(d_{compl}^{E_{rms}^{av}}, d_{compl}^{SAR_{wb}}, d_{compl}^{SAR_{10g,trunk}}) \tag{2.17}$$

$$d_{tot} = max(d_{compl}^{E_{rms}^{av}}, d_{compl}^{SAR_{10g,trunk}}, d_{compl}^{SAR_{10g,limbs}}) \tag{2.18}$$

$$d_{tot} = max(d_{compl}^{E_{rms}^{av}}, d_{compl}^{SAR_{10g,trunk}}, d_{compl}^{SAR_{10g,limbs}}, d_{compl}^{SAR_{wb}}) \tag{2.19}$$

When using numerical simulations, only one simulation is required to obtain field strength results for all investigated assessment distances. For SAR, however, one simulation is needed per assessment point. Furthermore, the SAR simulations normally make use of more cells in order to discretize the phantom. An assessment solely based on SAR values would not require the simulations to determine the electric field strength, thus Eqs. 2.10 to 2.12 require less computational power than Eqs. 2.13 to 2.19. Additional computations are needed to calculate the peak SAR_{10g}, since SAR values have to be averaged over several cubes in the phantom,

while the SAR_{wb} just requires one averaging. Therefore, methods that only use the SAR_{wb} are computationally less demanding than methods that use the SAR_{10g}. There is a difference in used storage space and computational effort when calculating the $SAR_{10g,limbs}$ or $SAR_{10g,trunk}$. A method that employs just one of these two averaging schemes requires less computational effort and since the limbs contain less volume, they are computationally less demanding. A method in which all the different studied quantities would have to be determined is the computationally most demanding method. We have discussed the use of the approaches listed above for the total compliance distance in front of the three studied antennas below.

At the two lowest frequencies (800 and 900 MHz), $SAR_{10g,limbs}$ is never the most conservative quantity in front of the antenna. Therefore, computational time could be saved by not considering this quantity in this direction. In fact, a conservative estimate of d_{tot} could be determined by only considering the E_{rms} values, averaged over the VFM's bounding box. If an assessment solely based on SAR values is preferred, then both the SAR_{wb} and $SAR_{10g,trunk}$ have to be considered (Eq. 2.11), see Figure 2.9.

At 1800 MHz, the most conservative quantity in front of the BSA - the quantity that determines d_{tot} - is dependent on the emitted power. For antennas 1 and 2 it suffices to use Equation 2.15. All quantities, even the $SAR_{10g,limbs}$ have to be considered for antenna 3.

At 2600 MHz, it suffices to determine the $SAR_{10g,trunk}$ for antennas 1 and 2, while for antenna 3 the SAR_{wb} and E_{rms} can be the most conservative quantity as well.

2.5.3 Generic Base Station Antennas

In section 2.4 compliance distances are determined based on the ICNIRP reference levels and basic restrictions for a generic model of a multi-band base station antenna, to evaluate the procedures described in CENELEC EN-50383 [4] and IEC 62232 [3]. An actual compliance distance, d_{tot}, at which the exposure is below relevant limits on both localized and whole-body exposure, can also be determined using these two standards. Since we use a box-shape phantom, there is only one peak SAR_{10g} value, this reduces the options of combining different quantities. We also considered the E_{rms}^{peak} value in the CENELEC plane. Equations 2.10 to 2.19 thus reduce to the following equations, listed below in order of increasing computational demands:

$$d_{tot} = max(d_{compl}^{E_{rms}^{av}}, d_{compl}^{E_{rms}^{peak}}) = d_{compl}^{E_{rms}^{peak}} \tag{2.20}$$

$$d_{tot} = max(d_{compl}^{E_{rms}^{av}}, d_{compl}^{SAR_{10g}}) \tag{2.21}$$

$$d_{tot} = max(d_{compl}^{SAR_{wb}}, d_{compl}^{SAR_{10g}}) \tag{2.22}$$

If the assessments are made using Eq. 2.21, i.e. the SAR assessment is made with respect to localized SAR only, the assessments may be simplified compared with Eq. 2.22 by using an elliptical phantom, significantly smaller than the box-shaped phantom required to assess whole-body SAR [3]. This elliptical phantom specified in IEC 62209-2 [31] and has a major and minor axis of 0.6 m and 0.4 m, respectively, which may be compared with the lateral dimensions of the box-shaped phantom of 1.54 m and 0.339 m.

As expected, Figure 2.14 shows that the simplest approach for assessing EMF compliance, i.e. E_{rms}^{peak} field assessment by using Eq. 2.20, will provide the most conservative results for adult exposure. For a given power level, the front compliance distance may be reduced significantly if a more laborious assessment method is chosen. As an example, for a transmitted power of 10 W at 900 MHz, the compliance distance is reduced from about 2 m to 1.5 m if a combination of averaged field strengths and peak SAR_{10g} is used, according to Eq. 2.21. If a pure SAR based assessment is made, the compliance distance is reduced to 0.5 m for adult exposure. When child exposure is considered, Figure 2.14 shows that there exist power levels at 1800 MHz and 2600 MHz for which Eq. 2.22 will predict a larger compliance distance than Eq. 2.20. This is partly a consequence of the very conservative approach specified in IEC 62232, where the SAR_{wb} is obtained as the power absorbed in an adult phantom divided by the mass of a child.

For the two lowest frequencies investigated (800 and 900 MHz), $d_{compl}^{E_{rms}^{av}} > d_{compl}^{SAR_{10g}}$ for all investigated power levels. At the two higher frequencies, this is not always true, which shows the need to also assess peak SAR_{10g}, if field strength results are averaged over the CENELEC plane.

For the two highest frequencies (1800 and 2600 MHz), $d_{compl}^{SAR_{wb}} > d_{compl}^{E_{rms}^{av}}$ for some levels of transmit power. This is not observed for the lowest frequencies, which may be attributed to the placement of the elements at the higher frequencies, the frequency dependent reference levels and the conservativeness of the whole-body SAR phantom [12].

By assuming that all power transmitted by the antenna is absorbed in the phantom, a theoretical lower limit in transmitted power (P_{lim}) that can result in a SAR_{wb} equal to the ICNIRP basic restriction can be calculated as the product of the basic restriction on SAR_{wb} and the mass of the phantom. For the adult phantom P_{lim} = 0.08 W/kg $\times$46 kg = 3.68 W, while for the child phantom $P_{lim} = 1$ W. As shown in Figure 2.14, the whole-body SAR approach of IEC 62232 may for small phantom-antenna separation distances produce even lower maximum allowed power levels than 3.68 W. This unphysical behavior is a consequence of the distance independent tissue layering correction factor specified in IEC 62232 [3].

2.6 Conclusions

This chapter numerically investigates compliance boundaries based on the whole-body averaged SAR (SAR_{wb}), peak 10 g averaged SAR (SAR_{10g}) in head and trunk or in the limbs, and on the root-mean-squared electric-field strength (E_{rms}) using the ICNIRP basic restrictions and reference levels for the general public and occupational exposure. Two different approaches are used to investigate compliance. First, a detailed, physically accurate compliance assessment is executed, using detailed antenna models of the studied Long Term Evolution (LTE), multi-band base station antennas and a realistic phantom: the virtual family male. Second, a generic model is used for compliance assessment of one of the studied LTE, multi-band antennas, using standardized procedures, described in CENELEC EN-50383 [4] and IEC 62232 [3].

In the first approach, both compliance distances and allowed powers are determined in three directions from three base station antennas that emit at four frequencies. Realistic maximal output powers are chosen for the antennas. The results based on different basic restrictions and reference levels are compared and a combined compliance distance, at which all basic restrictions and reference levels are met, is determined for every frequency. The ICNIRP reference levels are not always conservative and electric field measurements or simulations only are insufficient to obtain the actual compliance boundary of the studied antennas. A cumulative compliance distance, in the case that all the frequencies are emitted simultaneously, is defined. At short distances (< 1000 mm) the cumulative compliance boundaries in front of the antennas are determined by the $SAR_{10g,trunk}$, while at large distances other quantities can become more conservative. At the side and back of the antennas cumulative compliance distances only exist at short distances from the antenna (< 1000 mm) for realistic output powers ranging up to 300 W per frequency. Compliance with all basic restrictions is guaranteed for the studied antennas up to 10 cm at the back and side, if the total emitted output power is lower than 316 W, independent from the power distribution over the different frequencies. The relative errors on the compliance distances are also determined ($< 122\%$).

In the second approach, both frequency specific and cumulative compliance distances, based on different quantities such as peak SAR_{10g}, SAR_{wb}, and peak and spatially averaged E_{rms}, are determined. The gain in terms of more accurate compliance distances when using more laborious assessment methods is quantified. In general, assessments based on peak field strengths are less computationally intensive but lead to larger compliance distances. As expected, it is found that spatial field averaging used in combination with localized SAR assessments is an option to obtain shorter and more accurate compliance distances. As long as adult exposure is considered, the results also indicate that even shorter compliance dis-

tances may be obtained by using assessments based on SAR_{10g} and SAR_{wb}. The currently specified procedure in IEC 62232 for evaluating child SAR_{wb}, results in compliance distances larger than the peak field strength method. It is also shown that the currently standardized SAR_{wb} measurement approach in IEC 62232 may lead to unphysical results for small phantom-antenna separation distances.

Both modeling techniques are compared and discussed. The approach using the generic antenna provides conservative results using less modeling, less knowledge of antenna design, but with a slightly larger computational cost. This method can be used by manufacturers of radio base station products or their clients who want to efficiently determine compliance with exposure limits or regulations, even without doing an extensive modeling of the electromagnetic problem.

References

[1] ICNIRP International Commission on Non-Ionizing Radiation Protection. *Guidelines for limiting exposure to time-varying electric, magnetic, and electromagnetic fields (up to 300 GHz).* Health physics, 74:494–522, 1998.

[2] IEC International Electrotechnical Commission. *Guidance for evaluating exposure from multiple EM sources Guidance for evaluating exposure from multiple EM sources*. pages 1–38.

[3] IEC International Electrotechnical Commission. *IEC 62232 Ed.1: Determination of RF field strength and SAR in the vicinity of radiocommunication base stations for the purpose of evaluating human exposure*. 2011.

[4] CENELEC. *Basic standard for the calculation and measurement of electromagnetic field strength and SAR related to human exposure from radio base stations and fixed terminal stations for wireless telecommunication systems (110 MHz40 GHz). CENELEC EN 50383:2010. Brussels, Belgium*. 2010.

[5] P Bernardi, M Cavagnaro, S Pisa, and E Piuzzi. *Human Exposure to Radio Base-Station Antennas in Urban Environment*. IEEE Trans Microw Theory Tech, 48:1996–2002, November 2000.

[6] J Cooper, B Marx, J Buhl, and V Hombach. *Determination of safety distance limits for a human near a cellular base station antenna, adopting the IEEE standard or ICNIRP guidelines.* Bioelectromagnetics, 23(6):429–43, September 2002.

[7] W Joseph and L Martens. *Comparison of Safety Distances Based on the Electromagnetic Field and Based on the SAR for Occupational Exposure of a 900-MHz Base Station Antenna*. IEEE Trans Electromagn Compat, 47(4):977–985, November 2005.

[8] F Lacroux, E Conil, A Cortel Carrasco, A Gati, M Wong, and J Wiart. *Specific absorption rate assessment near a base-station antenna (2,140MHz): some key points*. Annals of Telecommunications - Annales Des Télécommunications, 63(1-2):55–64, January 2008.

[9] M Gosselin, A Christ, S Kühn, and N Kuster. *Dependence of the Occupational Exposure to Mobile Phone Base Stations on the Properties of the Antenna and the Human Body*. IEEE Transactions on Electromagnetic Compatibility, 51(2):227–235, May 2009.

[10] M Martínez-Búrdalo, A Martín, M Anguiano, and R Villar. *On the safety assessment of human exposure in the proximity of cellular communications base-station antennas at 900, 1800 and 2170 MHz.* Physics in medicine and biology, 50(17):4125–37, September 2005.

[11] B Thors, M L Strydom, F J C Meyer, and K Kimmo. *On the Estimation of SAR and Compliance Distance Related to RF Exposure From Mobile Communication Base Station Antennas*. IEEE Trans Electromagn Compat, 50(4):837–848, November 2008.

[12] M Gosselin, K Kühn, S, S Benkler, T M I Uusitupa, W Joseph, A Gati, J Wiart, F J C Meyer, L Martens, T Nojima, T Hikage, Q Balzano, A Christ, and N Kuster. *Estimation Formulas for the Specific Absorption Rate in Humans Exposed to Base-Station Antennas*. IEEE Trans Electromagn Compat, 53(4):1–14, 2011.

[13] B Kos, B Valič, T Kotnik, and P Gajšek. *Exposure assessment in front of a multi-band base station antenna.* Bioelectromagnetics, 32(3):234–42, April 2011.

[14] G Vermeeren, M Gosselin, S Kühn, V Kellerman, A Hadjem, A Gati, W Joseph, J Wiart, F Meyer, N Kuster, and L Martens. *The influence of the reflective environment on the absorption of a human male exposed to representative base station antennas from 300 MHz to 5 GHz.* Physics in medicine and biology, 55(18):5541–55, September 2010.

[15] 3rd Generation Partnership Project (3GPP). *LTE; Technical Specification Group Radio Access Network; Evolved Universal Terrestrial Radio Access (E-UTRA); User Equipment (UE) Radio Transmission and Reception (TS 36.101 v 9.1.0 Release 9).* 2009.

[16] S Cecil, K Martin, A Escortihuela-Navarro, G Friedrich, and G Neubauer. *Safety Distance Concept for LTEFrequencies*. 32nd Annual Meeting of the Bioelectromagnetics Society (BEMS 2011), Halifax, Canada,, 2011.

[17] A Christ, W Kainz, E G Hahn, K Honegger, M Zefferer, E Neufeld, W Rascher, R Janka, W Bautz, J Chen, B Kiefer, P Schmitt, H Hollenbach, J Shen, M Oberle, D Szczerba, A Kam, J W Guag, and N Kuster. *The Virtual Family–development of surface-based anatomical models of two adults and two children for dosimetric simulations.* Physics in medicine and biology, 55(2):N23–38, January 2010.

[18] Powerwave. *P65-15-XDHW2-MD1, Triple Broadband Cross Polarized 790-960 MHz, 1710-2170 MHz, 2500-2690 MHz integrated diplexer LB/HB.* datasheet by Powerwave (Santa Ana, CA, USA), 2011.

[19] Powerwave. *P65-17-XDHW2-MD1, Triple Broadband Cross Polarized 790-960 MHz, 1710-2170 MHz, 2500-2690 MHz integrated diplexer LB/HB.* datasheet by Powerwave (Santa Ana, CA, USA), 2011.

[20] Powerwave. *P65-18-XDHW2-MD1, Triple Broadband Cross Polarized 790-960 MHz, 1710-2170 MHz, 2500-2690 MHz integrated diplexer LB/HB.* datasheet by Powerwave (Santa Ana, CA, USA), 2011.

[21] M J van Wyk, M Bingle, and F J C Meyer. *Antenna modeling considerations for accurate SAR calculations in human phantoms in close proximity to GSM cellular base station antennas.* Bioelectromagnetics, 26(6):502–9, September 2005.

[22] B Hansson, B Thors, and C Törnevik. *Analysis of the effect of mobile phone base station antenna loading on localized SAR and its consequences for measurements.* Bioelectromagnetics, 32(8):664–72, December 2011.

[23] J W Hand. *Modelling the interaction of electromagnetic fields (10 MHz-10 GHz) with the human body: methods and applications.* Physics in medicine and biology, 53(16):R243–86, August 2008.

[24] R P Findlay and P J Dimbylow. *Variations in calculated SAR with distance to the perfectly matched layer boundary for a human voxel model.* Physics in medicine and biology, 51(23):N411–5, December 2006.

[25] C Gabriel, S Gabriel, and E Corthout. *The dielectric properties of biological tissues: I. Literature survey.* Physics in medicine and biology, 41(11):2231–49, November 1996.

[26] MMF Mobile Manufacturers Forum (MMF) and the GSM Association (GSMA). *MMF/GSMA Phase 2: Scientific Basis for Base Station Exposure Compliance Standards*. 2009.

[27] J F Bakker, M M Paulides, A Christ, N Kuster, and G C van Rhoon. *Assessment of induced SAR in children exposed to electromagnetic plane waves between 10 MHz and 5.6 GHz.* Physics in medicine and biology, 55(11):3115–3130, 2010.

[28] S Kühn, W Jennings, A Christ, and N Kuster. *Assessment of induced radio-frequency electromagnetic fields in various anatomical human body models.* Physics in medicine and biology, 54(4):875–90, February 2009.

[29] C A Balanis. *Antenna Theory: Analysis and Design*. 1982.

[30] R Cicchetti and A Faraone. *Estimation of the Peak Power Density in the Vicinity of Cellular and Radio Base Station Antennas*. IEEE Trans Electromagn Compat, 46(2):275–290, May 2004.

[31] IEC International Electrotechnical Commission. *Human exposure to radio frequency fields from hand-held and body-mounted wireless communication devices - Human models, instrumentation, and procedures - Part 2: Procedure to determine the specific absorption rate (SAR) for wireless communication devices used in close proximity to the human body (frequency range of 30 MHz to 6 GHz).* 2010.

3

Measurement Uncertainty of Personal Exposimeters

3.1 Introduction

The number of radio frequency (RF) sources, that emit at frequencies ranging from several kHz up to 300 GHz, has increased in the last decade [1, 2] and is expected to increase further in the next one [3]. This gives rise to a public concern about possible adverse health effects induced by RF radiation. Up till now, the only proven mechanism of an effect of RF radiation on the human body is tissue heating by absorption of electromagnetic (EM) energy. The quantity used to describe this, in the RF region, is the specific absorption rate (SAR) for which basic restrictions have been defined [4]. Because the SAR cannot be measured inside a living human, reference levels on the incident EM fields have been defined [4]. In Chapter 2 of this book, the electric field strengths near base station antennas are studied using numerical simulations. Alternatively these field strengths can also be studied using radio frequency (RF) measurement equipment such as broadband probes [5] or a combination of a spectrum analyzer and an isotropic antenna [6, 7]. The main advantage of these measurements is that they have a relatively low expanded measurement uncertainty (using a confidence interval of 95%) of around 3 dB (a factor of 2) [6, 7], but they have disadvantages as well. The measurements have to be executed in free-space by an instructed operator with certified, calibrated material. Therefore, the measured values are not obtained on the same moment as when the exposure of a person occurs. This kind of measurement is thus less suitable to

determine one's personal exposure.

Personal exposure assessment is a domain that is gaining importance in the research on RF electromagnetic fields. The World Health Organization (WHO) has indicated the need for a correct exposure assessment of RF radiation as one of the priorities in its 2010 research agenda regarding RF radiation [1, 2]. This exposure assessment is crucial for a correct description of the EM environment in which employees and the general public live and work, and is frequently used in several epidemiological studies that aim to evaluate health effects of RF radiation [8–12].

(a) The EME SPY 140 (Satimo, Brest, France)

(b) The ESM 140 (Maschek, Bad Wrishofen, Germany)

(c) The ExpoM 3 (Fields at work, Zürich, Switzerland)

(d) The Radman XT (Narda, Hauppauge, NY, USA)

Figure 3.1: Personal Exposimeters.

In exposure assessment studies, electric field strengths are usually registered using personal exposimeters (PEMs) [8–15]. These are body worn devices that measure time-varying electric-field strengths in different frequency bands and can be used by subjects wearing these devices without an extensive training [8–14]. Figure 3.1 shows some commercial examples of commonly used PEMs.

The currently existing PEMs have some clear advantages over the previously

mentioned EM measurement devices. First, they are worn on the body and will thus measure on the same location and time as the subject who is wearing the PEM. Secondly, they can measure simultaneously in different frequency bands. Therefore, PEMs are frequently used in measurement campaigns of RF exposures [8–13] and a protocol has been developed for a correct use of PEMs for personal exposure assessment [14]. However, PEMs are also faced with relatively large measurement uncertainties due to shadowing of the body [15–18]. Moreover, they measure the electric-field strengths on the body instead of the incident or unperturbed fields, which are typically used to represent exposure and for which reference levels exist [4]. These devices are calibrated in free space. Therefore, it is also questionable whether they can measure the electric-field strength on the body. They also exhibit an unwanted dependence on the polarization of the incident fields, while their recordings should only depend on the field strength [18]. Additionally, their measurements are confounded by crosstalk [18, 19], which means that some fields emitted in a certain frequency band are registered in another frequency band.

The goal of this chapter is to quantify these uncertainties numerically and compare them to existing studies. To this aim, the distribution of the electric fields strengths are studied near one of the base station antennas (BSAs) studied in the previous chapter and in realistic, far-field exposure situations. In Section 3.2, the methodology, simulation, and modeling techniques used to determine the distribution of a PEM's on-body response are presented. Section 3.3 presents the distribution of a PEM's on-body response near a multi-band, LTE antenna. In Section 3.4 this response is studied in realistic environments. The results obtained in Sections 3.3 and 3.4 are compared to those found in other studies in section 3.5. Conclusions are drawn in section 3.6.

3.2 Materials and Methods

In this section, first, the relevant studied quantities are outlined in subsection 3.2.1. Second, the methodology of how the performance of a PEM is studied is described in subsection 3.2.2.

3.2.1 Response and Measurement Uncertainty of a Personal Exposimeter

One's personal exposure is usually characterized by the root-mean-squared (RMS) magnitude of the incident electric fields: E_{rms}^{free} [4]. However, these fields cannot be measured by a body-worn device such as a PEM, since the body heavily perturbs the electric fields in its environment [15, 20]. The body does not only absorb EM radiation, but also scatters part of the incident radiation: $\overline{E}^{scattered}$. An antenna worn on the body, such as the one that is integrated in a PEM, will record a

certain field strength E_{rms}^{PEM}, which is the amplitude of the sum of both the scattered and the incident field at the position of the PEM:

$$\overline{E}^{PEM} = \overline{E}^{free} + \overline{E}^{scattered} \tag{3.1}$$

From Equation 3.1 it should be clear that the electric field strength recorded by the PEM, E_{rms}^{PEM}, is not always equal to the incident field strength E_{rms}^{free}. Therefore, in order to evaluate the performance of a PEM, the PEM's response (R) is studied:

$$R = (\frac{E_{rms}^{PEM}}{E_{rms}^{free}})^2 \tag{3.2}$$

Ideally, a PEM should record E_{rms}^{free} and R should thus be 1. However, in reality R might be different from 1: $R < 1$ indicates an underestimation of the incident electric-field strength by the PEM, while $R > 1$ means an overestimation. The response of a PEM is also not a constant; the scattering of the human body depends on the posture of the human [21], the orientation of the body towards the transmitter [17, 18], the frequency [15, 18, 20], the positioning of the PEM [15], and the characteristics of the environment in which the measurements are taking place [15]. The response R is to be studied as a statistical variable with a certain distribution.

The fact that R has a certain distribution and is not a constant, is a cause of measurement uncertainty of the incident field strengths when measuring with a PEM. If R would be a constant then E_{rms}^{free} could easily be obtained from equation 3.2:

$$E_{rms}^{free} = \frac{E_{rms}^{PEM}}{\sqrt{R}} \tag{3.3}$$

However, R is not a constant, but has a certain distribution. An estimate of the incident field strength can be obtained using the median or 50% percentile of R ($p_{50}(R)$):

$$\widehat{E}_{rms}^{free} = \frac{E_{rms}^{PEM}}{\sqrt{p_{50}(R)}} \tag{3.4}$$

This estimate comes with a certain prediction interval (PI), which is also the measurement uncertainty on E_{rms}^{free}. This is an interval around the estimate $\widehat{E}_{rms}^{free}$ in which the value E_{rms}^{free} will be located a certain percentage of times. For example, a 50% prediction interval can be defined, given the 25% percentile of R ($p_{25}(R)$) and the 75% percentile of R ($p_{75}(R)$). In 50% of repetitions of the same measurement of E_{rms}^{PEM}, the actual value of E_{rms}^{free} is located in the 50% prediction interval (PI_{50}):

$$[\frac{E_{rms}^{PEM}}{\sqrt{p_{75}(R)}}, \frac{E_{rms}^{PEM}}{\sqrt{p_{25}(R)}}] \tag{3.5}$$

In terms of relative measurement uncertainty on E_{rms}^{free} this becomes:

$$u_{up} = \sqrt{\frac{p_{50}(R)}{p_{25}(R)}} - 1 \tag{3.6}$$

$$u_{low} = 1 - \sqrt{\frac{p_{50}(R)}{p_{75}(R)}} \tag{3.7}$$

A convenient manner to describe this prediction interval is to study the ratio of both percentiles:

$$PI_{50} = \frac{p_{75}(R)}{p_{25}(R)} \tag{3.8}$$

If PI_{50} is close to 1, the prediction interval and consequently the measurement uncertainty will be small. If $PI_{50} >> 1$ then the measurement uncertainty will be large as well. Other prediction intervals can be defined using other percentiles. In this chapter the distribution of R is studied using the the 50% prediction interval or (logarithmically) the interquartile distance (PI_{50}), and the 95% prediction interval of R (c_{95}): the ratio of the 97.5% ($p_{97.5}(R)$) and 2.5% ($p_{2.5}(R)$) percentiles of the distribution of R.

3.2.2 Configuration using Numerical Simulations

The response of a PEM is studied using numerical simulations. Using finite-difference time-domain (FDTD) simulations, the electric fields inside and outside the body of a numerical phantom under exposure of RF radiation can be determined. Two factors that influence the distribution of R are studied: the position of the PEM on the body and the exposure scenario.

The numerical phantom chosen in this chapter is the Virtual Family Male (VFM) [22]. This is a heterogeneous human body model consisting of 81 different tissues, based upon magnetic resonance imaging of a healthy male volunteer with a BMI (body mass index) of 22.3 kg/m^2. The dielectric properties assigned to the phantom's tissues are taken from the Gabriel database [23]. To model the positioning of a PEM, a conformal surface at 1 cm from the phantom is determined. This surface is discretized by the FDTD algorithm. Figure 3.2 shows the discretized surface around the VFM. There are no measurement points selected in front of the phantom's face and on the phantom's legs, since these positions are considered unfit to place a PEM. An exposimeter placed on the legs or face, would influence the subject's behavior too much and therefore this might alter their exposure. Placement of a PEM on the head might seem unrealistic using the existing PEMs, see Figure 3.1, but is feasible using newer technologies such as wearable and miniaturized antennas [17, 24].

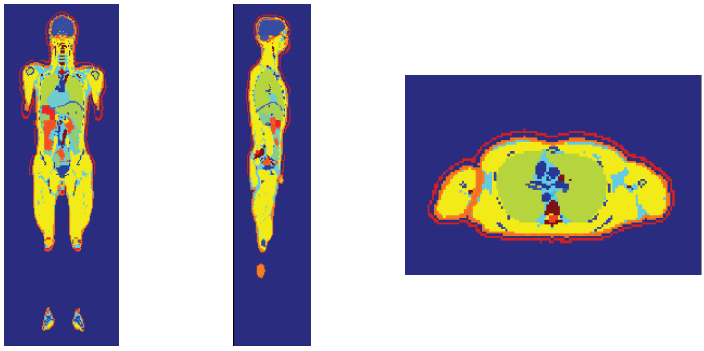

Figure 3.2: Surface (red) at 1 cm from the VFM. From left to right: Mid-Coronal plane, a Sagittal through the VFM's right leg, and a transverse plane trough the VFM's torus.

The considered surface at 1 cm from the upper-body consists of a large number of cells O(10^4), which can be very close (up to 1 mm) to one another. In order to reduce the number of potential locations of a PEM on the upper body, a discretization in the azimuth angle ϕ of 10° and 10 cm steps in the Z-coordinate is introduced. This reduces the number of potential locations to deploy a PEM to 401. Figure 3.3 shows the studied set of potential locations on the body. The VFM is not a cylinder and therefore the 401 points are not evenly distributed between the front ($\phi \in [-90, 90]$) and the back ($\phi \in [90, 270]$) of the VFM. 186 of the 401 potential locations are located on the front of the body, while 215 are located on the back.

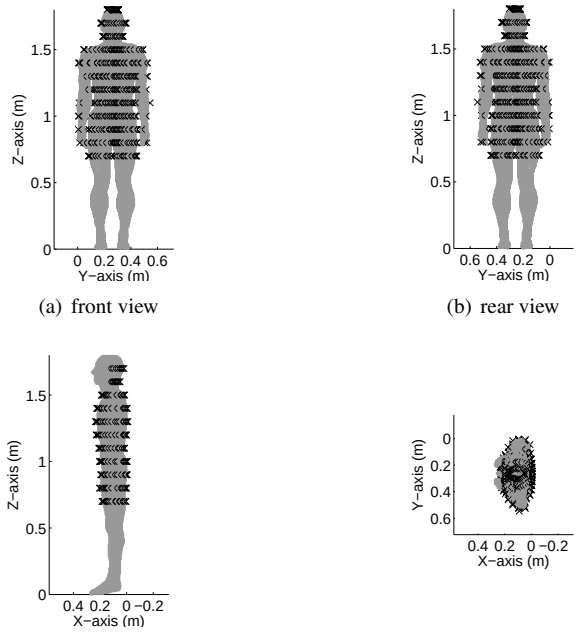

(a) front view (b) rear view

(c) side view (d) top view

Figure 3.3: The VFM (gray) and the potential locations to deploy a PEM (black) on the upper-body.

In this chapter two different exposure situations are studied: first, exposure to one of the detailed models of a base station antenna (BSA), investigated in the previous chapter and second, exposure in realistic, multi-path, far-field environments.

3.3 Uncertainty of Personal exposimeters near a Base Station Antenna

In this section the response of an individual PEM is studied near the detailed model of antenna 1, studied in Chapter 2. The characteristics of this model can be found in Table 2.2 in Section 2.2.3 in the same chapter.

3.3.1 Configuration

The VFM is placed in the same configuration as shown in Figures 2.5 and 2.6 in Section 2.2.5 of Chapter 2. The VFM is facing antenna 1 and is translated from 0.1 m to 5 m from the antenna's frontal surface. Distances closer than 0.1 m are not considered in this section, to ensure a minimal separation between the potential

PEM locations on the front of the upper body (see Fig. 3.3) of 0.09 m. The electric field strengths (E_{rms}^{PEM}) are extracted in the 401 locations on the body of the VFM for separation distances of 0.1, 0.3, 0.5, 1, 2, 3, and 5 m from the antenna 1 for four frequencies emitted by the antenna: 800, 900, 1800, and 2600 MHz, corresponding to the lower Long Term Evolution (LTE) band, the Global system for Mobile communications around 900 MHz band (GSM 900), Digital Cellular Service (DCS), and the upper LTE band, respectively. The E_{rms}^{free} values are presented in Section 2.3 of Chapter 2. These can be used to determine the response $R_i(d, f_n)$ in every potential location *i*=1..401 at distance d from the antenna emitting at frequency f_n, using Equation 3.2.

The distribution of R_i is studied for each frequency f_n at the seven studied distances d from the antenna and averaged over those distances. A first analysis can be performed to estimate the variation of R when the location of a PEM is not fixed. Here all the $R_i(d, f_n)$ values ($7 \times 401 = 2807$ values) are collected in one set of samples for every frequency f_n. The PI_{50} and PI_{95} of these data are measures of the variation in the recordings of a single PEM when it is worn on varying unknown positions on the (upper) body at varying distances from a BSA. In reality the PEM will never be worn on the same spot on the body by different subjects or even by the same subject when characterizing an environment. In a second analysis the $R_i(d, f_n)$ values are averaged over the distance d at each frequency f_n. This provides an average response $R_{av,i}(f_n)$. The variation on this set $R_{av,i}(f_n)$ is an estimation of the variation caused by the unknown positioning of a single PEM on the upper body, near a BSA, whereas the variation of $R_i(d, f_n)$ is caused by both the unknown location of the PEM on the body and the varying distance from the BSA.

In this analysis the $R_i(d, f_n)$ values are determined using Equation 3.2, which assumes that the PEM is able to perfectly register the total electric field strength on the body E_{rms}^{PEM}. This assumes that the operation of the antenna in the PEM is not influenced by the presence of the human body and that there is no coupling between the PEM and the BSA.

3.3.2 Distribution of the Response of Personal Exposimeters Near the Human Body

Figure 3.4 shows the distributions of the PEM's responses on the VFM's upper body for different distances from antenna 1 and the four studied frequencies. The median responses (indicated by bullets) are lower than 1 for all studied frequencies and all studied distances from the antenna. For example at 1 m from the antenna, the median responses are 0.39 (-4.1 dB), 0.37 (-4.3 dB), 0.17 (-7.7 dB), and 0.23 (-6.4 dB) at 800, 900, 1800, and 2600 MHz, respectively. A PEM will thus underestimate the incident fields, when worn by the VFM approaching antenna 1.

There is no clear dependence of the PEM's median response on the frequency, nor on the distance from the antenna. The reason for this underestimation becomes apparent in Figure 3.5. This figure shows the distributions of the responses averaged over the studied distances (2^{nd} analysis) for the front of the VFM (facing the antenna) and for the back of the VFM (shielded from the antenna) separately as a function of frequency. The median values in front of the VFM are close to 1: 0.94 (-0.25 dB), 0.98 (-0.10 dB), 0.72 (-1.4 dB), and 1.5 (1.8 dB) at 800, 900, 1800, and 2600 MHz, respectively. Whereas at the back of the VFM these values are several decibels lower: 0.064 (-12 dB), 0.064 (-12 dB), 0.010 (-20 dB), and 0.015 (-18 dB) at 800, 900, 1800, and 2600 MHz, respectively. The fields recorded by the PEM in front of the VFM are the sum of the incident fields and the scattered fields, which result in an E_{rms}^{PEM} close to or higher than E_{rms}^{free}, whereas at the back of the VFM the incident fields are weakened by the VFM which is in between the source (antenna 1) and the receiver (the PEM placed on the VFM's back). If the two datasets are combined, then the distribution shown in Figure 3.4 for the averaging over the different distances is obtained, resulting in a median underestimation, because the underestimation at the back is more than a factor of 10 higher than the possible overestimation in front of the VFM. The median responses averaged over all the studied distances are listed in Table 3.1 and shown in Figure 3.4. Note that even if the same amount of points in front of and at the back of the VFM are considered (a random selection of 186 points from the 215 points located at the back) the median response is still far below one, for all studied frequencies: namely 0.44 ± 0.013, 0.50 ± 0.0062, 0.18 ± 0.0063, and 0.53 ± 0.021 at 800, 900, 1800, and 2600 MHz, respectively, averaged over 100 repetitions (mean value $\pm$ standard deviation), although the median responses are higher than those listed in Table 3.1.

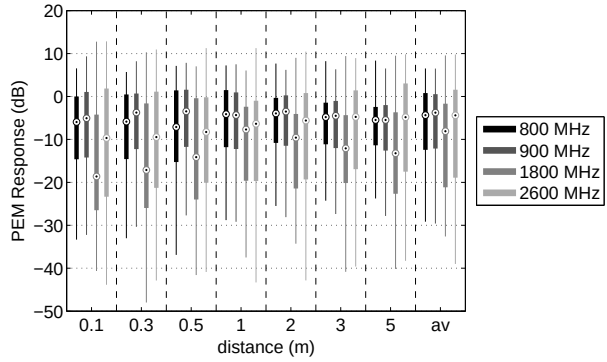

Figure 3.4: Boxplot of the response of a PEM as a function of distance from antenna 1 (see Section 2.2.5 in Chapter 2) and averaged over all 7 distances (denoted av) for the four studied frequencies. The bullet indicates the median value, the colored box the 50% prediction interval, and the lines the upper and lower adjacent values.

The variation on the PEM's response increases with the frequency. This variation is indicated in Figure 3.4 and Table 3.1 by the PI_{50} and PI_{95}, which are all largest at 2600 MHz and increase with frequency, with the exception of the $PI_{95}(f_n)$ which is larger at 800 MHz (29 dB) in comparison with 900 MHz (28 dB). Since the variation on the PEM's responses increases at higher frequencies, in this studied configuration, the measurement uncertainty will be higher as well. This is explained by Figure 3.5, which shows that both the potential overestimation in front of the VFM and the potential underestimation behind the VFM are larger at higher frequencies. The prediction intervals of $R_i(d)$ are equal to or larger than those listed for $R_{av,i}$ (except for the $PI_{50}(R)$ at 800 MHz), because of the averaging over the distance, which already reduces some possible variations.

Table 3.2 lists the upper and lower 50% measurement uncertainties on E_{rms}^{free}, derived using Equations 3.6 and 3.7, using the $p_{25}()$ and $p_{75}()$ of both all R_i samples and the samples $R_{av,i}$ averaged over the studied distances. A similar analysis can be executed for the 95% confidence interval. The lower boundaries of the uncertainty interval u_{low} values range from -39% at 900 MHz for the case where the position of the PEM is fixed ($R_{av,i}$) to -66% at 1800 MHz for the case where the location of the PEM may vary (R_i). The u_{up} values range from 130% at 800 MHz for the uncertainty determined using the distribution of R_i, to 430% at 2600 MHz for the 50% uncertainty determined using the distribution of $R_{av,i}$.

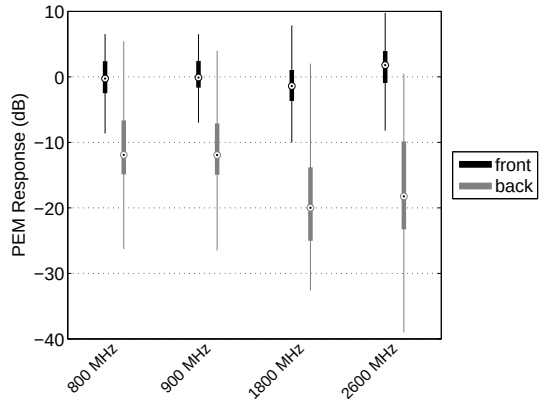

Figure 3.5: Boxplot of the response of a PEM in front of and at the back of the VFM averaged over the 7 studied distances from antenna 1 (see Section 2.2.5 in Chapter 2) for the four studied frequencies. The bullet indicates the median value, the colored box the 50% prediction interval, and the lines the upper and lower adjacent values.

Frequency (MHz)	800	900	1800	2600
	$R_{av,i}$			
p_{50}	0.37	0.42	0.16	0.36
PI_{50}	13 dB	13 dB	19 dB	21 dB
$[p_{25}, p_{75}]$	[0.057,1.2]	[0.061,1.1]	[0.0077,0.68]	[0.013,1.4]
PI_{95}	24 dB	27 dB	33 dB	37 dB
$[p_{2.5}, p_{97.5}]$	[0.012,3.2]	[0.071,3.3]	[0.0012,2.6]	[8.5×10^{-4},4.6]
	R_i			
p_{50}	0.30	0.36	0.057	0.21
PI_{50}	13 dB	13 dB	20 dB	21 dB
$[p_{25}, p_{75}]$	[0.055,0.99]	[0.059,1.1]	[0.0051,0.51]	[0.011,1.3]
PI_{95}	29 dB	28 dB	41 dB	42 dB
$[p_{2.5}, p_{97.5}]$	[0.0056,4.0]	[0.0056,3.6]	[3.3×10^{-4},4.0]	[3.5×10^{-4},5.9]

Table 3.1: Statistics of the responses averaged over all distances in front of the BSA ($R_{av,i}$) and all the studied responses (R_i) as a function of frequency.

3.4 Uncertainty of Personal exposimeters in a realistic far-field environment

The analysis of the measurement uncertainty on E_{rms}^{free} executed in the previous section is valid for a particular exposure situation where an adult approaches a BSA frontally and already provides an estimation of the order of magnitude of uncertainties that may be expected for PEM measurements, but are not usable in a more general exposure situation. Therefore, in this section the response of a PEM

Frequency (MHz)	$R_{av,i}$		R_i	
	u_{low} (%)	u_{up} (%)	u_{low} (%)	u_{up} (%)
800	-45	150	-45	130
900	-39	160	-42	140
1800	-52	350	-66	240
2600	-50	430	-59	340

Table 3.2: Relative boundaries of the 50% measurement uncertainty on E_{rms}^{free}.

(see Equation 3.2) is estimated in far-field exposure scenarios.

3.4.1 Configuration

As mentioned before, The VFM [22] is selected as the human body model or phantom in the numerical simulations that are executed using the FDTD method.

3.4.1.1 Finite-Difference Time-Domain Simulations

The electromagnetic fields (EMFs) inside and around the phantom, which are necessary to calculate R, are estimated using the FDTD method. A simulation domain is defined around the VFM and is bounded by perfectly matched layers (PML). This simulation domain is then discretized using a rectilinear grid. As a rule of thumb, the grid step should be smaller than λ/10 for a stable simulation, with λ the shortest wavelength in the simulation domain [25]. A small grid step is preferred because it will lead to more spatial resolution and thus accuracy, but is accompanied with a small time step due to the Courant limit for stability. A shorter time step will give rise to longer simulations before reaching a steady-state solution and more data processing. The Global System for Mobile Communications (GSM) down link frequency of 950 MHz and the Wireless Fidelity (WiFi) frequency of 2450 MHz have been chosen to determine the response of a PEM in a realistic multi-path environment. A grid step of 1.5 mm has been used, which corresponds to a time step of 2.9×10^{-12} s at 950 MHz and 2.8×10^{-12} s at 2450 MHz. The grid step of 1.5 mm allows the skin of the model to be resolved appropriately [26]. This resulted in a total number of 128 Mcells at 950 MHz and 127 Mcells at 2450 MHz. The commercial tool SEMCAD-X (Schmid & Partner Engineering (SPEAG), Zurich, Switzerland) is selected for the FDTD simulations. The simulations are accelerated using Graphics Processing Unit (GPU)-based computing provided by SPEAG.

3.4.2 Methodology

3.4.2.1 Exposure in Realistic Far-Field Environments

To determine the exposure of the VFM in realistic far-field (FF) environments, a statistically relevant number of exposure conditions or exposure samples has to be selected in each environment [15, 27, 28]. A FF exposure condition consists of a number of plane waves, distributed according to certain statistics. Every exposure condition is characterized by certain variables: the number of incident plane waves in the exposure condition (N_s), and their amplitude (A), polarization (ψ), phase (α), azimuth angle (ϕ), and polar angle (θ). A distribution exists for each of these variables and the parameters of this distribution vary in each environment.

Four exposure scenarios have been defined by [27, 29–31]: 'Urban Macro cell', 'Urban Micro cell', 'Indoor Pico cell', and 'Outdoor-Indoor'. The 'Rural' scenario is added to this set using propagation models from [29, 30, 32]. Table 3.3 lists the variables, their distributions, and the value of their characteristic parameters together with the references to the propagation studies used to determine the parameters. A uniform distribution is chosen for α and ϕ since these parameters depend on the position and orientation of the human body.

Scenario	Urban Macro cell	Urban Micro cell	Indoor Pico cell	Outdoor -Indoor	Rural
Polar angle (θ) [29]					
Asymmetric Double exponential distribution					
Peak polar angle: $\theta_0(^\circ)$	87.8	88.0	88.0	90.2	94.0
Spread parameter $\theta \in [0, \theta_0]$: $\sigma^-(^\circ)$	3.9	4.3	6.9	5.4	8.0
Spread parameter $\theta \in [\theta_0, \pi]$:$\sigma^+(^\circ)$	17.8	8.2	9.4	5.5	5.7
Polarization ψ [29]					
Gaussian Distribution					
Cross polarization ratio (dB)	7.3	11.1	7.0	10.7	6.6
Nr. of paths (N_s) [30]					
Gao distribution					
Maximum number of paths: N_T	22	14	16	21	9
Distribution parameter: η	2.7	3.5	4.7	4.5	4.0
Magnitude E Field (A)**, Shadowing** [31, 32]					
Lognormal distribution					
standard deviation: σ_E(dB)	6	9	6	12	6.0

Table 3.3: Variables of the used exposure scenarios and the distributions that characterize them (taken from [31]).

Normally, every exposure condition requires carrying out an FDTD simulation. To obtain a distribution of a PEM's response in a certain environment, several thousands of simulations would have to be performed in order to obtain a stochastic-representative set of exposure conditions, and a new set of simulations (> 1000) would have to be executed for every environment [15, 27, 28]. In order

to avoid this, a method that reduces the number of FDTD simulations that have to be executed has been developed by Vermeeren et al. [27]. As demonstrated in [27, 28], the required number of simulations can be reduced using the linearity of Maxwell's equations. This linearity allows one to combine different single plane wave (SPW) exposure conditions into one exposure condition with multiple plane waves. Therefore, only SPW simulations are needed. Because every incident plane wave can be decomposed into two orthogonally polarized plane waves, a transverse electric (TE) and transverse magnetic (TM) polarized plane wave, SPW exposure conditions only have to be calculated for these two polarizations. As is shown in Figure 3.6, the direction of incidence of a plane wave toward the phantom can be described in spherical coordinates using two incident angles: the azimuthal and polar angles (ϕ and θ, respectively). The ranges for ϕ and θ have been discretized in order to only perform FDTD simulations for a certain amount of basic incident plane waves. The fields in the 401 studied points around the phantom, induced by this set of incident plane waves are called basic field distributions (BFDs). These can be combined in order to approximate plane waves coming from any direction [27]. Note that the response of a PEM worn by a phantom can be estimated in any FF exposure condition using only a finite set of simulations when using this approach.

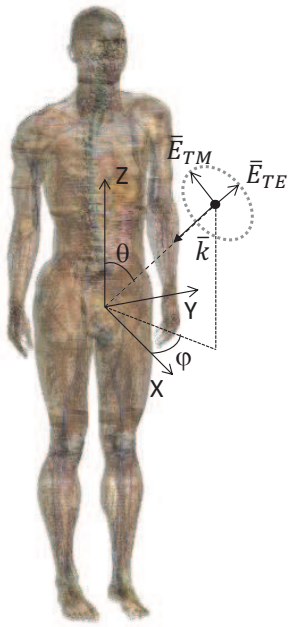

Figure 3.6: The VFM together with the used spherical coordinates system.

Two FDTD simulations with orthogonal incident fields are carried out for every pair (ϕ_i, θ_j), where:

$$\phi_i = i \times \Delta\phi, i = 0, 1, .., N_\phi \tag{3.9}$$

$$\theta_j = j \times \Delta\theta, i = 0, 1, .., N_\theta \tag{3.10}$$

$$\Delta\phi = \frac{2\pi}{N_\phi + 1} \tag{3.11}$$

$$\Delta\theta = \frac{\pi}{N_\theta + 1} \tag{3.12}$$

N_ϕ and N_θ are the number of steps in ϕ and θ and can be increased to reduce the interpolation error that occurs when approximating the fields induced in realistic exposure conditions [27, 28]. We extracted $\overline{E}_{TE,k}(\phi_i, \theta j)$ and $\overline{E}_{TM,k}(\phi_i, \theta j)$, the electric fields on the k^{th} point k=1..401 near the body induced by a TE or TM polarized plane wave, respectively, with incident angles (ϕ_i, θ_j). These are the BFDs, which can be combined to approximate a realistic exposure condition.

FF exposure is considered, so the incident EMFs are composed of a set of plane waves. Every plane wave is characterized by its amplitude (A), phase (α), polarization (ψ), and incident azimuth and polar angles (ϕ and θ, respectively). The resulting electric fields of an exposure sample with N incident plane waves will then be calculated as:

$$\overline{E}_k = \sum_{l=1}^{N} A_j(sin\psi_l.\overline{E}_{TE,k}(\phi_l, \theta_l) + cos\psi_l.\overline{E}_{TM,k}(\phi_l, \theta_l)).e^{i\alpha_l} \tag{3.13}$$

In order to determine $\overline{E}_{TE,k}(\phi_l, \theta_l)$ and $\overline{E}_{TM,k}(\phi_l, \theta_l)$ for all $\phi_l \in [0, 2\pi]$, and $\theta_l \in [0, \pi]$ with ($l = 1..N$), several interpolation methods using the extracted BFDs are applied .

The most straightforward way of doing this is choosing the **nearest neighbour** BFD for every incident plane wave. If $\phi_0 < \phi_1 < .. < \phi_j < \phi < \phi_{j+1} < .. < \phi_{N_\phi} < 2\pi$, and $\theta_0 < \theta_1 < .. < \theta_k < \theta < \theta_{k+1} < .. < \theta_{N_\theta}$:

$$\begin{aligned}
\overline{E}(\phi, \theta) = \quad & \overline{E}(\phi_j, \theta_k) : |\phi_j - \phi| \leq |\phi_{j+1} - \phi| \& |\theta_k - \theta| \leq |\theta_{k+1} - \theta| \\
& \overline{E}(\phi_{j+1}, \theta_k) : |\phi_j - \phi| > |\phi_{j+1} - \phi| \& |\theta_k - \theta| \leq |\theta_{k+1} - \theta| \\
& \overline{E}(\phi_j, \theta_{k+1}) : |\phi_j - \phi| \leq |\phi_{j+1} - \phi| \& |\theta_k - \theta| > |\theta_{k+1} - \theta| \\
& \overline{E}(\phi_{j+1}, \theta_{k+1}) : |\phi_j - \phi| > |\phi_{j+1} - \phi| \& |\theta_k - \theta| > |\theta_{k+1} - \theta|
\end{aligned}$$

Due to the periodic nature of the azimuth coordinate ϕ, all these values are reduced to the interval $[0, 2\pi[$. This method is especially sensitive to the number of BFDs $(N_\phi + 1).(N_\theta + 1)$ [27], but involves only a comparison between scalars and is thus relatively fast, compared to higher-order interpolation methods.

Another approximation method is using a **bilinear interpolation** between the nearest neighbours. In this method, first the nearest angles (ϕ_j, ϕ_{j+1}) and (θ_k, θ_{k+1}) are determined. Second, an interpolation over ϕ is carried out:

$$\overline{E}'(\phi, \theta_k) = \frac{\phi - \phi_j}{\phi_{j+1} - \phi_j}\overline{E}(\phi_j, \theta_k) + \frac{\phi_{j+1} - \phi}{\phi_{j+1} - \phi_j}\overline{E}(\phi_{j+1}, \theta_k) \tag{3.14}$$

$$\overline{E}'(\phi, \theta_{k+1}) = \frac{\phi - \phi_j}{\phi_{j+1} - \phi_j}\overline{E}(\phi_j, \theta_{k+1}) + \frac{\phi_{j+1} - \phi}{\phi_{j+1} - \phi_j}\overline{E}(\phi_{j+1}, \theta_{k+1}) \tag{3.15}$$

Third, an interpolation over θ is carried out:

$$\overline{E}''(\phi, \theta) = \frac{\theta - \theta_k}{\theta_{k+1} - \theta_k}\overline{E}'(\phi, \theta_k) + \frac{\theta_{k+1} - \theta}{\theta_{k+1} - \theta_k}\overline{E}'(\phi, \theta_{k+1}) \tag{3.16}$$

This method is more demanding because it not only requires the determination of the nearest BFDs, but also an interpolation for all the studied potential locations of a PEM on the upper-body. The coefficients, obtained using Equations 3.14 and 3.15, used in the θ-interpolation are different for every (ϕ, θ) couple so they have to be calculated for every interpolation.

A third option is to perform a **bicubic spline interpolation**. The different nature of the two coordinates ϕ and θ forces us to use a different interpolation scheme for both coordinates. The ϕ coordinate is periodic and extends over a domain that is twice as large as the domain for θ, therefore we first perform an interpolation in this dimension. A cubic spline $\overline{s_j}(\phi, \theta_k)$ consists out of different cubic polynomials:

$$\overline{s}_j(\phi, \theta_k), \forall \phi \in [\phi_j, \phi_{j+1}] \tag{3.17}$$

A general expression for these polynomials is given by:

$$\begin{aligned}\overline{s}_j(\phi, \theta_k) = \quad & \overline{E}(\phi_j, \theta_k) + \overline{m}_j(\phi - \phi_j) \\ & + (3\frac{(\overline{E}(\phi_{j+1}, \theta_k) - \overline{E}(\phi_j, \theta_k))}{h_j^2} - 2\frac{\overline{m}_j}{h_j} - \frac{\overline{m}_{j+1}}{h_j})(\phi - \phi_j)^2 \\ & + (-2\frac{(\overline{E}(\phi_{j+1}, \theta_k) - \overline{E}(\phi_j, \theta_k))}{h_j^3} + \frac{\overline{m}_j}{h_j^2} + \frac{\overline{m}_{j+1}}{h_j^2})(\phi - \phi_j)^3\end{aligned} \tag{3.18}$$

For $j = 0..N_\phi$, where $\overline{m}_j$ is the first derivative of $\overline{s}_j$ and $h_j = \phi_{j+1} - \phi_j$. Since $h_0 = h_1 = ... = h_{N_\phi}$, this can be simplified to $h_i = h \ \forall i$. Demanding that $\overline{s}(\phi, \theta_k)$, $\frac{\partial \overline{s}(\phi, \theta_k)}{\partial \phi}$ and $\frac{\partial^2 \overline{s}(\phi, \theta_k)}{\partial \phi^2}$ are continuous, gives rise to following set of equations:

$$h\overline{m}_j + 4h\overline{m}_{j+1} + h\overline{m}_{j+2} = 3(\overline{E}(\phi_{j+2}, \theta_k) - \overline{E}(\phi_{j+1}, \theta_k)) \tag{3.19}$$

For $j = 0..N_\phi - 1$. Leaving us with the choice of 2 extra constraints on the system of equations. We know that the values $\overline{E}(\phi_0, \theta_k)$ and $\overline{E}(\phi_{N_\phi+1}, \theta_k)$ are equal, but

this does not provide continuity for the derivatives. So two more constraints can be applied to the spline:

$$\begin{aligned} \overline{s}'_0(\phi_0, \theta_k) &= \overline{s}'_{N_\phi}(\phi_{N_\phi+1}, \theta_k) \\ \overline{s}''_0(\phi_0, \theta_k) &= \overline{s}''_{N_\phi}(\phi_{N_\phi+1}, \theta_k) \end{aligned} \tag{3.20}$$

This provides us with the matrix equation:

$$\overline{\overline{A}}.\overline{\overline{M}} = \frac{3}{h}\overline{\overline{B}} \tag{3.21}$$

with the matrices:

$$\overline{\overline{A}} = \begin{pmatrix} 1 & 0 & 0 & 0 & \dots & -1 \\ 1 & 4 & 1 & 0 & \dots & 0 \\ 0 & 1 & 4 & 1 & \dots & 0 \\ \vdots & \vdots & \vdots & \vdots & \ddots & \vdots \\ 0 & \dots & 0 & 1 & 4 & 1 \\ 4 & 1 & \dots & 0 & 1 & 0 \end{pmatrix}$$

$$\overline{\overline{M}} = \begin{pmatrix} \overline{m}_1 & \dots & \overline{m}_n \end{pmatrix}^T$$

$$\overline{\overline{B}} = \begin{pmatrix} 0 \\ \overline{E}(\phi_2, \theta_k) - \overline{E}(\phi_0, \theta_k) \\ \vdots \\ \overline{E}(\phi_{j+2}, \theta_k) - \overline{E}(\phi_{j+1}, \theta_k) \\ \vdots \\ \overline{E}(\phi_n, \theta_k) - \overline{E}(\phi_{n-2}, \theta_k) \\ \overline{E}(\phi_2, \theta_k) - \overline{E}(\phi_{n-1}, \theta_k) \end{pmatrix}^T$$

with solution:

$$\overline{\overline{M}} = \overline{\overline{A}}^{-1} \times \frac{3}{h}\overline{\overline{B}} \tag{3.22}$$

The matrices for the interpolation ($\overline{\overline{M}}$ and $\overline{\overline{B}}$) in the ϕ direction can be calculated in advance using a cyclic scheme and using all ϕ_i for every θ_j. They can thus be stored and loaded whenever necessary, speeding up the calculations. Unfortunately, the coefficients for the interpolation along the θ coordinate depend on ϕ and cannot be calculated in advance. Moreover, the spline interpolation in θ is not cyclic and boundary conditions of Equations 3.20 cannot be applied. A cubic spline interpolation using the fields calculated for the six nearest θ_j has been chosen. Both interpolations have to be carried out for every vectorial component of the electric field. The advantage of this scheme is its accuracy [27, 33]. The disadvantage is that the method is slower, because the interpolation coefficients have to be loaded into the random-access memory (RAM), whereas this is not necessary in the nearest interpolation scheme.

3.4.2.2 Response of the PEM

Three analyses can be performed to study the response (R) of a PEM worn on the body.

A first analysis can be performed to estimate a realistic variation of R of a PEM worn on an unknown, varying location on the upper body. In reality the PEM will never be worn on the same spot on the body by different subjects or even by the same subject when characterizing an environment. In this approach, $R_i(f_n)$ is calculated in every point (*i*) for 5000 samples. The distribution of all these $\boldsymbol{R}$ samples (401 locations $\times$ 5000 exposure samples) is then studied. The PI_{50} and PI_{95} of these data are measures of the variance in the recordings of a single PEM when it is worn on varying unknown positions on the (upper) body.

Second, the variation of $\boldsymbol{R_i(f_n)}$ in the individual potential PEM locations (*i*) is studied. For every point (*i*) the median response $R_{med,i}(f_n)$ is determined, together with the 50% prediction intervals $PI_{50,i}(f_n)$ and $PI_{95,i}(f_n)$. This results in 401 values for $R_{med,i}(f_n)$, $PI_{50,i}(f_n)$, and $PI_{95,i}(f_n)$ for which summary statistics can be provided. These are the summary statistics of the response of a PEM worn on the same, unknown position on the upper body.

Third, we consider $\boldsymbol{R_{av,i}(f_n)}$, the response in each potential location averaged over all 5000 exposure samples. the summary statistics of these 401 values provide us with an estimate of the variation of R, caused by the unknown location of the PEM at frequency f_n.

This difference in analysis is necessary because the processing of data registered by PEMs can be executed by a person that has no knowledge of how the exposure was assessed (double-blind) in order to prevent selection bias.

3.4.3 Simulation periods needed to reach steady state in plane-wave simulations

The VFM is exposed by SPWs coming from different directions (ϕ_i, θ_j). Depending on the direction the plane wave is coming from, the simulation time necessary to reach a steady-state solution of the simulation will vary. However, the BFDs are determined at the same delay time (relative phase) and therefore the same simulation time has to be chosen for all plane waves. This simulation time is usually expressed as a number of periods ($T = \lambda$/c). In the simulations used to determine the BFDs, the VFM is surrounded by PMLs, which are applied to the faces of a cuboid surrounding the phantom. The fields recorded after the simulation reaches a steady-state solution are located inside a smaller cuboid, denoted 'Field sensor', shown in green in Figure 3.7. Assuming that the UMPLs have no preference for absorbing a plane wave in a certain direction, the plane wave traveling along the largest diagonal of the cuboid requires the longest simulation time to reach a steady state. In the case of the cuboid shown in Figure 3.7 this is a plane wave incident

from $\theta = 158°$ and $\phi = 238°$.

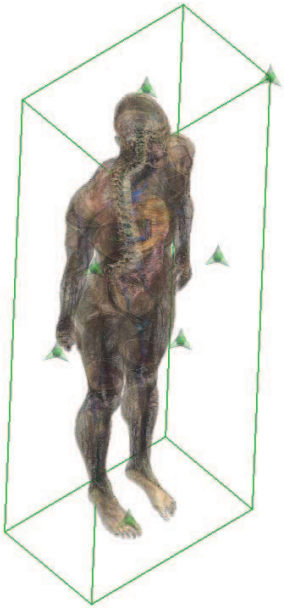

Figure 3.7: The VFM surrounded by the field sensor (green cuboid) in which the EMFs are registered during FDTD simulations. The green arrows indicate the used edge sensors.

In order to determine this simulation time, we have executed a simulation with this incident plane wave at different frequencies between 666 and 5500 MHz, because the most frequently used telecommunication signals (not broadcast signals) are located in between these two frequencies [11]. During this simulation the fields are recorded in every time step of the FDTD algorithm in 21 edge sensors, shown in Figure 3.7 as green arrows. These sensors record a current along their edge, proportional to the electric field strength along that direction at that location. We have placed three orthogonal edge sensors in each plane of the cuboid used to record the steady-state fields and one in the diametrically opposite corner of the cuboid. The current recorded by these edge sensors during the simulation will first equal zero, since the wave has not reached the sensors and will then show some transient behavior, due to reflections from the VFM and absorption in the VFM, and will finally stabilize around a steady-state value. The number of periods necessary to reach this value is stored for every edge sensor and the maximum of these simulation periods is selected. In order to account for possible numerical errors, an

extra period is added as a safety margin. Figure 3.8 shows the obtained number of periods necessary to obtain a steady-state solution of the FDTD simulation. Figure 3.8 also shows the number of periods necessary to cross the cuboid (the field sensor) one, two, or three times diagonally in free space. For the studied frequencies higher than 666 MHz the steady state is reached faster than the time it takes a plane wave to travel through the cuboid twice along its longest diagonal. The commonly used approach to use this value to determine the simulation time is thus conservative and can be used to obtain a steady-state solution in this studied frequency range. In this chapter, we have chosen a simulation time of 20 periods at 950 MHz and 52 periods at 2450 MHz. All FDTD simulations at the same frequency have the same simulation time. These values are conservative enough to obtain a steady-state solution, according to the results presented in Figure 3.8.

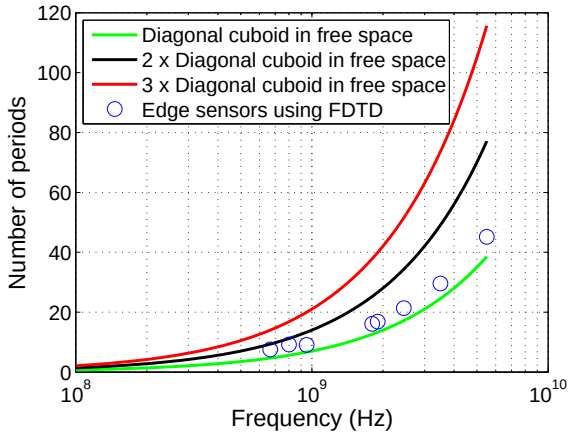

Figure 3.8: The number of periods necessary to obtain a steady-state solution of the studied FDTD simulation.

3.4.4 Validation of the Interpolation Method used to Determine Electric Field Strengths

The goal of our method is to avoid executing an FDTD simulation for every exposure sample. Since the proposed method serves as a substitute for FDTD simulations, the results of the method have to be compared to the results obtained from FDTD simulations. The relative error on the electric field strength is defined as:

$$err = 100 \times \frac{E_{rms,method} - E_{rms,FDTD}}{E_{rms,FDTD}}(\%) \tag{3.23}$$

This validation has already been performed at 950 MHz for another realistic

phantom (the virtual family boy (VFB) [26]) in [33]. There it was found that the spline interpolation scheme is the most accurate method, with a mean relative error on the electric field strengths on a closed surface around the phantom between -1.2% and 0.93% and a standard deviation on this error between -0.31% and 0.05%, using $\Delta\phi = 10°$ and $\Delta\theta = 5°$. Therefore, [27, 33] advise to use the spline interpolation scheme.

This validation is repeated here for the 401 points located near the VFM at 2450 MHz, using a spline interpolation scheme. The results obtained using our method are compared to the results obtained from 60 FDTD-simulated samples in the Urban Macro-cell environment. The electric fields are extracted in the 401 potential PEM locations under consideration, both using the proposed method and directly using FDTD simulations of the same multi-path exposure samples.

The influence of the spacing $(\Delta\phi, \Delta\theta)$ is investigated first. To this aim, we have determined the electric fields in the 401 points under consideration near the VFM using decreasing steps in ϕ and θ and the spline interpolation scheme. The step in the azimuth angle $\Delta\phi$ is changed from $40°$ to $20°$, while the step in polar angle $\Delta\theta$ is decreased from $16°$ to $4°$ in steps of $4°$. Figure 3.9 shows the dependence of the median and 68% confidence interval (CI_{68}), the difference between p_{84} and p_{16} of the error (this corresponds to the same probability as covered by 2 standard deviations of a normal distribution), and of the relative errors determined for the 60 studied validation samples, as a function of the $(\Delta\phi, \Delta\theta)$. The median

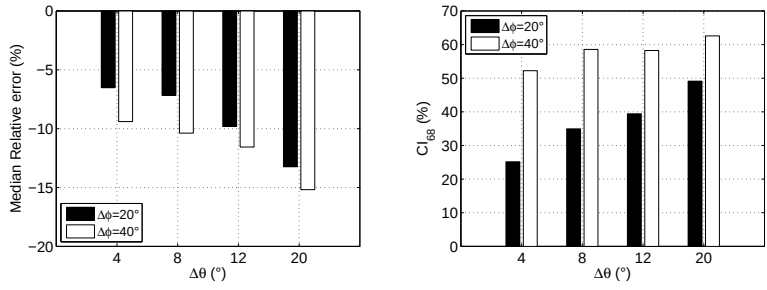

(a) Median (b) CI_{68}

Figure 3.9: Statistics of the relative error (see Eq 3.23 on the estimated E-field strengths at 2450 MHz.

value of the relative error is closer to 0% (the ideal case) if the steps $(\Delta\phi, \Delta\theta)$ are smaller. The confidence intervals also decrease with decreasing angular steps. Notice that the median error is smaller than 0, so the method will on average underestimate the electric-field strengths on the body. This is in line with the findings of [33].

interpolation scheme	Median(err) (%)	CI_{68}(err) (%)
Nearest	-30	150
Bilinear	-25	48
Bicubic Spline	-6.5	36

Table 3.4: Average relative error and standard deviation on the relative errors on the determination of the electric field strengths near the VFM.

Table 3.4 lists the median errors obtained using each of the interpolation schemes and the CI_{68} on these errors. The median error and the 68% confidence interval are closer to zero for the more elaborate, higher-order interpolation schemes. As mentionend before, the nearest interpolation scheme has the lowest memory and computational requirements, but is also associated with the highest relative error, whereas the bicubic spline interpolation has a lower relative error, but requires more data to be loaded in the RAM memory and more computational power. Given the lower relative error, we have chosen to continue using the bicubic spline interpolation in the next section.

3.4.5 Response of a PEM worn on the Human Body in Realistic Far-Field Environments

The electric fields in the 401 points near the VFM are determined in 5000 exposure samples in each of the five considered exposure scenarios, using the bicubic spline interpolation of the BFDs. This number of samples is associated with a variance smaller than 0.2% on the percentiles of R (the set of all R_i values for all exposure samples) between $p_{2.5}(R)$ and $p_{97.5}(R)$ at 2450 MHz in these studied environments. The variance on the percentiles of $R_i(f_n)$ (with *i*=1..401) between $p_{2.5}(R)$ and $p_{97.5}(R)$ is smaller than 3.7% at 2450 MHz in these studied environments. The variance on the percentiles of $R_{av,i}$ between $p_{2.5}(R)$ and $p_{97.5}(R)$ is smaller than 13% at 2450 MHz in these studied environments, which is still small compared to the obtained prediction intervals that are larger than 1.9 dB or 155%, see Table 3.5.

Figure 3.10 shows boxplots for R and $R_{av,i}$ for the five studied environments and the two studied frequencies. The bullets indicate the median value ($p_{50}()$), the box indicates the PI_{50} bounded by the p_{25} and p_{75}, and the whiskers indicate the upper and lower adjacent values (all values in between p_{75} and $p_{75} + 1.5 \times PI_{50}$ and all values between p_{25} and $p_{25} - 1.5 \times PI_{50}$, respectively). For example for 950 MHz in the 'Urban Macro cell' scenario, $p_{50}(R)$ = 0.32 (-6.0 dB) with a PI_{50} = 7 dB (the length of the black box). Table 3.5 lists some of the studied summary statistics of R and $R_{av,i}$. All the median responses are far below 1. The highest median response (0.32) is found for 950 MHz in the 'Urban Macro cell' scenario.

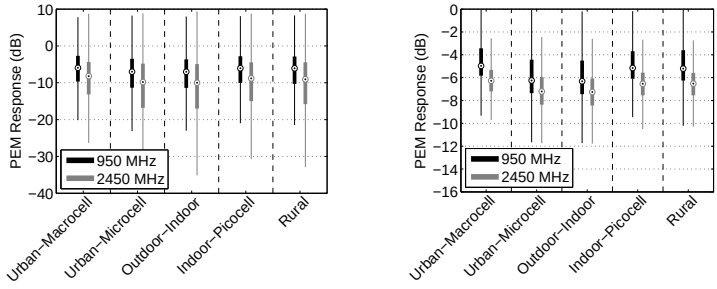

(a) R (b) $R_{av,i}$

Figure 3.10: Boxplots of the PEM's response (R) in five realistic multi-path scenarios for two frequencies.

However, Figure 3.10 (a) shows that there are exposure scenarios in which there is an overestimation of the incident fields. None of the considered potential locations on the body overestimates the incident field strength, when averaged over the exposure samples, see Figure 3.10 (b). The prediction intervals of R are higher than those of $R_{av,i}$, which is to be expected, since the latter only considers variation of the location on the body, where the former also takes into account the variation of the exposure samples. The prediction intervals of R are generally higher at 2450 MHz, compared to 950 MHz, but are smaller for $R_{av,i}$. The variation of the exposure thus causes more variation on the response at the higher frequency, whereas the variation on the body induces less differences. The median responses are smaller at 2450 MHz, compared to 950 MHz, both for R and $R_{av,i}$. The median responses vary in the different environments: $p_{50}(R_{av,i})$ varies from 0.24 to 0.32 at 950 MHz and from 0.19 to 0.24 at 2450 MHz, $p_{50}(R)$ varies from 0.20 to 0.25 at 950 MHz and from 0.10 to 0.15 at 2450 MHz. The prediction intervals are generally in the same order of magnitude in the different environments. For example, the $PI_{95}(R)$ varies from 21 to 24 dB at 950 MHz and from 25 to 30 dB at 2450 MHz.

950 MHz					
	Urban Macro cell	Urban Micro cell	Outdoor-Indoor	Indoor Pico cell	Rural
$R_{av,i}$					
p_{50}	0.32	0.24	0.23	0.31	0.30
PI_{50} (dB)	2.4	2.9	2.9	2.4	2.6
$[p_{25}, p_{75}]$	[0.26,0.45]	[0.18,0.36]	[0.18,0.35]	[0.25,0.43]	[0.24,0.44]
PI_{95} (dB)	11	12	12	11	11
$[p_{2.5}, p_{97.5}]$	[0.13,1.6]	[0.10,1.8]	[0.10,1.8]	[0.12,1.7]	[0.12,1.7]
R					
p_{50}	0.25	0.20	0.20	0.25	0.25
PI_{50} (dB)	7.0	7.8	7.8	7.3	7.4
$[p_{25}, p_{75}]$	[0.11,0.54]	[0.073,0.45]	[0.073,0.43]	[0.098,0.53]	[0.093,0.52]
PI_{95} (dB)	21	24	24	22	23
$[p_{2.5}, p_{97.5}]$	[0.016,2.1]	[0.0097,2.2]	[0.0095,2.2]	[0.012,2.2]	[0.011,2.2]
2450 MHz					
$R_{av,i}$					
p_{50}	0.24	0.19	0.19	0.22	0.22
PI_{50} (dB)	1.9	2.4	2.4	2.0	2.0
$[p_{25}, p_{75}]$	[0.19,0.29]	[0.15,0.25]	[0.14,0.25]	[0.18,0.28]	[0.18,0.28]
PI_{95} (dB)	8.3	10	9.5	7.9	7.4
$[p_{2.5}, p_{97.5}]$	[0.087,0.59]	[0.060,0.62]	[0.063,0.56]	[0.093,0.57]	[0.094,0.52]
R					
p_{50}	0.15	0.10	0.10	0.13	0.12
PI_{50} (dB)	8.8	12	12	11	11
$[p_{25}, p_{75}]$	[0.048,0.37]	[0.021,0.33]	[0.020,0.32]	[0.032,0.36]	[0.026,0.36]
PI_{95} (dB)	25	30	30	28	29
$[p_{2.5}, p_{97.5}]$	[0.0037,1.1]	[0.0011,1.1]	[0.0012,1.0]	[0.0017,1.1]	[0.0013,1.1]

Table 3.5: Statistics of the responses averaged over all the exposure samples ($R_{i,av}$) and all the studied responses (R_i) as a function of frequency.

Figure 3.11 (a) shows boxplots of the median values of the responses in each potential location: $R_{med,i}(f_n)$ with $i = 1..401$. The distribution of the median values is very similar to that of $R_{av,i}$. However, the median values are lower and the difference between the two frequencies is larger than when the $R_{av,i}$ is considered. For example, the median value of $R_{av,i}$ in the 'Urban macro-cell' scenario is 0.32 at 950 MHz and 0.24 at 2450 MHz, while the median values of the $R_{med,i}$ values are 0.23 at 950 MHz and 0.15 at 2450 MHz. Figures 3.11 (b) and (c) show boxplots of the $PI_{50,i}$ and $PI_{95,i}$. The prediction intervals are relatively constant in the different environments: the median $PI_{50,i}$ is around 8 dB at 950 MHz and between 9 and 11 dB at 2450 MHz. The median $PI_{95,i}$ values are close to 12.5 dB at 950 MHz and close to 14 dB at 2450 MHz. The prediction intervals have relatively narrow distributions. For example, all $PI_{95,i}$ values are within 4 dB for all studied scenarios at a given frequency. The same trend where the prediction intervals are larger at the higher frequency is also found in Figures 3.11 (b) and (c).

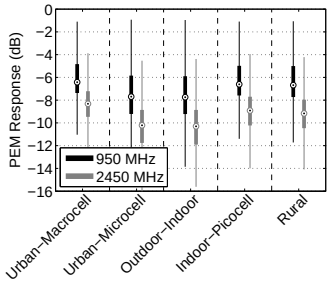

(a) $R_{med,i}(f_n)$

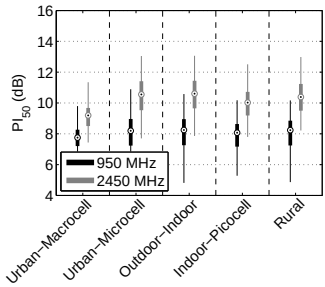

(b) $PI_{50,i}$

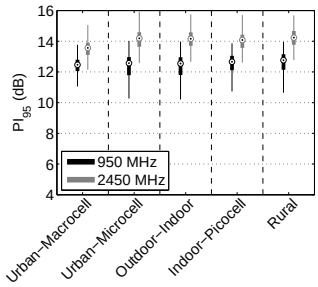

(c) $PI_{95,i}$

Figure 3.11: Boxplots of the summary statistics of the responses $R_i(f_n)$ in five different environments for the two studied frequencies.

3.5 Discussion and Comparison with Literature

In this section, the results obtained in this chapter are discussed and compared to other studies that investigated the influence of the body on the response of PEMs.

3.5.1 Discussion of Obtained Results

The distribution of the response of a PEM worn on the body is studied in two different exposure scenarios: in front of a multi-band BSA and in five realistic, far-field exposure scenarios. The variation of the potential location on the body is modeled as a set of 401 potential locations at 1 cm from the VFM's body surface. The variation of the exposure is modeled as a translation in front of the BSA in the first studied scenario and as variations on the parameters of the far-field exposure scenarios in the second studied case. The variation of the response is quantified using a 50% and 95% prediction interval.

The median values of the studied responses near BSAs are smaller than 1 for all studied frequencies. This indicates that a PEM will underestimate the incident

electric-field strength near a BSA. However, there does not exist a clear dependence on the frequency. The prediction intervals are relatively large, with PI_{50} values between 13 and 21 dB and PI_{95} values between 24 and 42 dB, considering that a prediction interval of 0 dB would allow for perfect measurements. We do find a frequency dependence of the prediction intervals, as they increase with the studied frequency. This is explained by Figure 3.5, which shows the increased difference between the responses in front of the VFM and behind the VFM at higher frequencies, due to the shadowing of the body that faces the BSA. This figure also shows that a frontally worn PEM, when approaching the studied BSA, will have a response close to 1. RF workers approaching these BSA should thus wear their PEM on the front torso.

In order to determine the response in a realistic environment, a method is used [27], which is based upon a set of simulation results (BFDs), where the VFM is exposed by a plane wave incident from the angles (ϕ, θ). The number of necessary periods to reach a steady-state solution in such simulations was investigated for the same simulation setup as used to study the PEM's response. The chosen simulation periods are conservative and ensure a steady-state solution. Our results show that a simulation time interval corresponding to twice the time necessary for a plane wave to travel along the largest diagonal of the field sensor is enough to ensure a steady state solution in the considered sensors. These BFDs are not determined for each pair of incident angles (ϕ, θ), but for a certain set of incident angles (ϕ_i, θ_j). To obtain results for an arbitrary pair (ϕ, θ), different interpolation schemes are investigated: nearest, bilinear, or bicubic spline. The third option results in the lowest median relative error (-6.5%) with the lowest CI_{68} (36%). This result is in line with [27, 28, 33, 34] where the spline interpolation was also found to be the one leading to the lowest relative errors. Moreover, the dependency of the interpolation scheme on the spacing in ϕ and θ is similar. Lower angular steps lead to more accuracy. However, the dependecy on θ seems to be less critical at 2450 MHz than at 950 MHz [33]. The median relative error found in this chapter at 2450 MHz has a negative value, but is larger in magnitude than the one found for 950 MHz in [33], where it was also found that the spline interpolation scheme is the most accurate method, with a mean relative error on the electric field strengths on a closed surface around the phantom between -1.2 % and 0.93% and a standard deviation on this error between -0.31% and 0.05%, using $\Delta\phi = 10^\circ$ and $\Delta\theta = 5^\circ$ at 950 MHz. The higher (in absolute value) relative error in this chapter can be attributed to the higher frequency considered in this chapter and the larger stepsize in ϕ. Moreover, the electric field values in [33] are determined on a cuboid at a distance of at least 5 cm from the VFB, whereas in this chapter the responses are studied at 1 cm from the phantom. In [15] the absolute value of the relative error was studied for points near (between 1 and 5 cm from the phantom) the visible human (VH) [35]. A mean relative error of $3.4 \pm 8.0\%$ was reported at 900 MHz,

while this error increased to $12.9 \pm 23.9\%$ at 2100 MHz using a linear interpolation based on incident angles with ($\Delta\phi = 10°, \Delta\theta = 10°$). The mean abolute value of the relative error using bilinear interpolation found in this chapter at 2450 MHz with ($\Delta\phi = 20°, \Delta\theta = 4°$) is $31 \pm 22\%$, which is higher due to the higher frequency, the fact that all our considered points are at 1 cm from the body and the larger step in ϕ.

The distributions of all the responses (R), the response averaged in every point over all exposure samples ($R_{i,av}$), the median value of the responses in every point ($R_{med,i}$), and the prediction intervals of the responses at a certain location on the body ($PI_{50,i}$ and $PI_{95,i}$), are determined using the aforementioned methods in five different environments. A median underestimation of the incident fields is found in all environments, regardless of the studied response. The summary statistics of these quantities are reported and studied. The response values are in general smaller than 1, corresponding to an underestimation. The incident field strength is underestimated more at the higher studied frequency (2450 MHz). This underestimation is inherent to the distribution of the electric fields around a lossy dielectric. A median response equal to 1 on a surface surrounding a scattering (and absorbing) object can only be obtained if no power is absorbed and all incident power is scattered from the object. In case of the VFM, part of the incident power density is scattered, which can result in a response > 1 in some points (see Fig. 3.10), and part of the power is absorbed by the VFM.

The prediction intervals are higher at 2450 MHz in comparisson to 950 MHz. This dependency of the underestimation and the prediction intervals is studied in [15], where both an adult and child phantom are simulated at three different frequencies: 450, 900, and 2100 MHz. The differences in average responses over all considered positions on the torso of the adult and child model are smaller than 4%. The average responses increase with frequency for both phantoms in [15] and the variation on the responses increases with frequency as well. In our research an opposite behaviour is found for the average and median responses, which both decrease with increasing frequency. Note that in our research we also did not find a clear relationship between the median response and the frequency. However, we do confirm that the prediction intervals increase with frequency. In [20], the average responses and variations on those responses were studied at 4 frequencies: 100, 946, 2140, and 2450 MHz. Differences between the average responses and their variation are observed in [20]. However, no frequency dependence is observed in [20]. In [18] no frequency-dependence was found in the measurements of the response.

The results obtained in Section 3.3 in the GSM 900 DL band near a BSA can be compared to those obtained in section 3.4 in realistic environments at 950 MHz. The median value of the set of all $R_i(d, 900\ MHz)$ values is 0.30 with a PI_{50} of 13 dB and a PI_{95} of 29 dB near the studied BSA, whereas these median values are

between 0.20 and 0.25 with a PI_{50} between 7.0 and 7.8 dB, and a PI_{95} between 21 and 24 dB at 950 MHz in the studied realistic environments. The underestimation is larger in the realistic environments. In front of the BSA, there are still a significant amount of samples that overestimate the incident fields, whereas these samples are rarer in the realistic exposure scenarios, where the azimuth angle of the incident plane waves is uniformly distributed between $[0, 2\pi[$. The prediction intervals are larger in front of the BSA, because of the shadowing which is more pronounced in this exposure scenario. The points at the back of the phantom are shielded severely from the incident EMFs, whereas in the multi-path exposure samples it is uncommon that the full power density is blocked by the human body, since the azimuth is uniformly distributed between $[0, 2\pi[$. In both exposure scenarios, the underestimation and the prediction intervals are unacceptably large for reliable measurements of the incident field strength, which can be obtained using isotropic antennas with an PI_{95} of 3 dB [6, 7]. This is more than 18 dB lower than what we can expect from a PEM worn on the upper body on an unknown location and more than 8 dB lower than the 'best' location found in Figure 3.11(c) ($PI_{95,i}$ = 11 dB).

3.5.2 Overview of Literature and Comparison with Obtained Results

3.5.3 Blas et al., 2007 [36]

The uncertainty caused by the positioning of PEMs was investigated for the first time in [36] using both numerical simulations and measurements of the electric fields in a transverse plane of the human body. A subject was placed in the far-field of BSAs emitting in the GSM 900 DL band and the Frequency Modulated (FM) broadcast band (a frequency band around 100 MHz). The electric fields are registered in front of and behind a human subject facing the BSAs. A similar setup is simulated using FDTD, where the Visible Human (VH) [37] is exposed by a frontally incident, vertically polarized plane wave at one of the frequencies in the considered frequency bands. Variations up to 30 dB (a factor of 10^3) in power density were found for constant incident field strength, both for FM and in the GSM 900 DL band.

3.5.4 Bahillo et al., 2008 [38]

Another numerical study was executed by the same group, where the VH is exposed by plane waves incident from different azimuth angles for a constant polar angle of 90° [38]. The electric field strengths caused by these incident fields in the transverse plane of the VH were studied for FM, GSM 900 DL, and DCS DL. Differences up to 25 and 35 dB in the response of a PEM are observed in the GSM 900

DL band and the DCS 1800 DL band, respectively.

3.5.5 Neubauer et al., 2010 [20]

In [20] numerical simulations were executed using the VH in a model for a realistic environment at 4 different frequencies 100 MHz, 946 MHz, 2140 MHz, and 2450 MHz. Ten potential locations to wear a PEM on the body were modeled as cuboids placed around the waist, on the back, and on the arms of the VH. The statistics of the responses of a PEM worn on the different potential locations are reported for every studied frequency. From the reported percentiles, the PI_{50} and PI_{90} can be calculated.

From these percentiles a PI_{50} of 8.0 dB and a PI_{90} of 18 dB can be determined in the **GSM 900 DL band**. The $PI_{50,i}$ (the prediction intervals on the individual locations) are located around 8 dB at 950 MHz in the studied realistic environments in this chapter, see Figure 3.11 (b).

Considering **WiFi 2G**, in [20], a PI_{50} and a PI_{90} of 9.6 dB and 17 dB, respectively, were found at 2450 MHz. In this chapter, the PI_{50} values on R range from 8.8 dB in the 'Urban Macro cell' scenario to 12 dB in the 'Urban Micro cell' and 'Outdoor-Indoor' scenario. The $PI_{50,i}$ values of the individual potential locations also range from 7 to 14 dB. Our results are thus in the same range as those found in [20].

3.5.6 Iskra et al., 2010 [16]

In [16] numerical simulations are executed using the NORMAN phantom [35] and a rescaled model to serve as a surrogate for a child model. A set of 56 BFDs are simulated at 900 MHz and the response of a PEM at several location either at 1 cm or 5 cm from NORMAN's torso are determined for these BFDs. These responses are then either averaged using certain weights that depend on the considered 'random' environment or collected in one set of samples in the 'stationary' environments. This method does not take into account possible interference on the PEM's location. A median underestimation of the incident power density ($R < 1$) was reported for both phantoms and both distances from the phantom's torso. PI_{50} values of several decibels are reported as well, for example in a 'random-urban' scenario the PI_{50} on the PEMs response at 1 cm from Norman is approximately 2 dB, while in a 'stationary urban' environment, this PI_{50} is about 13 dB.

3.5.7 Iskra et al., 2011 [15]

In a subsequent study by the same authors [15], numerical simulations are again executed using the NORMAN phantom [35] and the same rescaled model to serve as a surrogate for a child model. The simulation results are processed in a similar

way as described earlier in this chapter, in Section 3.4, in order to obtain statistics of the response of a PEM in realistic multi-path exposure scenarios. The study considered 60 randomly chosen points on NORMAN's torso: 30 on the front and 30 on the back. The study reports the mean value of the response in the different individually studied environments and of all the environments combined, together with the PI_{95} values for these distributions, both for the adult phantom and the child model. For example, at 900 MHz a mean R of 0.41 and PI_{95} of 18 dB are determined in an 'Indoor Pico cell' scenario.

Considering the **GSM 900 DL band**, a PI_{95} of 18.5 dB is listed for multi-path, far-field exposure in [15]. The PI_{95} of the set of all R values found in this chapter are somewhat higher, between 21 and 24 dB, than those reported in [15]. Note that [15] did not consider any points on the head, which reduces the variation on the set of all responses. The $PI_{95,i}$ values of the individual locations found in this study are generally lower, around 12.5 dB.

In [15] the response of a PEM is also studied at 2100 MHz, a frequency near the **DCS 1800 DL band** and the **WiFi 2G** band. The mean values of the 95% prediction interval over different (combinations of) positions of isotropic PEMs on the front and back of the body are 25.6 dB for a single PEM at 2100 MHz. The PI_{95} values values on the set R of responses R_i found in this chapter at 2450 MHz, range from 25 to 30 dB. However, on the individual locations studied in this chapter (see Figure 3.11 (c)) the PI_{95} values are smaller, between 12 and 16 dB. The simulated PI_{95} values in this chapter near a BSA emitting at 1800 MHz are 33 dB for $R_{i,av}$ and 41 dB for the full set of responses.

3.5.8 Bolte et al., 2011 [18]

In [18], the uncertainty on a PEM's response caused by the varying incident angle of the EM fields was investigated in eight different frequency bands (with GSM 900 DL, DCS 1800 DL, and WIFi 2G amongst them), using a PEM worn on a fixed position on a subject's hip exposed by a constant field strength incident from one direction. The subject was then rotated in order to study the variation caused by a changing direction of incidence. The incident fields were either horizontally or vertically polarized. All the reported PI_{50} values on the response of the exposimeter found in [18] are larger than 3 dB and range up to 21 dB for the PI_{50} for a Universal Mobile Telecommunications System (UMTS) up-link under vertically polarized exposure. The underestimation of PEMs was confirmed in [18], since only DCS 1800 DL was found to have a median overestimation (for horizontally polarized incident plane waves and a PEM worn on the right hip), whereas all other studied frequency bands showed an underestimation. The cross talk in the device used in [18] might explain the elevated response in the DCS 1800 DL band.

In the **GSM 900 DL band** PI_{50} values of 6.5 and 15.5 dB are reported for V and H polarized incident plane waves, respectively. In this chapter, the re-

sponse of a PEM worn in the body in front of a BSA antenna is studied and PI_{50} values of 13 dB are obtained, both for the distribution of R_i and $R_{i,av}$ at 900 MHz. These prediction intervals found near the BSA, are larger than those reported in [18], because in this chapter other directions of incidence are considered as well, whereas near a BSA the shadowing effect increases the variation on the response, see Fig. 3.5. The values of the PI_{50} that are found in the realistic multi-path environments, are more comparable to those presented in [18]. In this chapter, a $PI_{50}(R)$ between 7.0 and 7.8 dB is found at 950 MHz in the studied realistic environments, see Table 3.5, and the $PI_{50,i}$ (the prediction intervals on the individual locations) are located around 8 dB at 950 MHz, see Figure 3.11 (b).

Only [18] investigated the variation of R in the **DCS 1800 DL band**. Median responses 2.8 and 0.56 are reported, for H and V polarization, respectively, with corresponding PI_{50} values of approximately 5 dB and 20 dB. Near the BSA, we found a median response of 0.06 for the full set of R values and 0.16 for $R_{av,i}$. We do not find an overestimation, such as reported in [18], but both polarizations are emitted simultaneously by the (cross-polarized) BSA. Note that Figure 3.4 also shows some locations with an average overestimation at 1800 MHz. The PI_{50} values we found are 19 dB for $R_{i,av}$ and 20 dB for the full set of responses. These values are close to what was measured in [18] for vertical polarization.

Considering **WiFi 2G**, PI_{50}'s of 9 dB and 19 dB were measured in the WiFi band in [18], for H and V polarization, respectively. In this chapter, the PI_{50} values on the set of responses R_i range from 8.8 dB in the 'Urban Macro cell' scenario to 12 dB in the 'Urban Micro cell' and 'Outdoor-Indoor' scenario. The $PI_{50,i}$ values of the individual potential locations also range from 7 to 14 dB. Our results are thus in the same range as those found in [18].

3.5.9 Overview

None of the aforementioned studies considers LTE, since this frequency band was not in use on the moment of publication of these studies.

Figure 3.12 shows an overview of the prediction intervals obtained from literature and those presented in this chapter. The horizontal dashed lines show the uncertainty on power density values measured in free-space using an isotropic probe. A value of 3 dB is commonly used as expanded measurement uncertainty, which corresponds to a PI_{95}, for this setup [5–7]. Using this value for the PI_{95} (3 dB) we can also obtain a value for the PI_{50} of 1.3 dB, assuming a normal distribution of the uncertainty [6]. The bars indicate the values of the different prediction intervals. The prediction intervals of $R_{i,av}$ near the BSA are denoted as 'near BSA'. The values shown for 'unknown loc., best env.' correspond to the lowest prediction intervals of the full set of responses found in the different studied realistic environments. The values shown for 'known loc., all env.' are an average

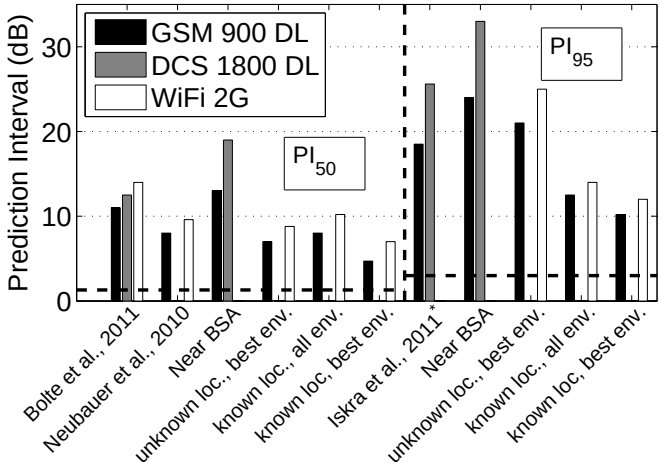

Figure 3.12: Overview of Prediction Intervals of single PEMs responses. The dashed line corresponds to the measurement uncertainty of isotropic field measurements setup [5–7] and is 1.3 dB for the PI_{50} and 3 dB for the PI_{95}.
* Value at 2100 MHz shown as DCS 1800 DL.

of all the 5 median values shown in Figure 3.11 (b) and (c), whereas 'known loc., best env.' is the lowest adjacent value shown in the same figure. Compared to the uncertainty on the free-space measurements, the prediction intervals on the PEMs responses are relatively high. None of the shown bars is near to the horizontally dashed lines, that correspond to the measurement uncertainty in free-space measurements. This relatively high measurement uncertainty in PEM measurements is the most prominent disadvantage of using PEMs for personal exposure measurements. In the following chapters we investigate how these prediction intervals and thus the measurement uncertainty can be reduced.

3.6 Conclusions

The response of a single, body-worn personal exposimeter (PEM) is studied in two different exposure scenarios: near a multi-band, base station antenna (BSA) and in five realistic, far-field environments. This response provides the relationship between the electrical field strengths measured by a PEM and the incident field strengths. In order to model a PEM worn on the body, a set of 401 points located near the body of a heterogeneous phantom are considered. Since both the location of a PEM and the exposure may vary, the response is studied as a statistical variable, with a certain distribution, from which prediction intervals can be obtained. In this chapter the 50% and 95% prediction intervals of a PEM's response

are studied.

The distribution of the response is determined for 4 frequencies near a previously studied BSA, see Chapter 2. The numerical simulations show that a PEM will on average underestimate the incident fields near a BSA, due to the shadowing of the body, and will exhibit relatively large prediction intervals. The 50% prediction intervals range from 13 dB at 800 MHz to 21 dB at 2600 MHz, averaged over all separation distances between the BSA and the phantom, while the 95% prediction intervals range from 14 dB at 800 MHz up to 37 dB at 2600 MHz, averaged over all studied distances in front of the BSA.

The PEM's response is also determined in 5 realistic, far-field exposure scenarios. To this aim, we adapted a method which was previously used to determine the whole-body averaged specific absorption rate in realistic environments, in order to determine the electric fields near the body. This method uses a limited set of finite-difference time-domain (FDTD) simulations to determine the exposure in any far-field exposure condition. The exposure values are not determined for every pair of incident angles (ϕ, θ), but for a certain set of incident angles (ϕ_i, θ_j). To obtain results for an arbitrary pair (ϕ, θ), different interpolation schemes are investigated: nearest, bilinear of bicubic spline. A bicubic spline was chosen as the most accurate with a median relative error of -6.5%. Two different approaches are used to study the variation on the PEM's responses in these environments: the response of a PEM on an unknown location is studied by studying the statistics of the PEM's responses on the different studied locations in all exposure scenarios. The response of a PEM on a fixed location is studied by investigating the responses of a PEM in the potential locations individually. In both cases, the results show an average underestimation of the incident electric fields in all environments and relatively large prediction intervals.

An overview of literature that studied a PEM's response is presented in this chapter. The results found in other studies correspond well to our findings: all studies seem to conclude that PEMs underestimate the incident fields and that their prediction intervals are relatively large. We have compared these values to commonly listed values for free-space measurements using an isotropic field probe and conclude that all studies show that PEM measurements are confronted with unacceptably large measurement uncertainties in terms of prediction intervals on the incident electric field strength. The next chapters in this book will focus on quantifying and reducing this measurement uncertainty.

References

[1] World Health Organization (WHO). *WHO Research Agenda For Radiofrequency Fields*. Technical report, 2010.

[2] E van Deventer, E van Rongen, and R Saunders. *WHO research agenda for radiofrequency fields.* Bioelectromagnetics, 32(5):417–21, 2011.

[3] Cisco. *Cisco Visual Networking Index: Global Mobile Data Traffic Forecast Update, 20132018.* White paper, Technical report, 2013.

[4] ICNIRP International Commission on Non-Ionizing Radiation Protection. *Guidelines for limiting exposure to time-varying electric, magnetic, and electromagnetic fields (up to 300 GHz).* Health physics, 74:494–522, 1998.

[5] S Aerts, D Deschrijver, L Verloock, T Dhaene, L Martens, and W Joseph. *Assessment of outdoor radiofrequency electromagnetic field exposure through hotspot localization using kriging-based sequential sampling.* Environmental Research, 126:184–91, 2013.

[6] CENELEC (European Committee for Electrotechnical Standardization). *TC 106x WG1 EN 50492 in situ. Basic standard for the in-situ measurement of electromagnetic field strength related to human exposure in the vicinity of base stations. Brussels, Belgium*. 2008.

[7] W Joseph, L Verloock, F Goeminne, Günter Vermeeren, and Luc Martens. *Assessment of RF exposures from emerging wireless communication technologies in different environments.* Health Physics, 102:161–172, 2012.

[8] John F B Bolte and Tessa Eikelboom. *Personal radiofrequency electromagnetic field measurements in The Netherlands: exposure level and variability for everyday activities, times of day and types of area.* Environment international, 48:133–42, November 2012.

[9] P Frei, E Mohler, G Neubauer, G Theis, A Bürgi, J Frölich, C Braun-Fährländer, J Bolte, M Egger, and M Röösli. *Temporal and spatial variability of personal exposure to radio frequency electromagnetic fields.* Environmental research, 109(6):779–85, August 2009.

[10] W Joseph, G Vermeeren, L Verloock, M Masache Heredia, and L Martens. *Characterization of personal RF electromagnetic field exposure and actual absorption for the general public.* Health physics, 95(3):317–30, September 2008.

[11] W Joseph, P Frei, M Roösli, G Thuróczy, P Gajsek, T Trcek, J Bolte, G Vermeeren, E Mohler, P Juhász, V Finta, and L Martens. *Comparison of personal radio frequency electromagnetic field exposure in different urban areas across Europe.* Environmental research, 110(7):658–63, October 2010.

[12] M Röösli, P Frei, E Mohler, C Braun-Fahrländer, A Bürgi, J Fröhlich, G Neubauer, G Theis, and M Egger. *Statistical analysis of personal radiofrequency electromagnetic field measurements with nondetects.* Bioelectromagnetics, 29(6):471–8, September 2008.

[13] G Neubauer, M Feychting, Y Hamnerius, L Kheifets, N Kuster, Io Ruiz, J Schüz, R Uberbacher, J Wiart, and M Röösli. *Feasibility of future epidemiological studies on possible health effects of mobile phone base stations.* Bioelectromagnetics, 28(3):224–30, April 2007.

[14] M Röösli, P Frei, J Bolte, G Neubauer, E Cardis, M Feychting, P Gajsek, S Heinrich, W Joseph, S Mann, L Martens, E Mohler, R C Parslow, A H Poulsen, K Radon, J Schüz, G Thuroczy, J F Viel, and M Vrijheid. *Conduct of a personal radiofrequency electromagnetic field measurement study: proposed study protocol.* Environmental health : a global access science source, 9:23, January 2010.

[15] S Iskra, R McKenzie, and I Cosic. *Monte Carlo simulations of the electric field close to the body in realistic environments for application in personal radiofrequency dosimetry.* Radiation Protection Dosimetry, 147(4):517–27, 2011.

[16] S Iskra, R McKenzie, and I Cosic. *Factors Influencing Uncertainty in Measurement of Electric Fields Close to the Body in Personal RF Dosimetry.* Radiation Protection Dosimetry, 140(1):25–33, 2010.

[17] A Thielens, H De Clercq, S Agneessens, J Lecoutere, L Verloock, G Declercq, Fand Vermeeren, E Tanghe, H Rogier, R Puers, L Martens, and W Joseph. *Personal distributed exposimeter for radio frequency exposure assessment in real environments.* Bioelectromagnetics, 34(7):563–7, 2013.

[18] J F B Bolte, G van der Zande, and J Kamer. *Calibration and uncertainties in personal exposure measurements of radiofrequency electromagnetic fields.* Bioelectromagnetics, 32(8):652–63, December 2011.

[19] O Lauer, G Neubauer, M Röösli, M Riederer, P Frei, E Mohler, and J Fröhlich. *Measurement setup and protocol for characterizing and testing radio frequency personal exposure meters.* Bioelectromagnetics, 33:75–85, 2012.

[20] G Neubauer, S Cecil, W Giczi, P Preiner, J Frölich, and Martin Röösli. *The Association Between Exposure Determined by Radiofrequency Personal Exposimeters and Human Exposure: A Simulation Study.* Bioelectromagnetics, 31(7):535–45, 2010.

[21] R P Findlay and P J Dimbylow. *Effects of posture on FDTD calculations of specific absorption rate in a voxel model of the human body.* Physics in medicine and biology, 50(16):3825–35, August 2005.

[22] A Christ, W Kainz, E G Hahn, K Honegger, M Zefferer, E Neufeld, R Rascher, W Janka, W Bautz, J Chen, B Kiefer, P Schmitt, H P Hollenbach, J Shen, M Oberle, D Szczerba, A Kam, J W Guag, and N Kuster. *The Virtual Family–development of surface-based anatomical models of two adults and two children for dosimetric simulations.* Physics in medicine and biology, 55(2):N23–38, January 2010.

[23] C Gabriel, S Gabriel, and E Corthout. *The dielectric properties of biological tissues: I. Literature survey.* Physics in medicine and biology, 41(11):2231–49, November 1996.

[24] F Declerq, A Georgadis, and H Rogier. *Wearable aperturecoupled shorted solar patch antenna for remote tracking and monitoring applications.* Proceedings of the 5th European Conference on Antennas and Propagation (EUCAP). Rome, Italy., 2011.

[25] J W Hand. *Modelling the interaction of electromagnetic fields (10 MHz-10 GHz) with the human body: methods and applications.* Physics in medicine and biology, 53(16):R243–86, August 2008.

[26] A Christ, T Samaras, A Klingenböck, and N Küster. *Characterization of the electromagnetic near-field absorption in layered biological tissue in the frequency range from 30 MHz to 6,000 MHz.* Physics in Medicine and Biology, 51:4951–4965, May 2006.

[27] G Vermeeren, W Joseph, and L Martens. *Whole-body SAR in spheroidal adult and child phantoms in realistic exposure environment*. Health Physics, 94(June):345–354, 2008.

[28] G Vermeeren, W Joseph, and L Martens. *Statistical multi-path exposure method for assessing the whole-body SAR in a heterogeneous human body model in a realistic environment.* Bioelectromagnetics, 34(3):240–51, April 2013.

[29] K Kalliola, K Sulonen, H Laitinen, J Krogerus, and P Vainikainen. *Angular Power Distribution and Mean Effective Gain of Mobile Antenna in Different Propagation*. IEEE Transactions on Vehicular Technology, (September):823–838, 2002.

[30] X Zhao, J Kivinen, P Vainikainen, and K Skog. *Propagation Characteristics for Wideband Outdoor*. IEEE Journal on Selected Areas in Communications, 20(April):507–514, 2002.

[31] C Olivier. *Characterisation of the Electromagnetic Radiation close to Broadcast and Wireless Communication Antennas.* PhD Book, Ghent, Belgium, 2007.

[32] H Asplund, A A Glazunov, A F Molisch, and K I Pedersen. *The COST 259 Directional Channel Model - Part II : Macrocells*.

[33] G Vermeeren. *Electromagnetic Human-Body Absorption Due to Near-Field Exposure from Hand-Held Wireless Devices and Multi-Path Exposure from Base Station Antennas.* PhD Book, Ghent, Belgium, 2014.

[34] A Thielens, G Vermeeren, W Joseph, and L Martens. *Stochastic Method for the Determination of the Organ-specific Averages SAR in Realistic Environments at 950 MHz.* Bioelectromagentics, 34(7):549–562, 2013.

[35] P J Dimbylow. *FDTD calculations of the whole-body averaged SAR in an anatomically realistic voxel model of the human body from 1 MHz to 1 GHz.* Physics in medicine and biology, 42:479–90, 1997.

[36] J Blas, F A Lago, P Fernández, R M Lorenzo, and E J Abril. *Potential exposure assessment errors associated with body-worn RF dosimeters.* Bioelectromagnetics, 28(7):573–6, October 2007.

[37] V Spitzer, MJ Ackerman, AL Scherzlinger, and D whitlock. *The visible human male: A technical report.* J Am Med Inform Assoc, 2:118–130, 1996.

[38] A Bahillo, J Blas, P Ferna, Solar, R M Lorenzo, S Mazuelas, and E J Abril. *E-Fiels Assessment Errors Associated with RF Dosemeters for Different Angles of Arrival*. Radiation Protection Dosimetry, 132(October):51–56, 2008.

4

Personal Exposure Assessment to RF EMFs using Multiple Conventional Personal Exposimeters

4.1 Introduction

An increasing number of studies [1–7] aim to quantify exposure of the human body to radio-frequency (RF) electromagnetic fields, due to the increasing number of RF sources in the environment and the possible adverse health effects associated with this exposure. The quantity used in these studies is the RF electric field incident on the human body [8]. Personal exposimeters (PEMs) are the devices used to quantify one's personal exposure to RF electromagnetic fields. These devices have the advantage that they can be worn on the body and thus enable a measurement of the electric fields on the same location as that of the subject wearing the device. However, PEMs are faced with relatively large uncertainties as shown in Chapter 3 and [9–14], caused by two effects: the uncertainty of the position of the PEM on the body and the varying multi-path RF fields incident on a subject. Although PEMs are faced with large measurement uncertainties, they are widespread amongst the research groups that are involved in exposure assessment. Therefore it is worthwhile investigating the best practice for using these devices and how an improvement of the exposure assessment can be made using the existing PEMs.

Chapter 3 and [9–13] showed that a PEM will on average underestimate the incident electric-field strengths due to body shadowing and absorption. In order to

take this effect into account and determine the real response of a PEM, an on-body calibration of a PEM can be executed. The methodology for such an on body calibration has been described in [10], where a PEM was calibrated on a male subject in an open area test site. However, it is unclear from [10] how these calibration results can straightforwardly be used for measurements in real environments. Not every possible polarization can be measured during a calibration and not every one of those polarizations will be equally likely to occur in a real exposure situation. In [10] every calibrated polarization was treated as being equally likely to occur, while studies like [15] show that this is not the case. In order to use the calibration data to process real measurement data, a statistical treatment of the polarization will be necessary.

Moreover, [10] and [13] indicate that when a subject is equipped with two PEMs worn on opposite sides of the body: front and back [13] or both hips [10], the measurement uncertainty on the incident field strength can be reduced. Most groups that use PEMs for exposure studies possess more than one PEM and thus are able to equip a volunteer with multiple PEMs. Taking these results into account would help epidemiologists to better estimate the exposure of their volunteers. The same holds for employers who measure the RF exposure of their employees.

Data measured using PEMs often have a large fraction of non-detects or left-censored data due to the relatively large detection limits of the PEMs [3, 6, 16]. The most widely applied technique to deal with these censored data is Robust Regression on Order Statistics (ROS) [6, 17]. This method fits a lognormal distribution to the (normalized probability of the) data above the detection limit. However, as is pointed out in [16, 18] there is a non-negligible crosstalk present in the measurements using PEMs. The univariate summary statistics, which are usually provided [6, 16] for the individual frequency bands, are therefore not the summary statistics of the real incident signal, if the output of the PEMs is significantly confounded by crosstalk. Moreover, it is not unrealistic to assume that certain signals will be correlated anyway [19], since they are frequently emitted from the same locations of base stations. This implies that, besides a correlation between data measured in the same frequency band, there will be a significant correlation between measurements in different frequency bands using PEMs, which means that the data are not univariate. Therefore, a *multivariate approach* is proposed here, where besides the summary statistics for the individual frequencies, the multivariate summary statistics: $\overline{\overline{\mu}}$ and $\overline{\overline{\Sigma}}$, the mean vector and the covariance matrix, respectively, are provided as well.

The goal of this chapter is to describe the calibration of two PEMs simultaneously in an anechoic chamber and confirm that a combination of measurements with multiple PEMs worn on the body can reduce the variation on measured incident field strength in realistic environment. To this end, two commercial, commonly used PEMs are calibrated on a subject, following the routine proposed

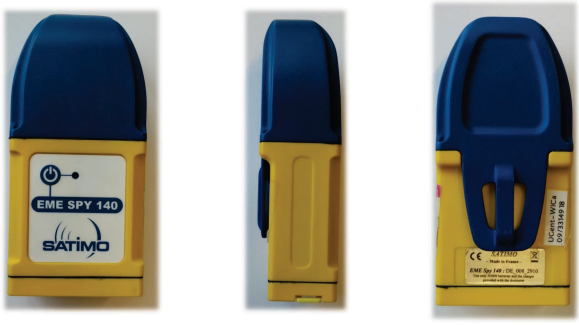

Figure 4.1: The EME SPY 140 (Satimo, Brest, France).

in [10] and [14], who is rotated in an anechoic chamber under exposure from 847 MHz to 5.9 GHz. We also aim at determining the crosstalk between the different bands using this calibration. Afterwards, the same volunteer on which the PEMs are calibrated performs measurements in a real environment, using the same setup, which allows for an estimation of the uncertainty on the measurements. To this end, the variation on the response of a PEM is estimated in a realistic exposure scenario. These data are then first processed using ROS [6] and then used to provide *multivariate summary statistics*.

4.2 Materials and Methods

On-body calibration measurements using two PEMs placed on the body are performed in an anechoic chamber.

4.2.1 Personal Exposimeter

The type of PEM used in this study is the EME SPY 140 (Satimo, Brest, France). This state-of-the-art PEM and its predecessors have frequently been used in epidemiological investigations of personal exposure to RF electromagnetic fields [1–7]. Figure 4.1 shows an example of an EME SPY 140.

The EME SPY 140 PEMs have a detection limit of 0.005 V/m from 88 MHz to 3 GHz and 0.02 V/m above 3 GHz, a maximal sample rate of 0.25 Hz, and measure the following frequency bands [10, 16]: Frequency Modulated Radio (FM), a first television broadcasting channel denoted TV3, Terrestrial Trunked Radio (TETRA), a second television broadcasting band denoted TV4 & 5, Global System for Mobile communications at 900 MHz (GSM 900) uplink (UL), GSM 900 downlink (DL), Digital Cellular Service (DCS) UL, DCS DL, Digital Enhanced Cordless Telecommunications (DECT), UMTS UL, UMTS DL, Wireless Fidelity

(WiFi) 2G, Worldwide Interoperability for Microwave Access (WiMax), and WiFi 5G.

4.2.2 Calibration in the Anechoic Chamber

4.2.2.1 Setup in the Anechoic Chamber

The calibrations are executed using the routine proposed in [10]. However, the measurements in this study are performed in an anechoic chamber instead of an open area test site. The anechoic chamber is designed to provide sufficient damping of the non-direct signals for frequencies > 800 MHz and is thus a better option for the calibration. Therefore, only the frequency bands that can be recorded by the PEM and that are fully located > 800 MHz are investigated. FM, TV 3, 4, and 5, and TETRA are thus not considered in this study. Table 4.1 lists the frequency bands studied and the centre frequency of the signals that are used during measurements. A network analyser, Agilent N5242A PNA-X (Agilent, Santa Clara, CA, USA), is used to deliver a signal with a bandwidth of 10 MHz at a constant input power to a linearly polarized transmitting antenna (TX) with a reflection coefficient lower than -10 dB (a factor of 0.1) from 846 MHz to 6 GHz. A bandwidth of 10 MHz is used in order to avoid non-detects by the EME SPY 140 due to a too small bandwidth and to have a signal around the center frequency, which is fully located in the bands listed in Table 4.1.

	Name	Frequency Range (MHz)	Measured Center Frequency (MHz)	E_{RMS}^{free} (V/m)	
				$\overline{\text{H}}$	$\overline{\text{V}}$
1	GSM 900 UL	880-915	897.5	0.12	0.12
2	GSM 900 DL	925-960	942.5	0.14	0.16
3	DCS UL	1710-1785	1747.5	0.14	0.15
4	DCS DL	1805-1880	1842.5	0.12	0.12
5	DECT	1880-1900	1890	0.11	0.12
6	UMTS UL	1920-1980	1950	0.11	0.12
7	UMTS DL	2110-2170	2140	0.13	0.14
8	WiFi 2G	2400-2500	2450	0.12	0.13
9	WIMAX	3400-3800	3500	0.12	0.12
10	WiFi 5G	5150-5850	5500	0.046	0.036

Table 4.1: Studied frequency ranges, their measured central frequencies, and incident electric fields averaged over the subject's height (191 cm) for an input power of 10 mW in the horizontally (H) and vertically (V) polarized TX, using a NARDA broadband field meter.

As Figure 4.2 (a) shows, the TX is positioned in the far field of a rotational platform on the other side of the anechoic chamber. The distance between the TX and the axis of the rotational platform is 4.5 m. In this study two orthogonal

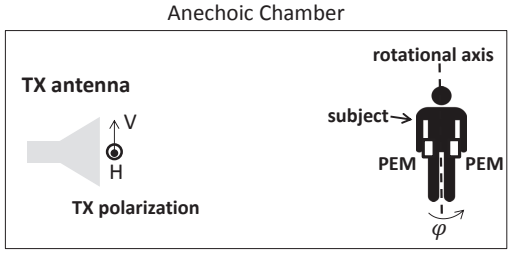

(a) Illustration of the calibration setup in the anechoic chamber. The rectangles indicate the locations of the PEMs on the subject's hip.

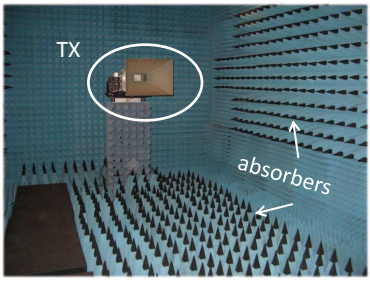

(b) TX in the anechoic chamber.

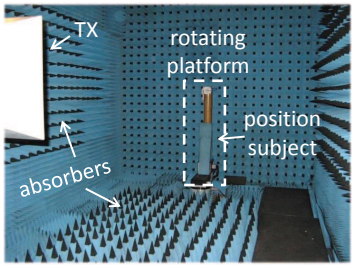

(c) Rotating Platform

Figure 4.2: Setup in the anechoic chamber.

polarizations of the TX are studied: a horizontal polarization (H) parallel to the floor of the anechoic chamber and perpendicular to the rotational platforms axis of rotation, and a vertical polarization (V) parallel to the rotational platforms axis of rotation. Figures 4.2 (b) and (c) show images of the actual setup in the anechoic chamber without the subject present.

Two types of measurements are performed in the calibration. First, free-space measurements of the incident electric fields using a Narda NBM-550 broadband field meter (Narda, Hauppauge, NY, USA) are carried out. Second, on-body measurements using two EME SPY 140 PEMs, placed on both of the subject's hips are executed.

4.2.2.2 Free-space measurements

The goal of measurements with PEMs is to determine the incident electric-field strength. This field strength is to be averaged over the human body [8]. The incident electric field is measured at different heights (from 0.5 to 2 m) from the

platform. The free-space incident electric field E_{RMS}^{free} is then averaged over the subject's total body height (h_{tot}).

4.2.2.3 On-body Measurements

After the determination of E_{RMS}^{free}, a 25-year-old male subject is placed on the rotational platform in the anechoic chamber. The subject has a h_{tot} of 1.91 m, a mass of 83 kg and thus a body mass index of 22.8 kg/m^2. The subject wears a casual outfit in order to emulate a real-life situation in which the subject might wear the PEMs. He does not carry electronic devices or metal(lized) objects.

Two EME SPYs are placed on both hips of the subject who stands on the rotating platform in upright anatomical position (see Figure 4.2). The subject is then rotated twice, once for each polarization of the TX (H and V), from $0°$ to $360°$ in the azimuthal angle (ϕ) in steps of $45° \pm 0.1°$. The TX emits a constant power at frequency f_j, thus inducing a constant $E_{RMS}^{free}(f_j)$. Both PEMs will measure an electric field value, denoted by $E_{RMS,ik}^{body}(f_j, \phi)$, with *i* = left or right hip and *k* the number of the frequency band in which the signal is recorded, as indicated in Table 4.1. Multiple values of $E_{RMS,ik}^{body}(f_j, \phi)$ are measured for every angle ϕ in order to include the effects of the subject's small movements and breathing on the measurements. $E_{RMS,ik}^{body}(f_j, \phi)$ is measured during 30 s at a sample rate of 0.25 Hz for every f_j and ϕ. Since the scattering of the body will be different for every angle ϕ [10, 11, 13], every rotation will result in a distribution of $E_{RMS,ij}^{body}(f_j, \phi)$ for a constant $E_{RMS}^{free}(f_j)$. The first quantity studied in this chapter is the PEMs response (R), which can be defined similarly to the R studied in the previous chapter (see Eq. 3.2):

$$R_{ij}(f_j, \phi) = \left(\frac{E_{RMS,ij}^{body}(f_j, \phi)}{E_{RMS}^{free}(f_j)}\right)^2 \tag{4.1}$$

with $E_{RMS,ij}^{body}(f_j, \phi)$ the electric field recorded by a PEM worn on position *i* = left or right hip in band *j* when a signal in band *j* is being emitted by the TX. Note that in Equation 4.1, the field $E_{RMS,ij}^{body}(f_j)$ is recorded in the same band (*j*) on the body as the band of the incident field $E_{RMS}^{free}(f_j)$. The responses $R_{ij}(f_j, \phi)$, have been studied in the previous chapter and in [10, 14, 16] in order to correct for the influence of the body. $R_{ij} < 1$ indicates an underestimation of the incident electric fields by the PEM, while $R_{ij} > 1$ means an overestimation. The average response ($R_{av,j}$) in the frequency band *j* is defined as:

$$R_{av,j} = \frac{R_{lefthip,j} + R_{righthip,j}}{2} \tag{4.2}$$

$R_{left/righthip,j}$ is the response measured in band j on the left or right hip, respectively. The distributions of R_{ij} and $R_{av,j}$ will be studied further in this chapter.

The third quantity studied in this study is the crosstalk (C_{ijk}):

$$C_{ijk} = (\frac{E^{body}_{RMS,ik}(f_j, \phi)}{E^{free}_{RMS}(f_j)})^2 \tag{4.3}$$

with $E^{body}_{RMS,ik}(f_j, \phi)$ the response recorded in band *k* when a signal in band *j* is being emitted by the TX. The different elements C_{ijk} constitute a square matrix $\overline{\overline{C_i}}$ for every *i* = left, right or average. This quantity (C_{ijk}) is important, because it represents the fraction of power that is registered as received in a certain frequency band (*k*), but is actually emitted in another frequency band (*j*). An ideal PEM has a crosstalk $C_{ijk} = \delta_{ij}$, i.e. $\overline{\overline{C_i}} = \overline{\overline{1}}$, with $\overline{\overline{1}}$ the unity matrix.

4.2.3 Measurements in a real environment

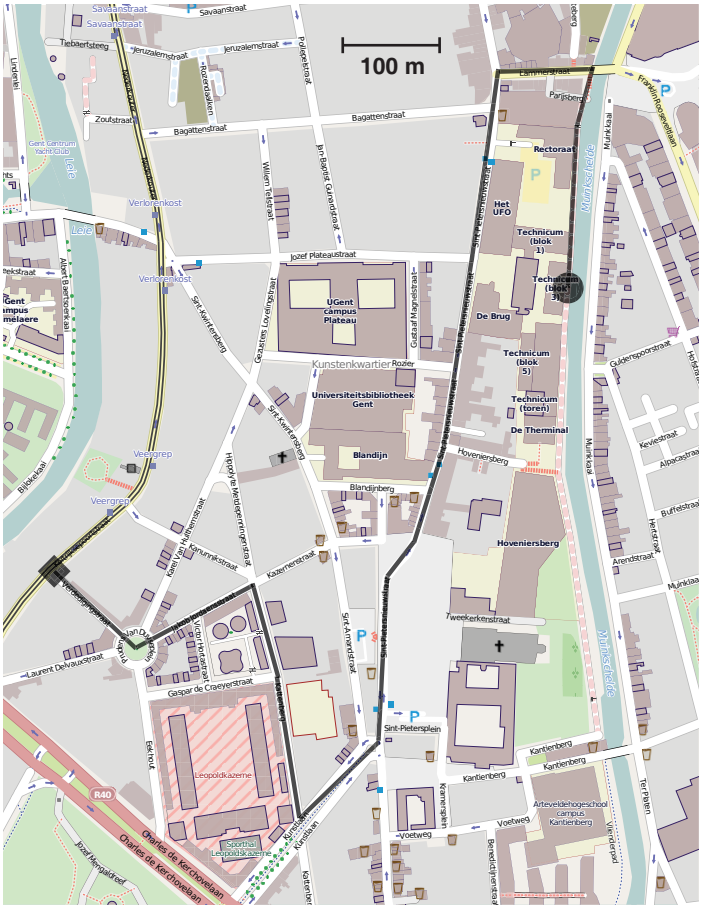

Figure 4.3: Trajectory in Ghent, Belgium (from openstreetmap.org), followed by the subject wearing two PEMs. The black line indicates the trajectory.

After the calibration, the subject follows a predefined walk in Ghent, Belgium, as shown in Figure 4.3. The walk in a suburban residential area is $\approx$ 1.9 km long and is performed on a weekday during business hours in the afternoon (12-16 h). The buildings along the trajectory are predominantly residential buildings of three to four stories high; some of the ground floors are occupied by bars, restaurants, supermarkets and clothing stores. The walk also includes a passage over a large square (Sint-Pietersplein, see Figure 4.3), where a shortest path across the square

is followed. The PEMs record the electric fields with a sample rate of 0.25 Hz. The same path is repeated four times in the same afternoon in order to increase the number of measured samples. The walk delivers six different estimates of the incident electric fields. In a first, naive estimate of the incident electric fields, these are assumed to be the same as the fields measured on-body:

$$\overline{\mathbf{E}}^{body}_{RMS,i} \tag{4.4}$$

where *i* is either left, right or averaged over both hips and $\overline{\mathbf{E}}^{body}_{RMS,i}$ an array containing the different measured $E^{body}_{RMS,ij}(f_j)$. In a second estimate, the electric fields measured on the body are corrected for the (median) influence of the body:

$$\sqrt{\frac{(E^{body}_{RMS,ij}(f_j))^2}{p_{50}(R_{ij}(f_j,\phi))}} \tag{4.5}$$

where $p_{50}()$ indicates the median value of its argument.

4.2.4 Using calibration data to process measurements in a real environment

All the calibration measurements are conducted for two orthogonal polarizations (see Figure 4.2) and the measured values for the response are only valid for those two polarizations. In contrast, Equation 4.5 requires R_{ij} values for an unknown polarization. Nevertheless, the response for a polarization ψ (R_{ij}) can be written as a sum of two orthogonal components:

$$R_{ij} = R^H_{ij} cos^2(\psi) + R^V_{ij} sin^2(\psi) \tag{4.6}$$

A Gaussian distribution for the polarization ψ has been used in [13, 20–23]. This distribution is based on values of the cross-polarization ratio (XPR), which is a well-studied quantity in propagation theory and has been measured in real environments [15]:

$$XPR = \frac{E^2_V}{E^2_H} \tag{4.7}$$

This Gaussian distribution is used to estimate the polarization for the down-link frequency bands. A value for XPR of 7.3 dB is taken from Table 3.3 for an 'Urban Macro cell' scenario [15]. This scenario corresponds best to the measurements that are executed in this study. For the up-link bands, DECT, and the WiFi bands, a uniform distribution from 0° to 360° is used since no *a priori* assumptions can be made about the polarization for these kinds of sources.

4.2.5 Statistical processing of measurements in a real environment

The goal of this processing technique is to provide summary statistics for the data measured in the individual bands and the data as a whole using a multivariate approach.

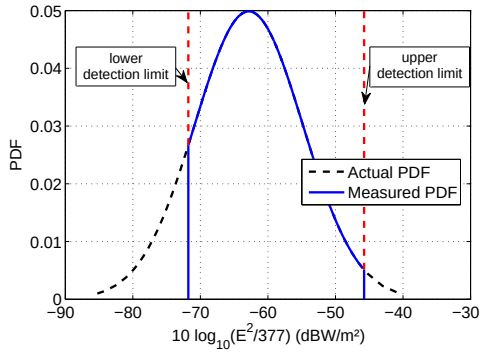

(a) example of censored data

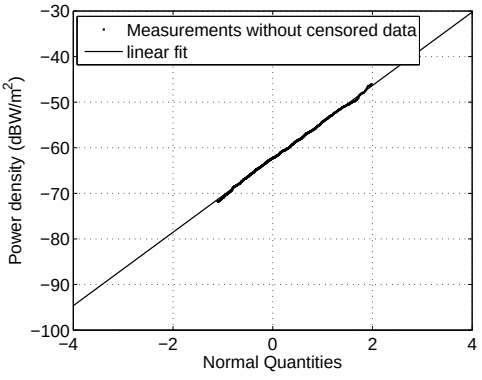

(b) example of ROS

Figure 4.4: Illustration of censored data and ROS.

Figure 4.4 (a) illustrates how detection limits can censor measurements. The data shown here are for lognormally distributed electric field strengths with a mean value of 0.014 V/m and a standard deviation of 8 dB, with a lower detection limit of 0.005 V/m and an upper detection limit of 0.1 V/m. The black dashed curve shows the actual, Gaussian probability distribution function (PDF), while the blue curve shows the measured PDF. No values can be measured that are higher than the upper detection limit (right-censoring) or lower than the lower detection limit (left-

censoring). This censoring will influence the summary statistics of the measured data. In Fig. 4.4 (a) the mean of the blue curve will be higher than the mean of the actual distribution of the power densities. In order to avoid this deviation from the true mean, in this case an overestimation, ROS is applied to the non-censored data in a first step [6, 17]. In this approach, the censored data (out of the dynamic range of the measurement device) are estimated using a log-normal extrapolation, shown in Figure 4.4 (b). Figure 4.4 (b) shows the measured, uncensored power density values and their normal quantities (z-score). This z-score can be obtained by ranking the log-normal data. Since the data are log-normally distributed, the logarithm of the values corresponding to a certain z-score, should form a straight line. In order to fit a log-normal distribution to the data, it suffices to fit a line through the data in Figure 4.4 (b). Summary statistics are then calculated on the original data where the censored data are replaced by samples drawn from this fitted distribution. ROS is applied to the measurements of the individual PEMs before averaging using Equation 4.2. This approach is used in Equation 4.5 and without correction (Equation 4.4) for the human body.

In a second step, $\overline{\mu}$ and $\overline{\overline{\Sigma}}$, the vector of means and the covariance matrix, respectively, are calculated, assuming a multivariate log-normal distribution $N(\overline{\mu}, \overline{\overline{\Sigma}})$ of the measured power densities [6]. Note that ROS on the individual frequencies can still be applied since, under the assumption of a multivariate log-normal distribution, each individual variable is log-normally distributed as well.

In a third step, the sum of the quadratic measured electric fields in the different frequency bands (see Table 4.1) is calculated. For the estimation of this sum, a multivariate approach using $\overline{\mu}$ and $\overline{\overline{\Sigma}}$ is chosen, instead of the usual approach to use ROS on the Total Power Density [6]. It is not certain that the sum of several log-normally distributed variables is log-normally distributed as well [24, 25] (but they are commonly approximated by a log-normal distribution [25]). However, using a multivariate approach, no assumptions have to be made on the distribution of the sum of the power densities measured in the individual bands. Samples consisting of several potential measurements can be generated according to $N(\overline{\mu}, \overline{\overline{\Sigma}})$ and summed. To this end an eigenvalue decomposition is performed for the positive definite, symmetric covariance matrix $\overline{\overline{\Sigma}} = \overline{\overline{U}}\,\overline{\overline{D}}\,\overline{\overline{U}}^T$, where $\overline{\overline{D}}$ is a diagonal matrix containing the eigenvalues of $\overline{\overline{\Sigma}}$ and $\overline{\overline{U}}$ a matrix consisting of the different eigenvectors of $\overline{\overline{\Sigma}}$.

Power density samples $\overline{s} = [s_1, ..., s_j, ..., s_{20}]$, where *j* are the different frequency bands, can then be generated according to the distribution:

$$N(\overline{\mu}, \overline{\overline{\Sigma}}) \sim \overline{\mu} + \overline{\overline{U}} \times \overline{\overline{D}}^{1/2} \times N(\overline{0}, \overline{\overline{1}}) \tag{4.8}$$

It is clear that if there is non-marginal crosstalk ($\overline{\overline{C}}_i$) present in the measurements of this study, this crosstalk will cause the off-diagonal elements of $\overline{\overline{\Sigma}}$ to be different from 0 and therefore, the measured quantities are not only electric fields in the

particular band, but a mixture of the different signals.

In a fourth step, summary statistics are determined for:

$$\overline{E}_{sum} = \sqrt{377 \times \sum_{j=1}^{10} s_j} \tag{4.9}$$

4.2.6 Uncertainty due to influence of the body on summary statistics

As mentioned before, $E^{body}_{RMS,ij}(f_j)$ will vary depending on the orientation of the human body and where the PEM is worn on the body. This variation will induce an uncertainty on the summary statistics of $E^{body}_{RMS,ij}(f_j)$ in Equations 4.4 and 4.5. The interquartile distance of R_{ij} (Equation 4.1) has previously been used as an estimation of the (standard) uncertainty due to the influence of the body on $E^{body}_{RMS,ij}(f_j)$ [10, 16]. However, it was assumed that the uncertainty follows a U-shaped distribution. A U-shaped distribution for the uncertainty is indeed a common assumption if the input variable is a rotational angle [26]. However, as is shown in the previous chapter, the distribution of R_{ij} can be asymmetric, whereas a U-shaped distribution is symmetric. This asymmetry in the distribution of R arises because of the asymmetric absorption and scattering of the human body.

Instead of this assumption on the distribution of the uncertainty, we have opted to report upper and lower limits. The relative upper $\overline{\mathbf{u}}_{up} = [u_{up}(f_1), ..., u_{up}(f_j), ..., u_{up}(f_{10})]$ and lower limits $\overline{\mathbf{u}}_{low} = [u_{low}(f_1), ..., u_{low}(f_j), ..., u_{low}(f_{10})]$ of the 50% prediction interval on $\overline{E}^{free}_{RMS,j}$, estimated using Equations 4.4 and 4.5, are calculated using Equations 3.6 and 3.7 from Chapter 3:

$$u_{up}(f_j) = \sqrt{\frac{p_{50}(R_{ij})}{p_{25}(R_{ij})}} - 1 \tag{4.10}$$

$$u_{low}(f_j) = 1 - \sqrt{\frac{p_{50}(R_{ij})}{p_{75}(R_{ij})}} \tag{4.11}$$

where $p_{25}()$, $p_{50}()$ and $p_{75}()$ are the 25, 50 and 75% percentiles of the responses, respectively. For the sum of the different electric fields at frequencies f_j, the 50% prediction interval can be calculated as:

$$u_{up,sum} = \frac{1}{N_{meas}} \sum_{p=1}^{N_{meas}} \left(\sqrt{\frac{\sum_{j=1}^{N_{bands}} (\overline{E}^{body}_{RMS,ij}(f_j, t_p))^2 / p_{25}(R_{ij}(f_j))}{\sum_{j=1}^{N_{bands}} (\overline{E}^{body}_{RMS,ij}(f_j, t_p))^2 / p_{50}(R_{ij}(f_j))}} - 1\right) \tag{4.12}$$

$$u_{low,sum} = \frac{1}{N_{meas}} \sum_{p=1}^{N_{meas}} \left(1 - \sqrt{\frac{\sum_{j=1}^{N_{bands}} (\overline{E}^{body}_{RMS,ij}(f_j, t_p))^2 / p_{75}(R_{ij}(f_j))}{\sum_{j=1}^{N_{bands}} (\overline{E}^{body}_{RMS,ij}(f_j, t_p))^2 / p_{50}(R_{ij}(f_j))}}\right) \tag{4.13}$$

where N_{meas} is the number of measured time instances, t_p the time at a measurement point p and N_{bands} the number of bands for which the electric fields are summed. Equations 4.12 and 4.13 reduce to Equations 4.10 and 4.11 for a single frequency and one time instance.

4.2.7 Comparison with the VFM

Calibration measurements have not yet been compared with numerical simulations. Numerical simulations, such as the ones executed in Chapter 3 could serve as a replacement for the more time-, resource-, and work-consuming calibration measurements, if they can provide the same results as calibration measurements.

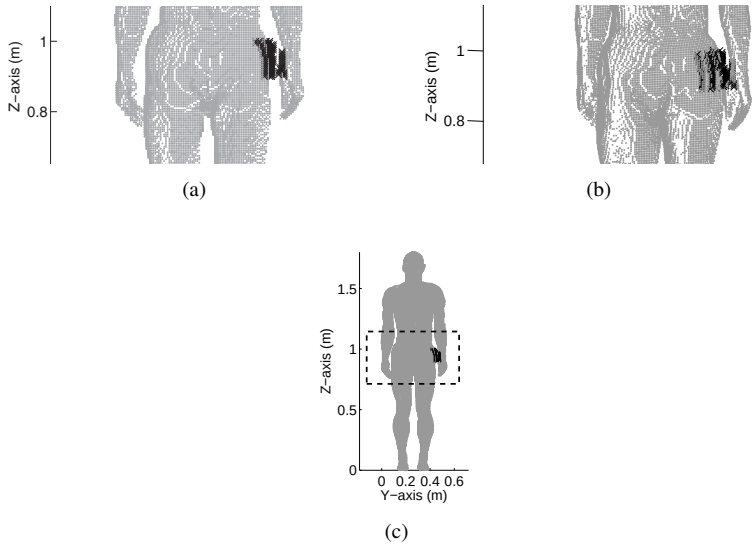

Figure 4.5: Points (black) at 1 cm from the VFM (grey), used to model a PEM worn on the left hip.

To this aim, the same method as introduced in Chapter 3 to determine the electric field strengths near the body of a heterogeneous phantom is used to determine the electric fields near the VFM [27] in a newly defined environment named 'Angular average' at 950 MHz and 2450 MHz. This scenario is chosen to compare numerical simulations with measurements using the calibration setup. In this scenario, a subject is under single plane-wave exposure, with an elevation angle of the incident fields equal to 90° and an azimuth angle between 0° and 360° in steps of 10°. Only two polarizations are considered in the 'Angular Average' scenario: vertical polarization (parallel to the phantoms/subjects rotation axis) and horizontal polarization (perpendicular to the phantoms/subjects rotation axis). This results

in 72 exposure samples. To model the positioning of a PEM, the same surface of potential measurement locations at 1 cm from the VFM's upper body are considered. However, in this case only points on the VFM's left hip are considered, in order to compare them to the measurement results of the PEM worn by both subjects on their left hip, and a smaller spacing of 1 cm (instead of 10 cm) in the Z-coordinate is used, in order to consider enough points on the VFMs hip. Figure 4.5 shows the considered points (105) on the VFM's hip.

The response is determined in all the 105 considered points in the 72 exposure samples using Equation 3.2, resulting in 7560 samples of the response R at 950 MHz and 2450 MHz, from which the median response $p_{50}(R)$ and a 50% prediction interval PI_{50} can be determined. The measurements using the subjects do not provide enough measurement points to accurately determine the 95% prediction interval PI_{95}, so this is also not considered for the simulation results.

4.3 Results and Discussion

4.3.1 Responses of PEMs

Table 4.1 lists the incident electric fields measured with the broadband field meter (Narda Probe), averaged over the subject's height. Two incident polarizations of the TX are measured for an input power of 10 mW. There is a relatively small difference between the averaged electric field measured for the two polarizations. The horizontally polarized incident electric field is slightly higher than the vertically polarized field for the same input power. The differences are attributed to small asymmetries in the anechoic chamber (the floor is different from the walls and the roof of the chamber).

Figure 4.6 shows a boxplot of the distribution in azimuth and polarization angles ϕ and ψ of the response $R_{ij}(f_j)$ measured in the N_{bands} different studied frequency bands. The distribution characteristics of $R_{left\ hip,j}(f_j)$ are shown by a transparent box, while the same characteristics for $R_{right\ hip,j}(f_j)$ are shown by a grey box and for the average $R_{av,j}(f_j)$ by a black box. The effect of polarization is simulated using 10^4 samples of ψ drawn from the Gaussian distribution described in [15] for the down-link bands and drawn from a uniform distribution from 0° to 360° for the up-link bands, DECT, and the WiFi bands. This is associated with an average Kaplan-Meier [28] estimate of the variance on the percentiles of the distribution of $R_{ij}(f_j) < 2\%$. The effect of the azimuth angle ϕ is determined using measurements.

When comparing the boxes in Figure 4.6, it becomes apparent that using an average over two PEMs reduces the variation on measured responses. For example: in the GSM 900 UL band, the interquartile distance is reduced by 3 dB (a

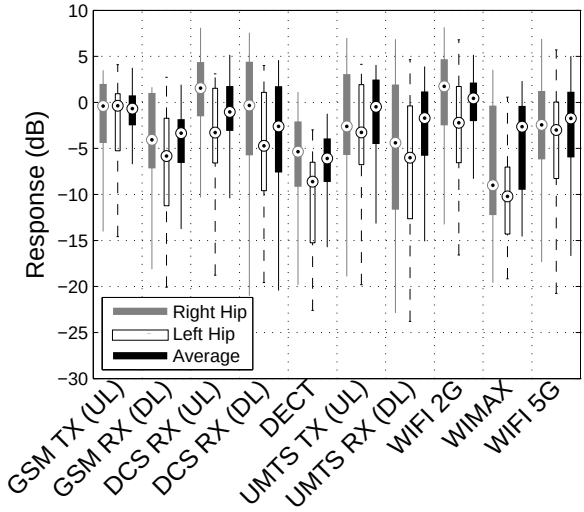

Figure 4.6: Boxplot of the responses for realistic polarizations and for all studied frequencies. The boxplot of the responses for the PEM worn on the right hip are shown in grey, while those for the PEM worn on the left hip are shown by transparent boxes. The average of the two PEMs is shown in black. The median values are indicated with a circle, the boxes are bound by the responses exceeding 75 and 25% of the measured values, the lines extending from the boxes indicate the upper and lower adjacent values.

factor of 2) from 6.2 and 6.4 dB (factors of 4.2 and 4.4, respectively) for the left and right hip, respectively, to 3.3 dB (a factor of 2.1) for the average value. Similar reductions are found for the other measured technologies (see Figure 4.6). Only for WIMAX, the PEM on the left hip is found to have a lower interquartile distance. For all the other technologies the average presented an improvement in an interquartile distance (2.5 and 3.2 dB (factors of 1.8 and 2.1, respectively) on average compared with the right hip and left hip, respectively). Given these results, it is concluded that wearing two PEMs on both hips is a viable approach to reducing the influence of the body on measurements of $\overline{E}_{RMS}^{free}$, Figure 4.6 also shows that the PEMs will usually underestimate the incident electric-field strength. The median values are < 0 dB in a majority of the cases studied. Using an average over two PEMs, median underestimations up to 6 dB, for DECT, (a factor of 4) are observed. However, in some configurations a median overestimation is observed: DCS UL with a PEM on the right hip and WiFi 2G for both the PEM on the right hip and the average over both hips. In [10], only DCS DL was found to have a median overestimation (for horizontally polarized incident plane waves and a PEM worn on the right hip). In [12, 13] the influence of polarization was also taken

into account and the simulated median responses are always < 0 dB (a factor of 1). However, since multiple positions are taken into account in these studies, an exact comparison is not possible. From the simulations in this study it can be concluded that an underestimation of $\overline{E}_{RMS}^{free}$ will be more likely in realistic exposure situations. The interquartile distances observed in the measurements of this study are comparable with those presented in [10]. Moreover, the reduction in variation using two exposimeters placed on both hips is similar.

We measured a median response in the GSM 900 DL band of -4.1 dB (a factor of 0.39) and -5.8 dB (a factor of 0.26) on the right and left hip, respectively. In the previous chapter, the median responses ($R_{med,i}$) found for the 401 studied potential locations are distributed around median values ranging from -7.7 dB (a factor of 0.17) to -6.4 dB (a factor of 0.23) in the GSM 900 DL band, see Figure 3.11 (a). The values measured on the hips reported in this chapter are higher than the median values, over the studied location on the upper body in the previous chapter. However, they are within the range of possible values shown in Figure 3.11 (a). In the WiFi 2G band, Figure 3.11 (a) shows median values from -10 dB (a factor of 0.1) to -8.3 dB (a factor of 0.15). In this chapter, we measured a median value of 1.8 dB (a factor of 1.5) and -2.2 dB (a factor of 0.60) on the right and left hip, respectively, in the WiFi 2G band. These values are not in agreement with what is predicted in Figure 3.11 (a). The values found here are higher than the simulated response at 2450 MHz in the previous chapter. These differences can be attributed to morphological differences between the studied subject and the VFM, uncertainty on the placement of the PEM on the subject, and the (unknown) measurement modus of the PEM during the rotation of the subject.

Figure 4.6 shows PI_{50} values of 8.1 dB and 9.4 dB (factors of 6.5 and 8.7, respectively) on the right and left hip, respectively. In the previous chapter, we reported the distribution of $PI_{50,i}$, the 50% prediction intervals of the different potential locations around the body, and found median values between 7.8 dB and 8.2 dB (factors of 6.0 and 6.6, respectively) in the GSM 900 DL band, see Figure 3.11 (b). The values measured here correspond very well to those predicted by numerical simulations described in the previous chapter. Figure 3.11 (b) shows median $PI_{50,i}$ values between 9.2 dB and 11 dB (factors of 8.3 and 13, respectively) in the five studied realistic environments at 2450 MHz. In this chapter we measure PI_{50} values of 7.3 dB and 12 dB (factors of 5.4 and 16, respectively) for the right and left hip, respectively, in the WiFi 2G band. These values also correspond well to those shown in Figure 3.11 (b).

The values found for the prediction intervals agree with simulations. However, the median response seems to be different for the VFM and the calibration measurements. Even between the two hips, there are relatively large differences (for example, 4 dB (a factor of 2.5) for WiFi 2G). This demonstrates the importance of a calibration of the PEMs on the body. The response will be very dependent

on the position on the body. However, the variation can be predicted by numerical simulations. In order to investigate this correspondence even further, we have investigated the response on the VFM's left hip (see Fig. 4.5).

4.3.2 Comparison with Numerical Simulations

	GSM 900 DL		WiFi 2G	
	Subject	VFM	Subject	VFM
$p_{50}(R)$	0.26	0.34	0.60	0.12
PI_{50} (dB)	9.4	10	12	12

Table 4.2: PEM's response and its 50% prediction interval on the left hip of a human subject (measured) and the VFM (simulated) in two frequency bands.

Table 4.2 shows the median values $p_{50}(R_{lefthip,j})$ and the measured interquartile distances (PI_{50}) for the GSM 900 DL band and the WiFi 2G band. The distribution of R for these two frequencies is also studied using numerical simulations of the VFM under exposure at 950 MHz and 2450 MHz in the 'Angular Average' scenario. Table 4.2 also lists $p_{50}(R_{lefthip,j})$ and the PI_{50} for the VFM for both frequency bands. In the GSM 900 DL band, the underestimation is larger than predicted by the FDTD simulations using the VFM for the human subject and the phantom. In the WiFi 2G band the underestimation is larger using the FDTD simulations. For a PEM worn on the left hip $p_{50}(R)$= 0.26 and 0.60 for the GSM 900 DL and WiFi 2G band, respectively, while it is 0.34 and 0.12 for the VFM. We attribute these differences mainly to the differences in morphology of the subject and the VMF and the placement on the hips, which is not exactly the same. Moreover, some of the radiation emitted by the TX will be recorded in other bands than the emitted band by the PEMs [18], which will also alter the response. The PI_{50} measured for both subjects are in excellent agreement with those found for the VFM: for example, PI_{50} = 9.4 dB and 12 dB for a PEM worn on the left hip of the subject in the GSM 900 DL band and the WiFi 2G band, respectively, while PI_{50} = 10 dB and 12 dB for a PEM on the left hip of the VFM in the same frequency bands. The FDTD simulations using the VFM will give a good estimation of the variance of the response (difference in $PI_{50} < 0.6$ dB), but might not be accurate in predicting the underestimation of a PEM. To compensate for underestimation by the PEM, calibration measurements on the body of the real subject will be necessary. In [10] a PEM on a subject's hip was calibrated in an open area test site for two incident polarizations, this resulted in a PI_{50} of 6.5 dB and 15.5 dB for horizontally and vertically polarized incident fields, respectively. These values are of the same order of magnitude as the values we measured for a PEM worn on the left hip in this study: 5.3 dB and 19 dB, for respectively H-and V-polarized incident

electric fields recorded by a PEM worn by the subject. A median underestimation of the incident electric field was measured in [10] as well.

4.3.3 Crosstalk

Accurately determining the crosstalk is a difficult task. It is always possible that part of the power that should be detected in one band is received and registered in another band, but is lower than the detection limit. In particular, in the case of the EME SPY 140, the detection limits are relatively high such that many of the actual values will be below the detection limits [6]. We have chosen to adopt the following procedure: if the PEM returns a value equal to its detection limit in another band (k) than the applied signal (f_j), one puts C_{ijk} (see Equation 4.3) equal to the value listed in the certificate of calibration of the EME SPY 140 [29]. Using a similar approach as shown in Equation 4.6, C_{ijk} is then calculated for realistic polarizations.

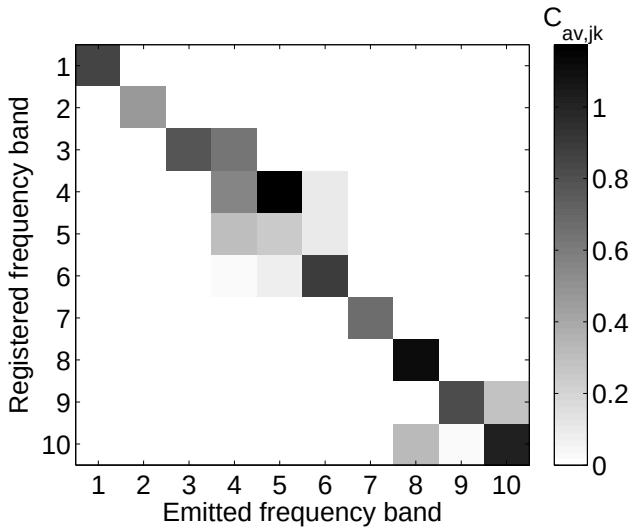

Figure 4.7: Median crosstalk matrix $\overline{\overline{C}}$ measured in the anechoic chamber in the frequency bands listed in Table 4.1, averaged over both hips for a realistic polarization.

Figure 4.7 shows the median crosstalk matrix $\overline{\overline{C}}_{av}$ for the average over the measurements on both hips. The frequency bands in which a signal is emitted are shown on the horizontal axis, while the vertical axis shows the frequency bands in which these signals are registered. The magnitude of the crosstalk is indicated by a gray scale, where darker regions indicate more crosstalk. $\overline{\overline{C}}_{av}$ is definitely not equal to the identity matrix, which would be the ideal scenario. As Figure 4.7

shows: $\overline{\overline{C}}_{av}$ is not even diagonal. The maximum off-diagonal element of $\overline{\overline{C}}_{av}$ (1.2) is measured when DECT is emitted and DCS DL is registered. In order to estimate how significant the crosstalk is, the matrix distance between $\overline{\overline{C}}_{av}$ and the identity matrix $\overline{\overline{1}}$ is calculated [30]. A matrix distance between two matrices $\overline{\overline{A}}$ and $\overline{\overline{B}}$ can be defined as:

$$d(\overline{\overline{A}}, \overline{\overline{B}}) = 1 - \frac{tr(\overline{\overline{A}}.\overline{\overline{B}})}{\left\|\overline{\overline{A}}\right\|_F \left\|\overline{\overline{B}}\right\|_F} \tag{4.14}$$

where $\|\|_F$ indicates the Frobenius norm of a matrix and $tr(\overline{\overline{A}}.\overline{\overline{B}})$ is the trace of the matrix product between $\overline{\overline{A}}$ and $\overline{\overline{B}}$. $d(\overline{\overline{A}}, \overline{\overline{B}})$ is located in between 0 and 1, where 0 indicates that $\overline{\overline{A}}$ and $\overline{\overline{B}}$ are identical (up to a scaling factor) and 1 indicates that both matrices are orthogonal [30]. In this case $d(\overline{\overline{C}}_{av}, \overline{\overline{1}})$ = 0.18, which indicates that the crosstalk is indeed diagonal dominant (see Figure 4.7), but is still different from a perfect crosstalk matrix (d=0). The crosstalk can therefore not be neglected in measurements using PEMs. The summary statistics presented for $\overline{E}^{free}_{RMS}$ further in this chapter and in other studies [1–6, 16] *should be treated with care* and under the condition that when removing the crosstalk from these measurements, different summary statistics might be obtained, in particular for DECT, UMTS UL, and DCS DL (see Figure 4.7). A possible solution to remove the crosstalk from the data is to solve the linear set of equations:

$$\overline{\overline{C}}_i.(\overline{\boldsymbol{E}}^{free}_{RMS,i})^2 = (\overline{\boldsymbol{E}}^{body}_{RMS,i})^2 \tag{4.15}$$

with $\overline{\boldsymbol{E}}^{free}_{RMS,i}$ a vector containing the incident electric field strengths in the different frequency bands and $\overline{\boldsymbol{E}}^{body}_{RMS,i}$ a vector containing the different electric field strengths measured in the different frequency bands by a PEM worn on the body on position *i*. This could be done by inverting the matrix $\overline{\overline{C}}_i$:

$$(\overline{\boldsymbol{E}}^{free}_{RMS,i})^2 = \overline{\overline{C}}_i.{}^{-1}(\overline{\boldsymbol{E}}^{body}_{RMS,i})^2 \tag{4.16}$$

However, to obtain physical results (all elements of $\overline{\boldsymbol{E}}^{body}_{RMS,i} > 0$), $\overline{\overline{C}}_i$ has to be known for the particular exposure situation at the moment that $\overline{\boldsymbol{E}}^{body}_{RMS,i}$ is measured. The crosstalk determined in this study can serve as an indication of the median influence of crosstalk, but cannot be used in Equations 4.15 and 4.16.

In [18] off-diagonal elements in $\overline{\overline{C}}$ were observed as well, using real signals. The frequency bands listed as the bands where the highest crosstalk was observed are the same as those where one finds off-diagonal elements (except for GSM 900 UL/DL). As mentioned before, this crosstalk has to be determined accurately for real signals in real environments in order to determine how this crosstalk contributes to the covariance between the different measured signals. A solution to

this crosstalk problem is proposed in [14], where instead of one broadband antenna, multiple narrow band antennas, tuned to the appropriate frequency band are used. A narrow band antenna provides a physical filter for out-of-band signals. When combined with a frequency selective power detector and an on-body calibration of the antenna, this can greatly reduce crosstalk.

4.3.4 Measurements in Ghent

The goal of this section is to provide an estimate for the incident electric fields using Equation 4.4 (no on-body calibration) and Equation 4.5 (on-body calibration using R_{ij}).

E_{RMS} (mV/m)	Censored Data (%)			Mean[a]		Q_1		Q_2		Q_3		p_{90}	
	R	L	R + L	Eq. 4.4	Eq. 4.5	Eq. 4.4	Eq. 4.5	Eq. 4.4	Eq. 4.5	Eq. 4.4	Eq. 4.5	Eq. 4.4	Eq. 4.5
GSM UL	64	59	48	4.7	5.1	2.3	2.5	4.4	4.8	9.6	10	19	21
GSM DL	0	0	0	99	140	58	86	110	160	180	260	240	360
DCS UL	38	38	30	12	13	5.2	5.9	13	15	23	26	41	46
DCS DL	0.07	0	0	52	70	32	43	50	67	78	100	140	180
DECT	16	28	10	18	37	8.0	16	18	37	38	77	84	170
UMTS UL	57	72	50	4.5	4.8	2.2	2.4	4.3	4.5	8.1	8.5	18	19
UMTS DL	0.07	0.6	0.1	42	51	26	3.2	42	51	72	87	120	150
WiFi 2G	19	22	10	15	14	8.1	7.7	15	14	26	25	41	39
WIMAX	97	97	95	NA[b]	NA	NA	NA	NA	NA	NA	NA	NA	NA
WiFi 5G	100	100	100	NA	NA	NA	NA	NA	NA	NA	NA	NA	NA
$\sqrt{\sum_{j=1}^{8} \overline{E}_{RMS,j}^2}$				140	220	95	150	140	210	210	330	320	500

[a] The mean presented here is calculated as $\sqrt{377 \times 10^{\mu}}$, with μ the mean of the logarithm of the power density used in Eq. 4.8 .

[b] NA is listed when ROS is Not Applicable due to an insufficient number of samples above the detection limit.

Table 4.3: Summary statistics of the conditional probabilities for the root-mean-squared electric field (in mV/m) registered in the frequency bands listed in Table 4.1. An estimation of the free-space incident electric field is provided, using Equations 4.4 (first column underneath the mean, Q_1, Q_2, Q_3, and p_{90}.) and 4.5 (second column underneath the mean, Q_1, Q_2, Q_3, and p_{90}.), for data averaged over two PEMs worn on both hips while following the trajectory described in Figure 4.3.

Table 4.3 lists the percentages of left-censored data. No values < 5 mV/m are detected, since this is the detection limit of the PEM. The two highest frequency bands even have a higher detection limit (20 mV/m) and insufficient samples are measured for a statistical analysis in these bands: $> 95\%$ left-censored data for WIMAX and 100% for WiFi 5G. This was to be expected since WIMAX radiation was not often present along the measured route and WiFi 5G (if emitted) is

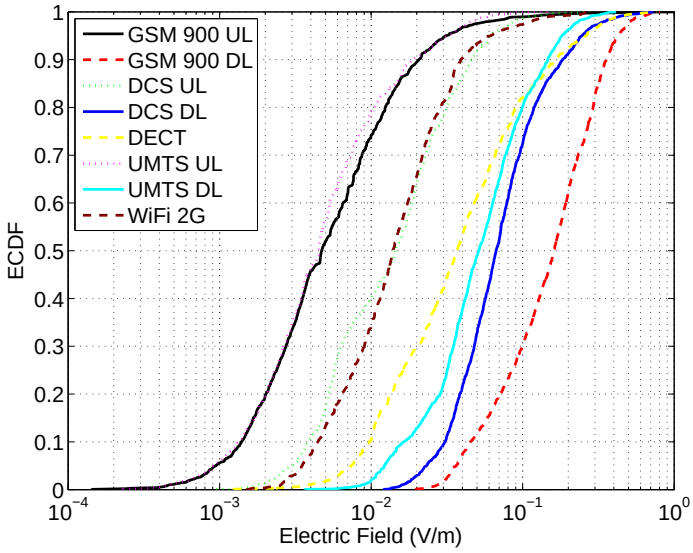

Figure 4.8: Experimental cumulative distribution function (ECDF) of the electric fields registered in the first eight frequency bands, listed in Table 4.1, after ROS and averaging over the two PEMs. Summary statistics of these ECDFs are provided in Table 4.3.

only emitted inside buildings along the trajectory. Since the trajectory is located outdoors, the signals are expected to be lower than the detection limit. ROS can only be applied to the data if $> 10\%$ of the data are uncensored [6]. Therefore, WIMAX and WiFi 5G are not treated further in this section. Besides WIMAX and WiFi 5G, UMTS UL, and GSM UL are the frequency bands in which the highest fraction of censored data are observed ($> 56\%$). Obviously, the combination of the right hip and the left hip has lower percentages of left-censored data, since it is more likely that one of the PEMs measures a value lower than its detection limit than that of both PEMs simultaneously left censored. Thus, using two PEMs enables one to measure instances when a measurement with only one of the two PEMs would result in a left-censored measurement.

Figure 4.8 shows the cumulative distribution functions of the electric fields after applying ROS to the measurements of the individual PEMs, averaging over the two PEMs using Equation 4.2, and corrected for the influence of the human body using Equation 4.5. Note that ROS is applied before averaging in order to avoid an overestimation of the mean. All the resulting incident electric fields are lower than the International Commission on Non-Ionising Radiation Protection (ICNIRP) reference levels [8] in these frequency bands.

Table 4.3 lists the summary statistics of the conditional probabilities of the

electric fields (in mV/m) shown in Figure 4.8 and the sum of the different measured frequency bands. The mean values for the individual frequency bands, calculated using the procedure mentioned above (Equation 4.2), are listed together with the quartiles Q_1, Q_2 and Q_3, corresponding to the values which are higher than 25, 50, and 75% of the measured values, respectively, and the 90% percentile (p_{90}). The highest exposure in these studied bands is measured for GSM DL, followed by DCS DL, and UMTS DL. The lowest exposure is measured for GSM UL and UMTS UL, since the subject is not allowed to carry a personal wireless device. The quantities listed using Equation 4.4 are lower than those determined using Equation 4.5, except for WiFi 2G. This is because only for WiFi 2G the median response averaged over both hips is > 1 (see Figure 4.6). For the sum of the eight first studied technologies, a multivariate approach was chosen instead of applying ROS to the raw data [6].

The mean values (with correction for the body) for GSM (power density equal to 0.052 mW/m^2) and UMTS (0.007 mW/m^2) down-link signals are of the same order (somewhat higher) as those measured in outdoor exposure situations in [16]: 0.022 and 0.005 mW/m^2, respectively. The mean value for DCS DL (0.013 mW/m^2) is lower than the one presented in [10]: 0.050 mW/m^2. The sum of the means for down-link is however in very good agreement: 0.072 mW/m^2 here and 0.077 mW/m^2 in [10]. The up-link signals are lower than those measured for GSM and DCS in outdoor scenarios and the same holds for UMTS. Note that the subject wearing the PEMs was not allowed to carry a personal wireless communication device and so the measured up-link originates from other users. Compared with [3] much lower exposure values (without correction for the body) for up-link, down-link and DECT were measured. For example, the sum of the means for down-link (without correction for the body) is 0.038 mW/m^2, while it (without correction for the body) is 0.33 mW/m^2 in [3]. The differences can, at least partly be explained by the different averaging used in this study (average on logarithmic basis) and a linear averaging in [3]. A linear averaging leads to a mean value of 0.1 mW/m^2 for the data found in our study, which is still lower than the 0.33 mW/m^2 found in [3].

For WiFi 2G a higher value of 0.0005 mW/m^2 versus a value of 0.000 mW/m^2 was found in [3]. This deviation for WiFi could be expected since WiFi sources are nowadays more present than during the measurements in [3]. The value for WiFi is relatively low compared to values measured indoors [31]: 0.038 mW/m^2 on average measured in an office environment. This can be explained due to the presence of WiFi access points indoors, whereas these are uncommon outdoors.

Table 4.4 contains the upper and lower limits of the 50% prediction interval. The largest uncertainty is found for DCS DL, whereas the smallest for GSM UL. The value for the 50% prediction interval on the sum of the eight different measured technologies is provided as well.

	Name	$u_{low}(\%)$	$u_{up}(\%)$
1	GSM 900 UL	15	23
2	GSM 900 DL	16	45
3	DCS UL	28	27
4	DCS DL	39	77
5	DECT	22	35
6	UMTS UL	29	60
7	UMTS DL	28	60
8	WiFi 2G	18	33
$\sqrt{\sum_{j=1}^{8} \overline{E}_{RMS,j}^2}$	ROS	24	45

Table 4.4: Uncertainties due to the influence on the body on the average of two PEMs worn on the left and right hip.

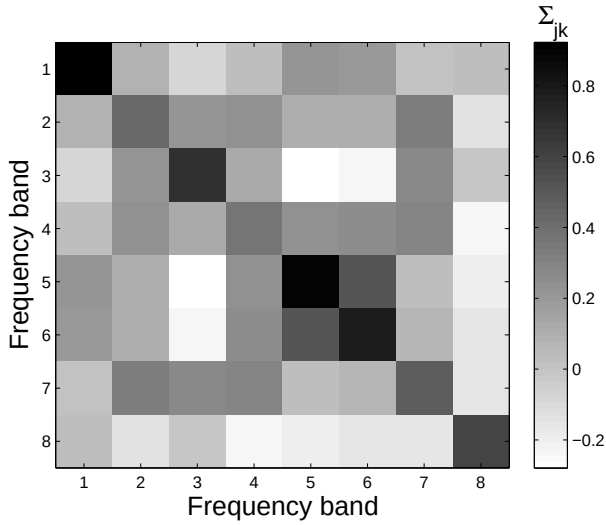

Figure 4.9: Covariance matrix $\overline{\overline{\Sigma}}$ of the power densities measured in the eight frequency bands where $> 10\%$ of the detected samples are higher than the detection limit (first eight bands listed in Table 4.1) using data from the PEMs after ROS averaged over both hips and corrected for the human body.

As mentioned before, the data measured by PEMs are usually described using univariate statistics, although the data might be multivariate. Figure 4.9 shows the covariance matrix ($\overline{\overline{\Sigma}}$) of the data after ROS averaged over both hips. The horizontal and vertical axes show the frequency bands (first eight bands listed in Table 4.1) measured during the walk shown in Figure 4.3. The value of the covariance between two frequency bands is indicated by a grey scale. A positive covariance indicates that two variables behave similarly, while a negative covariance indicates an opposite behavior. Univariate variables have a diagonal covariance matrix. From

Figure 4.9 it should be clear that the data are definitely multivariate. The vector of means ($\overline{\mu}$) is listed in Table 4.3 (in linear units) and $\overline{\overline{\Sigma}}$ is provided in Figure 4.9. In order to determine how strongly correlated the different signals are, the correlation matrix $\overline{\overline{R}}$ (normalized $\overline{\overline{\Sigma}}$) is calculated for the data after ROS (the raw data might include some additional correlation due to the censoring). The matrix distance (see Equation 4.14) $d(\overline{\overline{R}}, \overline{\overline{1}})$ is calculated in order to determine how different the measured data are from uncorrelated data ($\overline{\overline{R}} = \overline{\overline{1}}$). $d(\overline{\overline{R}}, \overline{\overline{1}})$ is 0.28 for the data after ROS. This indicates that there exists a significant (off-diagonal) correlation between the different frequency bands. The data are thus multivariate and therefore it is necessary to provide covariance estimates when discussing these data. Future research should determine how much of the covariance can be explained by the crosstalk, so that this can be removed from the data. Until then, the summary statistics provided for the conditional probabilities of the electric fields measured in the individual frequency bands using PEMs should be handled with caution. A comparison with covariance matrices from other studies or measured with other devices can be a first step in determining what part of the covariance is crosstalk and which part comes from the signals emitted in the same band.

4.4 Conclusions

Two RF PEMs worn simultaneously on both hips are calibrated on a male human subject in an anechoic chamber for 880 MHz-5.58 GHz and used for actual measurements. The response of the PEMs depends on the position on the body. However, this dependence can be reduced when averaging over both PEMs: on average 2.6 dB (a factor of 1.8) compared to a single PEM worn on the right or left hip. The variance for realistic polarizations of the PEM's response due to uncertainty on the azimuth of the incident electromagnetic fields is determined using this calibration and statistics for the polarization angle. The PEMs generally underestimate the incident electric field (up to a median underestimation of 6 dB (a factor of 4) measured for DECT) for a realistic polarization and an average over both hips, except for WiFi 2G where an overestimation of 0.4 dB (a factor of 1.1) is measured.

The response measured on the subjects left hip in the GSM 900 DL band and the WiFi 2G band are compared to results using numerical simulations. The measured interquartile distance of the PEM's responses is in good agreement (differences smaller than 0.6 dB) with the ones found using FDTD simulations using the VFM phantom. Both calibration measurements and the numerical simulations show an underestimation of the incident electric field strength. However, the values of the median response vary.

Besides the response, the crosstalk is determined during the calibration as well. Significant crosstalk (up to 1.2) is measured, indicating that measurements in the

individual bands with the PEMs will be obfuscated by crosstalk. Therefore, the results of PEM studies presented in previous studies and this study should be treated with care. Measurements using a combination of two PEMs are carried out in Ghent, Belgium.

The calibration data are used to correct PEM measurement data for the influence on the body and determine the uncertainty on the summary statistics of these data. The measured data are processed using ROS. The highest exposure was found for GSM DL: 0.052 mW/m^2 on average. All measured values are lower than the ICNIRP reference levels. The mean vector and the covariance matrix are also provided for the multivariate data, in addition to the summary statistics of the marginal probabilities for the different measured technologies. Statistics for the sum of the different measured technologies and an uncertainty on these statistics are provided using this multivariate distribution.

We recommend the practice of wearing two PEMs simultaneously, since it is shown in this chapter that this can reduce the variation on the response of the PEMs and thus the uncertainty on the measurements using PEMs. A correction for the human body has to be taken into account as this can influence the summary statistics. This correction should be determined for realistic polarizations, as proposed in this chapter. We also recommend other researchers to provide covariance estimates together with their univariate summary statistics in order to allow comparison of different studies.

Future research needs to be carried out in order to determine the crosstalk exactly for real signals (including modulation) and real individual exposure situations (including multi-path).

References

[1] P Frei, E Mohler, G Neubauer, G Theis, A Bürgi, J Frölich, C Braun-Fährländer, J Bolte, M Egger, and M Röösli. *Temporal and spatial variability of personal exposure to radio frequency electromagnetic fields.* Environmental research, 109(6):779–85, August 2009.

[2] W Joseph, G Vermeeren, L Verloock, M Masache Heredia, and L Martens. *Characterization of personal RF electromagnetic field exposure and actual absorption for the general public.* Health physics, 95(3):317–30, September 2008.

[3] W Joseph, P Frei, M Roösli, G Thuróczy, P Gajsek, T Trcek, J Bolte, G Vermeeren, E Mohler, P Juhász, V Finta, and L Martens. *Comparison of personal radio frequency electromagnetic field exposure in different urban areas across Europe.* Environmental research, 110(7):658–63, October 2010.

[4] U Knafl, H Lehmann, and M Riederer. *Electromagnetic field measurements using personal exposimeters.* Bioelectromagnetics, 29(2):160–2, February 2008.

[5] G Neubauer, M Feychting, Y Hamnerius, L Kheifets, N Kuster, Io Ruiz, J Schüz, R Uberbacher, J Wiart, and M Röösli. *Feasibility of future epidemiological studies on possible health effects of mobile phone base stations.* Bioelectromagnetics, 28(3):224–30, April 2007.

[6] M Röösli, P Frei, E Mohler, C Braun-Fahrländer, A Bürgi, J Fröhlich, G Neubauer, G Theis, and M Egger. *Statistical analysis of personal radiofrequency electromagnetic field measurements with nondetects.* Bioelectromagnetics, 29(6):471–8, September 2008.

[7] J F Viel, E Cardis, M Moissonnier, R de Seze, and M Hours. *Radiofrequency exposure in the French general population: band, time, location and activity variability.* Environment international, 35(8):1150–4, November 2009.

[8] ICNIRP International Commission on Non-Ionizing Radiation Protection. *Guidelines for limiting exposure to time-varying electric, magnetic, and electromagnetic fields (up to 300 GHz).* Health physics, 74:494–522, 1998.

[9] J Blas, F A Lago, P Fernández, R M Lorenzo, and E J Abril. *Potential exposure assessment errors associated with body-worn RF dosimeters.* Bioelectromagnetics, 28(7):573–6, October 2007.

[10] J F B Bolte, G van der Zande, and J Kamer. *Calibration and uncertainties in personal exposure measurements of radiofrequency electromagnetic fields.* Bioelectromagnetics, 32(8):652–63, December 2011.

[11] A Bahillo, J Blas, P Ferna, Solar, R M Lorenzo, S Mazuelas, and E J Abril. *E-Fiels Assessment Errors Associated with RF Dosemeters for Different Angles of Arrival*. Radiation Protection Dosimetry, 132(October):51–56, 2008.

[12] G Neubauer, S Cecil, W Giczi, P Preiner, J Frölich, and Martin Röösli. *The Association Between Exposure Determined by Radiofrequency Personal Exposimeters and Human Exposure: A Simulation Study.* Bioelectromagnetics, 31(7):535–45, 2010.

[13] S Iskra, R McKenzie, and I Cosic. *Monte Carlo simulations of the electric field close to the body in realistic environments for application in personal radiofrequency dosimetry.* Radiation Protection Dosimetry, 147(4):517–27, 2011.

[14] A Thielens, H De Clercq, S Agneessens, J Lecoutere, L Verloock, G Declercq, Fand Vermeeren, E Tanghe, H Rogier, R Puers, L Martens, and W Joseph. *Personal distributed exposimeter for radio frequency exposure assessment in real environments.* Bioelectromagnetics, 34(7):563–7, 2013.

[15] K Kalliola, K Sulonen, H Laitinen, J Krogerus, and P Vainikainen. *Angular Power Distribution and Mean Effective Gain of Mobile Antenna in Different Propagation*. (September):823–838, 2002.

[16] J F B Bolte and T Eikelboom. *Personal radiofrequency electromagnetic field measurements in The Netherlands: exposure level and variability for everyday activities, times of day and types of area.* Environment international, 48:133–42, November 2012.

[17] DR Helsel. *In: Nondetects and Data Analysis.* Scott, M. and Barnett, V.,Eds. JohnWiley & Sons Inc., 2005.

[18] O Lauer, G Neubauer, M Röösli, M Riederer, P Frei, E Mohler, and J Fröhlich. *Measurement setup and protocol for characterizing and testing radio frequency personal exposure meters.* Bioelectromagnetics, 33:75–85, 2012.

[19] B Van Laethem, F Quitin, F Bellens, C Oestges, and P De Doncker. *Correlation for multi-frequency propagation in urban environments.* Prog. Electromagn. Res. Lett., 29:151–156, 2012.

[20] S Iskra, R McKenzie, and I Cosic. *Factors Influencing Uncertainty in Measurement of Electric Fields Close to the Body in Personal RF Dosimetry.* Radiation Protection Dosimetry, 140(1):25–33, 2010.

[21] A Thielens, G Vermeeren, W Joseph, and L Martens. *Stochastic Method for the Determination of the Organ-specific Averages SAR in Realistic Environments at 950 MHz.* Bioelectromagentics, 34(7):549–562, 2013.

[22] G Vermeeren, W Joseph, and L Martens. *Whole-body SAR in spheroidal adult and child phantoms in realistic exposure environment*. Health Physics, 94(June):345–354, 2008.

[23] G Vermeeren, W Joseph, and L Martens. *Statistical multi-path exposure method for assessing the whole-body SAR in a heterogeneous human body model in a realistic environment.* Bioelectromagnetics, 34(3):240–51, April 2013.

[24] S C Schwartz and Y S Yeh. *On the Distribution Function and Moments of Power Sums with Log-normal Components*. The Bell System Technical journal, 61(7):1441–1462, 1982.

[25] N C Beaulieu and Q Xie. *An Optimal Lognormal Approximation to Lognormal Sum Distributions*. IEEE Trans Vehic Tech, 53(2):479–489, 2004.

[26] I Harris and F L Warner. *Re-examination of mismatch uncertainty when measuring microwave power and attenuation.* IEE Proc., 128(1):35–41, 1981.

[27] A Christ, W Kainz, E G Hahn, K Honegger, M Zefferer, E Neufeld, R Rascher, W Janka, W Bautz, J Chen, B Kiefer, P Schmitt, H P Hollenbach, J Shen, M Oberle, D Szczerba, A Kam, J W Guag, and N Kuster. *The Virtual Family–development of surface-based anatomical models of two adults and two children for dosimetric simulations.* Physics in medicine and biology, 55(2):N23–38, January 2010.

[28] EL Kaplan and P Meier. *Nonparametric estimation from incomplete observations.* J Am Stat Assoc, 53:457–481, 1958.

[29] Satimo. *Certificate of Calibration (EME SPY 140).* Brest, France, 2010.

[30] M Herdin, N Czink, H Özcelik, and E Bonek. *Correlation matrix distance, a meaningful measure for evaluation of non-stationary MIMO channels.* IEEE VTC, 1(1):136–140, 2005.

[31] L Verloock, W Joseph, G Vermeeren, and L Martens. *Procedure for assessment of general public exposure from WLAN in offices and in wireless sensor network testbed.* Health Phys., 98(4):628–638, 2010.

5 Design of a Personal, Distributed Exposimeter

5.1 Introduction

The previous chapters introduced the topic of personal exposure assessment and also illustrated some of the main advantages and disadvantages of the use of personal exposimeters (PEMs). The main disadvantages are the relatively large measurement uncertainty and the underestimation caused by the presence of the human body, see Chapters 3 and 4 and [1–4]. Chapter 4 and [1, 2] do provide us with a potential approach to reduce the measurement uncertainty on the incident power density. Wearing two PEMs on diametrically opposite sides of the body, on both hips [1] or simultaneously on the front and back of the torso [2] produces a reduced measurement uncertainty of at least a factor 2. Therefore, it is studied in this chapter whether a Personal, Distributed Exposimeter (PDE), a collection of body-worn Radio Frequency (RF) nodes, can be used to measure the incident power densities with an acceptably low measurement uncertainty.

In order to design a PDE, it is necessary to list the design specifications of such an on-body worn device. The configuration and the potential location of the RF nodes on the body will be dependent on the specific requirements for a accurate exposure assessment or epidemiological study, requirements on the antennas used in the RF nodes, and requirements on the way the measurement data is processed and stored. The results presented in the previous chapters and previous exposure assessment studies such as [5–11] provide information relevant for this design.

In this chapter we will first demonstrate the concept of a PDE using the results of the numerical simulations presented in Chapter 3. A method based on a step-wise linear regression is used to demonstrate the viability of a PDE. In a second step, a more realistic design approach where the geometry of the human body is taken into account is used. In a third approach, the geometry and characteristics of the antennas are also taken into account in the numerical simulations. The (dis)advantages of the different approaches are discussed and conclusions are drawn at the end of the chapter.

5.2 Design Specifications of a Personal, Distributed Exposimeter

5.2.1 Disadvantages of Conventional PEMs

The previous chapters indicate that a body-worn PEM will (on average) underestimate the incident fields when the location of the PEM is unknown. An on-body calibration is therefore necessary. Moreover, any realistic antenna will exhibit a certain polarization dependence. This dependence should be taken into account in the processing of calibration data, as demonstrated in Eq. 4.6. The methods outlined in the previous chapter and [1] can be applied for any on-body worn antenna and can, when executed and applied correctly, be used to compensate for the underestimation on the body.

Influence of the body This calibration can only correct for the median or mean of the distribution of a PEM's response. The previous chapters show that the distribution of the response can be relatively broad, which results in relatively large measurement uncertainties on the incident power density or field strength. However, [1, 2] show that this measurement uncertainty can be reduced when multiple PEMs are used, worn on diametrically opposite sides of the body. This method also proved to be successful in reducing the measurement uncertainty when using a combination of two PEMs worn on both hips, see Chapter 4. The goal of this chapter is to investigate whether the measurement uncertainty can be reduced even further when multiple nodes of a PDE are placed intelligently on the body.

Detection Limits As shown in Chapter 4, conventional PEMs, such as the EME SPY 140, have relatively large lower detection limits (0.005 V/m), which leads to a large fraction of non-detects or censored data (for example 64% in the GSM UL band during our measurements in Ghent, see Table 4.3). This censoring is problematic, since it can lead to an over- or underestimation of summary statistics [10]. The amount of censored data should thus be kept to a minimum. Therefore, it is important to tune the detection limits to the quantity which is to be measured,

for example: the measured values shown in Figure 4.8 in the GSM 900 UL band are approximately a factor thousand higher than those measured in the UMTS UL band. It is thus advisable to use different detection limits in both frequency bands.

Crosstalk Conventional PEMs exhibit a significant crosstalk, see Chapter 4 and [12]. This effect can cause a misclassification of exposure and might lead to erroneous summary statistics of measured exposure values, particularly if this effect is combined with stringent detection limits. The main cause of this crosstalk is the use of a single, broadband antenna in the PEMs. Signals in multiple frequency bands are received on a single antenna. Therefore, the frequency filtering has to be carried out solely by the receiver electronics. As demonstrated in [12] and Chapter 4, these are not performing well enough to prevent crosstalk. A possible approach to reduce the crosstalk is to use different antennas for each frequency band [13] combined with filters that provides enough out-of-band attenuation and frequency selective receiver electronics. The reflection coefficient of the antennas can then serve as an additional filter to prevent crosstalk. Obviously, this approach will increase the number of required antennas to register the full exposure and makes the PEM more bulky.

Measurement Settings A less-investigated disadvantage of PEMs are the relatively large sampling intervals that are used by the PEMs. The EME SPY 140, used in the previous chapter, has a sampling period larger than 4 s. The PEM only stores one measured value in each band during every sampling period. Moreover, this sampling is combined with fixed measurement and averaging methods within the sampling interval, which are not mentioned in the data sheet of the PEMs [14]. When measuring RF signals emitted by an unknown source, it is always important to have a sufficiently large measurement period, since the duty cycle and frequency used by the emitter in the considered frequency band are not a-priori known. If the measurement time is too short, for example consisting of just a single sweep of the frequency band, then the possibility exists that the detector does not register the (full) emitted signal. If the measurement time is too long, then an overestimation of the exposure is possible depending on the used measurement techniques [15]. Therefore, different settings have to be used in different frequency bands during measurements with standardized equipment [15, 16]. These settings depend on the used modulation of the emitted signal, the bandwidth of the signals, and the expected magnitude of the signals. For most of the signals a root-mean-square (RMS) detector can be used [15]. A common approach to register the magnitude of an uncontrolled emitted signal is to use a maximum-hold (max-hold) modus [15, 16], possibly with a correction for the duty cycle of the signal [16]. This approach stores the maximally measured value during a fixed amount of traces or during a fixed time of measurements in a certain frequency

band. It should be clear that this approach overestimates the true exposure during the measured period [15]. This overestimation is worse if the sampling period is larger. The calibration measurements executed in [12], suggest that conventional PEMs use this registration mode at least in some of the registered bands. However, since the true measurement modes in a PEM are unknown, no quantitative assessment of this effect is possible. Even if another measurement mode than max-hold is used, the summary statistics of measured signals can still depend on the used statistical processing. This is demonstrated in Subsection 4.3.4, where we compared our summary statistics, obtained using a rank-based, multivariate approach with other references that use, for example, a linear averaging. During the design of our PDE, we thus aim to use a detector and detection mode which is suitable for the measured signals, combined with a short sampling period, and rank based statistics.

5.2.2 Epidemiological Requirements

The goal of epidemiological studies is to determine what the (potential) health effect of a certain agent, in this case RF radiation, is on the whole population. In order to determine the exposure to RF radiation, certain volunteers are equipped with PEMs. Since not every person in the whole population can be equipped with a PEM, the participants have to be selected in such a way that their exposure can be representative for the whole population. However, the willingness of certain volunteers to participate in an exposure assessment study might be limited when excessive demands on the volunteers are made. This could lead to a biased sample of participants, compared to the whole population, since only people with a higher motivation to participate in a study (for example: people with a particular interest in the study or people who are worried about their exposure) will be willing to participate [17, 18]. Preferably it should thus be possible to easily wear and operate a PEM without help, since this could also exclude part of the population (elderly people or singles) or decrease their willingness to wear the device.

Besides being easy to use, a PEM cannot inhibit the volunteers to execute their daily activities, since this could alter their exposure pattern and therefore their exposure could not be representative for their exposure during everyday life. For example: a PEM must not bother the participants while they are using public transport or driving a car. Moreover, participants might feel observed by others when wearing a PEM and accordingly alter their behavior in order to reduce contact with other humans. Participants are more likely to restrict their activities or even leave the device at home [18]. Therefore, a PEM is preferably not visible for the public. A potential approach would be to wear the PEM inconspicuously underneath a jacket or integrate it in a piece of clothing. It is important to determine whether this influences the PEM's measurements.

The goal of the exposure measurements is to get a representative set of data for

a person's daily exposure. In order to achieve this, a PEM has to be very robust and durable. The PEM has to be able to function well at different temperatures, during both indoor and outdoor measurements [1], and must be able to withstand small shocks or contact. A robust device obviously also has the advantage that no data are lost and that the costs of the maintenance of the device are lower. Since the device will be given to multiple participants, its hygiene is also of importance. It should be possible to clean and disinfect the device, in order not to transmit parasites or diseases from one participant to the other. A PEM should thus be water proof.

Most epidemiological studies in the field of RF electromagnetic fields, intend to measure for periods exceeding 24 h [18–20], in order to obtain RF exposure values during as many activities of an individual as possible. This implies that the battery time of a PEM should be able to exceed this time period or that charging or replacing batteries should be made as easy as possible, without disturbing the participant's daily routine. Reliable batteries are also important in order not to lose any data. More recent studies also combine exposure values and Global Positioning System (GPS) data. If a GPS would be integrated in the PEM, then the burden of the participant could be reduced, since no extra device has to be carried. Similarly to the PEM, a GPS device can be integrated in the clothing as well [21].

Although a display of the measured values might be convenient during exposure assessment, a PEM should not provide the participants wearing the device any information on their exposure, since this might alter their behavior. Participants might intentionally go to locations with higher or lower exposure or to locations where they would like to know the exposure and consequently falsify the exposure pattern. The data should be stored on the device and an easy way to read out the data from the device should be available. Alternatively, the PEM could transmit the data to another device (not seen by the participant) wirelessly [22].

5.2.3 Frequency Bands

The most common RF bands and their allocated frequencies in Belgium are listed in Table 1.1 in Chapter 1. The different communication bands are described in Section 1.1.1 of Chapter 1. These bands range from 88 MHz to 6 GHz. Developing on-body antennas (see subsection 5.2.4) with good on-body characteristics and wearable dimensions at frequencies lower than 700 MHz is cumbersome. Moreover, a relatively large anechoic chamber would be necessary to calibrate the antennas. Therefore, we will focus here on telecommunication bands above 790 MHz. Table 5.1 lists the studied communication bands and their allocated frequency bands in Belgium.

Name	Frequency Range (MHz)
Lower 3GPP LTE	791-821
	832-862
GSM-R UL	876-880
GSM 900 UL	880-915
GSM-R DL	921-925
GSM 900 DL	925-960
DCS UL/ GSM 1800 UL	1710-1785
DCS DL/ GSM 1800 DL	1805-1880
DECT	1880-1900
UMTS/HSPA	1900-1920
UMTS UL / HSUPA	1920-1980
UMTS DL / HSDPA	2110-2170
WiFi 2G	2400-2483.5
Upper 3GPP LTE	2500-2570
	2575-2620
	2620-2690
WIMAX	3400-3600
WiFi 5G	5150-5350
	5470-5725
	5725-5875

Table 5.1: Name and frequency band of the most used frequency bands for telecommunication in Belgium [23] above 790 MHz.

5.2.4 Body-worn RF-Antennas

The RF-nodes that constitute a PDE should contain an antenna that can register the exposure in the frequency bands listed in Table 5.1 and fulfill the requirements listed in Subsection 5.2.2. In the research described later, we have opted to work with textile integrated antennas. These types of antennas have been used in several applications such as radar communication for firefighters [24], bio-sensor systems [25], and GPS systems [21]. Textile antennas offer several advantages for on-body usage. First, their flexibility and low mass allow them to be worn without impeding movement of the human body, a requirement for epidemiological studies, while maintaining their characteristics. These antennas can be fabricated in order to withstand adverse environmental conditions [26] and techniques exist to reduce the vulnerability and increase the stability of the antennas [27]. Second, textile antennas can be developed that have comparable performance to their rigid counterparts [24, 28]. Third, the antennas can be combined with wearable electronics [26], which can both be unobtrusively integrated in clothing in order to maximize wearability of the PDE. Fourth, it is possible to design these textile antennas so that their performance is not degraded when used on the body. When an absorbing body is placed in close proximity of an antenna, this can heavily perturb the antenna's radiation efficiency and power reflection coefficient [28, 29].

Several techniques can be used to design textile antennas that experience a

limited influence by the presence of the human body. A first approach is to use a planar topology based on coplanar waveguides, also known as patch antennas. These antennas contain a radiating (or receiving) patch that is separated from a ground plane by a textile or foam material [24, 30]. More advanced techniques also include micro-strip lines and slots in order to tune the antenna's bandwidth or decrease the antenna's size. The disadvantage of this design is that the antennas require a ground plane, which is larger than the used patch, in order to shield the antenna from the body. This decreases wearablility, especially at the lower frequencies that require a larger patch. A second kind of antenna used in our reserach is a cavity-backed slot antenna made with substrate integrated waveguide (SIW) technology [28]. Cavity-backed antennas typically experience small influences by the presence of a human body and emit mainly away from the human body [31]. The SIW technology allows for an additional decrease in antenna dimensions, because it eliminates the need for a ground plane [28].

5.3 Materials and Methods

Using the design aspects of the previous section, the potential of distributing different antennas on a subject's body is investigated using numerical simulations in this chapter. Three different approaches are investigated and compared. First, an approach based on the correlation between the electric field strengths on the body and the incident field strength is investigated. Second, the responses on the body are averaged, based on their geometrical location on the body. A third method investigates the influence of the actual antenna on the response of a PDE.

5.3.1 Responses of On-Body Textile Antennas

In Section 3.2.1 of Chapter 3 the response (R_i) of a PEM is studied in *i*=1..401 points located on a surface at 1 cm from the torso of the VFM, see Figure 3.3. These responses are determined for perfect antennas that can register the full electric field strength on the body ($\overline{E}_i^{body}$).

$$R = (\frac{|\overline{E}_i^{body}|}{E_{RMS}^{free}})^2 \tag{5.1}$$

with E_{RMS}^{free} the incident root-mean-squared (RMS) electric field strength.

However, as outlined in the previous section, most textile antennas suitable for the construction of a PDE are planar and often linearly polarized as well. Therefore, two projections of $\overline{E}_i^{body}$ are considered in this chapter. Figure 5.1 shows an illustration of the considered projections on the studied surface.

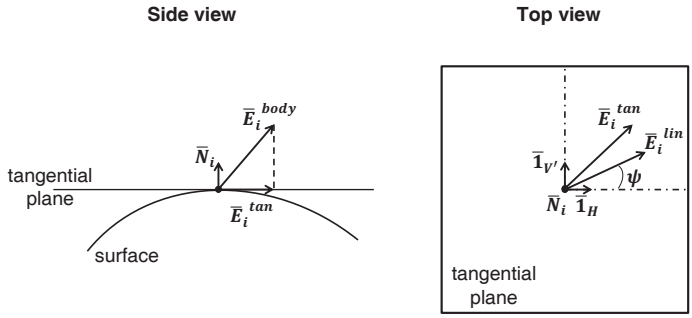

Figure 5.1: Different considered projections of the on body electric field $\overline{E}_i^{body}$.

First, for the case of a *planar* antenna, the projection of $\overline{E}_i^{body}$ in the tangential plane to the studied surface ($\overline{E}_i^{tan}$) is (see Fig. 5.1) defined as:

$$\overline{E}_i^{tan} = (\overline{E}_i^{body}.\overline{1}_H).\overline{1}_H + (\overline{E}_i^{body}.\overline{1}_{V'}).\overline{1}_{V'} \tag{5.2}$$

$\overline{1}_H$ is the unity vector parallel to the incident horizontal (H) polarization and $\overline{1}_{V'} = \overline{N}_i \times \overline{1}_H$ the unity vector orthogonal to both the outward normal (unity) vector to the surface in location *i* ($\overline{N}_i$) and $\overline{1}_H$. A tangential response (R_i^{tan}) is defined using this projected electric field:

$$R_i^{tan} = (\frac{|\overline{E}_i^{tan}|}{E_{rms}^{free}})^2 \tag{5.3}$$

Second, a *linear* projection of the electric field strength in the tangential plane to the studied surface ($\overline{E}_i^{lin}$) (see Fig. 5.1) is defined as:

$$\overline{E}_i^{lin} = (\overline{E}_i^{body}.\overline{1}_H).cos(\psi)\overline{1}_H + (\overline{E}_i^{body}.\overline{1}_{V'}).sin(\psi)\overline{1}_{V'} \tag{5.4}$$

with $\overline{E}_i^{lin}$ the projection of the on-body electric field in location *i* along a certain polarization ψ in the tangential plane to the studied surface. A linearly polarized response (R_i^{lin}) is defined using this projected electric field:

$$R_i^{lin} = (\frac{|\overline{E}_i^{lin}|}{E_{rms}^{free}})^2 \tag{5.5}$$

The domain of $\psi \in [0, 2\pi[$ is discretized in steps of $\pi/9$, since a more accurate positioning on the body is unrealistic.

5.3.2 Step-wise Linear Regression

When constructing a PDE, multiple nodes will be deployed on the upper body of a subject instead of a single PEM. The response will then be averaged over

N different points. It is computationally not possible to determine the average response of every combination *k* for every N locations drawn from 401 potential locations, since the total number of possibilities would amount to 2^{401}. Even for relatively small values of N the number of combinations is unrealistically high, for example $C_{401}^{6} = 5.56 \times 10^{12}$. Therefore, a step-wise approach is used in this section, which only requires $\sum_{i=0}^{N}(401 - i)$ calculations.

In this approach, a linear regression is executed between the electric field strengths registered in location *i*=1..401 (shown in Fig. 3.3) on the body ($E_{rms,i}^{body}$), and the incident electric field strengths (E_{rms}^{free}):

$$E_{rms}^{free} = b_0 + \sum_{k=1}^{N} b_k \times E_{rms,k}^{body} + res \tag{5.6}$$

with $\overline{b} = [b_0, b_1, .., b_N]$ the regression coefficients and res the residual. This regression is executed on a set of 4000 exposure samples in the 'Indoor Pico-cell' scenario at 950 and 2450 MHz. For every set of 4000 samples for (E_{rms}^{free}) and the corresponding set of samples for ($E_{rms,i}^{body}$) the regression results in a set of regression coefficients $\overline{b}$ that minimize the sum of the squared residual (res).

In order to reduce the number of necessary calculations, a step-wise algorithm that selects a set of potential locations is implemented. In a first step, the location on the body i that predicts E_{rms}^{free} with the smallest error-on-prediction is determined. The error-on-prediction (err) is the relative difference between an estimation $\hat{E}_{rms}^{free}$, obtained using Equation 5.6, and E_{rms}^{free}. To this aim a regression using the model presented in Equation 5.6 is executed using 4000 samples of $E_{rms,i}^{body}$ and the corresponding E_{rms}^{free} values for the same incident fields. This regression yields regression coefficients $\overline{b}$ and res for every location *i* on the body. The obtained regression coefficients are then used to predict another 1000 samples of E_{rms}^{free} using a corresponding set of 1000 $E_{rms,i}^{body}$ samples. The relative difference (err) between the predicted $\hat{E}_{rms}^{free}$, obtained using the previously determined regression coefficients, and E_{rms}^{free}, is then determined for every location on the body i. The location l with the smallest error-on-prediction is retained.

Second, a linear regression is executed, using the original 4000 samples, where location *l* is combined with the 400 remaining potential locations. The regression coefficients are obtained for the 400 pairs and the error-on-prediction is determined again using the remaining 1000 exposure samples. The pair (l, m) with the lowest error-on-prediction is retained. This process is repeated until N positions are found. This algorithm is also executed using a linear projection of the response in the tangential plane to the VFM's body surface (R_i^{lin}).

Note that there are two ways to reduce the error-on-prediction in the incident electric field strength: shifting the median of the distribution of R to 1 and reducing the spread or variation on R. Our approach combines both. However, the algorithm

only looks for a best combination of on-body locations and does not provide any information on the other potential combinations of locations on the body.

5.3.3 Geometry of the body

The previous subsection reported the methodology for a step-wise linear regression in order to investigate the error-on-prediction on the incident power density when using multiple antennas placed on 401 potential locations on the VFM. Although this approach provides an estimate of the potential of using multiple measurement nodes, the resulting locations (and polarizations) with the lowest measurement uncertainty on the incident power density can be quite difficult to reproduce exactly on the body of a real human subject. An approach based on the geometry of the body is better suited for this purpose. Two different approaches are followed in this chapter: placing antennas on diametrically opposite locations on the body and dividing the body in different potential zones to locate an antenna.

5.3.3.1 Diametrically Opposite Locations

Placing two PEMs on diametrically opposite locations on the body has already been proven successful: in [1] two PEMs are worn on the two hips of a subject, while in [2] two PEMs are worn on the front and back of the human torso. The former has already been studied in Chapter 4 and has shown to reduce the measurement uncertainty using calibration measurements. The latter is investigated in this chapter.

First, the responses in the same 401 points on the VFMs upper body (shown in Fig. 3.3) are determined in the 'Urban Macro-cell' and 'Indoor Pico-cell' scenarios at 950 and 2450 MHz. In Chapter 3, 401 positions at 1 cm from the phantom's upper body (except the face) were allowed as possible locations to deploy antennas. Yet, it is unrealistic to expect a reproducible placement of antennas on the head and limbs, due to the movement of those body parts during measurements. Therefore, those positions are not allowed in this approach. In order to eliminate these positions, we have excluded all points above and on the VFM's shoulders, locations on the VFMs hips and upper legs are excluded as well. We have also not considered any points on or underneath the arms. This reduces the number of potential locations to deploy antennas to N_{cell} = 187. The locations are then divided into two groups: front of the torso (103 points) and back of the torso (84 points). Fig 5.2 shows these potential locations to deploy antennas as blue circles (front) and red circles (back).

Second, for every possible location on the body *i* (i =1..N_{cell}), R_i is determined (using Eq. 3.2) in 5000 realistic exposure samples, resulting in a distribution of R_i. From each of these *i* distributions prediction intervals $PI_{50,i}$ can be

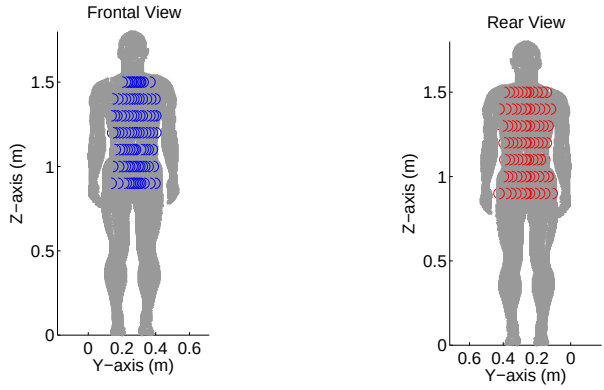

(a) Frontal View (b) Rear View

Figure 5.2: Considered potential locations to deploy antennas on the front and rear torso of the VFM.

determined.

Third, combinations of two different positions are investigated. One position on the front of the body and one on the back of the body are considered. In this case the responses are averaged over both locations on the body. The weighted arithmetic (R_l^{av}) and geometric (R_l^{geom}) averaged responses for every combination l of one location on the front and one location on the back of the VFM, are then defined as:

$$R_l^{av}(w) = w \times R_{front,l} + (1-w) \times R_{back,l} \tag{5.7}$$

$$R_l^{geom}(w) = R_{front,l}^{w} \times R_{back,l}^{1-w} \tag{5.8}$$

with $R_{front,l}$ and $R_{back,l}$ the l^{th} combination of two locations on the body and the weight $w \in [0,1]$. For every combination of two locations (l) and weight w, values $R_l^{av}(w)$ and $R_l^{geom}(w)$ are determined in 5000 realistic exposure samples, resulting in distributions of $R_l^{av}(w)$ and $R_l^{geom}(w)$. The interquartile distances of these distributions ($PI_{50,l}^{av}(w)$ and $PI_{50,l}^{geom}(w)$) are determined for every $w \in [0,1]$. The distributions of these prediction intervals are then compared to those of single measurement points in order to show the advantage of a (weighted) averaging over two nodes placed on diametrically opposite locations on the upper body.

5.3.3.2 On-body Zones

In a subsequent approach, an equilibrium is found between reproducibility and spatial variation on the body. The upper body of the VFM (or any subject) is di-

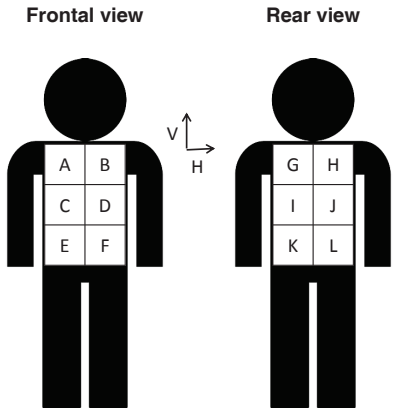

(a)

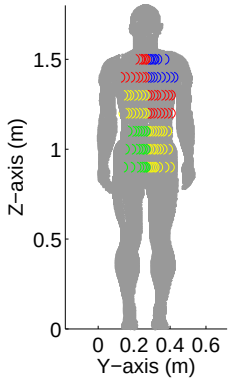

(b) Frontal View

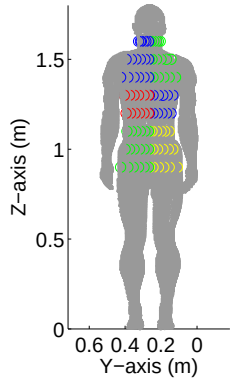

(c) Rear View

Figure 5.3: 12 potential zones (A to L) to deploy antennas on the upper torso.

vided in twelve possible locations (A to L) to deploy the antennas on the human body. The limbs, neck, and head are excluded as possible areas for the deployment of antennas, since their movement would influence the performance of the antennas. Considering a human in upright anatomical position, only the torso of the human body is considered as valid to position antennas. Locations on the torso, but underneath the arms (in anatomical position) are excluded as well. This leaves us with the anterior and posterior sides of the trunk. Both the front and back of the human body are then divided in 6 zones, as indicated in Figures 5.3 (a), where the antennas could be located. In total 12 different zones A to L are considered.

The surface of these zones is 300 $cm^2 \pm 27\ cm^2$. Figure 5.3 (b) and (c) show the corresponding 12 zones on the body of the VFM and the measurement locations that belong to this zone. The locations on the body are the same as those presented in Section 3.2.2 of Chapter 3. These are obtained by discretizing a surface at 1 cm from the upper torso of the VFM. This separation of 1 cm corresponds to the thickness of the antennas [13, 28, 30] that can be used to construct the PDE in reality. The discretization uses steps of 10 cm along the Z-coordinate (see Fig. 5.3 (b)) and 10° in the azimuth coordinate ϕ. However, only locations that are located between $[-71^\circ, +71^\circ]$ are considered on the front of the body and between $[-121^\circ, +121^\circ]$ on the back of the VFM. In order to obtain 12 zones on the upper body, the length of the torso is divided in 3 and the 2 angular domains are divided in 2, resulting in the 12 zones shown in Figure 5.3 (b) and (c).

The responses R_i are spatially averaged over each of the 12 potential zones on the body. Either arithmetically:

$$R_l^{spat,av} = \frac{1}{N_l} \sum_{j=1}^{N_l} R_j \qquad l = 1, .., 12 \tag{5.9}$$

with R_j the response of an antenna worn on zone l and N_l the number of locations j that are located in zone l. Or geometrically:

$$R_l^{spat,geom} = \prod_{j=1}^{N_l} {R_j}^{1/N_l} \qquad l = 1, .., 12 \tag{5.10}$$

The responses $R_l^{spat,av}$ and $R_l^{spat,geom}$ are then averaged over C_{12}^N different combinations of zones with $N = 1$,..,12. The appropriate spatial averaging (arithmetic or geometric) is combined with the same averaging over the different considered zones on the body. Either an arithmetic:

$$R_k^{av} = \frac{1}{N} \sum_{j=1}^{N} R_j^{spat,av} \tag{5.11}$$

or geometric averaging:

$$R_k^{geom} = \prod_{j=1}^{N} (R_j^{spat,geom})^{1/N} \tag{5.12}$$

is executed over *N* different zones. R_k^{av} and R_k^{geom} are the arithmetic or geometric averaged response of the k^{th} combination of N zones from 12 zones.

The analysis is executed for 5000 exposure samples in the 'Urban Macro-cell' and 'Indoor Pico-cell' scenarios at 950 and 2450 MHz. In this section, only the full response R (see Eq. 5.1) is studied. Neither, the tangential (R^{tan}, see Eq. 5.3)

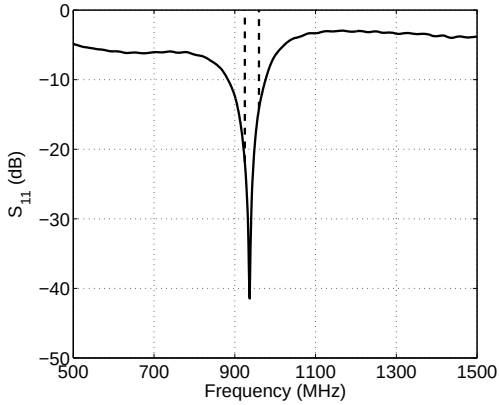

Figure 5.4: Measured power reflection coefficient (S_{11}) of the textiles antennas used for the GSM 900 DL band.

nor the linear projection of the response (R^{lin}, see Eq. 5.5) are taken into account. However, this approach is studied in the next subsection using numerical models for real textile antennas.

5.3.4 Numerical Simulations of Textile Antennas

In the final numerical approach to model a PDE, an actual model for a textile antenna is used in the numerical simulations. The simulated textile antenna is the antenna presented in [13, 30]. This is an aperture coupled shorted patch antenna made from textile materials [30], which covers the GSM 900 DL band (925 MHz-960 MHz). The antenna is linearly polarized and operates at quarter wavelength length to keep down the overall dimensions, resulting in a size of 11.5 cm x 13.5 cm x 1 cm (width x length x height). The conductive parts of this antenna are fabricated using copper plated nylon fabric (conductivity = 0.18 Ω/sq) and the antenna feed substrate is a foam material (ϵ_r =1.16, tan δ = 0.01), while the feed substrate is made from aramid fabric (ϵ_r= 1.68, tan δ = 0.015). An on-body efficiency of 82%, a maximal gain of 3.1 dBi, and a bandwidth of 6.7% ensure good coverage of the GSM 900 DL band. The on-body measured reflection coefficient is shown in Figure 5.4 and is lower than -10 dB (0.1) over the full GSM 900 DL band.

First, the on-body directive gain of the textile antennas on different locations (i) of the body has to be determined. This directive gain (D_i) can be used to calculate

the on-body aperture of the i^{th} antenna (AA_i) [32]:

$$AA_i(\phi,\theta) = \eta_{rad}(1-|S_{11}|)D_i(\phi,\theta)\frac{\lambda^2}{4\pi} \tag{5.13}$$

With η_{rad} the radiation efficiency, S_{11} the antenna's power reflection coefficient, and λ the wavelength. $AA_i(\phi,\theta)$ can be determined for two orthogonal polarizations of the incident electric fields: θ and ϕ, which are the polarizations parallel to the unity vectors $\overline{1}_\theta$ and $\overline{1}_\phi$ in a spherical coordinate system. These antenna apertures are denoted $AA_i(\phi,\theta,0°)$ and $AA_i(\phi,\theta,90°)$ and can be used to calculate the antenna aperture for any polarization angle ψ:

$$AA_i(\phi,\theta,\psi) = AA_i(\phi,\theta,90°).cos^2(\psi) + AA_i(\phi,\theta,0°).sin^2(\psi) \tag{5.14}$$

This results in $AA_i(\phi,\theta,\psi)$, a polarization dependent effective on-body antenna aperture of an antenna placed on position *i* on the body.

Using this $AA_i(\phi,\theta,\psi)$, the received power ($P_{r,i}$) on textile antennas *i* can be calculated as a function of the incident power density (S_{inc}):

$$P_{r,i}(\phi,\theta,\psi) = AA_i(\phi,\theta,\psi).S_{inc} \tag{5.15}$$

with S_{inc} the power density incident from angles (ϕ,θ) with a ψ polarization.

Considering that multiple plane waves are incident on the antenna, it does not suffice to simply add the received powers from the different incident plane waves, since incident plane waves are able to interfere with each other. The received power should be considered as a function of the incident electric fields:

$$\begin{aligned} P_{r,i} = &\frac{1}{|Z_i|}\Big|\sum_{j=1}^{N_{pw}} AF_i(\theta_j,\phi_j,0°).(\overline{E}_{inc,j}(\theta_j,\phi_j,\psi_j).\overline{1}_\theta).e^{i\alpha_j}\Big|^2 \\ &+\frac{1}{|Z_i|}\Big|\sum_{j=1}^{N_{pw}} AF_i(\theta_j,\phi_j,90°).(\overline{E}_{inc,j}(\theta_j,\phi_j,\psi_j).\overline{1}_\phi).e^{i\alpha_j}\Big|^2 \end{aligned} \tag{5.16}$$

with $|Z_i|$ the magnitude of the input impedance of antenna *i*, $\overline{E}_{inc,j}(\theta_j,\phi_j,\psi_j)$ the incident electric field of plane wave *j* with phase α_j, polar angle θ_j, azimuth angle ϕ_j, polarization ψ_j, and amplitude $|\overline{E}_{inc,j}|$, and N_{pw} the number of simultaneously incident plane waves. $AF_i(\theta_j,\phi_j,\psi_j)$ is the antenna factor, defined as:

$$AF_i(\theta_j,\phi_j,\psi_j) = \sqrt{AA_i(\theta_j,\phi_j,\psi_j)\times\frac{|Z_i|}{377}} \tag{5.17}$$

The usage of the antenna factor in Equation 5.16 ensures a proper normalization of the incident electric fields according to the directive gain of the antennas.

The number of plane waves and their relative amplitude and phase will constantly change in a real environment. In this chapter, we will focus on the analysis

in two previously studied environments: an 'Urban Macro-cell' and an 'Indoor Pico-cell' scenario in the GSM DL bands. The scenarios are far-field, multi-path environments and therefore the exposure in these environments has to be studied stochastically. To that end, a large number of exposure samples, consisting of a number of plane waves, are generated according to certain statistics for the properties of the incident plane waves: the number of incident plane waves, and their amplitude, phase, polarization, and polar angle. The distributions of each of these parameters are listed in Table 3.3 (Chapter 3).

The received power on the antennas can be calculated in every exposure sample using Equation 5.16. Consequently, a distribution of different received powers will be obtained in this environment. These received powers are then normalized to the total incident power density, i.e. the sum of the power densities of the different incident plane waves. This results in an effective, multi-path antenna aperture (AA_i^{mp}):

$$AA_i^{mp} = \frac{P_{r,i}}{S_{inc}} \tag{5.18}$$

AA_i^{mp} can be used to estimate incident power densities from received powers registered on the different antennas *i*. However, this antenna aperture is not a constant, but will have a certain distribution. From this distribution, the three quartiles: $Q_{i,1}$, $Q_{i,2}$, and $Q_{i,3}$ are determined. These quartiles can be used to translate measured received powers on textile antennas during measurements in a real environment to incident power densities. The incident power density is estimated as the ratio of the registered received power and the median of the distribution of the antenna aperture:

$$S_{inc,i}^{meas} = \frac{P_{r,i}^{meas}}{Q_{i,2}} \tag{5.19}$$

Where $P_{r,i}^{meas}$ is the power received on a textile antenna placed in zone *i* during a measurement and $S_{inc,i}^{meas}$ is the incident power density estimated using this measurement. The other quartiles of the effective antenna aperture are used to determine relative upper (u_{up}) and lower (u_{low}) limits of the 50% confidence interval on $S_{inc,i}^{meas}$:

$$u_{up} = \frac{Q_{i,2}}{Q_{i,1}} - 1 \tag{5.20}$$

$$u_{low} = 1 - \frac{Q_{i,2}}{Q_{i,3}} \tag{5.21}$$

From Equations 5.20 and 5.21 it should be clear that when the interquartile distance of the distribution of the effective antenna aperture is reduced, then the uncertainty on the measured incident power densities will be reduced as well. In order to reduce this interquartile distance an average over different antennas will be used. The received power on the textile antennas is then averaged (either arithmetically

or geometrically) over N different nodes placed on the body:

$$AA_l^{av} = \frac{1}{N}\sum_{k=1}^{N} AA_k^{mp} \tag{5.22}$$

$$AA_l^{geom} = \prod_{k=1}^{N} (AA_k^{mp})^{1/N} \tag{5.23}$$

with AA_l^{av} and AA_l^{geom} the arithmetic and geometric averaged antenna apertures averaged over the l^{th} combination of N antennas placed on the body, respectively. These averaged antenna apertures will have a certain distribution as well, from which quartiles can be obtained: $Q_{l,1}^{av/geom}$, $Q_{l,2}^{av/geom}$, and $Q_{l,3}^{av/geom}$. The incident power density can then be estimated using:

$$S_{inc}^{meas} = \frac{\frac{1}{N}\sum_{k=1}^{N} P_{r,k}^{meas}}{Q_{l,2}^{av}} \tag{5.24}$$

$$S_{inc}^{meas} = \frac{\prod_{k=1}^{N} (P_{r,k}^{meas})^{1/N}}{Q_{l,2}^{geom}} \tag{5.25}$$

The uncertainty on this incident power density can be calculated with the appropriate quartiles inserted in Equations 5.20 and 5.21. The goal is to find the combination *l* of N antennas, minimizing this uncertainty. To this aim we will use numerical simulations of a model of a textile antenna placed on the VFM [33].

FDTD simulations are executed at 950 MHz, a frequency in the GSM 900 DL band, using SEMCAD-X (SPEAG, Zürich, Switzerland). First, the textile antenna is modeled in the simulation software. Secondly, the antennas are placed on the heterogeneous phantom (VFM) in upright anatomical posture. The dielectric parameters found in the Gabriel database are assigned [34] to the phantoms tissues, which are discretized in space with a grid step of 1.5 mm in each direction. The antennas are placed centered on 12 points (A to L) located at the front and back of the upper torso, shown in Figure 5.5.

The 12 points on the torso are chosen so that they are distributed equidistantly over the full height of the VFM's torso (from 0.9 m to 1.6 m) and are located at -150° and 150° at the back and, -35°, and 35° (positions C and D) or -45° and 45° (positions A, B, E, and F) at the front of the torso, using cylindrical coordinates. The textile antennas are placed on the body so that their rear plane does not intersect the phantom (this requires small shifts of the antennas < 2 cm in the +X or -X directions) and are oriented along the grid, so that their rear plane is parallel to the Z-axis shown in Figure 5.6.

The textile antennas are placed in two different orientations: vertical (V), with their linear polarization parallel to the Z-axis, or horizontal (H), with their linear

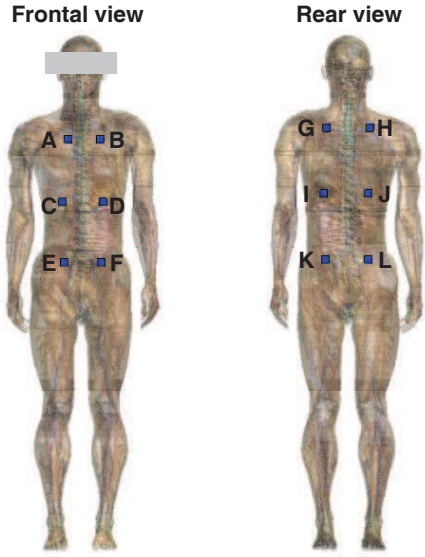

Figure 5.5: Locations of the geometrical centers of the textile antennas placed on the VFM.

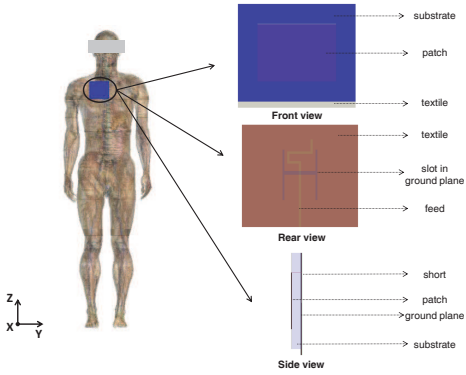

Figure 5.6: Model of the textile antenna and an example of the placement of the textile antenna on location A on the VFM.

polarization orthogonal to the Z-axis and their rear plane parallel to the Z-axis. The antennas are fed by a voltage source with an impedance of 50 Ohms and radiate during 20 time periods, which is long enough to reach a steady-state when the antennas are located on the body. Figure 5.6 shows an illustration of the antenna's parts and one of the antennas placed on position A on the VFM.

The on-body directive gain of the antennas is then extracted using a far-field

sensor. This directive gain can be used to calculate $AA_i(\theta, \phi, \psi)$, using Equations 5.13 and 5.14. Since the directive gain is determined using a numerical simulation which is excited with one source, all the values of the antenna aperture are in phase. Therefore, they can be used to determine the antenna factors, using Eq. 5.17. The calibration procedure described above is then followed in order to determine the measurement uncertainty for every combination l of $N = 1..5$ antennas chosen from 2×12 antennas. To this end, 1000 multi-path exposure samples consisting of N_{pw} simultaneously incident plane waves with phase α_j, polar angle θ_j, azimuth angle ϕ_j, polarization ψ_j, and amplitude $|E_{inc,j}|$, see Eq. 5.16, are generated in order to determine the distribution of AA_i^{mp} using Eq. 5.18. The calibration is then continued as outlined above and is repeated a 100 times in order to determine the variation on this approach.

5.4 Results and Discussion

5.4.1 Step-wise Linear Regression

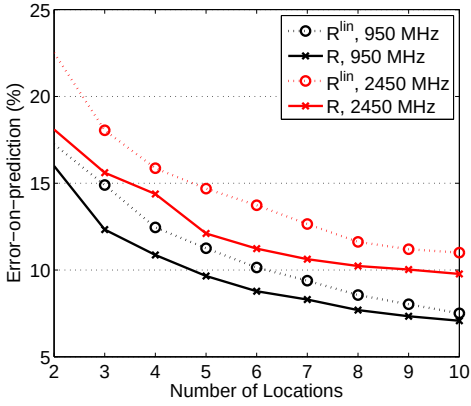

Figure 5.7: Error-on-prediction of the PDE as a function of the number of measurement positions (number of on-body antennas) for 4000 observations and 1000 control values at 950 and 2450 MHz. The errors are given for perfect sensors (R) and for linearly polarized sensors (R^{lin}) at 1 cm from the phantom. The resolution of the antennas' linear polarization is 20°.

Figure 1 shows the results of the step-wise linear regression, using Eq. 5.6, considering 4000 observations and 1000 control values in the (realistic) 'Indoor Pico-cell' environment. Both perfect sensors and linearly polarized sensors, representing textile antennas, are considered. The allowed orientations of the linearly polarized sensors in the tangent plane to the body are multiples of $\pi/9$ of rotation around the

normal vector to the tangential plane ($\overline{N}$, see Fig. 5.1). Table 5.2 lists the error-on-predictions of the single sensors that are chosen out of 401 potential locations and different potential orientations on the body, in the first step of the step-wise algorithm (those with the lowest error-on-prediction).

	950 MHz	2450 MHz
R	59%	180%
R^{lin} ($\Delta\psi = \pi/9$)	100%	190%

Table 5.2: Error-on-prediction of the single antennas chosen as first location on the body by the step-wise linear algorithm in the 'Indoor Pico-cell' scenario.

As outlined in Chapter 3, the error-on-prediction (related to the prediction intervals determined from the responses' distribution by Eqs.3.6 and 3.7) can be relatively large for single sensors or antennas, see Table 5.2 where only for the response of a perfect sensor at 950 MHz a value below 100% is obtained. Figure 5.7 shows that by adding a second antenna, these error-on-predictions can be reduced drastically (more than 40%).

Some accuracy is lost (1.7% on average at 950 MHz and 2.1% at 2450 MHz) when only one component of the field can be measured, compared to a perfect measurement of the full root RMS values. Using a resolution of 20° ($\pi/9$) we can predict the incident electric fields with an average error of 13% using 3 measurement positions (i.e. 3 antennas on the body) and 9.2% using 10 measurement positions at 950 MHz. At 2450 MHz average error-on-predictions of 18% and 11% are found using 3 and 10 linearly polarized responses on the VFM's body. We thus prove that it is possible to accurately predict the incident electric fields using only a few measurement positions on the body, even when only a linear polarization can be recorded.

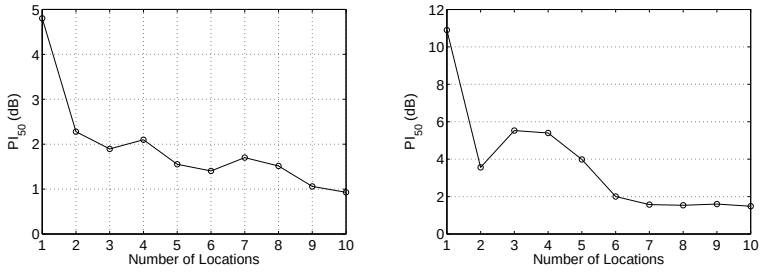

(a) 950 MHz (b) 2450 MHz

Figure 5.8: PI_{50} as a function of the number of locations chosen by the step-wise algorithm for a response R of a perfect sensor at 950 MHz and 2450 MHz.

Figure 5.8 (a) shows the PI_{50} of the distribution of the arithmetically averaged responses at 950 MHz in the 'Indoor Pico-cell' scenario with the same locations that are chosen by the step-wise linear regression. This figure shows that the main improvement in variation of the response (quantified by the PI_{50} of their distributions) is made by adding the second sensor (decrease of PI_{50} with 2.5 dB) to the PDE, whereas the improvements on the PI_{50} are much smaller if more sensors are added (1.3 dB in total). This difference is even more pronounced at 2450 MHz in Figure 5.8 (b). The reduction in PI_{50} is more than 8 dB when a second sensor is added, but adding more sensors does not significantly improve the PI_{50}. Note that the algorithm selects the combinations with the lowest error-on-prediction and not the lowest PI_{50}, which explains the small increase of PI_{50} after the addition of the third sensor.

In Chapter 3 the PI_{50} is determined for different locations on the VFM. The lowest values found for the PI_{50} are 3.4 dB and 6 dB at 950 and 2450 MHz, respectively, in the 'Indoor Pico-cell' scenario, while the median values found in the same environment are 8.06 and 10 dB at 950 and 2450 MHz, respectively. The combinations found using the step-wise algorithm do reduce the PI_{50}, in comparison with single locations on the body. However, the combinations found by the algorithm might be difficult to reproduce on a real human. Therefore an approach is followed that takes into account geometrical aspects of the human body.

5.4.2 Geometry of the body

5.4.2.1 Diametrically Opposite Locations

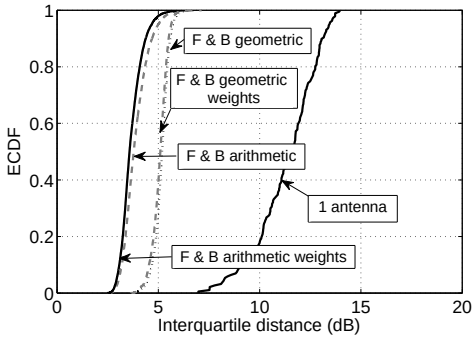

Figure 5.9: Numerically simulated Experimental Cumulative Distribution Function (ECDF) of the PI_{50} of a single textile antenna placed on the upper body, compared to the interquartile distance of a (weighted) average of two antennas placed on the front and back of the torso at 2450 MHz in the 'Urban Macro-cell' environment. F = front and B = back.

Figure 5.9 shows an experimental cumulative distribution function (ECDF) of the PI_{50} for a single PEM placed on any of the locations shown in Figure 5.2 in comparison to the ECDFs that are obtained for (weighted) combinations of antennas placed on the front and the back. The results of the numerical simulations shown in Figure 5.9 indicate that a (weighted) average over two antennas on the front and back of the upper torso does reduce the PI_{50} or interquartile distance on the simulated response: 8 dB and 6.5 dB reductions on the median interquartile distance of the response of the PDE, using a weighted arithmetic and geometric average. The simulations also show that the exact positions of the antennas are not that critical for the value of the interquartile distance, due to the steep ECDF. 95% of all studied combinations of two antennas yield an interquartile distance within an interval of 2.1 dB and 1.6 dB around median values of 3.6 dB and 5.1 dB, for a weighted arithmetic and geometric average, respectively. Moreover, as Fig. 5.9 shows, any combination of two textile antennas placed on the front and back of the torso leads to a lower interquartile distance than the one obtained by a single antenna.

Table 5.3 lists the average correlation coefficients between the responses on the front and back of the VFM's torso in the same environment as shown in Figure 5.9. A correlation of zero indicates statistical independence of two variables. A positive correlation indicates statistical dependence between two variables, i.e. the variables will behave similarly. In this case the responses on one side of the body

	R_{front}	R_{back}
R_{front}	0.58	-0.36
R_{back}	-0.36	0.57

Table 5.3: Averaged correlation coefficients between the studied responses on the front and the back of the VFM's torso at 2450 MHz in the 'Urban Macro-cell' scenario.

are correlated positively with the other responses on the same side of the body, because they experience a similar shadowing of the body. A negative correlation implies a statistical opposite dependence. In this case the responses on one side of the body are negatively correlated with the responses on the other side of the body, because their responses show an opposite behavior as a function of the angle of incidence due to shadowing of the body. These correlation values explain why the averaged responses have lower PI_{50} values than the single antennas. Generally, the variance of an average of two responses can be calculated as:

$$Var(\frac{1}{2}(R_{front,l} + R_{back,l})) = \frac{1}{4}(Var(R_{front,l}) + Var(R_{back,l})) + \frac{1}{2}Cov(R_{front,l}, R_{back,l}) \quad (5.26)$$

with $Var()$ the variance on its input and $Cov()$ the covariance on its input. An average of two uncorrelated sets of observations of the same variable, in this case the incident power density, should reduce the variance on the average observations with a factor of two if the variance of both observations is the same. In case of a negative correlation (normalized covariance) between R^{front} and R^{back}, the variance will be reduced even further. In this section, the variances of R^{front} and R^{back} are not identical, nor are they (log-)normally distributed, but the same principle applies to this averaging. A negative correlation will cause the percentiles of the distributions of R^{av} and R^{geom} to migrate closer to the mean and therefore the PI_{50} will be reduced as well.

In [2], numerical simulations with an adult human body model are performed to investigate the variation of the response of a single and a dual PEM (one PEM on both front and back of the torso) in different fading scenarios. The mean values of the 95% prediction interval (the ratio of the 97.5% and 2.5% percentiles) over different combinations of positions of isotropic PEMs on the front and back of the body equal 10.8 dB for a combination of two PEMs at 2100 MHz. The simulations in the current study (at 2450 MHz) result in a mean 95% prediction interval of 12.3 dB for a combination of two textile antennas placed on the front and the back of the torso. The values found in this study are larger because of the higher frequency, which causes more variation of the electric fields near the body [2].

Figure 5.9 shows that a weighted arithmetic averaging of the responses on the

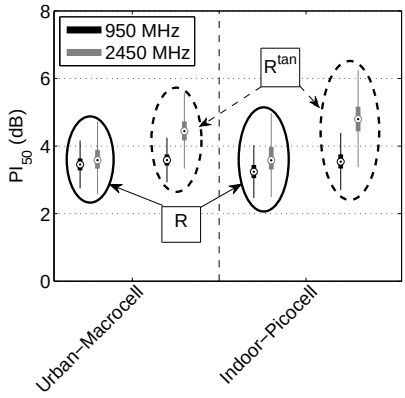

Figure 5.10: Boxplots of the PI_{50} values for weighted arithmetic averaged responses R and R^{tan} in the 'Urban Macro-cell' and 'indoor Pico-cell' scenarios at 950 and 2450 MHz.

front and back is the best technique to obtain low PI_{50} values at 2450 MHz in the 'Indoor Pico-cell' scenario. Similar results are found in the 'Urban-Macrocell' scenario, also at 950 MHz and for a tangential projection of the electric fields registered on the VFM's torso. Figure 5.10 shows a boxplot of the PI_{50} values using a weighted arithmetic averaging of the responses on the front and back of the VFM for the two studied exposure scenarios, the two studied frequencies, and both the perfect antennas and the tangential projection of the responses. Boxplots of the PI_{50} values of the single antennas in the same environments are shown in Figure 3.11 (b) in Chapter 3. When comparing both figures, we can conclude that in all the studied cases the averaging over two antennas placed on the front and back of the VFM's torso causes a decrease of the PI_{50}. The lowest median PI_{50} of 3.2 dB is found in the 'Indoor Pico-cell' scenario at 950 MHz. In these two studied environments, the boxplots for the tangentially projected electric fields are located at higher PI_{50} values than those that use the total electric field vector. The knowledge of the total electric field should cause a better estimation of the incident field strength, because it contains more information about the actual fields.

5.4.2.2 On-body Zones

In this design approach, the responses are determined for 5000 exposure samples in the 'Indoor Pico-cell' and 'Urban Macro-cell' scenarios at 950 and 2450 MHz. Those responses are then averaged over 12 different zones, shown in Figure 5.3, using Eqs. 5.9 and 5.10. Subsequently, the responses are averaged over all combinations C_{12}^{N} with $N = 1..12$. Figure 5.11 shows boxplots of the distribution of

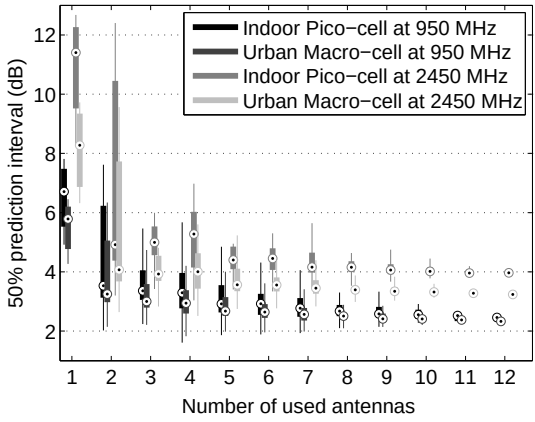

(a) Geometric Average

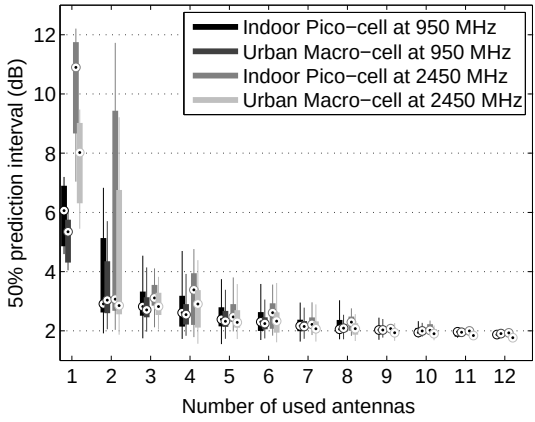

(b) Arithmetic Average

Figure 5.11: PI_{50} as a function of the number of locations chosen from 12 zones at 950 MHz and 2450 MHz. Outliers are suppressed in this figure.

the PI_{50} of all C_{12}^{N} combinations of the exposimeter worn on N out of 12 possible zones to deploy them. Figure 5.11 (a) shows this distribution for a geometric averaging over several antennas as a function of the number of used on-body antennas, whereas Figure 5.11 (b) shows the same dependency using an arithmetic averaging.

Figure 5.11 shows that the largest median reduction in terms of PI_{50} happens when a second antenna is added to a single on-body antenna. Using a geomet-

ric averaging the median values of the PI_{50} for a **single** antenna placed on the 12 studied positions are 6.7 dB and 5.8 dB in the 'Indoor Pico-cell' and 'Urban Macro-cell' at 950 MHz, respectively, while these values are 11 dB and 8.3 dB in the 'Indoor Pico-cell' and 'Urban Macro-cell' at 2450 MHz, respectively. A combination of **two** antennas reduces these median values to 3.5 dB and 3.3 dB in the 'Indoor Pico-cell' and 'Urban Macro-cell' at 950 MHz, respectively, and 4.9 dB and 4.1 dB in the 'Indoor Pico-cell' and 'Urban Macro-cell' at 2450 MHz, respectively.

Similar results are found for the arithmetically averaged responses in Figure 5.11 (b), where the median PI_{50} values for a **single** antenna worn on one of the 12 zones are 6.1 dB and 5.3 dB in the 'Indoor Pico-cell' and 'Urban Macro-cell' at 950 MHz, respectively, and 11 dB and 8.0 dB in the 'Indoor Pico-cell' and 'Urban Macro-cell' at 2450 MHz, respectively. For a combination of **two** antennas, these are reduced to median values of 2.9 dB and 3.0 dB respectively in the 'Indoor Pico-cell' and 'Urban Macro-cell' at 950 MHz, and 3.1 dB and 2.9 dB , respectively in the 'Indoor Pico-cell' and 'Urban Macro-cell' at 2450 MHz, see Figure 5.11 (b). Also note that using more than two antennas reduces the median responses even further.

The distribution of the responses is such that the arithmetic spatial averaging causes less variance than the geometric averaging. This results in lower PI_{50} values in Figure 5.11 (b) (arithmetic averaging) compared to Figure 5.11 (a) (geometric averaging). The large reduction in variation when adding a second antenna to the PDE, can be explained by the negative correlation (or covariance) that exists between the responses on the front and the back of the VFM's body.

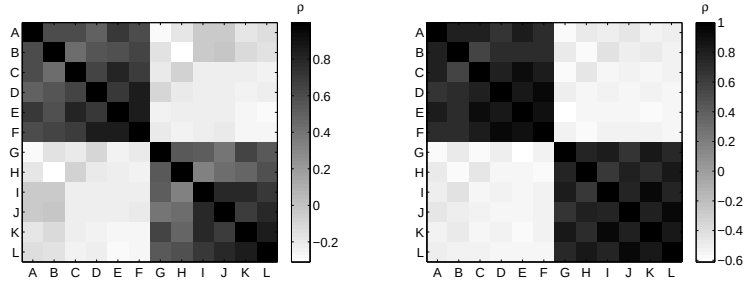

(a) 950 MHz (b) 2450 MHz

Figure 5.12: Correlation between the responses in the 'Urban Macro-cell' scenario.

Figure 5.12 shows the correlation between the responses arithmetically averaged over the 12 considered zones, at 950 MHz (Fig. 5.12 (a)) and 2450 MHz (Fig. 5.12 (b)) in the 'Urban Macro-cell' scenario. Similar results are obtained in

the 'Indoor Pico-cell' environment. The zones that are located on the same side of the body (front or back) show a clear positive correlation between 0.43 and 0.85 at 950 MHz and between 0.57 and 0.93 at 2450 MHz, while zones located on opposite sides of the body are negatively correlated with values between -0.022 and -0.29 at 950 MHz and between -0.43 and -0.61 at 2450 MHz. This negative correlation (or normalized covariance) explains the reduction in variance (or in this case PI_{50}) when two responses are averaged. The variance of responses averaged over N zones is given by:

$$Var(\frac{1}{N}\sum_{i=1}^{N} R_i) = \frac{1}{N^2}\sum_{i=1}^{N} Var(R_i) + \frac{1}{N^2}\sum_{i=1}^{N}\sum_{j=1}^{N} Cov(R_i, R_j)(1-\delta_{ij}) \tag{5.27}$$

with Var(), the variance of its input, Cov() the covariance of its input, and $\delta_{ij} = 1$ if $i = j$ and $\delta_{ij} = 0$ if $i \neq j$. If the responses R_i would be uncorrelated ($Cov(R_i, R_j) = 0$) then the variation of the average would be the sum of the individual variances divided by the number of uncorrelated responses. This would mean that the variance reduces if the number of used antennas (N) increases. In the special case of an average over two uncorrelated sensors that have a response with the same variance, which is not the case here, the variance would decrease with a factor of 2. In case the case of negatively correlated responses ($Cov(R_i, R_j) < 0$), then this reduction in variance is even higher, because of the negative term in Equation 5.27. This is the case for combinations of an antenna worn on the front and an antenna worn on the back. Equation 5.27 also shows than when two positively correlated responses are combined ($Cov(R_i, R_j) > 0$), the variance might be reduced, due to the increased number of used antennas, but will be less reduced due to the positive covariance term. This is the case when two antennas on the same side of the body are combined. Since the responses studied in this chapter are not normally distributed, we have chosen to work with rank-based quantities, such as the PI_{50}, to quantify the variation on the response. The same principles described here (in Eq. 5.27) for the variance also apply to the PI_{50}, but no closed expressions exist for unknown distributions.

Figure 5.12 also explains why the reduction in variance or PI_{50} decreases with an increasing number of antennas. As soon as two antennas are chosen, it is impossible to add another antenna from this set that is not positively correlated with one of the two previously chose antennas. Since the positive correlations are higher than the negative ones, the reduction in variance must be smaller when adding a third, fourth, etc. antenna to the previous set of antennas.

Table 5.4 lists the differences between the median PI_{50} values ($\Delta_{N,N+1}$) when a $(N+1)^{th}$ antenna is added to a set of N antennas in the two studied

$\Delta_{N,N+1}$ (dB)	$\Delta_{1,2}$	$\Delta_{2,3}$	$\Delta_{3,4}$	$\Delta_{4,5}$	$\Delta_{5,6}$	$\Delta_{6,7}$	$\Delta_{7,8}$	$\Delta_{8,9}$	$\Delta_{9,10}$	$\Delta_{10,11}$	$\Delta_{11,12}$
(a)	-3.2	-0.1	-0.2	-0.2	-0.1	-0.1	-0.1	-0.1	-0.05	+0.1	-0.09
(b)	-2.3	-0.3	-0.2	-0.2	-0.1	-0.02	-0.04	-0.06	-0.03	-0.04	-0.04
(c)	-7.0	+0.03	+0.3	-0.9	+0.1	-0.4	+0.1	-0.2	-0.1	-0.1	-0.1
(d)	-5.1	-0.1	+0.1	-0.6	+0.04	-0.3	+0.003	-0.1	-0.03	-0.06	-0.07

Table 5.4: Difference ($\Delta_{N,N+1}$) between the median PI_{50} values of all combinations of $N+1$ and N zones, with $N = 1..11$. Each row presents values for (a) 'Indoor Pico-cell' at 950 MHz, (b) 'Urban Macro-cell' at 950 MHz, (c) 'Indoor Pico-cell' at 2450 MHz, and (d) 'Urban Macro-cell' at 2450 MHz, using arithmetic averaging.

environments and at the two studied frequencies. $\Delta_{N,N+1}$ is defined as:

$$\Delta_{N,N+1} = p_{50}(PI_{50}(N)) - p_{50}(PI_{50}(N+1)) \tag{5.28}$$

with $p_{50}(PI_{50}(N))$ the median value of all the PI_{50} values of all combinations of N zones drawn from 12 zones. In Table 5.4 the main reduction in PI_{50} is obtained when adding the second antenna. The addition of the other antennas amounts to a total additional reduction which is smaller than the reduction obtained by adding the second antenna. These results are important, because they show that it is useful to employ multiple antennas on the body, in order to reduce the measurement uncertainty, but they also show that it has limited use to deploy a large number of antennas, since the additional gain in measurement uncertainty will be relatively small.

In Section 3.4.5 of Chapter 3 the variance on the percentiles of the distribution of R_i is determined to be smaller than 3.7%, which corresponds to an interval of ± 0.16 dB. A large number of the $\Delta_{N,N+1}$ values with $N > 1$ shown in Table 5.4 are smaller than this variance. Therefore it cannot be determined whether these changes in median PI_{50} value are caused by chance or by the addition of an extra antenna. Mutiple antennas have to be added in order to obtain a significant reduction in the PI_{50}. For example, $\Delta_{2,3} = -0.1$ dB in the 'Indoor Pico-cell' scenario at 950 MHz, which is smaller than the variance on the PI_{50} values, but the sum of $\Delta_{2,3} + \Delta_{3,4} = -0.3$ dB, which is larger than 0.16 dB. The $\Delta_{1,2}$ values are all larger than 0.16 dB in amplitude.

Using an arithmetic averaging, see Figure 5.11 (b), the PI_{50} will ultimately reduce to a value of 1.9 dB (1.8 dB for the 'Urban Macro-cell' scenario at 2450 MHz). It will not be possible to obtain a PI_{50} value lower than this, using this set-up on the body. A further reduction will only be possible when other (uncorrelated) locations on the body would be investigated. However, these locations have the disadvantage that they are either moving during measurements and therefore difficult to calibrate using numerical simulations or calibration measurements, see Chapter 6, or are unsuitable for placing an antenna that does not hinder subjects during their

daily activities. This is also illustrated in Figure 5.8, where the step-wise linear regression succeeds in reducing the PI_{50} to a value lower than 1.9 dB (1.0 dB), because also other locations on the VFM are allowed besides the VFM's torso. Although this might seem an interesting option to reduce measurement uncertainty, practically it will be difficult to use these positions during a real measurement, see Chapter 6. Using a geometric averaging, see Figure 5.11 (a), the PI_{50} will ultimately reduce to values of 2.5 dB and 2.3 dB in the 'Indoor Pico-cell' and 'Urban Macro-cell' scenario at 950 MHz, respectively, and to 4.0 dB and 3.2 dB in the 'Indoor Pico-cell' and 'Urban Macro-cell' scenario at 2450 MHz, respectively. These values are higher - the values for the single antennas are higher as well - which indicates that a spatial, arithmetic average leads to a lower variation on the response, given the distributions of R_i on the different potential locations.

In Chapter 4 the reduction $\Delta_{1,2}$ in the PI_{50} values of a combination of two conventional exposimeters worn on the two hips of a subject is studied. The reductions are -3.3 dB and -4.7 dB for the right hip and left hip, respectively, compared to an average over both hips in the GSM 900 DL band. These values are higher than the median reductions shown in Table 5.4 at 950 MHz, which was to be expected since the two exposimeters are located on diametrically opposite locations of the body and are thus expected to have a larger reduction in PI_{50} than the median reduction found for two zones on the body, which includes zones on the same side of the torso. For WiFi 2G $\Delta_{1,2}$ values of 3.0 dB and 4.1 dB are measured in Chapter 4, see Fig. 4.6. These reductions are smaller than the median reductions shown in Table 5.4 at 2450 MHz, but were expected to be larger since the PEMs are located on two opposite locations of the body. This unexpected behavior might be attributed to the presence of the arms near the PEMs when they are worn on the hips and the different distribution chosen for the polarization of the WiFi 2G signals in Chapter 4 in comparison to the simulations executed in this chapter. In [1] a $\Delta_{1,2}$ of 3.8 dB is measured in the GSM 900 DL band and a value of 7.9 dB is measured in the WiFi 2G band. These values are higher than the median reductions shown in Table 5.4, which was expected since they are obtained by combining two exposimeters located on diametrically opposite locations on the body.

5.4.3 Numerical Simulations of Textile Antennas

Figure 5.13 shows a polar plot of the Directive Gain in the VFM's azimuthal plane of one of the textile antennas placed vertically on position A on the VFM. The co-polarized gain (in black) - where the incident polarization is parallel to the antenna's - is obviously higher than the cross-polarized gain (in grey). The maximal directive gain is 3.2 dBi at $\phi = 2°$. The main lobe of the directive gain is located in the fourth quadrant, because the antenna is also located in this quadrant on the body. The directive gain is much lower in the second and third quadrant because

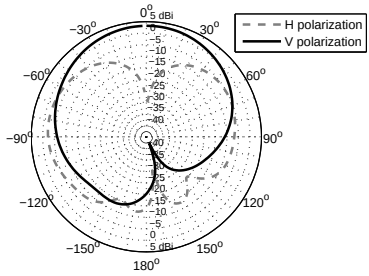

Figure 5.13: Directive gain of a model of a textile antenna placed vertically polarized on position A (see Fig.5.5) at 950 MHz in the VFM's azimuthal plane.

the body is blocking incident radiation from reaching the antenna at these angles. Table 5.5 lists the main performance characteristics of the antenna on the body: the power reflection coefficient (S_{11}), the mismatch efficiency (η_{mis}), the radiation efficiency (η_{rad}), and the on-body directive gain. The listed values are the mean values and standard deviations, calculated over all 12 studied positions and two studied orientations of the on-body antennas.

on-body performance characteristics	
S_{11}	-14 ± 2.7 dB
η_{mis}	0.53 ± 0.056
η_{rad}	0.96 ± 0.032
Gain	3.1 ± 1.1 dBi

Table 5.5: Average performance characteristics of the textile antenna on the body of the VFM at 950 MHz.

The directive gain and properties of the different on-body antennas and Equations 5.13 to 5.18 are then used to determine the AA_i^{mp}. This results in distributions for every AA_i^{mp}. From the distribution of these antenna apertures, the PI_{50} values and median antenna apertures are determined. The single antennas have an average median multi-path antenna aperture of 9.8 ± 5.7 cm^2 in the 'Indoor Pico-cell' scenario and 10 ± 5.0 cm^2 in the 'Urban Macro-cell' scenario. The distribution of the PI_{50} values is shown in Figure 5.14.

Figure 5.14 shows the distribution of the PI_{50} of the response of a combination of N antennas placed either horizontally or vertically polarized on positions A to L, shown in Figure 5.5. The 50% confidence interval on these values determined using a 100 repetitions of the determination of the PI_{50} values in the same environments is smaller than 0.35 dB. The PI_{50} decreases with increasing number

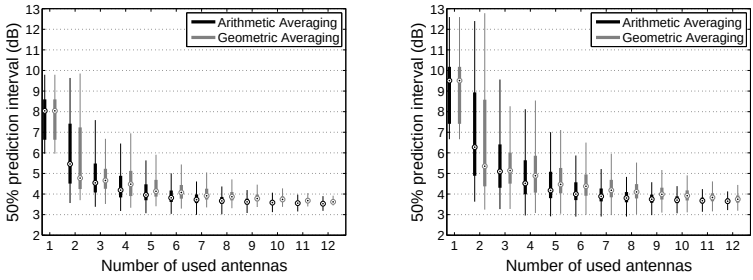

(a) Urban Macro-cell (b) Indoor Pico-cell

Figure 5.14: Boxplot of the distribution of the simulated PI_{50} in two scenarios as a function of the number of antennas. The grey boxes indicate the distribution of the PI_{50} using a geometric averaging, while the black boxes indicate the distribution using an arithmetic averaging. Outliers are suppressed in this figure.

of antennas, which is logical due to the $1/N^2$ dependence of the variation on the number of used antennas based on Equation 5.27. The largest reduction in PI_{50} is again found for the situation where a second antennas is added to the first antenna. The single antennas have median PI_{50} values of 9.5 dB and 8.0 dB in the 'Indoor Pico-cell' and 'Urban Macro-cell' scenarios, respectively. These values are larger than the ones found in the previous section using the electric fields near the body of the VFM. The linear polarization and radiation pattern of the antennas thus introduce more variation in the antenna aperture. These values are reduced to median PI_{50} values of 5.5 dB and 4.8 dB when averaging arithmetically or geometrically over 2 antennas, respectively, in the 'Urban Macro-cell' scenario. Similar reductions are found in the 'Indoor Pico-cell' scenario. The median PI_{50} values are 6.3 dB and 5.3 dB when averaging arithmetically or geometrically over 2 antennas, respectively.

Figure 5.15 shows the correlations between the antenna apertures for one of the bootstrap sample sets used to determine the distribution of the antenna aperture in the 'Urban Macro-cell' scenario. The correlations between the antennas on the same side of the body are positive, between 0.66 and 0.95 for the co-polarized case and between 0.38 and 0.70 in the cross-polarized case, while the correlation between antennas on opposite sides of the body is predominantly negative, between -0.29 and 0.09 in the co-polarized case and between -0.29 and -0.16 in the cross-polarized case. Note that there are positive correlations between horizontally polarized antennas on the front and back of the VFM. For example, the correlation between horizontally polarized textile antennas placed on position D and I is 0.041. The correlations are similar to those shown in Figure 5.12 (a). This causes a similar reduction in median PI_{50} when using an arithmetic averaging over two

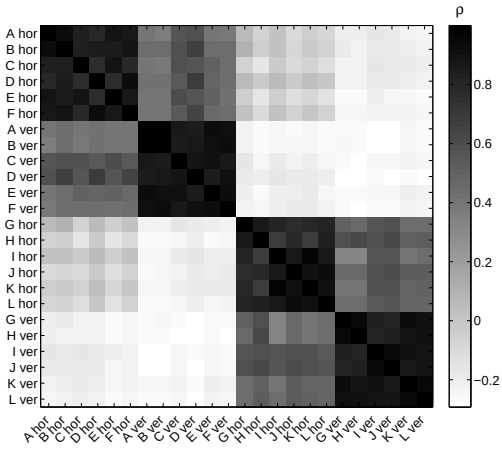

Figure 5.15: Correlation coefficient of the linear multi-path antenna apertures in the 'Urban Macro-cell' scenario for the simulated textile antenna placed horizontally (hor) or vertically (ver) on positions A to L on the VFM.

antennas: 2.5 dB and 3.2 dB in the 'Urban Macro-cell' and 'Indoor Pico-cell' scenarios, respectively, when simulations including the antennas are used, while these reductions are 2.3 dB and 3.2 dB in the 'Urban Macro-cell' and 'Indoor Pico-cell' scenarios, respectively, when simulations of the PDE's response are used without the antennas present (see Fig.5.11).

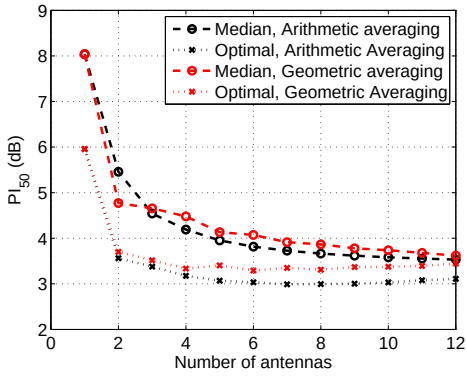

Figure 5.16: Median and minimum PI_{50} as a function of the number of used antennas, selected from antennas placed either horizontally or vertically on positions A to L in the 'Urban Macro-cell' scenario.

Figure 5.16 shows the median values of the boxplots of the PI_{50} in the 'Urban Macro-cell' scenario shown in Figure 5.14 (a), together with the PI_{50} of the combination with the lowest PI_{50} of all combinations C_{12}^{N}. This clearly illustrates again how both averaging techniques cause a reduction in PI_{50} on the median antenna aperture. Note that the median value and the optimal value do not have to be the same in this case since there are still 2^{12} possibilities to place the antennas on the 12 locations on the body.

Figure 5.16 shows that there is a small increase in optimal PI_{50} when the received power on more than 4 antennas is geometrically averaged. Note that adding an extra antenna to a set of antennas does not necessarily reduce the PI_{50} value since there exist positive correlations between the additional antenna and the antennas that are already in the optimal set of antennas. To obtain an additional reduction in PI_{50}, other locations on the human body have to be explored.

$\Delta_{N,N+1}$ (dB)	$\Delta_{1,2}$	$\Delta_{2,3}$	$\Delta_{3,4}$	$\Delta_{4,5}$	$\Delta_{5,6}$	$\Delta_{6,7}$	$\Delta_{7,8}$	$\Delta_{8,9}$	$\Delta_{9,10}$	$\Delta_{10,11}$	$\Delta_{11,12}$
(a)	-2.5	-1.0	-0.3	-0.2	-0.2	-0.1	-0.07	-0.04	-0.04	-0.02	-0.03
(b)	-3.2	-0.11	-0.2	-0.4	-0.07	-0.2	-0.04	-0.09	-0.04	-0.06	-0.06
(c)	-3.2	-1.2	-0.6	-0.3	-0.2	-0.1	-0.1	-0.1	-0.04	-0.04	-0.02
(d)	-4.2	-0.2	-0.2	-0.4	-0.09	-0.2	-0.1	-0.1	-0.1	-0.1	-0.1

Table 5.6: Difference ($\Delta_{N,N+1}$) between the median PI_{50} values of all combinations of $N+1$ and N antennas, with $N = 1..11$. Each row presents values for (a) 'Urban Macro-cell' and arithmetic averaging, (b) 'Urban Macro-cell' and geometric averaging, (c) 'Indoor Pico-cell' and arithmetic averaging, (d) 'Indoor Pico-cell' and geometric averaging.

Table 5.6 lists the median reductions in PI_{50} ($\Delta_{N,N+1}$, see Eq. 5.28) for the two studied environments and the two studied averaging methods. $\Delta_{1,2}$ is larger than the sum of the other $\Delta_{N,N+1}$. This is in agreement with the results presented in Table 5.4 using 12 on-body zones. The resulting cumulative reduction in PI_{50} are higher than those obtained without the antenna models. Cumulative reduction of 5.9 dB and 4.5 dB are found when averaging arithmetically over 12 antennas using FDTD simulations of the textile antennas in the 'Indoor Pico-cell' and 'Urban Macro-cell' environments, respectively, while these cumulative reductions are 4.3 dB and 3.3 dB using the responses averaged arithmetically over 12 zones in the same environments. However, the PI_{50} of the AA_i^{mp} of the single antennas are higher than that found for the responses in the single zones, which results in higher values when using 12 antennas.

The same conclusions as drawn in the previous section thus hold: the PI_{50} can be reduced when using multiple antennas, but the reduction decreases as a function of the number of used antennas. The 50% confidence interval on the PI_{50} values is smaller than 0.35 dB, determined by 100 repetitions of the experiment. All the

values of $\Delta_{N,N+1}$ for $N > 7$ are smaller than half this value, so the reduction in PI_{50} is within the confidence interval on the PI_{50} values. The cumulative reduction when more than one antenna is added to a set of seven antennas, can be significant.

It is already mentioned that the $\Delta_{1,2}$ values are comparable for the simulations using 12 zones and the simulations using the antennas. In Chapter 4 the reductions $\Delta_{1,2}$ for an arithmetic averaging of the responses of two conventional PEMs are -3.3 dB and -4.7 dB for the right hip and left hip, respectively, compared to an average over both hips in the GSM 900 DL band. In [1] a $\Delta_{1,2}$ of -3.8 dB is measured in the GSM 900 DL band. These values are higher than the median reductions using arithmetic averaging shown in Table 5.6, because the negative correlation between diametrically opposite locations on the body is larger in amplitude than the median correlation between two antennas worn on the upper torso (and thus potentially on the same side).

5.4.4 Comparing Different Design Approaches

In the previous subsection, the results of different design approaches to construct a PDE were presented and discussed. All the different approaches show that equipping a subject with multiple antennas will reduce the variation on the PDE's response or antenna aperture and consequently the measurement uncertainty caused by the presence of the human body. The (dis)advantages of the different design approaches are discussed in this subsection.

The **step-wise, linear regression** is a computationally simple technique to obtain a set of locations on the human body to deploy antennas. The technique has the advantage that it only requires $\sum_{i=1}^{N_{ant}} (N_{body} - i + 1)$ calculations of the error-on-prediction to select a certain set of antennas, with N_{body} the number of potential locations on the body and N_{ant} the number of antennas to be placed on the body, whereas a full solution would require $2^{N_{body}}$ calculations. This is often a number too large to handle computationally (in our case 2^{401}). Another advantage is that incorporation of the different projections of the electric field on the human body (E_i^{tan} and E_i^{lin}) is straightforward, since it only requires the addition of more values (N_{body}) to the vector of potential electric field strengths. A disadvantage of this technique is that it does not necessarily provide the optimal solution to place the antennas on the body, since a step-wise approach is followed. Another disadvantage is that the solution provided by the algorithm is quite sensitive to small changes in the input parameters, the properties of the exposure samples, since it essentially looks for an outlier in the data. Finally, the algorithm only provides us with one set-up for every number of antennas (N_{ant}) and does not provide any statistical data on how sets of antennas on the body behave.

Placing two antennas on **diametrically opposite locations** of the body is probably the most easily implementable approach in reality and could be executed even

with the existing PEMs. We demonstrated that this approach will reduce the measurement uncertainty, due to the negative correlation between the responses on the front and back of the body. The main disadvantage of this technique is that it does not use the full potential of distributing antennas on the body. The main reduction in variation of the response is indeed made when two antennas are used on the front and the back, see Sections 5.4.2 and 5.4.3, but additional (smaller) reductions are possible using more antennas.

The technique where the antennas are distributed on different **on-body zones** seems to entail a balance between keeping the distributed concept and reproducibility. The zones considered in section 5.4.2.2 are distinct enough to avoid imprecise placement of the antennas. Since 12 zones are considered, the distributed concept of a PDE can be exploited more and an additional reduction in variation is possible on top of the first reduction when adding a second antenna on a diametrically opposite location on the body. However, further reductions will always be smaller due to the correlation between the positions on the same side of the human body. The main disadvantage of this technique is the computational demand: first, the electric fields have to be determined on the body using the approach outlined in Chapter 3. In a second step, these have to be averaged over the different zones, and then, all 12! combinations of zones are studied. Another disadvantage is that a linear projection of the response is difficult to be taken into account due to the computational demand. The number of necessary calculations will increase with the number of considered linear polarizations (N_p) since the total number of combinations would amount to $\sum_{i=1}^{12} C_{12}^{i} N_p^i$. The advantage of this technique is that not only an optimal combination of antenna locations is provided, but also the distribution of all the potential combinations of antennas on the body. This provides us with more information on the behavior of sets of antennas on the body, than the two previously discussed techniques.

The previous techniques use (projected) on-body electric-field strengths to determine the on-body response of exposimeters worn by a subject. These techniques provide general insights on how the measurement uncertainty on the incident power density depends on the number of used nodes. However, in reality a PDE will be constructed using textile antennas and therefore the antenna properties have to be taken into account, see Eq. 5.13. Therefore, a design based on **numerical simulations of textile antennas** was investigated. This technique has the same advantages as the approach where 12 on-body zones are considered: the simulations are reproducible in reality, make use of the potential of the human torso to distribute antennas, and provide information on the statistics of sets of antennas on the body. Another advantage is that this technique requires less computational effort than the previous techniques, since the electric fields on the body do not have to be computed (only the aperture of the antennas is required). All the information can be obtained from FDTD simulations using single textile antennas

(if the mutual coupling between the antennas is negligible [32], see Chapter 6). A final advantage is, that this technique is the most realistic for modeling of a real PDE that can be obtained using numerical simulations, since both heterogeneous models for the phantom and the antennas are used. A disadvantage of this technique is that it requires an extra effort to model the antennas in the software that is used for the FDTD simulations. Another disadvantage is that the results are antenna-dependent and therefore less generally applicable than the previously discussed techniques.

All the techniques used in this chapter depend upon numerical simulations. These simulations have some **disadvantages compared to calibration measurements**. The first disadvantage is that simulation models have to be used both for the human subject and the antenna, which will deviate from reality. A second disadvantage is that the real positioning of the antennas on the body is impossible to reproduce in a simulation in comparison to the antennas that are worn on the body in reality. A third disadvantage is that the inclusion of extra frequency bands has a large simulation cost in some of the approaches, due to the large number of necessary simulations, whereas for calibration measurements it suffices to design and construct a new antenna. The numerical simulations do have the advantage that they can easily include the effect of the polar angle and phase of the incident plane waves, which is difficult to include using calibration measurements. The comparison between numerical simulations and calibration measurements is elaborated in the next chapter.

5.5 Conclusions

This chapter investigated the potential of a personal, distributed exposimeter (PDE) for the reduction of the measurement uncertainty caused by the presence of the human body on the incident power density. To this aim, first, the design specifications of a PDE were investigated, and second, different design approaches were investigated using numerical simulations.

A PDE should counter the disadvantages of conventional personal exposimeters (PEMs) investigated in the two previous chapters. The underestimation of the incident power densities by PEMs should be compensated and the measurement uncertainty caused by the presence of the body should be reduced. Appropriate dynamic ranges and detections schemes should be employed, in order to correctly record the exposure in different frequency bands. The frequency bands that should be measured by a PDE were listed and discussed.

Besides technical requirements, a PDE should also fulfill some epidemiological requirements, in order to provide reliable and unbiased measurements of a subject's personal exposure. A PDE should be robust, pose low requirements on a subject, and should be invisible for others. Measurements over longer periods of

time should be possible and measured values cannot be visible for subjects wearing the device.

Textile antennas are chosen as body-worn RF antennas for the fabrication of a PDE. These antennas can be worn without impeding movement of the human body, while maintaining their characteristics. They can be made robust and have good antenna performance. Moreover, they can potentially be integrated in clothing.

Numerical simulations are executed to investigate the design of a PDE. In a first approach, a step-wise linear regression is used to simultaneously determine locations on the body to employ antennas the error-on-prediction of the antennas on the incident field strength on these locations. This approach is demonstrated in the 'Indoor Pico-cell' at 950 and 2450 MHz. This approach proves that is it possible to reduce the error-on-prediction when multiple antennas on-the body are used.

In a second approach, two antennas are placed on the front and back of the VFM. Using this approach, we prove that any combination of an antenna placed on the front and the back of the VFM will cause a reduction in the 50% prediction interval (PI_{50}), due to the negative correlation between the responses on the front and the back. The largest reduction in PI_{50} is obtained using a weighted, arithmetic average. Using this averaging, the knowledge of the response determined using the full electric field strength will result in a lower PI_{50} than when only a projection of the response in the tangential plane to the VFM's body surface is known.

A third approach, divides the torso of the VFM in 12 zones: six at the front and six at the back, in order to have a more reproducible set-up on the body. The responses of all the combinations of N antennas from 12 are studied at 950 and 2450 MHz in both the 'Indoor Pico-cell' and 'Urban Macro-cell' scenarios and show that the PI_{50} on the response can be reduced using multiple antennas placed on the body. The largest reduction in PI_{50} is obtained when a pair of antennas is considered in comparison to a single antenna. This is due to the negative correlation between the responses on the front and the back of the VFM. Adding more antennas to this pair will further reduce the PI_{50}, but smaller reductions are found.

In a fourth approach, numerical simulations of on-body textile antennas are used to determine the antennas' on-body antenna aperture (AA). This AA can be determined for multi-path exposure and will have a certain distribution, which is characterized by its PI_{50}. This PI_{50} shows a similar reduction when multiple antennas are used than the previous approach. The median reduction in PI_{50} is smaller, due to a smaller negative correlation between the antennas placed on the front and the back. The reductions in PI_{50} are smaller if more antennas are added.

The different approaches are discussed and their (dis)advantages are compared. In general, a PDE seems a viable approach to reduce the measurement uncertainty caused by the human body, as all the design approaches suggest that the variation

on the response of a PDE will reduce if multiple antennas are used on the body. However, since the relative reduction in variation becomes smaller as more antennas are added, it is unnecessary to use a large number of antennas. A PDE with a limited number of antennas will have a comparable measurement uncertainty. In the following chapter, calibration measurements (using a method similar the the fourth approach in this chapter) are used to characterize a PDE for multiple frequencies on a real human subject.

5.6 Acknowledgment

The author would like to thank S. Gängler and prof. dr. M. Röösli for their contributions to the epidemiological design aspects of a personal exposimeter, see Subsection 5.2.2.

References

[1] J F B Bolte, G van der Zande, and J Kamer. *Calibration and uncertainties in personal exposure measurements of radiofrequency electromagnetic fields.* Bioelectromagnetics, 32(8):652–63, December 2011.

[2] S Iskra, R McKenzie, and I Cosic. *Monte Carlo simulations of the electric field close to the body in realistic environments for application in personal radiofrequency dosimetry.* Radiation Protection Dosimetry, 147(4):517–27, 2011.

[3] G Neubauer, S Cecil, W Giczi, P Preiner, J Frölich, and Martin Röösli. *The Association Between Exposure Determined by Radiofrequency Personal Exposimeters and Human Exposure: A Simulation Study.* Bioelectromagnetics, 31(7):535–45, 2010.

[4] A Thielens, H De Clercq, S Agneessens, J Lecoutere, L Verloock, G Declercq, Fand Vermeeren, E Tanghe, H Rogier, R Puers, L Martens, and W Joseph. *Personal distributed exposimeter for radio frequency exposure assessment in real environments.* Bioelectromagnetics, 34(7):563–7, 2013.

[5] P Frei, E Mohler, G Neubauer, G Theis, A Bürgi, J Frölich, C Braun-Fährländer, J Bolte, M Egger, and M Röösli. *Temporal and spatial variability of personal exposure to radio frequency electromagnetic fields.* Environmental research, 109(6):779–85, August 2009.

[6] W Joseph, G Vermeeren, L Verloock, M Masache Heredia, and L Martens. *Characterization of personal RF electromagnetic field exposure and actual*

absorption for the general public. Health physics, 95(3):317–30, September 2008.

[7] W Joseph, P Frei, M Roösli, G Thuróczy, P Gajsek, T Trcek, J Bolte, G Vermeeren, E Mohler, P Juhász, V Finta, and L Martens. *Comparison of personal radio frequency electromagnetic field exposure in different urban areas across Europe.* Environmental research, 110(7):658–63, October 2010.

[8] U Knafl, H Lehmann, and M Riederer. *Electromagnetic field measurements using personal exposimeters.* Bioelectromagnetics, 29(2):160–2, February 2008.

[9] G Neubauer, M Feychting, Y Hamnerius, L Kheifets, N Kuster, Io Ruiz, J Schüz, R Uberbacher, J Wiart, and M Röösli. *Feasibility of future epidemiological studies on possible health effects of mobile phone base stations.* Bioelectromagnetics, 28(3):224–30, April 2007.

[10] M Röösli, P Frei, E Mohler, C Braun-Fahrländer, A Bürgi, J Fröhlich, G Neubauer, G Theis, and M Egger. *Statistical analysis of personal radiofrequency electromagnetic field measurements with nondetects.* Bioelectromagnetics, 29(6):471–8, September 2008.

[11] J F Viel, E Cardis, M Moissonnier, R de Seze, and M Hours. *Radiofrequency exposure in the French general population: band, time, location and activity variability.* Environment international, 35(8):1150–4, November 2009.

[12] O Lauer, G Neubauer, M Röösli, M Riederer, P Frei, E Mohler, and J Fröhlich. *Measurement setup and protocol for characterizing and testing radio frequency personal exposure meters.* Bioelectromagnetics, 33:75–85, 2012.

[13] A Thielens, G Vermeeren, W Joseph, and L Martens. *Stochastic Method for the Determination of the Organ-specific Averages SAR in Realistic Environments at 950 MHz.* Bioelectromagentics, 34(7):549–562, 2013.

[14] Satimo. *Certificate of Calibration (EME SPY 140).* Brest, France, 2010.

[15] W Joseph, L Verloock, F Goeminne, Günter Vermeeren, and Luc Martens. *Assessment of RF exposures from emerging wireless communication technologies in different environments.* Health Physics, 102:161–172, 2012.

[16] L Verloock, W Joseph, G Vermeeren, and L Martens. *Procedure for assessment of general public exposure from WLAN in offices and in wireless sensor network testbed.* Health Phys., 98(4):628–638, 2010.

[17] M Berglund, C G Elinder, and L Järup. *Human Exposure Assessment* . ed. WHO, 2001.

[18] S M Mann, D S Addison, R S P Blackwell, and M Khalid. *Personal Dosimetry of RF Radiation: Laboratory and Volunteer Trials of an RF Dosimeter*. Health Protection Agency, Chilton, UK, 2005.

[19] E Mohler, P Frei, C Braun-Fahrländer, M Röösli, and the Qualifex-team. *Exposure to Radiofrequency Electromagnetic Fields and Sleep Quality: A Prospective Cohort Study.* Plos One, 7(5), 2012.

[20] J F Viel, M Tiv, M Moissonnier, E Cardis, and M Hours. *Variability of radiofrequency exposure across days of the week: A population-based study.* Environmental Research, 111(4):501–513, 2011.

[21] A Dierck, T De Keulenaer, F Declerq, and H Rogier. *A wearable active GPS antenna for application in smart textiles*. Proceedings of the 32nd ESA Antenna workshop on Antennas for Space Applications, 2010.

[22] A Thielens, S Agneessens, H De Clerq, J Lecoutere, L Verloock, E Tanghe, S Aerts, R Puers, H Rogier, L Martens, and W Joseph. *On-Body Calibration and Measurements using a Personal, Distributed Exposimeter for Wireless Fidelity.* Health Physics, page accepted, 2014.

[23] Belgian Institute for Postal services and Telecommunications (BIPT). *www.bipt.be*.

[24] S Agneessens, P Van Torre, F Declerq, G J Spinnewyn, H Stockman, and H. Rogier. *Design of a wearable, low-cost, through-wall doppler radar system.* Int. J. Antennas and Propagation, 2012.

[25] A Pantelopoulos and N Bourbakis. *Asurveyonwearable sensor- based systems for health monitoring and prognosis.* IEEE Trans. Syst., Man, Cybern.C,Appl. Reviews, 40(1):1–12, 2010.

[26] A Dierck, S Agneessens, F Declercq, B Spinnewyn, GJ Stockman, P Van Torre, L Vallozzi, D Vande Ginste, T Vervust, J Vanfleteren, and H Rogier. *Active textile antennas in professional garments for sensing, localisation and communication*. International Journal of Microwave and Wireless Technologies, 6:331, 2014.

[27] ML Scarpello, I Kazani, C Hertleer, H Rogier, and D Vande Ginste. *Stability and Efficiency of Screen-Printed Wearable and Washable Antennas.* IEEE antennas and wireless propagation letters, 11:838–841, 2012.

[28] S Agneessens and H Rogier. *Compact Half Diamond Dual-Band Textile HMSIW On-Body Antenna.* IEEE Transactions on Antennas and Propagation, 162(5):2374–2381, 2014.

[29] K Lui, O Murphy, and C Toumazou. *A wearable wideband circularly polarized textile antenna for effective power transmission on a wirelessly-powered sensor platform.* IEEE Transactions on Antennas and Propagation, 61(57):3873–3876, 2013.

[30] F Declerq, A Georgadis, and H Rogier. *Wearable aperturecoupled shorted solar patch antenna for remote tracking and monitoring applications.* Proceedings of the 5th European Conference on Antennas and Propagation (EUCAP). Rome, Italy., 2011.

[31] R Moro, S Agneessens, H Rogier, and M Bozzi. *Wearable textile antenna in substrate integrated waveguide technology.* Electron. Lett., 48(16):985–986, 2012.

[32] C A Balanis. *Antenna Theory: Analysis and Design*. 1982.

[33] A Christ, W Kainz, E G Hahn, K Honegger, M Zefferer, E Neufeld, R Rascher, W Janka, W Bautz, J Chen, B Kiefer, P Schmitt, H P Hollenbach, J Shen, M Oberle, D Szczerba, A Kam, J W Guag, and N Kuster. *The Virtual Family–development of surface-based anatomical models of two adults and two children for dosimetric simulations.* Physics in medicine and biology, 55(2):N23–38, January 2010.

[34] C Gabriel, S Gabriel, and E Corthout. *The dielectric properties of biological tissues: I. Literature survey.* Physics in medicine and biology, 41(11):2231–49, November 1996.

6

Calibration of a Personal, Distributed Exposimeter

6.1 Introduction

A personal, distributed exposimeter (PDE) is a device consisting of body-worn antennas. It is used to measure one's personal exposure to radio frequency (RF) incident power density. In the previous chapter, numerical simulations are used to demonstrate that combining multiple measurements of the electric field strength on the body can reduce the measurement uncertainty on the incident power densities. In this chapter, a multi-frequency calibration method to determine the measurement uncertainty of a PDE is described. Following this calibration, a PDE is constructed using textile antennas [1–4] and RF receiver nodes.

6.2 Setup of On-Body Calibration Measurements

The calibration procedure proposed in this chapter is executed using measurements in an anechoic chamber, see Figure 4.2 (b) and (c). During these measurements, we have used textile antennas designed to receive signals on-body in the selected frequency bands. First, the properties of the used antennas are described. Second, the used calibration procedure for a PDE is introduced.

6.2.1 Textile Antennas

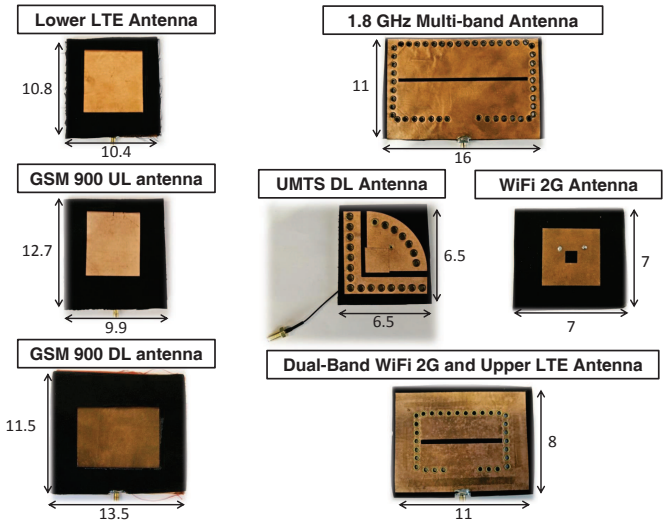

(a) Frontal view of the used antennas

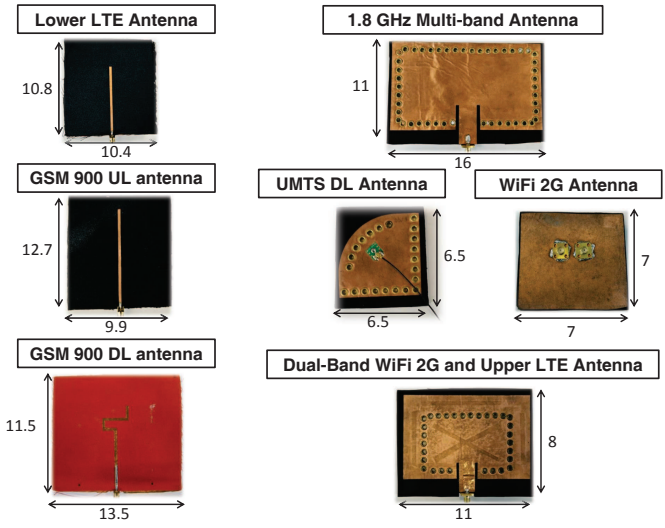

(b) Rear view of the used antennas

Figure 6.1: Illustration of the used antennas. The antenna's length and width are shown in cm. The pictures of the antennas are not to scale. The mentioned frequency bands are listed in Table 6.1.

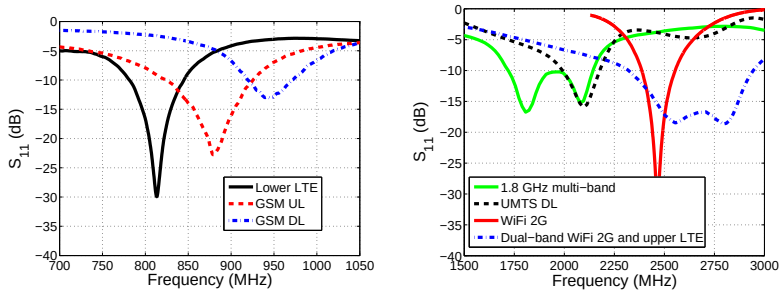

(a) (b)

Figure 6.2: Measured on-body power reflection coefficients of the used antennas. (a) S_{11} of the Lower LTE, GSM UL, and GSM DL antennas, and (b) S_{11} of the 1.8 GHz Multi-Band, UMTS DL, WiFi 2G, and Dual-Band WiFi 2G and Upper LTE antennas.

In this subsection, the textile antennas used in the research are discussed and presented. These antennas are designed and produced by the Electromagnetics Group of Ghent University. Textile antennas are introduced and discussed in Section 5.2.4. As outlined in Section 5.2.3, we only focus on frequency bands that are located above 700 MHz because they can be calibrated in the available anechoic chamber and textile antennas of wearable dimensions can be developed for these frequency bands. We have studied a total of 7 textile antennas, that cover 11 telecommunication bands of the 15 bands listed in Table 6.1. The bands listed in Table 6.1 that are not covered in this chapter are: GSM-R, since this is a telecommunication band only used by the railway operators, WIMAX, and WiFi 5G, because these bands are either not used frequently (WIMAX) or do currently not contribute significantly to the exposure (WiFi 5G), see Chapter 4 and [6, 7]. In the future the exposure in the WiFi 5G band will increase due to spectrum scarcity in the WiFi 2G band. Figures 6.1 (a) and (b) show images of the studied antennas with their respective spatial dimensions, while Figures 6.2 (a) and (b) show the power reflection coefficients (S_{11}) of the antennas. All antennas exhibit a low S_{11} (mostly <-10 dB) over the full frequency band for which they are designed. As Equation 5.13 indicates, a low S_{11} value in the band is required to have a sufficiently large antenna aperture or equivalently a sufficiently large antenna efficiency [8].

6.2.1.1 Lower LTE Antenna

The lowest measured band is covered by an aperture coupled shorted patch antenna made from textile materials [1]. This antenna type is also referred to as a planar inverted F-antenna (PIFA). The antenna, see Fig. 6.1, is linearly polarized along

Name	Frequency Range (MHz)
Lower 3GPP LTE	791-821
	832-862
GSM-R UL	876-880
GSM 900 UL	880-915
GSM-R DL	921-925
GSM 900 DL	925-960
DCS UL/ GSM 1800 UL	1710-1785
DCS DL/ GSM 1800 DL	1805-1880
DECT	1880-1900
UMTS/HSPA	1900-1920
UMTS UL / HSUPA	1920-1980
UMTS DL / HSDPA	2110-2170
WiFi 2G	2400-2483.5
Upper 3GPP LTE	2500-2570
	2575-2620
	2620-2690
WIMAX	3400-3600
WiFi 5G	5150-5350
	5470-5725
	5725-5875

Table 6.1: Name and frequency range of the frequency bands for telecommunication above 700 MHz in Belgium [5].

its feed line, located at the back of the antenna. The dimensions of the antenna are 10.4 cm $\times$ 10.8 cm $\times$ 1.2 cm (width (w) $\times$ length (l) $\times$ height (h)). The antenna contains a slotted ground plane, which minimizes the influence of the human body on the antenna's performance [1]. The antenna's conductive planes and the feed line are made from copper plated nylon, which has a sheet resistance equal to 0.18 Ω/sq. The antenna's substrate is made from a textile-compatible (polyurethane) foam material, with a thickness of 1.1 cm a relative permittivity $\epsilon_r = 1.16$ and a $tan\delta = 0.01$ at 800 MHz, while the feed's substrate is made of aramid fabric with a thickness of 0.95 mm, an $\epsilon_r = 1.97$, and a $tan\delta = 0.02$ at 800 MHz. The antenna's simulated efficiency is 76% and its gain is 2.1 dBi. The on-body power reflection coefficient of the antenna is shown in Figure 6.2 (a) and is lower than -7 dB (0.2) over the full band that needs to be covered. An S_{11} lower than -10 dB was not obtainable at the center frequency of the antenna (847 MHz) using this type of antenna, given the relatively large bandwidth (71 MHz).

6.2.1.2 GSM 900 UL Antenna

The textile antenna that covers the GSM 900 UL band (880-915 MHz) is also an aperture coupled, shorted patch antenna [1] made with the same materials described in the previous paragraph. The antenna consists of a frontal conductive plane on a textile compatible foam substrate (ϵ_r =1.16, tan δ = 0.01 at 900 MHz).

The antenna is fed by a linear feed line at the back of the antenna, which is separated from a slotted conductive plane by a layer of aramid fabric (ϵ_r= 1.97, tan δ = 0.02 at 900 MHz). The influence of the body on the antenna's characteristics is reduced using this ground plane [1]. The antenna's polarization is parallel to this feed line, see Figure 6.1. The dimensions of the antenna are 9.9 cm $\times$ 12.7 cm $\times$ 1.1 cm (w $\times$ l $\times$ h). The antenna's simulated efficiency is 77% and its gain is 2.6 dBi. An S_{11} lower than -10 dB is obtained over the full GSM 900 UL band, see Figure 6.2 (a).

6.2.1.3 GSM 900 DL Antenna

The textile antenna used for measurements in the GSM 900 DL band is the antenna presented in [1, 9] and simulated on-body in Section 5.3.4 of Chapter 5. This is an aperture coupled, shorted patch antenna [1] which covers the GSM 900 DL band (925 MHz-960 MHz). The antenna is linearly polarized and operates at quarter wavelength length to keep down the overall dimensions, resulting in a size of 13.5 cm $\times$ 11.5 cm $\times$ 1 cm (w $\times$ l $\times$ h). A picture of the front and back of the antenna are shown in Figure 6.1. The conductive parts of this antenna are fabricated using copper plated nylon fabric. The antenna's feed substrate is a foam material (ϵ_r =1.16, tan δ = 0.01 at 950 MHz), while the feed substrate is made from aramid fabric (ϵ_r= 1.68, tan δ = 0.015 at 950 MHz). The antenna has an on-body efficiency of 82% and a maximal gain of 3.1 dBi. The power reflection coefficient is shown in Figure 6.2 (a) and is lower than -10 dB (0.1) over the full GSM 900 DL band.

6.2.1.4 1.8 GHz Multi-band Antenna

A linearly polarized Substrate Integrated Waveguide (SIW) cavity backed slot antenna which is fed by a micro strip feed line, is developed to cover five different bands around 1.8 GHz [2]. The cavity induces an increased isolation of the antenna from the human body, which makes the antenna suitable for on-body use [2]. The linear polarization of the antenna is orthogonal to the slot shown in Figure 6.1. The dimensions of the antenna are 16 cm$\times$11 cm$\times$0.4 cm (w $\times$ l $\times$ h). The conducting parts of the antenna are made of copper plated nylon and the substrate is a rubber material with (ϵ_r= 1.495, tan δ = 0.016 at 1.8 GHz). The antenna's power reflection coefficient is shown in Figure 6.2 (b) and is lower than -8 dB (0.16) in the DECT, GSM 1800 UL, GSM 1800 DL, UMTS/HSPA, and the UMTS UL bands (from 1710-1980 MHz). The maximal gain of the antenna ranges from 2.5 to 5.5 dBi, depending on the band. The antenna has a simulated efficiency of approximately 70%.

6.2.1.5 UMTS DL Antenna

In order to cover the UMTS DL band (2110-2170 MHz), a quarter mode SIW antenna with folded ground plane is developed [3]. The antenna is miniaturized in the sense that it uses a magnetic wall and shorting pins placed on the outer edges and axes of symmetry of a cavity backed slot antenna in order to reduce this antenna to a quarter of its original size [3]. The antenna has an eyelet feed, which makes it more suitable for wearing it on the body, since no connectors have to be placed in between the body and the antenna. The ground plane also ensures isolation between the antenna and the body [3]. The conducting parts of the antenna are made with copper plated nylon, while the substrate is an expanded-rubber foam material (ϵ_r= 1.495, tan δ = 0.016 at 2.1 GHz). The vias and the eyelet feed have a diameter of 4 mm. The total dimensions of the antenna are 6.5 cm$\times$6.5 cm$\times$0.4 cm (w $\times$ l $\times$ h), while the antenna has a simulated efficiency around 85% and a maximal gain of 4.8 dBi. The antenna's polarization is along the symmetry axis of the antenna, shown in Figure 6.1 (a). The S_{11} of the antenna is lower than -10 dB over the full UMTS DL band.

6.2.1.6 WiFi 2G Antenna

The RF radiation in the WiFi 2G band (2400-2500 MHz) is measured using a dual-polarized patch antenna [4]. Dual polarization enables the capturing of two orthogonal components of the RF fields with one antenna, making antenna orientation with respect to the human body less critical. This antenna operates at half-wavelength length (approximate dimensions (w $\times$ l $\times$ h): 7 cm $\times$ 7 cm $\times$ 0.4 cm) and is fabricated from textile materials to ensure wearability. The conductive parts are made from copper plated nylon (σ = 0.18 Ω/sq), while the antenna substrate is a closed-cell expanded-rubber (ϵ_r = 1.49, tanδ = 0.016 at 2.45 GHz). The antenna's radiation efficiency is 66% and the maximal gain is 6.7 dBi. Figure 6.2 (b) shows the magnitude of the measured power reflection coefficient (S_{11}) of the textile antenna around the frequencies of interest. The S_{11} is smaller than -10 dB in the full WiFi 2G band.

6.2.1.7 Dual-Band WiFi 2G and Upper LTE Antenna

Another linearly polarized SIW cavity backed slot antenna which is fed by a micro strip feed line [2], is developed to cover simultaneously the WiFi 2G band (2.4-2.5 GHz) and the upper LTE band (2.5-2.69 GHz). The antenna consists of a ground plane and a slotted frontal plane, both made from copper plated nylon (sheet resistance 0.18Ω/sq at 2.45 GHz), placed on both sides of a closed-cell expanded-rubber substrate with relative permittivity $\epsilon_r = 1.495$ and tanδ = 0.016 at 2.45 GHz. The antenna is a cavity-backed slot antenna, with w x l x h = 11 cm x 8 cm x 0.4 cm. Vias (diameter = 0.4 cm) create a cavity in which a resonance of the

electric fields can occur. The cavity's walls also shield the antenna from the human body. The antenna's polarization is orthogonal to the slot shown in Figure 6.1 (a). The antenna has a maximal gain (away from the body) between 4 and 6 dBi and an efficiency of approximately 70%. The antenna's S_{11} is smaller than -10 dB in both bands.

6.2.2 Calibration Procedure

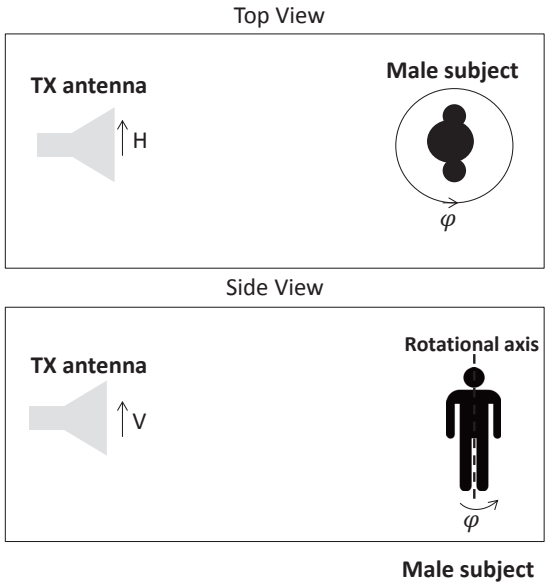

Figure 6.3: Illustration of the calibration setup in the anechoic chamber.

The calibration measurements are executed using the same setup as in [10] and Chapter 4. Figure 6.3 shows an illustration of the setup. The calibration is executed in an anechoic chamber, which is designed to provide damping of the reflected signals for the studied frequency bands. A standard gain antenna with a power reflection coefficient smaller than -10 dB in the studied frequency band is used as source. This TX is fed by a vector network analyzer (VNA), Agilent N5242A PNA-X (Keysight Technologies, Santa Rosa, CA, USA). The network analyzer delivers a continuous wave signal at the studied center frequencies with a constant input power of 10 mW to the TX, which is placed in the far field of a rotation platform on the other side of the anechoic chamber. In this chapter, two orthogonal polarizations of the TX are studied: a vertical polarization (V)

parallel to the rotational platforms axis of rotation and a horizontal polarization (H) perpendicular to this axis of rotation.

Two steps are performed in the calibration: First, the incident electric fields are measured in free space using a broadband field meter (Narda NBM-550, Narda Microwave, Hauppauge, NY, USA). Second, on-body measurements using textile antennas placed on different positions *i* on the body are executed. The considered positions *i* on the body vary depending on the design approach chosen while constructing the PDE.

The goal of the measurements with the PDE is to determine the incident power density. This power density is to be averaged over the human body [11]. In the first calibration step, the incident (free-space) power density is measured using an isotropic antenna at different heights (0.5 m to 2 m) of the rotational axis above the platform. Since the subject is placed on the platform, this is the rotational axis of the subject as well. The free-space incident power density (S_{inc}^{free}) is determined as an average over these measured incident power densities ($S_{inc}(h)$) using:

$$S_{inc}^{free} = \frac{1}{N_h} \sum_{i=1}^{N_h} S_{inc}(h_i) \tag{6.1}$$

where N_h is the number of measured heights h_i along the rotational axis from 0.5 m to h_{tot}, being the subject's total body height.

In the second step of the calibration, a 25 year old male subject wearing a textile antenna is placed on the rotation platform in the anechoic chamber. The subject has a body mass index of 22.8 kg/m^2, a h_{tot} of 1.91 m, and a mass of 83 kg. Two types of on-body measurements are carried out. First, the subject is rotated over 360° in azimuth (ϕ), in order to emulate a random orientation regarding azimuth in a real environment, for a constant transmitted power at the studied frequency using both H- and V-polarization. During the rotation, the received power ($P_{r,i}(\phi)$) on antenna *i* (the i^{th} studied position on the body) is recorded as a function of the azimuth angle ϕ. Second, the subject is stationary, facing the TX, and the power at the TX (P_{in}) is varied. During this power sweep, the received powers on the antennas are recorded ($P_{r,i}(P_{in})$). This is necessary to determine an on-body detection limit.

During measurements in a real environment, a power ($P_{r,i}^{meas}$) is received on each antenna *i*. The incident power density (S_{inc}^{free}) can be determined from this received power using:

$$S_{inc}^{free} = \frac{P_{r,i}^{meas}}{AA_i} \tag{6.2}$$

where AA_i (m^2) is the effective median on-body antenna aperture of an antenna placed on position i on the body, which is the quantity that will be determined during the calibration procedure.

During the calibration, the received powers ($P_{r,i}(\phi)$), on the different antennas *i* are registered while rotating a subject, equipped with a textile antenna, in the anechoic chamber under exposure of RF radiation emitted by the H- or V-polarized TX at a constant input power P_{in}. The free-space incident power densities $S_{inc}^{free,H}$ and $S_{inc}^{free,V}$ are measured using an isotropic antenna for these same polarizations and input power. The antenna apertures for the H- and V-polarization, AA_i^H and AA_i^V, respectively, are then determined using:

$$AA_i^{H/V} = \frac{P_{r,i}^{H/V}}{S_{inc}^{H/V}} \tag{6.3}$$

with $AA_i^{V/H}$ the antenna aperture for vertically (S_{inc}^V) or horizontally (S_{inc}^H) polarized incident power densities.

These antenna apertures have a certain distribution as a function of the azimuth angle ϕ, corresponding to the angle of incidence of RF radiation. Since this distribution has a certain spread (quantified as a certain prediction interval), there will be a measurement uncertainty on the incident power density (S_{inc}^{meas}), determined using Eq. 6.2.

A 50% prediction interval around a median value of the AA can be determined using the three quartiles $Q_{1,i}$, $Q_{2,i}$, and $Q_{3,i}$, being the 25%, 50%, and 75% percentiles of the antenna aperture of antenna *i*, respectively. The quartiles are then used to determine relative upper (u_{up}) and lower (u_{low}) limits of the 50% prediction interval, caused by the presence of the body, on S_{inc}^{meas}:

$$u_{up} = \frac{Q_{2,i}}{Q_{1,i}} - 1 \tag{6.4}$$

$$u_{low} = 1 - \frac{Q_{2,i}}{Q_{3,i}} \tag{6.5}$$

The goal of the PDE is to combine N different antennas in order to reduce this measurement uncertainty. In practice, the received power during the calibration will be averaged over N different antennas:

$$P_r^{av} = \sum_{i=1}^{N} w_i P_{r,i} \qquad \sum_{i=1}^{N} w_i = 1 \tag{6.6}$$

$$P_r^{geom} = \prod_{i=1}^{N} P_{r,i}^{w_i} \qquad \sum_{i=1}^{N} w_i = 1 \tag{6.7}$$

with P_r^{av}, the weighted, arithmetic averaged received power; P_r^{geom} the weighted, geometric averaged received power; and w_i weight coefficients for the individual received powers. P_r^{av} and P_r^{geom} can be used to determine averaged antenna apertures AA^{av} and AA^{geom} with their own distributions and associated prediction

intervals. These should be smaller than those obtained for single antennas, see Chapter 5. The weight coefficients w_i could be chosen equal to $1/N$, to obtain regular arithmetic or geometric averages.

6.3 Proof-of-Concept: Calibration of a PDE for GSM 900 DL Designed using Numerical Simulations

6.3.1 Materials and Methods

A first goal of this research is to demonstrate the viability of a PDE. To this end, a PDE is designed and simulated for 950 MHz, a frequency in the Global System for Mobile Communications (GSM) down-link band that is present in most environments [7] and for which incident fields can be described using stochastic parameters [12, 13]. This exposimeter is designed and constructed using three textile antennas [14–16] tuned to the GSM 900 DL band and described in subsection 6.2.1.3, and wearable electronics [17, 18], which can both be unobtrusively integrated in clothing in order to maximize wearability of the PDE. The antennas are developed by the EM group of Ghent University, while the electronics are developed by the Department of Electrical Engineering (ESAT) of the Catholic University of Leuven (KUL). Each textile antenna is connected to an RF exposure acquisition system. These RF acquisition nodes contain a commercially available receiver that is tuned for a 950 MHz link (CC1100E, Texas Instruments, Dallas, TX), and a micro-controller (PIC18f14k22, Microchip, Chandler, AZ) for data management. In this first prototype, the RF exposure data are communicated via an inter-integrated circuit (I2C) to a main unit that can be connected to a personal computer using a USB interface. The architecture is modular such that the amount of nodes is easily extendable and other frequency bands could be explored. Acquisition parameters such as sampling rate and frequency channel can be adjusted during measurements. Since the antennas, acquisition nodes, and all interconnections are all flexible and lightweight, they can be comfortably worn by volunteers without impeding body movement.

The design of the distributed exposimeter is based on the results obtained using the step-wise linear regression of linear projections of the response in the tangential plane to the VFM's surface at 950 MHz in the 'Indoor Pico-cell' scenario, presented in Section 5.4.1 of Chapter 5. The error-on-prediction obtained using this algorithm is 14% using 3 measurement positions on the body. Figure 6.4 shows the three positions (blue ellipses) that, when combined, have the lowest error-on-prediction found by the model. The approximate polarizations are shown by black arrows and a possible location for the processing unit is shown as a red rectangle.

Using a set of three textile antennas placed on the positions predicted by the

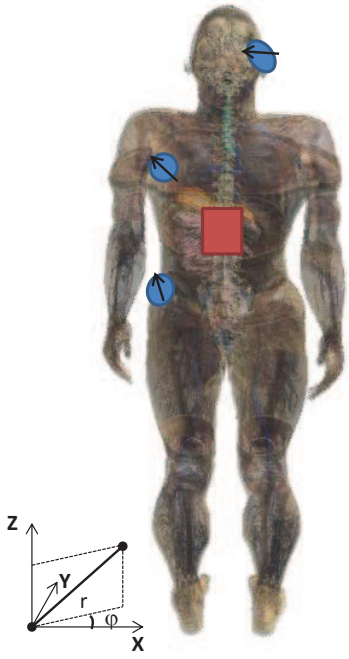

Figure 6.4: Positions and linear polarizations of a personal, distributed exposimeter at 950 MHz. Optimal positions determined by the step-wise algorithm (indicated by blue ellipses), possible location of the central processing unit (red rectangle), and linear polarizations (black arrows) of the textile antennas at 1 cm from the VFM are shown.

step-wise algorithm (Fig. 6.4), a first prototype of the exposimeter is constructed. This model is calibrated in an anechoic chamber on the previously described human subject who has a BMI comparable to that of the VFM ($\pm 1\ kg/m^2$). In this particular calibration setup, the subject is placed in an anechoic chamber in an upright anatomical position in the far field of a dipole radiating at 950 MHz, and is rotated over $360°$ in azimuth angle ϕ for two orthogonal polarizations of the dipole (H and V, perpendicular and parallel to the subject's axis of rotation, respectively), which emits at a constant output power. The subject is rotated in ϕ because in reality the azimuthal angle of incidence of a measured incident plane wave is unknown. Each antenna (i) will receive a certain power $P_{r,i}$ ($i = 1..3$) as a function of ϕ. These powers are then averaged over the three antennas using Equation 6.6 with $w_i = 1/3,\ \forall i$.

It suffices to study the (averaged) response of the PDE instead of the (average) antenna aperture, in order to determine whether a PDE would reduce the measurement uncertainty on incident EM fields. This avoids the need for an additional

measurement of the incident power density in the calibration setup. In this section, the measured response R_{meas} is determined using the averaged received power P_r^{av}, averaged over the three antennas, and the received power of the antennas in free-space P_r^{free} , averaged over the subject's rotation axis [19]:

$$R_{meas} = \frac{P_r^{av}}{P_r^{free}} \tag{6.8}$$

The response R_{meas} is related to the antenna aperture (AA) through the following relation:

$$AA = \frac{P_r^{av}}{S_{inc}^{free}} = R_{meas} \times \frac{P_r^{free}}{S_{inc}^{free}} = R_{meas} \times AA^{free} \tag{6.9}$$

with AA^{free} the free-space antenna aperture of the used antennas. This response R_{meas} will have a certain distribution, from which the 97.5% ($p_{97.5}$) and 2.5% ($p_{2.5}$) percentiles are obtained to determine a 95% prediction interval (PI_{95}), using:

$$PI_{95} = \frac{p_{97.5}}{p_{2.5}} \tag{6.10}$$

6.3.2 Results

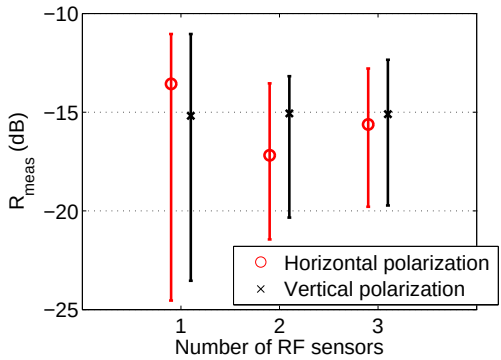

Figure 6.5: Angular averaged response (R_{meas}) with smallest 95% prediction interval as a function of the number of combined antennas on a human subject; 95% prediction intervals are shown as error bars.

Figure 6.5 shows the response R_{meas} corresponding to the smallest 95% prediction interval as a function of the number of antennas in the PDE (one antenna corresponds to a single exposimeter). The shown response is that of the combination which has the smallest 95% prediction interval of all combinations of the considered number of antennas. The markers show the angular averaged R_{meas},

while the error bars show the PI_{95}. For horizontal polarization, a 6.5 dB reduction (division by a factor of 4.5) in PI_{95} for three antennas is measured on an initial PI_{95} of 13.5 dB (factor of 22.4) for the best measurement with one textile antenna (a single exposimeter). A 5 dB reduction (division by a factor of 3) on 12.4 dB (factor of 17.4) is measured on the PI_{95} for vertically polarized incident plane waves. This results in a final PI_{95} of 7 dB (factor of 5 for horizontal polarization) and 7.4 dB (factor of 5.5 for vertical polarization). Other prediction intervals are determined as well: the 90% prediction intevals are 7.0 dB (a factor 5) and 7.1 dB (a factor 5.1) for H- and V-polarization, respectively, while the 50% prediction intervals are 4.5 dB (a factor 2.8) for both polarizations.

6.3.3 Discussion

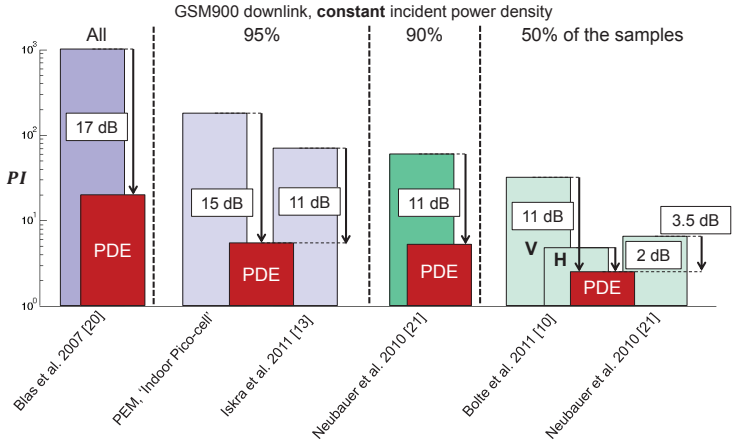

Figure 6.6: Overview of Prediction Intervals (PI) of single PEM responses in the GSM 900 DL band, taken from Chapter 3, in comparison to the corresponding values shown for the PDE (in red), which are averaged over both polarizations. The bars indicate the measured or simulated prediction intervals, while the arrows indicate the reduction obtained by the PDE. The value of the reduction (in dB) is shown next to each arrow.

In Figure 3.12 of Chapter 3 an overview is presented of the prediction intervals estimated in the GSM 900 DL band by previous studies [10, 13, 20, 21] and numerical simulations at 950 MHz. Figure 6.6 repeats the relevant results in the GSM 900 DL band in comparison with the values obtained in this section for three textile antennas calibrated on the body.

As Figure 6.6 shows, the PDE reduces the considered prediction intervals by several decibels. In [10], a commercial, single exposimeter was worn on the right

hip of a subject rotated over 360° under exposure to a GSM down-link signal. A 50% prediction interval of 6.5 dB (factor of 4.5) and 15.5 dB (factor of 35) was measured for incident horizontal and vertical polarization, respectively, see Figure 6.6. In [21], different possible locations of an exposimeter on the human body were investigated on a human body phantom in a simulated multi-path environment at 946 MHz. This led to an interquartile distance of 8 dB (factor of 6) and a PI_{90} of 18 dB (factor of 62), see Figure 6.6. The interquartile distances measured using three antennas in this section are considerably lower (4.5 dB). A PI_{95} of 18.5 dB (factor of 70.8) on the body is estimated for commercial exposimeters at 900 MHz in realistic environments [13]. The FDTD simulations at 950 MHz, executed in Chapter 3, show a PI_{95} of 22 dB (factor of 158) in the 'Indoor Pico-cell' scenario. All these values are much larger than the PI_{95} measured in this section (7-7.4 dB).

The measurements show that a huge improvement in variance and thus accuracy can be obtained using just three antennas. Moreover, the PDE also exhibits excellent performance in terms of isotropy (I), defined as the ratio of R_{meas} for the two orthogonal polarizations. Figure 6.5 shows that for the combination of the three textile antennas, I = 0.5 dB (factor of 1.1), which is much better than the I of 6.4 dB (factor of 4.4) for commercial exposimeters located on the body [10].

In Chapter 5, the results of numerical simulations with models for the same antennas placed on the torso of the VFM are presented and discussed. These can be compared to the calibration measurements presented in this section. The PI_{50} values of the measured response in this section, 4.5 dB, are lower than the median value predicted by numerical simulations using models for the same antennas in Section 5.4.3 of Chapter 5. Combinations of 3 antennas placed either vertically or horizontally on the upper torso of the human body have a median PI_{50} of 5.1 dB in the 'Indoor Pico-cell' and a minimal value of 3.3 dB. The PI_{50} value found in this section is thus situated in the lower end of the distribution of PI_{50} values of combinations of three antennas on the upper torso, which is to be expected since a position on the head is considered in this section as well. As shown in the previous chapter: smaller PI_{50} values can be obtained when other locations on the body than the upper torso are considered as well.

The measured prediction intervals are larger than the error-on-prediction of 14%, corresponding to a $PI_{68} = 2.4$ dB determined by the error-on-prediction based algorithm. We attribute this difference to the fact that the antennas are not taken into account in the linear regression, which decreases the variation (see the previous chapter) and differences in the antenna positioning and morphology on the VFM and the human subject.

The PDE thus shows promising characteristics for measurements of the incident power density with less measurement uncertainty. However, the results are not directly usable in reality, since they do not take into account the polarization

of the incident EM fields and the positions are not suitable for reproducible measurements, since the antenna on the head might attract unwanted attention and the antenna's polarization is difficult to reproduce in reality.

6.4 Processing of On-Body Calibration Measurements

In reality, Equation 6.2 requires AA_i values for an unknown polarization, but the calibration measurements are conducted for two orthogonal polarizations H and V (see Equation 6.3). The effective antenna aperture AA_i will depend on the polarization ψ of the incident plane wave according to [8]:

$$AA_i(\phi,\psi) = AA_i^H(\phi).cos^2(\psi) + AA_i^V(\phi).sin^2(\psi) \tag{6.11}$$

with $AA_i^{V/H}$ the antenna aperture for vertically or horizontally polarized incident power densities and ψ the polarization. A Gaussian distribution for the polarization ψ has been proposed in [22] and [23], used in [12, 13, 24, 25], and used in the previous chapters. This distribution is applicable for communication signals emitted from base stations located outdoor that cover large areas using an array of linearly (or cross-) polarized antennas. For telecommunication signals mainly emitted by devices with an unknown polarization, such as WiFi and DECT, a uniform distribution for $\psi \in [0, 2\pi]$ is used, since no a priori assumptions can be made about the polarization for these sources.

Equation 6.11 is calculated for every (ϕ, ψ) pair, resulting in a distribution of $AA_i(\phi, \psi)$ for every antenna *i*. In [10] this distribution was assumed to be U-shaped and thus symmetric, which would allow one to describe the distribution using a median or mean value and a standard deviation. However, it has been shown in the previous chapters, that depending on the antenna's position, this distribution is asymmetric and is, therefore, better described using three quartiles: $Q_{1,i}$, $Q_{2,i}$, and $Q_{3,i}$, being the 25%, 50%, and 75% percentiles of the antenna aperture of antenna *i*, respectively. Using these interquartile distances, the corresponding measurement uncertainties can be determined using Equations 6.4 and 6.5. If the interquartile distance ($Q_{3,i}/Q_{1,i}$) of the distribution of the effective antenna aperture decreases, then the uncertainty on the measured incident power densities decreases as well. In order to reduce this interquartile distance, an average over different antennas will be used. The antenna apertures of the textile antennas are then averaged (either arithmetically or geometrically) over N different nodes placed on the body:

$$AA_l^{av} = \sum_{j \in P_l} w_j AA_j, \qquad \sum_{j \in P_l} w_j = 1 \tag{6.12}$$

$$AA_l^{geom} = \prod_{j \in P_l} AA_j^{w_j}, \qquad \sum_{j \in P_l} w_j = 1 \tag{6.13}$$

with AA_l^{av} and AA_l^{geom} the arithmetic and geometric averaged antenna apertures averaged over the l^{th} combination of N antennas placed on the body and P_l the set of these N positions on the body. For example, if $N = 4$ then $P_l = \{A, B, C, D\}$ is a possible set of positions on the body over which the antenna apertures can be averaged. These averaged antenna apertures will have a certain distribution as well, from which quartiles can be obtained: $Q_{l,1}^{av/geom}$, $Q_{l,2}^{av/geom}$, and $Q_{l,3}^{av/geom}$. The incident power density can then be estimated using:

$$S_{inc}^{meas} = \frac{\sum_{j \in P_l} w_j . P_{r,j}^{meas}}{Q_{l,2}^{av}} \tag{6.14}$$

$$S_{inc}^{meas} = \frac{\prod_{j \in P_l} (P_{r,j}^{meas})^{w_j}}{Q_{l,2}^{geom}} \tag{6.15}$$

The uncertainty on this incident power density can be calculated with the appropriate quartiles inserted in Equations 6.4 and 6.5. The goal is to find the combination *l* and set of weights w_i of N antennas which minimizes this uncertainty.

6.5 Calibration of a PDE, Designed using Diametrically Opposite Locations on the Subject's Torso

In Section 5.4.2.1 of Chapter 5, we demonstrated that a combination of two antennas worn on the front and back of the human body will have a lower measurement uncertainty, due to the negative correlation between measurement positions on the front and the back of the VFM. In this section, a PDE to measure the incident power density in the WiFi 2G communication band is calibrated using two textile antennas.

6.5.1 Materials and Methods

The used textile antennas are the dual polarized WiFi 2G antennas described in subsection 6.2.1.7 of this chapter. Two of these antennas are placed on the front and back of a human subject with a body mass index of 22.8 kg/m^2, a h_{tot} of 1.91 m, and a mass of 83 kg.

Each textile antenna is extended with an RF-exposure acquisition node, developed by ESAT. The nodes contain a commercially available receiver that is tuned for a 2450 MHz link (CC2500, Texas Instruments, Dallas, TX, USA) and a microcontroller (CC430F5137, Texas Instruments, Dallas, TX, USA) for data management. RF-exposure data are communicated via a 433 MHz wireless link, with an input power of -6 dBm, to an off-body unit that can be connected with a personal computer using a USB interface. A modular architecture is adopted, such that the amount of nodes is easily extendable and other frequency bands can be explored.

Acquisition parameters, such as the sampling rate and the frequency channel, can be adjusted during the experiment to optimize the quality of the acquired data. Instead of sampling the full spectrum of the measured band at once, an adjustable filter is added in order to be able to sweep the full spectrum using more narrow bands, achieving a high frequency resolution. The maximum value measured in each frequency sweep is saved. This version of the PDE is designed with attention to battery power consumption and the on-body wireless communication link. The RF nodes have an RF power sensitivity of -90.5 $\pm$0.5 dBm with a dynamic range of 100 dB and show a linear power response.

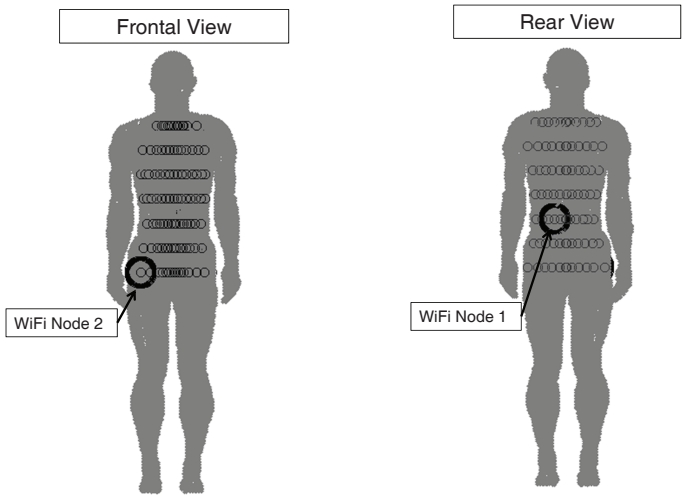

(a) Frontal view (b) Rear view

Figure 6.7: On-body positions where the RF nodes are placed during calibration and measurements. The positions of the WiFi antennas are indicated by a green circle. The grey surface indicates all the positions at 1 cm from the VFM.

As shown in Section 5.4.2.1 of Chapter 5, any combination of two nodes on the front and the back reduces the uncertainty on measurements of the incident power density. For the measurements, we have chosen to work with the positions indicated in Figure 6.7.

In a first step, the incident fields are measured. The measured incident electric-fields strengths at 2450 MHz for an input power of 10 mW at the input of the transmitting antenna are 0.12 V/m, for a horizontally polarized antenna, and 0.13 V/m, for a vertically polarized transmitting antenna.

In a second step, the on-body antennas, placed on the front and back, as indicated in Fig. 6.7, are calibrated. The powers $P_{r,i}^{H/V}(\phi)$ are registered in steps of

$\Delta\phi = 45°$ during the calibration for both H- and V-polarization. Multiple samples are recorded at every step in angle ϕ. The antenna apertures $AA_i^{H/V}$ are calculated using these powers $P_{r,i}^{H/V}(\phi)$ and the measured incident power densities S_{inc}^{free} using Equation 6.2. Afterwards, the antenna apertures AA_i are recalculated for a realistic polarization ψ, using Equation 6.11. To this aim, a bootstrap approach is implemented, where, in every repetition of the analysis, 1000 ψ-samples are generated for every measured value. This number of ψ-samples is associated with an uncertainty on the summary statistics $Q_k^{av/geom}$ (k=1,2,3) smaller than 1% (determined using 100 bootstrap samples). The received powers are then averaged using weight coefficients $w_i \in [0, 1]$ (with a resolution of 10^{-2}) under the constraints indicated in Equations 6.12 and 6.13. This is repeated during 100 bootstrap iterations. For every bootstrap sample (every set of 1000 ψ-samples), the quartiles of the antenna aperture $Q_k^{av/geom}$ are stored, together with the weights that correspond to the lowest interquartile distance. The median of the stored quantities is then determined from this set of quartiles, weights, and interquartile distances.

6.5.2 Results

Combination of Nodes		WiFi 2G	
		arithmetic	geometric
1	AA_1 (cm^2)	1.3 ± 0.0	
	DL (nW/m^2)	6.9 ± 0.0	
2	AA_2 (cm^2)	1.2 ± 0.0	
	DL (nW/m^2)	7.4 ± 0.0	
(1,2)	$AA^{av/geom}$ (cm^2)	9.8 ± 0.0	1.7 ± 0.0
	weights (w_1, w_2)	$(0.40, 0.60) \pm 0.01$	$(0.49, 0.51) \pm 0.01$
	DL (nW/m^2)	0.91 ± 0.00	5.2 ± 0.0

*AA_1 = antenna aperture of antenna 1, AA_2 = antenna aperture of antenna 2, DL = detection limit, $AA^{av/geom}$ = the arithmetic or geometric weighted averaged antenna aperture.

Table 6.2: Median on-body antenna apertures (AA_i), detection limits (DLs), and Weight factors (w_i), found for different combinations of the calibrated antennas for WiFi. The values are accompanied by an uncertainty, estimated as half the interquartile distance over 100 bootstrap samples.

Table 6.2 lists the weight factors that yield the lowest interquartile distance for a realistic polarization, together with the determined AA_i. Figure 6.8 shows the corresponding interquartile distances. From Fig. 6.8 it is clear that using a weighted average of the power received by multiple antennas, positioned intelligently on the body, reduces the variation caused by the presence of the body (here quantified by the 50% prediction interval) on measurements using these antennas. At 2450 MHz, the interquartile distance is reduced down to 3.2 dB using

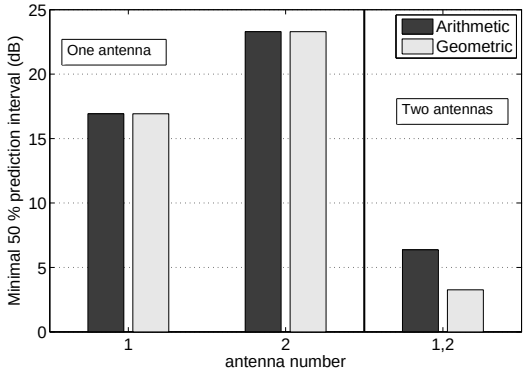

Figure 6.8: Minimal 50% prediction interval on the antenna aperture measured during calibration for a realistic polarization and all combinations of 2 antennas using an arithmetic and geometric weighted average.

two cross-polarized antennas. As Fig. 6.8 shows, this interquartile distance is lowest for geometric averaging. This averaging scheme is, therefore, used during the measurements in a real environment. The Geometric averaging leads to a lower prediction interval because the correlation between the received powers on the two antennas is more negative for logarithmic values than the linear values.

Applying the antenna apertures and weights listed in Table 6.2, the detection limits for the received powers (dBm) are converted to values in power density (W/m^2). The detection limits in the WiFi band range from 0.9 to 7.4 $\times 10^{-9}$ W/m^2. The detection limit of the PDE in the WiFi band is about 10 times lower than that of a commercial exposimeter $O(10^{-8} W/m^2)$.

6.5.3 Discussion

As Figure 6.8 shows, the improvements using weight coefficients and averaging over multiple antennas can be relatively large. For the WiFi 2G (2450 MHz) band, the single antenna with the lowest interquartile distance has an interquartile distance of 17 dB, which can be reduced considerably using geometric averaging over two antennas to 3 dB. This interquartile distance is small compared to previous studies [10, 21, 25]. In [21], the variation of the response of a single PEM was investigated near the body of a phantom, placed in a model for a real indoor environment. A 50% prediction interval of 9.6 dB was obtained at 2450 MHz. In [10], an exposimeter was worn on the hip of a male subject. This exposimeter was calibrated using the same procedure described here in this study. However, only two polarizations were considered. 50% prediction intervals of 9 dB and 19 dB were measured in the WiFi band, for horizontal and vertical polarization, respectively.

In Section 6.3 of this chapter a 50% prediction interval of 4.5 dB for a prototype of a PDE at 950 MHz was measured for both incident polarizations using the same calibration procedure. However, no weight factors were used. All previously mentioned 50% prediction interval values are larger than 3 dB, which indicates that the proposed calibration method will reduce the variation on the measurements. Moreover, it should be noted, that, in contrast to existing portable solutions, the system proposed in this section is fully wearable and may be comfortably and unobtrusively integrated into a garment. The studied system is completely invisible and it does not hinder the movements, nor the behaviour of the wearer.

6.6 Design of a Multi-Band PDE Using Calibration Measurements

In the previous section, the results of Chapter 5 were used for the design of a PDE which is then calibrated in practice. In this section, the on-body calibration itself is used as a design for the PDE. In order to demonstrate this concept, we first outline all the steps for a PDE that estimates the incident power density in the GSM 900 DL band. In a second subsection, the analysis is repeated and compared for *all the other studied frequency bands* in this chapter.

6.6.1 A PDE for the GSM 900 DL band

The calibration procedure proposed in this chapter can be used for the design of a PDE. In this section the same design procedure as outlined in Section 5.3.4 in Chapter 5 is used, but using calibration measurements of textile antennas placed on the body instead of numerical simulations of those antennas.

6.6.1.1 Materials and Methods

Textile antennas and Receiver Nodes The used textile antennas to register EM fields in the GSM 900 DL band are described in Section 6.2.1.3. The antennas are linearly polarized PIFAs, designed to receive signals on-body in the GSM 900 DL band. These antennas are combined with RF receiver nodes, that are developed by the EM group of Ghent University for the detection of the received powers on the textile antennas. These nodes are connected to the textile antennas using a short (15 cm) Sub-Miniature version A (SMA) cable (CCSMA-MM-RG316DS-6, Crystek Corporation, FL, USA). The receiver nodes contain a broadband power detector (1 MHz - 4 GHz, ADL5513, Analog Devices, Norwood, MA, USA), placed in series with a band-selective, surface acoustic wave (SAW) filter tuned to the GSM 900 DL band (part 856528, Triquint Semiconductor, Singapore). Note that the antenna also provides an initial filtering on the incident electric fields (see

Figure 6.2). The different nodes can be powered individually and register received powers on the textile antennas individually, making any interconnection, whether wired or wireless, between the different nodes unnecessary. Synchronization of the nodes is ensured by a simultaneous initialization of the nodes at the beginning of the measurements. The receiver nodes sample the received power at an approximate sample rate of 1 kHz and calculate statistics of these measurements every second. The following four quantities are calculated by the micro-controller during every second (thus with a sample rate of 1 Hz): the maximal, minimal, geometrically, and arithmetic averaged received powers on the textile antennas. These values are stored logarithmically (in dBm) with an accuracy of 1 dB. The power detection limit of the nodes is determined using a network analyzer Agilent N5242A PNA-X (Keysight Technologies, Santa Rosa, CA, USA), and is -70 dBm (10^{-7} mW).

First Calibration Step The same setup described in Section 6.2.2 is used for the calibration measurements. In this case, the TX is powered by a vector network analyzer Agilent N5242A PNA-X (Keysight Technologies, Santa Rosa, CA, USA), at a harmonic frequency of 942.5 MHz (the center frequency of the GSM 900 DL band (925-960 MHz), see Table 5.1) with an input power of 10 mW. The incident power densities of the fields emitted by the TX are measured along the axis of the rotational platform as a function of height, using a NARDA broadband probe (Narda NBM-550, Narda Microwave, Hauppauge, NY, USA).

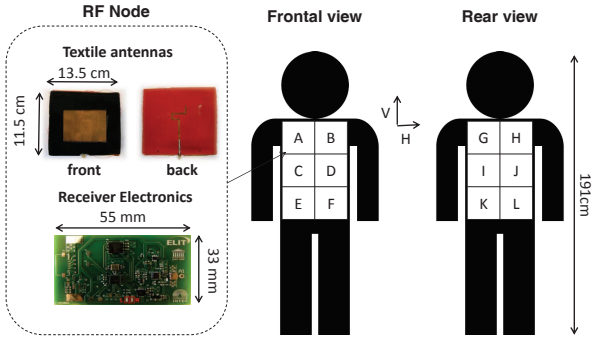

Figure 6.9: Potential zones (A to L) to deploy textile antennas on the upper body.

A 26 year old male subject of body mass 82 kg and a height of 1.91 m is placed on the rotational platform in the far-field of the TX antenna, see Figures 4.2 (b) and 6.3. This subject is equipped with a textile antenna and a receiver node placed on one of the 12 zones indicated in Figure 6.9. The textile antenna is either V- or H-polarized. The subject is then rotated in the azimuth angle ϕ over 360° with an

angular speed of $2^\circ/s$. This is repeated for all 12 considered zones, 2 polarizations of the textile antennas (H and V) and 2 polarizations of the TX antenna (V and H). The effective on-body aperture $AA_i(\theta = 90^\circ, \phi, \psi)$ can be determined using the received power on the different antennas and the measured incident power density, see Equation 6.3. Note that it is not possible to measure other incident polar angles using this setup in this anechoic chamber. Therefore, the analysis of the measured data is continued for $\theta = 90^\circ$.

The used measurement equipment and calibration setup do not allow for a simultaneous registration of the phase and the amplitude of the received power on the antennas. Therefore, it is impossible to obtain the correct antenna factor (AF_i) (see Equation 5.17 in Chapter 5) for a constant phase. This phase information is necessary to correctly estimate the effect of interference during multi-path exposure.

The analysis of the distribution of the antenna aperture shall thus be executed using the $AA_i(\theta, \phi, \psi)$ obtained in Eq. 6.3. To this aim, 1000 polarization samples ψ are generated in the studied environment for every measured $(\theta = 90^\circ, \phi)$ sample. This leads to a distribution of $AA_i(\theta = 90^\circ, \phi, \psi)$ from which the respective quartiles $Q_{i,1}$, $Q_{i,2}$, and $Q_{i,3}$ are determined. The analysis outlined in Section 6.4 can be executed using these quartiles and the $AA_i(\theta = 90^\circ, \phi, \psi)$ values. This analysis is then repeated 100 times to determine the variation on the analysis.

In total 12 (positions on the body: A to L) x 2 (polarizations on the body) antenna apertures and their distributions can be determined using the proposed calibration setup and procedure. These antenna apertures are then averaged arithmetically and geometrically over combinations of N antennas drawn from 12 potential locations (C_{12}^N). This results in a total number of $\sum_{N=1}^{12} C_{12}^N \times 2^N$ possible combinations of antennas on the body, since two potential polarizations are allowed. The best combinations are then selected for a given number of selected antennas N.

Second Calibration Step In the previous analysis, using measurements and numerical simulations, only single antennas on the body are used. In order to actually measure with a PDE, we have produced four textile antennas and receiver nodes. In this second calibration step, these are placed on the body of the same volunteer simultaneously and are again calibrated in the anechoic chamber.

The four textile antennas are placed on the subject's body on the positions and corresponding polarizations that are determined to lead to the lowest measurement uncertainty using the previous calibration step. In this step, an additional constraint is chosen for the placement of the antennas. The PDE has to consist of two H-polarized and two V-polarized antennas in order to minimize the anisotropy of the device. This step is necessary to calibrate differences in the positioning of the antennas between the first calibration and the setup used for measurements in real-

ity. The subject is again rotated in the azimuth angle ϕ over $360°$ with an angular speed of $2°/s$. During this rotation the receiver nodes will again record the received powers on the four textile antennas. The same procedure, described above, is followed in order to determine the measurement uncertainty for this configuration.

Additionally, the power transfer coefficient $|S_{12}|^2$ between the different antennas is measured, to quantify any potential coupling between the antennas.

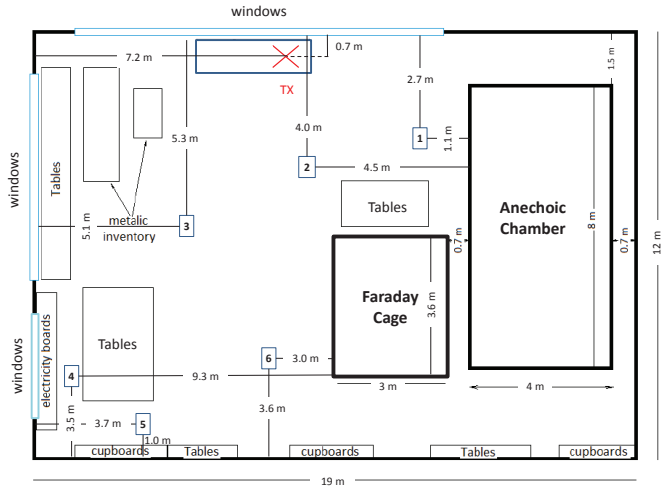

Figure 6.10: Locations (1 to 6) of the validation measurements and the transmitter (TX) used during the measurements (Courtesy of Marina Marinova).

Validation Measurements Using calibration measurements or numerical simulations one can obtain the $AA_l^{av/geom}$ for every combination *l* of a certain number of antennas. However, these antenna apertures are based on propagation models for the environments in which measurements should take place. There are uncertainties as well on the assumptions made about the exposure. Therefore, the incident power density that we estimate using the PDE might deviate from the power density measured using an isotropic field probe. In order to determine this deviation, validation measurements are executed on six locations in an indoor environment shown in Figure 6.10. The subject wearing the PDE moves around in a square of $1.5 \times 1.5\ m^2$ around each of the six measurement locations for 60 s. During these 60 s the room is first excited during 30 s using a pico-cell (Dual band micro-cell antenna 5027, Jaybeam Wireless/Amphenol antennas, Rockford, Illinois, USA) for use in the GSM 900 DL band, which is fed with a sinusoidal signal

of 19 dBm (79 mW) at 942.5 MHz. This corresponds to the 'Indoor Pico-cell' scenario listed in Table 3.3. During the next 30 s, the input power of the pico-cell is switched off. In this phase, all the exposure is caused by outdoor sources. This corresponds to the 'Outdoor-Indoor' scenario listed in Table 3.3. Immediately following these measurements, the incident power densities are measured using a combination of an isotropic, tri-axial antenna and a spectrum analyzer ($R\&S$ FSL, Rhode & Schwartz, Munich, Germany). The antenna is placed 1.5 m above the ground on each of the 6 locations and measures the incident power density with and without the pico-cell emitting at 942.5 MHz with the same input power as during the previous measurements. The difference between both measurements is then compared in order to determine the deviation between the used models and reality.

6.6.1.2 Results

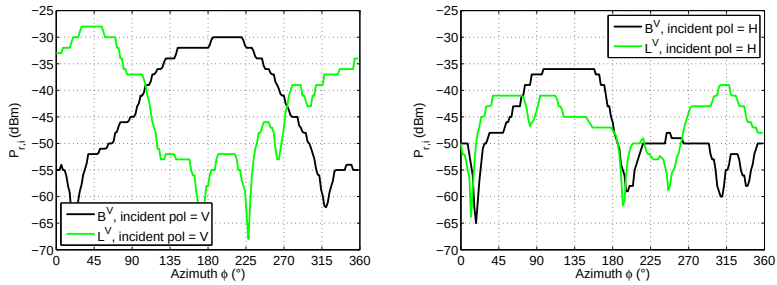

(a) co-polarized (b) cross-polarized

Figure 6.11: On-body measurements of the received power $P_{r,i}$ on vertically polarized antennas placed on positions B and L as a function of the azimuth angle.

Figure 6.11 shows an example of the received power on two on-body antennas during the first calibration step. Figure 6.11 (a) clearly shows the different response of the two antennas on the incident plane waves. Antenna B is placed on the left side of the front of the subject's torso and receives its maximal power (-30 dBm or 1 μW) for a $\phi \in [186°, 220°]$, whereas antenna L is placed on a diametrically opposite location on the body and receives its maximal power (-28 dBm or 16 μW) for a $\phi \in [30°, 54°]$ in the opposite quadrant. In Figure 6.11 (b) the difference between the two antennas is not that clear. Note that a perfect, linearly polarized antenna should not receive any power in the cross-polarized case. The received power in the co-polarized case is higher for both antennas: on average 3.7 ± 10 dB and 3.2 ± 9.3 dB for antenna B and L, respectively. Averaged over all antennas,

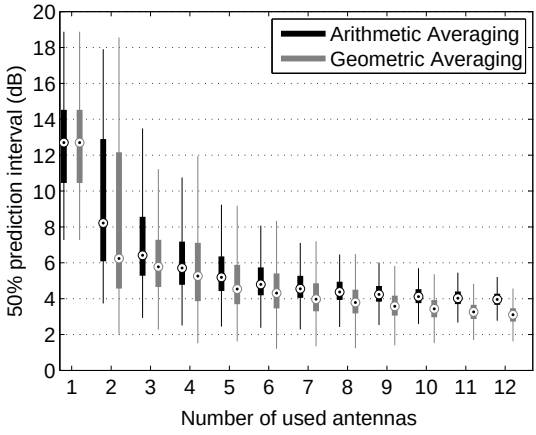

Figure 6.12: Boxplot of the distribution of the measured PI_{50} on the antenna aperture in the 'Urban Macro-cell' scenario as a function of the number of antennas. The gray boxes indicate the distribution of the PI_{50} using a geometric averaging, while the black boxes indicate the distribution using an arithmetic averaging. Outliers (more than 1.5 times the interquartile distance deviation from the edges of the boxes) are suppressed in this figure.

the isotropy regarding the polarization is 4.32 ± 2.4 dB.

Using the processing method described in the previous subsections, the distribution of the antenna apertures is determined using a 1000 exposure samples in three environments. From these distributions, the median antenna apertures and the PI_{50} values are determined. This process is then repeated a 100 times in order to determine the repeatability of the procedure. The mean antenna aperture for the single antennas found in the 'Urban Macro-cell' scenario is $6.8 \pm 3.7\ cm^2$, which is smaller than the value of $10 \pm 5.0\ cm^2$ found using the numerical simulations. The real antennas are thus less efficient than the numerical models, which was to be expected.

A sensitivity study is executed using a bootstrap of a 100 repetitions. The average 50% confidence interval on these values is $0.52 \pm 0.43\ cm^2$, calculated using the bootstrap approach. This corresponds to an average relative 50% confidence interval of 7.7%. This is acceptable given the variation on the AA, which is of the order of several decibels, see Figure 6.12. The 50% confidence intervals on the PI_{50} values are 0.23 ± 0.06 dB on the single antennas, calculated using the 100 repetitions, which reduces to 0.08 ± 0.01 dB for combinations of 12 antennas.

Figure 6.12 shows box-plots of the PI_{50} values of all different combinations of N antennas on the body in the 'Urban Macro-cell' scenario for both an arithmetic and geometric averaging over multiple antennas. The measurements confirm that

the PI_{50} on the antenna aperture is (on average) reduced when multiple antennas are placed on the on the body. A geometric averaging leads to slightly lower PI_{50} values in case of the measurements. Note that the distribution of the antenna apertures is different from the ones studied using simulations, since during the measurements in the anechoic room the EMFs can only be incident with a polar angle of 90°. The largest median reduction in PI_{50} is obtained when a second antenna is added to a single antenna: 6.5 dB for geometric averaging, while adding 10 more antennas 'only' reduces the median PI_{50} additionally by 3.1 dB. Considering the combinations with the smallest PI_{50} values, these differences are even larger: the best single antenna has a PI_{50} of 7.3 dB, the best pair antennas has a PI_{50} of 2 dB, while the best combination of 12 antennas has a PI_{50} of 1.4 dB. A limited number of antennas will thus suffice to achieve an acceptably low PI_{50} value, which is in line with the numerical simulations presented in the previous chapter.

The distributions of the PI_{50} values (such as those shown in Fig. 6.12) are almost identical in the 'Urban Macro-cell' and 'Indoor Pico-cell' environments. The differences in median PI_{50} values and the size of the boxes shown in Fig. 6.12 are smaller than 0.1 dB. Small differences are expected since in this processing method only the distribution of the polarization is changed when a different environment is considered. As Table 3.3 shows, the cross-polarization ratio, which determines the polarization distribution, is similar in both environments as there is a difference of only 0.3 dB on a value of 7 dB.

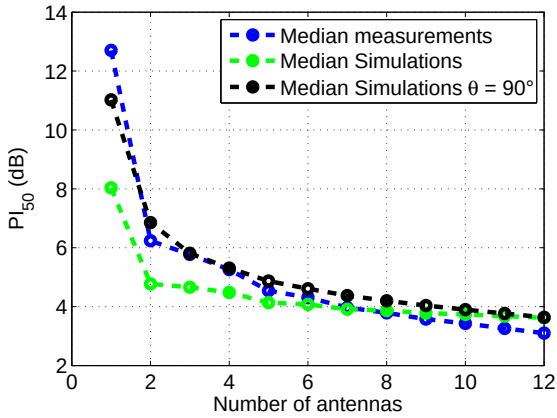

Figure 6.13: Median PI_{50} on the antenna aperture for a geometric averaging in the 'Urban Macro-cell' scenario as a function of the number of antennas using calibration measurements, numerical simulations, restricted to a $\theta = 90^{\circ}$, and the numerical simulations shown in Figure 5.16.

Figure 6.13 shows the median PI_{50} values as a function of the number of antennas using the calibration measurements (blue) and the numerical simulations (black) presented in Section 5.4.3 of Chapter 5, processed using the same procedure as used for the measurements: restricting the polar angle to 90° and excluding interference of incident fields (no multi-path exposure). Both results are in excellent agreement: for the single antennas the median PI_{50} differs 1.7 dB, while for higher numbers of antennas the differences are smaller than 0.6 dB.

Figure 6.13 also shows the median PI_{50} values as a function of the number of antennas in the same environment, for the numerical simulations presented in Figure 5.16 (green). This is thus obtained using numerical simulations, including interference on the antenna and other polar angles. If combinations of less than six antennas are considered, the median PI_{50} is lower predicted by the numerical simulations including all polar angles, than the measurements and the simulations when only $\theta = 90^\circ$ is considered. This difference decrease for higher numbers of antennas from 4.7 dB for single antennas up to 0.5 dB when 12 antennas are used.

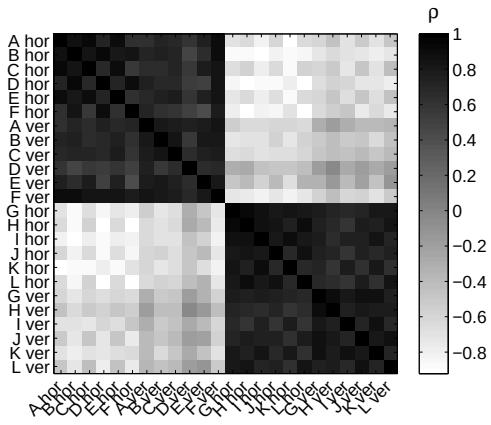

Figure 6.14: Correlations between the logarithm of the received powers on the different calibrated antenna positions in the 'Urban Macro-cell' scenario.

Figure 6.14 explains why the PI_{50} values of the calibration measurements decrease when multiple antennas are used. It shows the correlations (ρ) between the antennas located on the studied positions on the upper body. The correlations shown in Figure 6.14 range from 0.40 to 0.92 with an average value of 0.74 for antennas on the same side of the body, while they range from -0.11 to -0.92 with an average value of -0.60 for antennas on opposite sides of the body.

The logarithmic received powers on the antennas determined using numerical simulations in the same environment show correlations that range from 0.51 to

0.94 with an average of 0.74 for antennas located on the same side of the body and correlations that range from -0.37 to +0.14 with a mean value of -0.17 for antennas located on opposite sides of the body. There is thus less negative correlation between the antennas on opposite sides of the body when other polar angles than $\theta = 90^\circ$ and interference are considered. This explains why the relative reduction in PI_{50} when adding a second antenna to a single antenna is smaller for the simulations ($\Delta_{1,2} = -3.2\ dB$ on an initial value of 8.0 dB) than for the measurements ($\Delta_{1,2} = -6.7\ dB$ on an initial value of 13 dB). Also note that the median PI_{50} of the single antennas is lower for the simulations considering all angles than the simulations and the measurements, where only $\theta = 90^\circ$ is considered. This is because the directivity of these antennas shows the most variation in the azimuthal plane when they are worn on the body.

The variation caused by interference of incident fields from all polar angles (including other θ values than $\theta = 90^\circ$), and a varying azimuth angle, cannot be measured using calibration measurements (in the anechoic room). During future calibration measurements, the effect of other polar angles than $\theta = 90^\circ$ can be measured by using a transmitting antenna that can be rotated in both azimuth and polar angle around the subject or a spherical array of antennas surrounding the subject. The phase of the received powers (voltages) can be recorded by a vector network analyzer.

Quantities	'Urban Macro-cell'	'Indoor Pico-cell'	'Outdoor-Indoor'
positions^{polarizations}	B^H, D^V, G^H, I^V		
Averaging	geometric		
$p_{50}(AA_{geom})$ (cm^2)	6.06 ± 0.05	5.41 ± 0.06	4.42 ± 0.03
PI_{50} of AA_{geom} or S_{inc} (dB)	3.09 ± 0.02	3.71 ± 0.02	3.66 ± 0.01
Detection limit (μ W/m^2)	0.104 ± 0.001	0.117 ± 0.002	0.143 ± 0.002

Table 6.3: Performance characteristics of the selected combination of 4 nodes on the body.

The combination of 4 antennas with the lowest PI_{50} in the 'Urban Macro-cell' scenario and the additional constraint that the set must consist of two H- and V-polarized antennas, is chosen and re-calibrated with all the antennas worn simultaneously on the body. The received powers recorded during the calibration measurements are then processed in order to determine the AA_{geom} in the three studied environments. The chosen set of four antennas are two horizontally polarized antennas placed on positions B and G and two V-polarized antennas placed on D and I, see Table 6.3. The measured mutual coupling ($|S_{21}|^2$) between the 4 simultaneously worn antennas, averaged over the GSM 900 DL band, is smaller than -27 dB.

Table 6.3 lists the performance characteristics of the selected combination of antennas in all three studied environments. The median AA_{geom} values for the

set of four antennas are between 4.4 and 6.1 cm^2, given these median antenna apertures and the power detection limit of -72 dBm, a detection limit in terms of the incident power density can be calculated. Commercial PEMs have a detection limit of 0.07 μW/m^2, which is a factor of 1.5 lower than our detection limit in the 'Urban Macro-cell' scenario. However, single PEMs tend to underestimate the incident power density by a factor larger than 1.5 (see Chapters 3 and 4). The PI_{50} values on the median AA's range from 3.1 to 3.7 dB, depending on the environment.

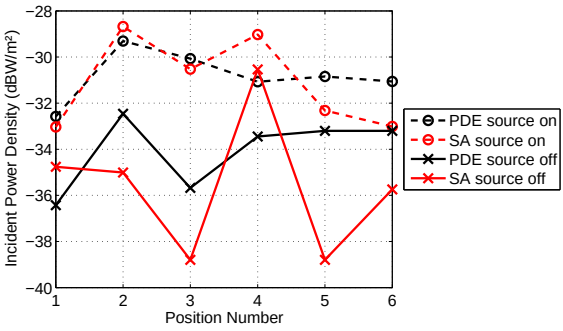

Figure 6.15: Results of the validation measurements, outlined in Figure 6.10.

Validation measurements in an indoor environment (see Fig. 6.10) are executed using the set-up on the body listed in Table 6.3. Figure 6.15 shows the incident power densities measured on the six locations shown in Fig. 6.10 with a spectrum analyzer (SA) and an isotropic antenna (in red) and with a subject equipped with the PDE (in black). The values with the pico-cell switched on (input power = 79 mW) are connected by dashed lines, while those without a controlled source are indicated by a full line. With the pico-cell emitting at 942.5 MHz, the correspondence between the SA and the PDE is excellent. The average difference between the two measured (logarithmic) power densities is +0.35 dB, which is much smaller than the measurement uncertainties expected in this scenario. For the measurements without the pico-cell emitting, the correspondence is worse: the average difference is +1.5 dB, with a deviation up to 5.6 dB. A larger deviation was to be expected for the 'Outdoor-Indoor' signal, since both the uncertainty due to traffic on the channel and the temporal fading [26] are larger in this case, which increases the measurement uncertainty of both the PDE and the SA (see Chapter 7).

6.6.1.3 Discussion

In this section, a PDE for the GSM 900 DL band was designed using calibration measurements in an anechoic chamber. From these calibration measurements, the distribution of antenna apertures of different combinations of antennas on the body can be determined. The variation on this distribution is characterized by the PI_{50}. These PI_{50} values decrease as a function of the number of used antennas on the body, see Figure 6.12, which is in line with the results obtained using numerical simulations in the previous chapters. The calibration measurements correspond very well with the numerical simulations if both are processed in the same way. If the influence of a polar angle of the incident plane waves and interference of those waves on the antennas is included in the processing of the simulations, then larger differences between simulations and measurements are observed.

The median reduction in PI_{50} when adding more antennas to a set of antennas, is larger for the distributions of the AA determined using calibration measurements than the reductions obtained using numerical simulations. This is explained by the more negative correlation between the antennas on different sides of the torso, due to the fixed $\theta = 90°$ during the calibration measurements.

Following the calibration measurements, the set of four antennas consisting of two H-and two V-polarized antennas with the lowest PI_{50} value was calibrated again in the anechoic chamber. This set of antennas is used for measurements in a real environment (see Chapter 7) and validation measurements. The PI_{50} value of this configuration is between 3.1 and 3.7 dB, depending on the environment. This value is a measure for the uncertainty caused by the human body and is low compared to the values found for single antennas. For the single antennas, either H- or V-polarized on positions A-L, the minimal and median PI_{50} values are 7.1 and 12 dB, respectively. In [21], a PI_{50} on the measured S_{inc} of 8.0 dB was found using numerical simulations in the same frequency bands. For a PEM worn on the hips, PI_{50} values of 6.5 and 16 dB, for H- and V-polarized incident fields in the GSM 900 DL band are recorded [10], respectively. A calibration of a couple of simultaneously worn PEMs on both hips of a subject showed a PI_{50} of 8.2 and 9.5 dB for the individual PEMs on the two hips and a PI_{50} of 4.8 dB for the combination of the two PEMs in a realistic environment (see Chapter 4). For a previous prototype of the PDE using three RF nodes, we obtained a PI_{50} of 4.5 dB (see section 6.3.2). The listed PI_{50} values in Table 6.3 are lower than all these values. This indicates that the PDE, presented here, can be used for measurements of the incident power density with less uncertainty.

Validation measurement using a spectrum analyzer and an isotropic antenna in an indoor environment show an excellent correspondence with PDE measurements, confirming the correct calibration of the measurement device.

The calibration approach used in this section is very similar to the one used in Section 5.4.3 of Chapter 5, where the same textile antennas are modeled and

placed on the virtual family male on similar positions on the body, but has some clear **advantages**. First, this design approach uses the actual antennas, which eliminates a large number of potential uncertainties, such as vertical and horizontal offset of the antennas, rotation of the antennas, differences in antenna's efficiency, and mismatch losses. Second, the subject with the same posture and morphology is used in the calibration and the (validation) measurements. When numerical simulations are used, it is (currently) not possible to use a detailed phantom for every subject and even when a detailed phantom of each subject could be made using magnetic resonance imaging, there would still remain several uncertainties on their dielectric parameters [27] and uncertainties associated with the FDTD simulation algorithm [28]. Therefore, we use the antenna apertures and PI_{50} values obtained from calibration measurements to process any measurements in a real environment. However, there are also some **drawbacks** associated with this technique. First, the dependence of the AA on the polar angle cannot be taken into account using this calibration set-up, while numerical simulations readily provide us with 3 dimensional information on the AA. Second, interference on the antenna cannot be properly taken into account using calibration measurements. Third, the reproducibility of the numerical simulations is perfect, whereas it is worse for the calibration measurements. An antenna can never be placed twice on the same subject on exactly the same position, with exactly the same orientation.

6.6.2 On-body Calibration of Multiple Frequency bands

Different single-band PDE's are presented in the previous sections. However, in reality, multiple frequency bands are present and should be measured simultaneously. In this section a calibration method of a multi-band PDE is presented.

6.6.2.1 Materials and Methods

Calibration setup Calibration measurements are executed using the procedure described in Section 6.6.1. However, in this section all the different frequency bands covered by the antennas described in Section 6.2.1 are calibrated on the body of a human subject. This subject is a 26 year old male who has a body mass index of 22.8 kg/m^2, a h_{tot} of 1.91 m, and a mass of 83 kg.

First, free-space measurements are executed along the axis of the rotational platform used to support the subject (see Figures 6.16 and 4.2). These measurements are performed at the center frequencies of eleven RF telecommunication bands covered by the six textile antennas described in Section 6.2.1, listed in Table 6.4, using a NARDA broadband probe (Narda NBM-550, Narda Microwave, Hauppauge, NY, USA). The incident power densities are measured for two polarizations of the TX (H and V) at six heights above the rotational platform (54,

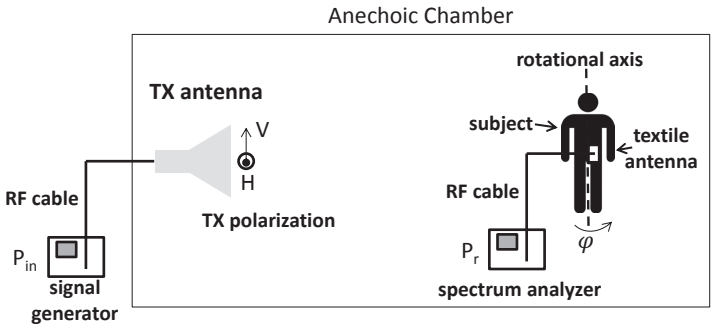

Figure 6.16: Illustration of the used calibration setup.

79, 128, 153, 177, and 204 cm) and are then averaged over the subject's height. Measurements closer to the floor than 54 cm are not possible using the NARDA broadband probe. The TX is a standard gain horn antenna, which is fed by a signal generator (SG) which sweeps the measured frequency band with an input power (P_{in}) of 10 mW.

Antenna type i	Bands
antenna 1	Lower LTE
antenna 2	GSM 900 UL
antenna 3	GSM 900 DL
antenna 4	DECT DCS UL DCS DL UMTS/HSPA UMTS UL
antenna 5	UMTS DL
antenna 6	WiFi 2G Upper LTE

Table 6.4: Studied antennas and their respective frequency bands.

Second, individual textile antennas are placed either H- or V-polarized on the 12 positions (A to L) on the subject's torso shown in Figure 6.9. The subject is then rotated over 360° around his rotational axis (see Figure 6.16), for two polarizations of the transmitting antenna (H and V). During the rotation, the received power (P_r) on the the textile antennas is recorded using a spectrum analyzer (SA) (R&S FSL, Rhode & Schwartz, Munich, Germany).

Table 6.5 lists the used settings of the SA and the SG. The center frequencies and frequency spans used by the SA and the SG are the same and depend on

Spectrum Analyzer	
Detection Mode	Positive Peak
Sweep Time	500 ms
Sweep Mode	Single
Reference Level	-20 dBm
Resolution Bandwidth	1 MHz
Signal Generator	
Number of points	21
Sweep Time	224 μs
Sweep Type	Linear Frequency
Power	10 mW

Table 6.5: Settings of the Spectrum Analyzer and Signal Generator during the calibration measurements.

the measured frequency band (see Table 6.1). For the GSM 900 DL band, the calibration using the RF nodes described in the previous paragraph is used. It is important that the sweep time of the spectrum analyzer is much larger than the sweep time of the SG, since this allows the SG to sweep the measured frequency band several times while the SA is measuring. If the difference in sweep times is too small, then the SA might not detect a received power in part of the frequency band. Therefore, a relative small number of frequency steps (22) is chosen for the SG, since this allows for a short sweep time. The reference level of the SA is chosen so that the full signal can be received without pre-amplification. The sweep mode cannot be continuous during these measurements, since we want to maintain a relationship between the rotation of the subject and the received powers. A single sweep ensures that the time at which the lowest frequency step is measured is always lower than the time at which the following frequency steps are measured, while this is not the case with a continuous measurement.

This setup has the advantage that it can be used for any frequency band in the RF range, since only the frequency settings of the SA and the SG have to be adapted, but it has the disadvantage that it uses a frequency sweep instead of a broadband detector (such as the RF nodes). A frequency sweep inevitably takes some time to complete, during which the subject will have rotated. In this case the maximum value during the sweep time of 0.5 s is measured, which might cause a small overestimation of the received power. The calibration measurements in the GSM 900 DL band use RF nodes that register both the positive peak and the mean received power during 1 s. During these measurements, the difference between the geometric mean and the positive peak power cannot be measured using a sensitivity of 1 dB. The same values are thus stored on the RF nodes. This means that the difference within a 1 s period is smaller than 0.5 dB. The difference during 0.5 s consequently has to be smaller.

Calibration processing The received powers ($P_{r,l}^{H/V}(f,\phi)$) on the different antenna positions l=A to L in the different frequency bands with center frequency f, can be combined with the measured incident power densities ($S_{inc}^{H/V}$) to calculate frequency, azimuth, and polarization dependent antenna apertures:

$$AA_l(f,\phi,\psi) = \frac{P_{r,l}^{V}(f,\phi)}{S_{inc}^{V}(f)} \times sin^2(\psi) + \frac{P_{r,l}^{H}(f,\phi)}{S_{inc}^{H}(f)} \times cos^2(\psi) \tag{6.16}$$

with $AA_l(f,\phi,\psi)$ the antenna aperture of a textile antenna with center frequency (f) placed on position l on the torso of the subject, as a function of the azimuth angle (ϕ) and the polarization (ψ). The distribution of the AA_l is determined using 1000 (ϕ,ψ) samples drawn from an appropriate distribution, see Section 6.6. The azimuth (ϕ) samples are drawn from a uniform distribution $[0, 2\pi[$. In the case of the down-link bands (GSM 900 DL, DCS DL, and UMTS DL), the polarization samples (ψ) are drawn from the Gaussian polarization distribution in an 'Urban Macro-cell' scenario, as described in Table 3.3. A uniform polarization between $[0, 2\pi[$ is chosen for the other bands, since no a priori assumptions can be made about the orientation of the sources that emit the radiation and consequently no assumptions can be made on the incident polarization.

The median AA_l and the interquartile distance $PI_{50,l}$ of the distribution are then extracted and compared for the different frequency bands. The same averaging process is applied over the different antennas is applied in the different frequency bands, in order to estimate the distributions of the AA of a PDE at the different studied frequencies.

Combining Multiple Frequency Bands on the Human Body PDEs that measure in individual frequency bands are extensively discussed in the previous sections. However, the goal is to measure the RF incident power density ($S_{inc,tot}^{meas}$) in different frequency bands:

$$S_{inc,tot}^{meas} = \sum_{i=1}^{11} S_{inc}^{meas}(f_i) \tag{6.17}$$

with $S_{inc}^{meas}(f_i)$ the incident power density measured in the eleven bands listed in Table 6.6. Note that if the total exposure is compared to the ICNIRP reference levels [11], then the sum of the ratios of the measured power densities over the reference levels at the measured frequencies should be calculated and this sum may not exceed one:

$$\sum_{i=1}^{11} \frac{S_{inc}^{meas}(f_i)}{S_{RL}(f_i)} \leq 1 \tag{6.18}$$

with $S_{RL}(f_i)$ the ICNIRP reference level [11] on the incident power density at frequency f_i.

The upper and lower uncertainties caused by the presence of the body on the total power density (see Eq. 6.17) are:

$$u_{low,tot} = \sqrt{\sum_{i=1}^{11} u_{low,i}^2} \tag{6.19}$$

$$u_{up,tot} = \sqrt{\sum_{i=1}^{11} u_{up,i}^2} \tag{6.20}$$

with $u_{low,i}$ and $u_{up,i}$ the upper and lower (relative) standard uncertainties [29] on the incident power densities in the individual frequency bands. This calculation of the total uncertainty holds if the uncertainties on the different measured power densities caused by the presence of the human body can be considered as uncorrelated [29]. In this case the uncertainties are caused by the variation in polarization, the azimuth angle, and the presence of the body.

Standard uncertainties usually correspond to the standard deviations of the distributions of the antenna apertures determined for the PDEs in the individual frequency bands (AA_i) [29]. However, we have shown that the distributions of the AA_i can be asymmetric. Therefore, the lower standard uncertainty $s_{low,i}$ and upper standard uncertainty $s_{up,i}$ are defined as:

$$s_{low,i} = 1 - \frac{p_{50}(AA_i)}{p_{84}(AA_i)} \tag{6.21}$$

$$s_{up,i} = \frac{p_{50}(AA_i)}{p_{16}(AA_i)} - 1 \tag{6.22}$$

with $p_{16}(AA_i)$ and $p_{84}(AA_i)$ the 16% and 84% percentiles of the antenna aperture AA_i in frequency band i.

The distribution of the AA_i will depend on the chosen positions to place the antennas on the body. In the design there are **twelve** potential locations on the human body (A to L), see Figure 6.9 to place **six** types of antennas, listed in Table 6.4.

The goal is to place these antennas on the 12 potential locations, minimizing the uncertainty on the incident power density. This would imply that we would have to minimize a sum of upper or lower uncertainties:

$$min \left\{ \sqrt{\sum_{j=1}^{N_{bands}} (s_{low/up,j}^{V/H})^2} \right\} \tag{6.23}$$

with $s_{low/up,j}^{V/H}$ the lower or upper uncertainties in the frequency bands j covered by the antenna for a V/H polarized antenna. However, the optimal placement which minimizes the lower and upper uncertainties might be different. Therefore, we

have chosen to minimize the (linear) 68% prediction interval (PI_{68}, denoted here as D_i) on the AA_i:

$$D_i = \frac{p_{84}(AA_i)}{p_{16}(AA_i)} \tag{6.24}$$

It is clear that if D_i is minimal, then the uncertainties will be minimal as well. A minimal D_i can be determined for every location l for each antenna i. If the antenna only registers in a single frequency band (antennas 1-3 and 5), this PI_{68} is the minimum of the PI_{68}'s on measurements with a H-or V-polarized antenna registering in frequency band i placed on location l. If the considered antenna is a multi-band antenna, the quadratic sum of the D_i values in the different bands covered by the antenna is used:

$$D_{l,i} = min\left\{\sqrt{\sum_{j=1}^{N_{bands}} (D_{l,j}^{V/H})^2}\right\} \tag{6.25}$$

with $D_{l,j}^{V/H}$ the PI_{68} in the frequency bands j covered by the antenna, for a V/H polarized antenna placed on location l. Similar 68% prediction intervals $D_{l,i}$ can be defined for any combination of locations on the body found in the powerset $P(G) = \{P1, P2, .., PN\}$ of $G = \{A, .., L\}$ the group of all potential locations. This powerset contains all possible combinations of locations drawn from G (including the empty set). This gives rise to an $|P(G)| \times 6$ matrix $\overline{\overline{D}}$:

$$\overline{\overline{D}} = \begin{pmatrix} D_{1,1} & \dots & D_{1,6} \\ D_{2,1} & \dots & D_{2,6} \\ \vdots & \vdots & \vdots \\ D_{|P(G)|,1} & \dots & D_{|P(G)|,6} \end{pmatrix}$$

with $|P(G)|$ the number of elements in the power set $P(G)$. Each element $D_{P,i}$ of $\overline{\overline{D}}$ corresponds to the PI_{68} of a type of antenna i ($i = 1..6$) if it were placed on a combination of locations $P : P \subset P(G)$. For the empty set $P = \{\}$ the uncertainty $D_{P,i} = \infty$, which ensures that at least one antenna is chosen for each band. $D_{P,i}$ corresponds to twice the standard uncertainty in case of a normal distribution.

In order to find the best locations to place a certain antenna type on the torso of the subject, it suffices to minimize the columns of $\overline{\overline{D}}$. However, this might lead to an unwanted overlap of antennas.

Instead, we want to find the best possible combination e.g. minimize the combined PI_{68} of the different frequency bands over the complete matrix $\overline{\overline{D}}$. To this aim, the following sum (the combined PI_{68}) is minimized:

$$\frac{1}{4}\sum_{i=1}^{6}\sum_{P\in P(G)} b_i^P \times D_{P,i}^2 \tag{6.26}$$

with b_i^P a binary variable which fulfills the following restrictions:

$$\sum_{i=1}^{6} b_i^P \leq 1, \qquad \forall P : P \subset P(G) \tag{6.27}$$

which ensures that a certain subset P can be chosen only once, and:

$$\sum_{P \in P(G)} b_i^P = 1, \qquad \forall i \tag{6.28}$$

which ensures that there is only one subset P chosen for every type of antenna i. Note that these restrictions do not exclude a potential overlap of antennas, since different subsets P might contain the same location $l = A..L$. Therefore, we define another binary variable z_i^l, with $i = 1..6$ and $l = A..L$. z_i^l is equal to one if an antenna of type i is placed on location l, otherwise $z_i^l = 0$. We then impose the following condition on z_i^l:

$$\sum_{i=1}^{6} z_i^l = 1, \qquad \forall l \tag{6.29}$$

which makes sure that every location l has to be taken by one antenna i. b_i^P and z_i^l are connected by the following relationship:

$$b_i^P \leq z_i^l, \qquad \forall i, \forall P : P \subset P(G), \forall l : l \in P \tag{6.30}$$

which makes sure that if a subset P is assigned to antenna type i, then the z_i^l values of locations $l \in P$ have to be one.

The combined PI_{68}, see Equation 6.26, is determined for any potential combination of z_i^l and b_i^P, fulfilling the requirements listed in Equations 6.27 to 6.30. The combination with the lowest combined PI_{68}, subject to 6.27 to 6.30, is then chosen.

6.6.2.2 Results

On-body Calibration Table 6.6 lists the results of the calibration measurements of the single textile antennas on the body. The median antenna apertures of the single antennas range from 0.39 cm^2 (for WiFi 2G) to 6.8 cm^2 (for GSM 900 DL). The antenna aperture depends on the directive gain of the used antenna, which is in this case averaged over the azimuth angle ϕ and polarization ψ according to the distributions listed in Table 6.6, on the antenna efficiency, and on the square of the wavelength of the received signals [8]. The median PI_{50} values range from 6.7 dB (for the lower LTE band) to 14 dB (for the HSPA/UMTS band) and roughly increase with increasing frequency (Pearson correlation coefficient of 0.77 with p-value of 0.006). The median PI_{68} values range from 10 dB (lower LTE band) to

	Name	Frequency Range (MHz)	Polarization distribution	$p_{50}(AA)$ (cm^2)	$p_{50}(PI_{50})$ (dB)	$p_{50}(PI_{68})$ (dB)
1	LTE low	791-862	Random	0.70	6.7	10
2	GSM 900 UL	880-915	Random	3.8	8.3	12
3	GSM 900 DL	925-960	Urban Macro-cell	6.8	12	16
4	DCS UL	1710-1785	Random	1.8	13	17
5	DCS DL	1805-1880	Urban Macro-cell	1.1	12	17
6	DECT	1880-1900	Random	1.3	13	19
7	UMTS/HSPA	1900-1920	Random	1.3	14	19
8	UMTS UL	1920-1980	Random	1.4	13	19
9	UMTS DL	2110-2170	Urban Macro-cell	0.81	13	17
10	WiFi 2G	2400-2500	Random	0.39	13	18
11	LTE upper	2500-2690	Random	0.51	13	17

Table 6.6: Studied frequency bands, their frequency range, their polarization distribution, median antenna aperture ($p_{50}(AA)$) of the single antennas, median 50% prediction interval ($p_{50}(PI_{50})$), and median 68% prediction interval ($p_{50}(PI_{68})$) on the incident power density.

19 dB (for DECT, UMTS/HSPA, and UMTS UL). These values are also positively correlated (0.74 with a p-value of 0.009) with the increasing center frequency.

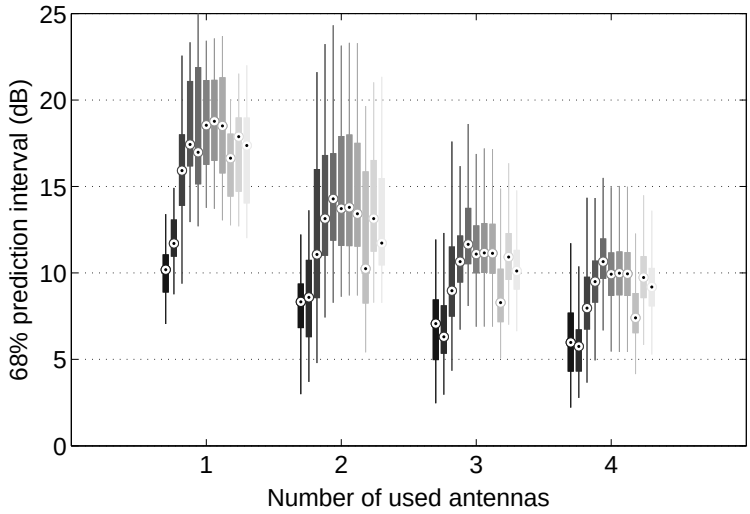

Figure 6.17: 68% prediction interval on the incident power density measured in the different frequency bands listed in Table 6.6 as a function of the number of used on-body antennas for a geometric averaging over the different antennas. The box-plots are for increasing frequency (11 bands) from left to right and from dark to light grey.

Figure 6.17 shows box-plots of the PI_{68} of all the combinations of N antennas ($N = 1..4$) that measure in the 11 frequency bands listed in Table 6.6 chosen from 12 potential locations on the body (A to L, see Fig. 6.9) and two orientations of the (linearly polarized) antennas on the body. Similar to the previous chapter, we find that single antennas have relatively high prediction intervals on the incident power density, with median PI_{68} values ranging from 10 dB in the lower LTE band to 19 dB in the DECT, UMTS/HSPA, and the UMTS UL bands. The distributions of the PI_{68} values are located at lower values when the received power is averaged over two antennas, with median PI_{68} values ranging from 8.3 dB in the lower LTE band to 14 dB in the DCS DL band. In comparison with single antennas this corresponds to median reductions in the PI_{68} ranging from 1.9 dB in the lower LTE band to 6.4 dB in the UMTS DL band. When combinations of three antennas are considered the median PI_{68} values range from 6.3 dB in the GSM UL band to 12 dB in the DCS DL band. In comparison with single antennas these median values correspond to reductions in PI_{68} ranging from 3.1 dB in the lower LTE band to 8.4 dB in the UMTS DL band. The PI_{68} values range from 5.7 dB in the GSM UL band to 11 dB in the DCS DL band for combinations of 4 antennas. In comparison with single antennas median reductions in PI_{68} ranging from 4.2 dB in the lower LTE band to 9.2 dB in the UMTS DL band are measured.

The reductions in prediction interval are obtained due to the negative correlation between the antennas located on the front and back of the body and the reduction in prediction interval which is associated with averaging over different measurements of the same quantity. Similar results are found for an arithmetic averaging over multiple antennas, but the distributions of the PI_{68} using multiple antennas are located at higher values.

Combining Multiple Frequency Bands on the Human Body Table 6.7 lists the optimal placement of the antennas on the subject's upper torso, fulfilling Equation 6.26. The combination of antennas with the lowest PI_{68} consists of 12 antennas chosen pairwise from each of the six antenna types. Each pair consists of an antenna placed on the front of the body and one on the back of the torso. The PI_{68} values for the three PIFA's (antenna types 1 to 3) range from 4.3 dB to 4.8 dB. The pair of 1.8 GHz antennas (type 4) has a combined PI_{68} of 12 dB using the setup listed in Table 6.7. The pair of UMTS DL antennas (type 5) have a PI_{68} of 7.1 dB and the two antennas of type 6 have a PI_{68} of 8.4 dB. These PI_{68} values are indeed located in the lower end of the distributions shown in Figure 6.17. The optimal combined PI_{68} value of all antennas is 12.6 dB.

A second case in which two orthogonal antennas are chosen per antenna type, is analyzed as well. This configuration is more isotropic regarding the polarization of the incident fields, which is desirable for a measurement device. However,

Antenna Type	Frequency Band	Number of antennas	$Positions^{Polarizations}$	PI_{68} (.)	PI_{68} (dB)
Optimal Combination					
1	Lower LTE	2	E^V,H^V	2.8	4.5
2	GSM 900 UL	2	F^V,J^V	2.7	4.3
3	GSM 900 DL	2	D^V,I^V	3.0	4.8
4	DECT, DCS DL, DCS UL, UMTS/HSPA, UMTS UL	2	A^H,K^V	16	12
5	UMTS DL	2	C^V,G^V	5.1	7.1
6	WiFi 2G, Upper LTE	2	B^H,L^H	6.9	8.4
			$min(\sqrt{\sum_{j=1}^{n_{bands}} D_{i,j}^2}) =$	**18.4**	**12.6**
Two cross-polarized antennas per type					
1	Lower LTE	2	E^V,I^H	3.0	4.8
2	GSM 900 UL	2	F^H,H^V	3.6	5.5
3	GSM 900 DL	2	C^V,G^H	4.3	6.4
4	DECT, DCS DL, DCS UL, UMTS/HSPA, UMTS UL	2	A^H,K^V	16	12
5	UMTS DL	2	D^V,J^H	6.0	7.8
6	WiFi 2G, Upper LTE	2	B^H,L^V	7.4	8.7
			$min(\sqrt{\sum_{j=1}^{n_{bands}} D_{i,j}^2}) =$	**19.3**	**12.9**

Table 6.7: Optimal positioning of the 6 studied antenna types and an optimal positioning of two antennas of each type on the body of the subject with the corresponding positions, polarizations, and PI_{68}.

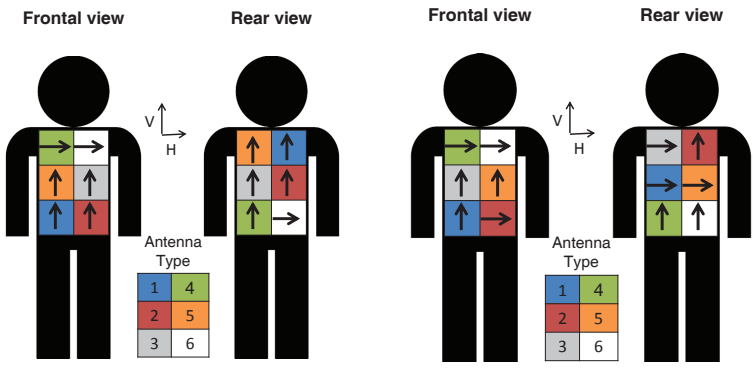

(a) Optimal combination (b) Two cross-polarized antennas per type

Figure 6.18: Optimal positioning of the six antenna types on the subjects torso. The colors indicate the different antenna types, while the arrows indicate the polarizations.

this does not ensure the lowest measurement uncertainty in an environment where the polarization has a Gaussian distribution, see Table 6.7. In this case the PI_{68} values are larger than or equal to those found for the optimal case. The resulting

combined PI_{68} value is 12.9 dB, which is only 0.3 dB higher than the optimal case. Figure 6.18 shows the optimal positioning of the six antenna types on the body, if two orthogonal antennas are chosen per antenna type.

6.6.2.3 Discussion

Comparing Frequency Bands The effective on-body antenna apertures of the different studied textile antennas are listed in Table 6.6. The GSM 900 DL antenna has the highest antenna aperture. Note that this antenna has a higher radiation efficiency than the other antennas, which leads to a more effective antenna aperture. Since the antenna aperture depends quadratically on the resonance wavelength, the antenna aperture decreases at higher frequencies. This is not the case for the lower LTE antenna and the GSM 900 UL antenna in comparison with the GSM 900 DL antenna. The three antennas are all PIFA's, with relatively high radiation efficiencies, but the GSM 900 DL antenna has the highest efficiency (and gain), which increases its antenna aperture.

The median PI_{50} and PI_{68} values of the individual antennas are also listed in Table 6.6. The prediction intervals generally increase with frequency, as we find positive correlations of 0.77 and 0.74 between the center frequency of the antennas and the PI_{50} and PI_{68} values, as well. In Chapter 3 it is shown that the PI_{50} and PI_{95} values of a single personal exposimeter (PEM) in front of a BSA increase with frequency. In the same chapter we found that the response of a single PEM in the WiFi 2G band shows more variation than the response in the GSM 900 DL band. In [13] an increase with frequency of the variation on the response was found, while in [10, 21] no clear frequency dependence is established. In the calibration measurements of Chapter 4, no clear frequency dependence of the PI_{50} is found. The currently available knowledge indicates that there might be an increase in variation due to the scattering of the human body (above the resonance of the human body), but that the antennas also play a role in the variation of the response. This re-enforces the importance of calibration measurements to determine the actual prediction intervals.

Figure 6.17 shows the distribution of the PI_{68} for all the possible combinations using N antennas for $N = 1..4$. The distribution of the PI_{68} values is located at lower values when an averaging over multiple antennas is used. We previously demonstrated that this is caused by the averaging over multiple antennas and by the negative correlation that exists between antennas placed on different sides of the torso.

Comparison with Numerical Simulations and Literature The **lower LTE band** has not yet been studied in literature. In Chapter 3 the response of a single PEM is simulated at 800 MHz in front of a BSA. A PI_{50} value of 13 dB was found near the BSA. The PI_{50} values measured for the single antennas in this chapter are

considerably lower with a median value of 6.7 dB and a 50% confidence interval on this median value of 2.2 dB. The large difference between the responses in front of the body and at the back of the body explain the relatively large PI_{50} value in front of the BSA.

The **GSM 900 UL band** is studied in Chapter 4 of this book. PI_{50} values of 6.2 dB and 6.3 dB are found on the response of a conventional PEM worn on the right and left hip of the same subject, for the same processing of the calibration data. In this chapter a median PI_{50} value of 8.3 dB is found. The lowest PI_{50} value in this chapter is 5.4 dB, so the value measured for the conventional PEM is within the range of our calibration measurements. The PI_{50} of the average over the two PEMs is found to be 3.3 dB, which corresponds to a reduction of about 3 dB. In this chapter, a median reduction in PI_{50} in the GSM 900 DL band of 2.7 dB is measured. The median PI_{50} of all pairs of antennas is 5.6 dB. A higher median variation and reduction in variation was expected since in this calibration also combinations of antennas on the same side of the body are taken into account, while the two PEMs in Chapter 4 are located on opposite sides of the body.

The PI_{50} value of 8.0 dB found in [21] is lower than the median value of 12 dB found in the **GSM 900 DL band**. Figure 6.13 already demonstrated that the median PI_{50} using calibration measurements of single antennas is higher than what is predicted using numerical simulations. Figure 6.13 also demonstrates that the behavior of the PI_{50} as a function of the number of antennas can be predicted well using numerical simulations. In [10] a PEM is worn on the hip of a subject during calibration measurements, this resulted in PI_{50} values of 6.5 and 16 dB, for H- and V-polarized incident fields, respectively. The median value found in the GSM 900 DL band for a realistic polarization is in between these values. Both values measured in [10] are within the range of PI_{50} values measured in this chapter. The same holds for the values measured for a PEM worn on the left (9.5 dB) and right hip (8.1 dB) in Chapter 4, although they are located in the lower quartile of the distribution.

The median PI_{50} values measured using antenna type 4 in the **DCS UL, DCS DL, DECT, UMTS/HSPA, and UMTS UL bands** range from 12 to 13 dB. In Chapter 4, PI_{50} values between 5.9 dB and 10.6 dB are measured on response of a PEM worn on the right and left hip, respectively, in DCS UL, DCS DL, DECT, and UMTS UL bands. These values are lower than those found using the cavity backed planar antenna. In [10], PI_{50} values of approximately 4 dB and 20 dB are measured in the DCS DL band, for H- and V- polarized incident electromagnetic fields, respectively, while values of 6.7 dB and 18 dB are measured for the same polarizations in the UMTS UL band. The median values found in this chapter for a realistic polarization are comparable to the average of the two polarizations measured in [10].

The response of a PEM in the **UMTS DL band** is described in Chapter 4

and in [10, 21]. The PI_{50} value on the response of a body-worn single PEM is measured to be approximately 8 dB and 20 dB for H- and V-polarized incident fields, respectively, in [10]. In Chapter 4, PI_{50}'s of 14 dB and 12 dB are estimated for the response of a PEM worn on the left and right hip, respectively. In [21], the PI_{50} on the response of a PEM worn on the body is estimated to be relatively low at 2140 MHz, a value of only 5.0 dB was found using numerical simulations. The median value of the PI_{50} of the single antennas tuned to the UMTS DL band found in this chapter in an 'Urban Macro-cell' scenario is 13.1 dB, with 50% of the values located in a 2.5 dB interval around this value. This value is in between the two values found in [10] for the two orthogonal polarizations studied in [10]. This is expected since a realistic polarization is studied in this chapter. The values found in Chapter 4 correspond to those found in this chapter. The value found in [21] is out of the range of our measurements. Note that a lower variation is expected for the numerical simulations, since they do not take into account the additional variation caused by the directivity of the antennas. The used patch antenna has a certain front-to-back ratio in its directivity, which is not taken into account in the numerical simulations where the sensors are considered to be perfectly isotropic and only shadowing by the human body occurs.

There are more previous studies that focus on PEMs used in the **WiFi 2G band**. In Chapter 4, PI_{50}'s of 7.3 dB and 8.4 dB are estimated for the response of a PEM worn on the left and right hip, respectively. In section 6.5 of this chapter, two other on-body textile antennas tuned to the WiFi 2G band are calibrated on the front and back of the body using the same set-up, which resulted in PI_{50} values of 17 dB and 23 dB on the back and the front of the human subject, respectively. In Section 5.4.2 of the previous chapter, the PI_{50} of the response of a single PEM worn on the upper torso of the VFM is simulated at 2450 MHz in the 'Urban Macro-cell' scenario, which resulted in a median PI_{50} of 8.3 dB with 50% of all the simulated values located in an interval of 2.4 dB around this value. The PI_{50} value on the response of a body-worn single PEM is measured to be approximately 9 dB and 18 dB for H- and V-polarized incident fields, respectively, in [10]. In [21], the PI_{50} on the response of a PEM worn on the body of a numerical phantom in a model for a realistic environment is estimated to be 9.6 dB. The median value of the PI_{50} of all the different single antenna positions studied in this section, using a dual-band antenna, is 13.2 dB with 50% of all the PI_{50} values located in a region of 5 dB around this median value. Note that the PI_{50} values found using the calibration measurements are higher than those found using numerical simulations in Chapter 5 and [21]. We attribute this larger PI_{50} to the use of antennas in the calibration measurements which cause an additional decrease in received power of fields incident from the back of the antennas due to the metallic plane on the back of the antennas, whereas in the numerical simulations only the body causes shadowing of plane waves incident from the back of the human body.

The measurements presented in section 6.5 are higher than the median value found in this section and are located on the upper end of the distribution of the PI_{50} values using the dual polarized antenna. The PI_{50}'s measured in [10] are located around the PI_{50} value found in this section for a random polarization, as was to be expected.

The **upper LTE band** has not yet been studied in literature. In Chapter 3 of this book, a median PI_{50} value of 21 dB is found for a single PEM worn on the body in front of a BSA, whereas in this section the calibration measurements show a median PI_{50} of 13 dB for single antennas worn on the body with 50% of the PI_{50} values of single antennas in an interval of 5.4 dB around this median value. The variation on the response in front of the BSA is higher due to the relatively large shadowing of the body (see Figure 3.5).

Combining Multiple Frequency Bands on the Human Body Table 6.7 lists the combined uncertainty in terms of the PI_{68} of the best combination of 12 antennas placed on the subject's torso and the best combination where 2 orthogonal antennas of each type are placed on the subject's torso. In this study all the potential distributions of 12 antennas on the body where studied. Note that a configuration where each frequency band is assigned two antennas, is selected as the one leading to the lowest combined PI_{68} from all potential configurations. This is due to the large improvement in PI_{68} which is obtained when a second antenna is added to a single antenna. A potential reduction in combined uncertainty could be made by adding a third antenna of type 4, which could reduce the measurement uncertainty in five bands simultaneously, but the cost of removing one of the other antennas is too high (the PI_{68} of a single antenna would be too high). Assigning two antennas to each band turns out to be the optimal solution. However, the antennas in each band are not orthogonally polarized. This is explained by the used calibration and processing method, which looks for positions which are isotropic in the azimuthal angle, rather than antennas that are isotropic regarding the polarization angle.

Therefore, a second optimization is carried out for combinations of two orthogonal antennas. The results listed in Table 6.7 show that more isotropy in terms of polarization can be obtained at a small cost in combined PI_{68}. The PI_{68} of the optimal combination of two orthogonal antennas per frequency band is only 0.3 dB higher on a value of 12.6 dB. The differences are smaller than 1.6 dB for the individual bands.

Other optimizations, where certain frequency bands are prioritized, are possible using this calibration data by adding weight factors to the sum shown in Equation 6.25.

The combined PI_{68} for the optimal combination of antennas on the body, 12.6 dB, or the best combination using two orthogonal antennas in each band each, 12.9 dB, is low compared to the combined median and lowest PI_{68} values for the

single antennas, which are 22.5 dB and 17.6 dB, respectively.

6.7 Conclusions

The calibration of a personal distributed exposimeter (PDE) for the registration of one's personal exposure to radio frequency (RF) incident power density is studied.

In a first section of this chapter, it is demonstrated that a PDE for measurements with good accuracy and low uncertainty in the GSM 900 DL band can be constructed using a limited number of antennas. This design of this PDE is based on a regression model of numerical simulations. A preliminary model of the exposimeter consisting of 1, 2, or 3 antennas is calibrated in an anechoic chamber using a real human. It is shown that the prototype of the PDE performs much better than commercially available exposimeters.

In the second part of the chapter, a PDE for the detection of Wireless Fidelity (WiFi) around 2450 MHz is calibrated. The PDE is constructed using flexible textile antennas and wearable electronics, which can both be integrated in clothing, do not impede movement of a subject wearing the PDE, and communicate wirelessly with a receiver on a laptop, personal computer, or personal device. Therefore, the PDE can be made invisible for other humans and will not alter a subject's behavior while performing measurements. A calibration of the wireless PDE shows that the uncertainty in terms of the 50% prediction interval (PI_{50}) of the measured incident electric-field strength can be significantly reduced to a minimal value of 3.2 dB for WiFi signals. This value is low in comparison with state-of-the-art personal exposimeters. In this way, one obtains lower uncertainties on measurements of the incident electric-field strength, calculated using these PI_{50} values.

In a third section of this chapter, a PDE for measurements in the GSM 900 DL band is designed based on calibration measurements of textile antennas on 12 potential location on the torso of a human subject in an anechoic chamber. The calibration measurements are processed in order to determine the (averaged), antenna aperture (AA) in a real environment. The calibration measurements show that the variation on the AA, in terms of the PI_{50}, can be reduced when multiple antennas are worn on the body. The calibration measurements correspond well with numerical simulations that are processed in the same way. A set of four antennas is then calibrated simultaneously on the body of the same subject. The resulting PDE has a lower PI_{50} than any previously studied personal exposimeter and performs excellently during calibration measurements in an indoor environment.

In a final part of this chapter, for the first time, a multi-band PDE consisting of six types of antennas that measure eleven frequency bands is calibrated in an anechoic chamber. The calibration measurements show that the measurement uncertainty in the different frequency bands, in terms of the 68% prediction interval, can be reduced when multiple antennas are placed on the body. An optimal place-

ment to measure simultaneously on the 12 potential locations on the body in the eleven different frequency bands is determined. A combination of two antennas in each frequency band and on each side of the body, leads to the lowest combined 68% prediction interval of 13 dB.

In the following chapter, the calibration results obtained in this chapter will be used to conduct measurements with a PDE in a realistic environment.

6.8 Acknowledgment

The author would like to thank D. Verleye for his contributions to Subsection 6.6.2.1, S. Agneessens and D. Van Baelen for their contributions to Subsection 6.2.1, and S. Agneessens, L. Verloock, H. Declerq, J. Lecoutere, S. Aerts and P. Vanveerdeghem for their assistance during the calibration measurements.

References

[1] F Declerq, A Georgadis, and H Rogier. *Wearable aperturecoupled shorted solar patch antenna for remote tracking and monitoring applications.* Proceedings of the 5th European Conference on Antennas and Propagation (EUCAP). Rome, Italy., 2011.

[2] S Lemey, F Declerq, and H Rogier. *Dual-Band Substrate Integrated Waveguide Textile Antenna With Integrated Solar Harvester.* IEEE Antennas and Wireless Propagation Letters, 13:269–272, 2014.

[3] S Agneessens and H Rogier. *Compact Half Diamond Dual-Band Textile HMSIW On-Body Antenna.* IEEE Transactions on Antennas and Propagation, 162(5):2374–2381, 2014.

[4] L Vallozzi, H Rogier, and C Hertleer. *Dual polarized textile patch antenna for integration into protective garments.* IEEE Antennas and Wireless Propagation Letters., 7:440–443, 2008.

[5] Belgian Institute for Postal services and Telecommunications (BIPT). *www.bipt.be*.

[6] J F B Bolte and T Eikelboom. *Personal radiofrequency electromagnetic field measurements in The Netherlands: exposure level and variability for everyday activities, times of day and types of area.* Environment international, 48:133–42, November 2012.

[7] W Joseph, P Frei, M Roösli, G Thuróczy, P Gajsek, T Trcek, J Bolte, G Vermeeren, E Mohler, P Juhász, V Finta, and L Martens. *Comparison of per-*

sonal radio frequency electromagnetic field exposure in different urban areas across Europe. Environmental research, 110(7):658–63, October 2010.

[8] C A Balanis. *Antenna Theory: Analysis and Design*. 1982.

[9] A Thielens, G Vermeeren, W Joseph, and L Martens. *Stochastic Method for the Determination of the Organ-specific Averages SAR in Realistic Environments at 950 MHz.* Bioelectromagentics, 34(7):549–562, 2013.

[10] J F B Bolte, G van der Zande, and J Kamer. *Calibration and uncertainties in personal exposure measurements of radiofrequency electromagnetic fields.* Bioelectromagnetics, 32(8):652–63, December 2011.

[11] ICNIRP International Commission on Non-Ionizing Radiation Protection. *Guidelines for limiting exposure to time-varying electric, magnetic, and electromagnetic fields (up to 300 GHz).* Health physics, 74:494–522, 1998.

[12] G Vermeeren, W Joseph, and L Martens. *Whole-body SAR in spheroidal adult and child phantoms in realistic exposure environment*. Health Physics, 94(June):345–354, 2008.

[13] S Iskra, R McKenzie, and I Cosic. *Monte Carlo simulations of the electric field close to the body in realistic environments for application in personal radiofrequency dosimetry.* Radiation Protection Dosimetry, 147(4):517–27, 2011.

[14] I Locher, M Klemm, T Kirstein, and G Troster. *Design and characterization of purely textile patch antennas.* IEEE Trans Adv Packag, 29:777–788, 2006.

[15] C Hertleer, A Tronquo, H Rogier, L Vallozzi, and L Van Langenhove. *Aperture-coupled patch antenna for integration into wearable textile systems.* IEEE Antenn Wirel Propagation Lett, 6:392–395, 2007.

[16] S Agneessens, P Van Torre, F Declerq, G J Spinnewyn, H Stockman, and H. Rogier. *Design of a wearable, low-cost, through-wall doppler radar system.* Int. J. Antennas and Propagation, 2012.

[17] R Carta, P Jourand, B Hermans, J Thone, D Brosteaux, T Vervust, F Bossuyt, F Axisa, J Vanfleteren, and R Puers. *Design and implementation of advanced systems in a flexible stretchable technology for biomedical applications.* Sensor Actuat A Phys, 156:79–87, 2009.

[18] P Jourand, H De Clercq, and R Puers. *Robust monitoring of vital signs integrated in textile.* Sensor Actuat A Phys, 161:288–296, 2010.

[19] CENELEC (European Committee for Electrotechnical Standardization). *TC 106x WG1 EN 50492 in situ. Basic standard for the in-situ measurement of electromagnetic field strength related to human exposure in the vicinity of base stations. Brussels, Belgium*. 2008.

[20] J Blas, F A Lago, P Fernández, R M Lorenzo, and E J Abril. *Potential exposure assessment errors associated with body-worn RF dosimeters.* Bioelectromagnetics, 28(7):573–6, October 2007.

[21] G Neubauer, S Cecil, W Giczi, P Preiner, J Frölich, and Martin Röösli. *The Association Between Exposure Determined by Radiofrequency Personal Exposimeters and Human Exposure: A Simulation Study.* Bioelectromagnetics, 31(7):535–45, 2010.

[22] C Olivier. *Characterisation of the Electromagnetic Radiation close to Broadcast and Wireless Communication Antennas.* PhD Book, Ghent, Belgium, 2007.

[23] K Kalliola, K Sulonen, H Laitinen, J Krogerus, and P Vainikainen. *Angular Power Distribution and Mean Effective Gain of Mobile Antenna in Different Propagation*. (September):823–838, 2002.

[24] G Vermeeren, W Joseph, and L Martens. *Statistical multi-path exposure method for assessing the whole-body SAR in a heterogeneous human body model in a realistic environment.* Bioelectromagnetics, 34(3):240–51, April 2013.

[25] A Thielens, H De Clercq, S Agneessens, J Lecoutere, L Verloock, G Declercq, Fand Vermeeren, E Tanghe, H Rogier, R Puers, L Martens, and W Joseph. *Personal distributed exposimeter for radio frequency exposure assessment in real environments.* Bioelectromagnetics, 34(7):563–7, 2013.

[26] S R Saunders. *Antennas and Propagation for Wireless Communication Systems.* TJ Wiley and Sons Ltd, 1999.

[27] J F Bakker, M M Paulides, A Christ, N Kuster, and G C van Rhoon. *Assessment of induced SAR in children exposed to electromagnetic plane waves between 10 MHz and 5.6 GHz.* Physics in medicine and biology, 55(11):3115–3130, 2010.

[28] J W Hand. *Modelling the interaction of electromagnetic fields (10 MHz-10 GHz) with the human body: methods and applications.* Physics in medicine and biology, 53(16):R243–86, August 2008.

[29] B N Taylor and C E Kuyatt. *Guidelines for Evaluating and Expressing the Uncertainty of NIST Measurement Results.* NIST Technical note 1297, 1994.

7

Measurements of the S_{inc} and SAR_{wb} using a Personal, Distributed Exposimeter

7.1 Introduction

The absorption of radio frequency (RF) radiation is studied using the specific absorption rate (SAR). This quantity is defined as the rate at which energy is absorbed in an amount of mass. The SAR is to be averaged over a certain volume or mass [1]. When considering far-field exposure, the most commonly studied SAR is the whole-body averaged SAR (SAR_{wb}) [2]. However, this quantity can only be assessed using numerical simulations. Therefore, reference levels have been defined on the incident power density (S_{inc}) [1]. In exposure assessment studies, incident power densities are usually registered using personal exposimeters (PEMs). These devices and their usage have been described in Chapter 3. The S_{inc} can be estimated from measurements using PEMs, but with a relatively large measurement uncertainty, as demonstrated in the previous chapters. Consequently, the SAR_{wb}, which can also be estimated using on-body measurements [3], will also exhibit a large measurement uncertainty. In the previous chapter, a personal distributed exposimeter (PDE) is introduced. This measurement device allows for measurements of the S_{inc} with a lower measurement uncertainty. However, it has not yet been used to estimate the SAR_{wb}. Potential health effects of RF exposure are usually investigated in relation to the SAR values [4, 5] and not the incident

power densities that only serve as a proxy of the SAR. Therefore, it is useful to also estimate the SAR_{wb} from PDE measurements.

The first goal of the reported research in this chapter is to calibrate a PDE and use this PDE for measurements in a real outdoor environment. To this aim, RF measurement electronics are developed (by the Electromagnetics (EM) group of Ghent University and the Department of Electrical Engineering (ESAT) of the Catholic University of Leuven (KUL)) that can be paired with the antennas described in Section 6.2.1 of the previous chapter, in order to construct wearable RF nodes. These RF nodes are developed both for the Global System for Mobile communications around 900 MHz downlink band (GSM 900 DL) and the Wireless Fidelity band around 2.5 GHz (Wifi 2G) and are used for measurements in Ghent, Belgium.

Simultaneously, numerical simulations are executed to determine the SAR_{wb} of the subject wearing the PDE in the GSM 900 DL band, in a realistic environment. The calibration results and the numerical simulations can be combined to measure both the S_{inc} and the SAR_{wb} with a relatively low measurement uncertainty, using the PDE as both an exposimeter and a SAR_{wb}-meter.

A second goal of the reported research is to determine the total uncertainty on measurements of the S_{inc} when using a PDE. The uncertainty caused by the presence of the human body, investigated in the previous chapters is only one component of the extended measurement uncertainty of the device. To this aim, we have investigated several contributors to the expanded measurement uncertainty in the GSM 900 DL band. The determined measurement uncertainty can then be used in combination with the measurement results.

7.2 Materials and Methods

First, the method used to determine the expanded measurement uncertainty of the PDE is outlined, together with a description of the different contributors to the measurement uncertainty. Second, the measurements in the WiFi 2G band are described. Third, the measurement procedure in the GSM 900 DL band is introduced.

7.2.1 Extended Measurement Uncertainty during Personal Exposure Assessment

7.2.1.1 Theory

Any measurement of a certain quantity y that is a function of different input variables x_i ($y = f(x_1, x_2, .., x_N)$) will have an uncertainty. Each of the input variables x_i will have an associated standard uncertainty u_i, which is defined as the positive square root of the variance u_i^2 of y when x_i is varied. In case of a statis-

tically estimated variance, the standard uncertainty ($u_i = s_i$) equals the standard deviation on y [6].

Two types of uncertainties exist [6]: a first type are uncertainties that can be determined statistically from a certain distribution of output data. A second type of uncertainties relies on scientific judgment of the observer and uses assumptions on the underlying distribution of the observed phenomena.

The combined standard uncertainty u_c on y, which is a function of uncorrelated input variables x_i, can be obtained by using a summation of all the individual standard uncertainties u_i [6]:

$$u_c^2 = \sum_{i=1}^{N} u_i^2 + 2 \sum_{i=1}^{N-1} \sum_{j=i+1}^{N} u_{i,j} \tag{7.1}$$

with u_i the uncertainty caused by input variable x_i and $u_{i,j}$ the additional uncertainty caused by the joint influence of x_i and x_j on y. In practical situations, the resulting distribution of y and its standard uncertainty u_c will be approximately normal [6] or log-normal, depending on whether the different contributions are considered to be additive or multiplicative. This means that in 68% of repeated measurements, the result should lie in the interval $[y - u_c, y + u_c]$. This analysis holds for symmetric distributions. In case of asymetric distributions, the upper uncertainties $u_{up,i}$ and lower uncertainties $u_{low,i}$ have to be combined separately:

$$u_{low,c}^2 = \sum_{i=1}^{N} u_{low,i}^2 + 2 \sum_{i=1}^{N-1} \sum_{j=i+1}^{N} u_{low,i,j} \tag{7.2}$$

$$u_{up,c}^2 = \sum_{i=1}^{N} u_{up,i}^2 + 2 \sum_{i=1}^{N-1} \sum_{j=i+1}^{N} u_{up,i,j} \tag{7.3}$$

with $u_{low,c}$ and $u_{up,c}$ the lower and upper combined uncertainty, respectively, $u_{low,i}$ and $u_{up,i}$ the lower and upper uncertainty, respectively, caused by input variable x_i, and $u_{low,i,j}$ and $u_{up,i,j}$ the additional lower and upper uncertainty, respectively, caused by both variables x_i and x_j. Equations 7.2 and 7.3 reduce to Equation 7.1 if $u_{low,i} = u_{up,i} = u_i$ and $u_{low,i,j} = u_{up,i,j} = u_{i,j}$.

In this section, we assume all the contributions to the uncertainty to be multiplicative. This implies that in order to apply Equation 7.1 to calculate the combined uncertainty, the individual standard uncertainties u_i or $u_{low,i}$ and $u_{up,i}$ have to be expressed in logarithmic quantities (decibels or dB).

The expanded measurement uncertainty will estimate a larger confidence interval than the 68% confidence interval, by applying a scaling factor. The distribution of y and its standard uncertainy u_c is then assumed to be (log-)normal. The expanded uncertainty $U = k \times u_c$ corresponding to a 95% confidence interval is obtained by using a coverage factor $k = 2$.

7.2.1.2 Application Set-up

	Single Antenna	Personal, Distributed Exposimeter
position^{polarization}	G^H	(B^H,D^V,G^H,I^V)
averaging	none	geometric
$p_{50}(AA_{geom})$ (cm^2)	5.1 ± 0.12	6.06 ± 0.05

Table 7.1: Positions (see Fig. 7.5), polarizations (H = Horizontal and V = Vertical), and median antenna apertures in the 'Urban Macro-cell' scenario of the PDE used for measurements in the GSM 900 DL band, and the best antenna from this set of used antennas.

In the previous chapters, the measurement uncertainty caused by the presence of the human body on the incident power densities has been studied. Although this uncertainty might be relatively large, especially for single antennas on the body, it is not the only contributor to the total measurement uncertainty when assessing the incident power density. In this section, an extended measurement uncertainty [6–8] will be described for a PDE consisting of 4 antennas that measure in the GSM 900 DL band in an 'Urban Macro-cell' scenario and the best single antenna measuring in the same frequency band, found in Section 6.6.1. The contributions to the combined uncertainty that are considered in this chapter will be the same for other PDEs. However, the values obtained for the uncertainties, presented in Section 7.3.1 of this chapter, are only valid for the measurement set-up studied in this chapter.

Table 7.1 lists the positions and polarizations of the set of antennas studied in this section, together with the used averaging scheme and the median antenna aperture (AA) in the 'Urban Macro-cell' scenario, determined in Section 6.6.1. The same quantities are also listed for the antenna in this set with the lowest PI_{50} on the incident power density, in this case G^H. This set is chosen for the calculation of the expanded measurement uncertainty, because it is also used in measurements in Ghent, Belgium, described in Section 7.2.3.3.

The different contributions to the expanded uncertainty on the measurements in the GSM 900 DL band, using the system described in Section 6.6.1, are listed in the next paragraphs.

7.2.1.3 Contributions to the Expanded Measurement Uncertainty

Figure 7.1 shows an overview of the different contributions to the expanded measurement uncertainty that are considered in this chapter and where in the measurement device, the calibration method, or the measurement process they might arise. The following paragraphs contain a description of the studied effects, how these

effects might cause an uncertainty of the incident power density measured by the PDE, and how this uncertainty has been estimated.

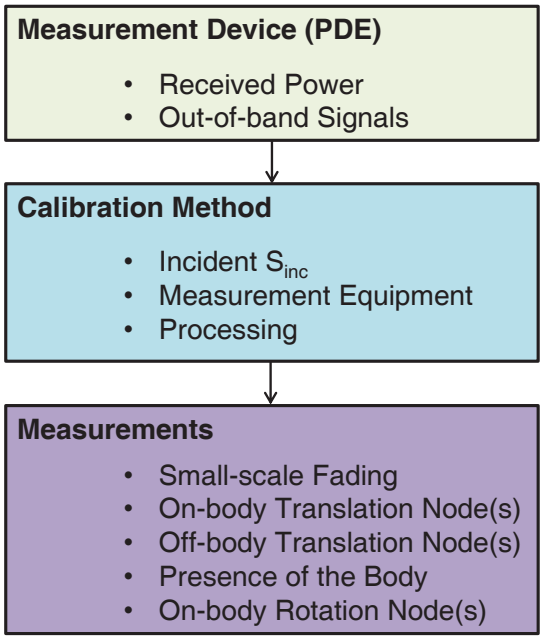

Figure 7.1: Overview of the different contributions to the expanded measurement uncertainty. The rectangles indicate where in the measurement device, the calibration method, or the measurement process the studied contributions (bullets) might arise.

Uncertainty on the measurements of received power The used power detector is a log-linear detector: ADL5513 (ANALOG DEVICES, Norwood, MA, USA). This means that received powers on the detector give a response in output voltage that is linearly dependent on the logarithm of the received power. However, at lower received power, the output might deviate from a linear response, due to (electrical) noise at these lower powers. This can be measured using a calibration of the receiver node that can be connected to a signal generator. This allows to measure the registered power (P_{reg}) as a function of the input power (P_{in}). Ideally, this calibration curve should be the first bisector, but P_{reg} contains an offset for low powers from P_{in} due to the presence of electrical noise ($P_{reg} = P_{in} + P_{noise}$). In practice, this curve will be compensated for in the post-processing of the measurements. However, only the average value of the noise can be compensated and

some additional variation on the signal exists, which causes an uncertainty on the measured signal.

In order to quantify this, we have varied the input power from 10 dBm to -80 dBm in steps of 5 dBm and measured 20 samples of the received power for every step of the input power. This leads to a set of $N = 19 \times 20 = 380$ received powers, from which a (log-normal) standard deviation is calculated:

$$\sigma(dB) = \sqrt{\frac{1}{N}\sum_{i=1}^{N}(P_{reg}(P_{in}) - P_{in})^2} \tag{7.4}$$

for registered powers (P_{reg}) that are compensated for the mean electrical noise (i.e., $< P_{reg}(P_{in}) > = P_{in}$) and the input power ($P_{in}$) both in (dBm). Note that σ is a factor ($1/N_{nodes}$) smaller if the received power is averaged over N_{nodes} nodes, assuming that σ is the same for all nodes and the deviations on the different nodes are uncorrelated.

Uncertainty caused by out-of-band Signals The filter (part 856528, Triquint Semiconductor, Singapore) is a band-pass filter tuned to the GSM 900 DL band. However, this filter is not perfect and can pass some out-of-band signals that will then be recorded in the measurements. The same holds for the antennas. Both the filter and the antenna have a certain power transmission coefficient ($|S_{21}|^2$). The cascade of both the antenna and the filter will consequently have a power transmission coefficient $|S_{21}|^2$ as well. The frequency dependence of this $|S_{21}|^2$ can be obtained using calibration measurements with a controlled source. As we will show in Section 7.3.1.1, the cascade of the antenna and the surface acoustic wave (SAW) filter provides more than 30 dB of out-of-band attenuation at frequencies that are located more than 100 MHz from the GSM 900 DL band. Therefore, only signals emitted close to the band could cause out-of-band received powers. According to Table 5.1, only the GSM 900 UL band is close enough to cause out-of band received powers. In order to assess this uncertainty, we have measured the received powers on the RF node between 840 MHz and 1.04 GHz for a vertically polarized node at 4.24 m from the TX antenna. These received powers are then used to determine the $AA(\phi = 0°, \theta = 90°, \psi, f)$ for f either in the GSM 900 UL or DL band. The received power on the antenna is then equal to:

$$P_r = AA_{UL} \times S_{inc,UL} + AA_{DL} \times S_{inc,DL} \tag{7.5}$$

with $S_{inc,UL/DL}$ the incident power density in the GSM 900 UL/DL band and $AA_{UL/DL}$ the antenna aperture averaged over the frequencies in the GSM 900 UL/DL band. The received power that we want to obtain in the GSM 900 DL band is:

$$P_{r,DL} = AA_{DL} \times S_{inc,DL} \tag{7.6}$$

In order to determine the uncertainty on $P_{r,DL}$, 1000 samples are drawn from the $S_{inc,j}$ (j= DL or UL) distributions measured in Chapter 4 using a pair of PEMs (for a subject that is not using a hand-held device). As the AA_DL has a polarization dependence, simultaneously, 1000 samples for the polarization are drawn from a Gaussian distribution in the 'Urban Macro-cell', see Table 3.3, to determine the antenna aperture in the GSM 900 DL band. In the GSM 900 UL band, the polarization is considered to be uniformly distributed in the interval $[0, 2\pi[$, since no a priori assumption can be made on the polarization of the devices emitting this radiation.

For each of these sets of incident power densities, the relative difference (δ in dB) between $P_{r,DL}$ and P_r is determined:

$$\delta = 10 \times log_{10}(\frac{P_{r,DL}}{P_r})(dB) \tag{7.7}$$

The mean value of δ should be subtracted from P_r values during the measurements, while the standard deviation of δ is the standard uncertainty. In this approach it is assumed that the out-of-band AA is the same for every ϕ and is the same when the antenna is worn on and off the body. This analysis holds for subjects that do not use a personal device that emits in the GSM UL band close to the body.

Uncertainty on the Measurement of the Incident Power Density during the Calibration According to the relevant CENELEC standard [8] there are three contributors to the uncertainty on the incident power density: the uncertainty caused by the measurement device, the uncertainty caused by physical parameters (in particular small-scale fading), and the uncertainty caused by the averaging method [8]. The first contribution has to be obtained from the data sheet of the used measurement device (NARDA NBM 550, Narda, Hauppage, NY, USA). The second contribution is studied using measurements described further in this section. The quantification of the uncertainty caused by the averaging method is discussed here.

The incident power density used to determine the antenna apertures in Equation 6.3 is a value averaged over the length of the subject. There is an uncertainty on this averaged value. In this study, this uncertainty is quantified by the standard deviation (in dB) on the measured power density samples along the subject's rotational axis.

Uncertainty due to the Measurement Equipment used to measure S_{inc} during the Calibration The used isotropic field probe, the Narda NBM 550 in combination with an EF 0391 probe, has an uncertainty on its measured values as well, which we obtain from the data sheet [9].

Uncertainty on the Processing of Calibration data During the processing of the measured antenna apertures, a set of 1000 polarization samples is generated in order to determine the distribution of the AA. From this distribution the median value is extracted to use in Equations 6.14 and 6.15 for the determination of the incident power densities from the measured powers on the RF nodes. This processing is repeated a 100 times. From these repetitions the log-normal standard deviation can be determined.

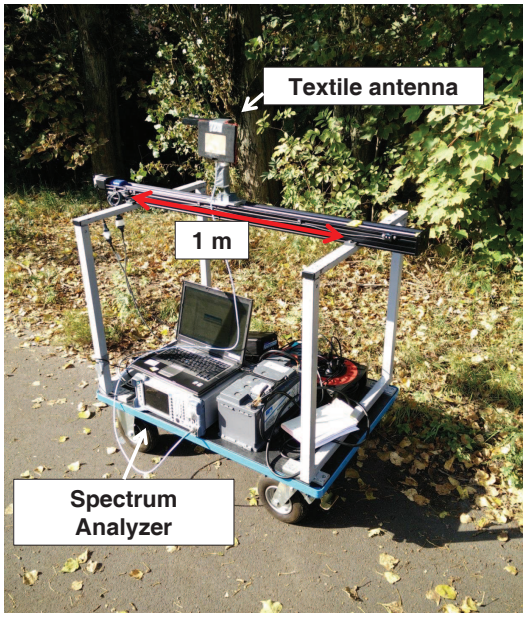

Figure 7.2: Measurement set-up used to measure small-scale fading in the GSM 900 DL band.

Uncertainty due to Small-Scale Fading There are different sources that can lead to a variation of the received power of the down-link signal from a GSM base station within the sampling period. First, the received power on the antennas will vary due to movement of the subject. Disregarding the shadowing of the subject's own body, which is treated as a separate uncertainty, there will be a variation on the received power on an antenna due to shadowing [10]. This variation which is significant over a scale of several wavelengths (= 0.32 m at 942.5 MHz) is what is measured using the PDE. However, there also exist variations of the received power over much smaller distances ($<$ 10 wavelengths) due to fast fading or small-scale fading [10]. As the subject moves through an environment, the properties of the paths incident on the subject may change and therefore also the resulting

received power, see Eq. 5.13. These variations are not captured by the RF nodes and should be treated as an uncertainty. Second, even if the subject would remain on a constant position the received power would not be constant on that position, but would vary with time. There are two different factors contributing to this variation: the variation in the traffic on the frequency band, i.e., the variation of data sent to the varying number of users, and the variations in the environment of the subject, due to for example moving scatterers or absorbers. This variation can happen within the measurement period of the RF nodes (1 s) and thus causes an additional uncertainty in our measurements. In order to estimate the magnitude of this small-scale fading (spatial as well as temporal), we have connected one of the textile antennas to a spectrum analyzer (SA) (R& S FSL, Rhode & Schwarz, Munich, Germany) tuned to the GSM 900 DL band. The textile antenna is moved on three locations within a square area of 3x3 m^2 (in the same environment as the trajectory we measured using the PDE) over 1 m in steps of 0.02 m at a height of 1.2 m. The SA measures at a center frequency of 942.5 MHz with a span of 35 MHz (501 points) and a resolution bandwidth of 300 kHz. This results in a sweep time of 2.5 ms. At every position 50 measurements are taken: this results in 50 $\times$ 150 samples of the received power summed over the GSM 900 DL band, which have a certain variation caused by the aforementioned mechanisms. This measurement is than repeated in two other squares of 3×3 m^2. Figure 7.2 shows a picture of the used set-up to measure the received powers on the antenna.

Uncertainty due to translation of the nodes on the body surface In order to determine the possible effect of a translation of the nodes during the measurements, the received power during the calibration measurements are measured by the node centered on position D, see Figure 6.9 and by the same node placed on each of the 4 corners of position D. These received powers are then used to determine worst-case upper (a^+) and lower (a^-) deviations on the median antenna aperture of the antenna placed on D. If a rectangular distribution of the deviation is assumed, the standard uncertainty is defined as $u = (a^+ - a^-)/(2\sqrt{3})$ [6]. In this approach we assume that the translation of the node only changes the amplitude of the antenna aperture and not the distribution. This uncertainty belongs to the second type (based on scientific judgment [6]) for which we have assumed a rectangular distribution between two extreme cases. The rectangular distribution assumes that all cases between the two extreme cases are equally probable.

Uncertainty due to translation of the nodes away from the body The nodes might be translated perpendicularly to the body during measurements. This will influence the power reflection coefficient, the radiation efficiency, and the directive gain, see Eq 5.13 and thus also the antenna aperture. This uncertainty is studied using numerical simulations of a textile antenna placed H polarized on position A

on the body and translated perpendicularly to the body from the position shown in Figure 6.9, to a position 20 mm in the positive X direction, with steps of 5 mm. The median AA is then determined for every step and used to determine worst-case upper (b^+) and lower (b^-) deviations on the median antenna aperture of the translated antenna. If a rectangular distribution of the deviation is assumed, the standard uncertainty is defined as $u = (b^+ - b^-)/(2\sqrt{3})$ [6]. In this approach, we assume that the translation of the node only changes the amplitude of the AA and not the distribution. This uncertainty belongs to the second type (based on scientific judgment [6]) for which we have assumed a rectangular distribution between two extreme cases.

Uncertainty due to the presence of the human body This uncertainty is studied in Section 6.6.1, using the PI_{50}. In order to translate this to standard uncertainties, the PI_{68} is studied here, where $u_{low} = 10 \times log_{10}(\frac{p_{50}(AA)}{p_{84}(AA)})$ and $u_{up} = 10 \times log_{10}(\frac{p_{50}(AA)}{p_{16}(AA)})$, with $p_x(AA)$ the 16%, 50%, and 84% percentiles of the antenna aperture's distribution for the best single antenna (G^H) and the PDE used in the measurements (B^H,D^V,G^H,I^V).

Uncertainty due to rotation of the nodes The linearly polarized nodes might rotate during the measurements. This will influence their received power. This effect is commonly described as polarization loss and reduces the antenna aperture of a perfectly linearly polarized antenna by a factor of $cos^2(\gamma)$, with γ the rotation angle [11]. However, each of the antennas used in this study have both a H- and V-polarized antenna aperture and a rotation of an antenna thus has an a priori unknown effect on the received power.

Moreover, the rotation of an antenna will not only introduce a certain additional variation on the antenna aperture, but might change the distribution of the (averaged) antenna aperture. In other words, the uncertainty due to the rotation of a node and the uncertainty due to the presence of the human body are correlated. According to [6], the standard uncertainty can be calculated using Equation 7.1. From this equation the terms involving the uncertainty caused by the presence of the human body and the rotation of the nodes can be grouped into a term u_{br}^2:

$$u_{br}^2 = u_{body}^2 + u_{rot}^2 + 2 \times u_{body,rot} \tag{7.8}$$

with u_{br} all the uncertainty caused by both the presence of the body and the rotation of the nodes, u_{body} the uncertainty caused by the presence of the human body, u_{rot} the uncertainty caused by the rotation of the antennas, and $u_{body,rot}$ the uncertainty caused by both variables. In this chapter, the uncertainty of the body u_{body} is determined separately, while the uncertainty caused by the rotation u_{rot} cannot be determined separately from u_{body}. u_{br} can only be determined using an alternative processing of the calibration data.

When only considering the presence of the body as an uncertainty, the incident power density lies 68% of the times within the (absolute) interval:

$$[\frac{P_r}{p_{84}(AA)}, \frac{P_r}{p_{16}(AA)}] \tag{7.9}$$

Logarithmically, this interval can be written as:

$$[u_{low,body}, u_{up,body}] = [10 \times log_{10}(\frac{p_{50}(AA)}{p_{84}(AA)}), 10 \times log_{10}(\frac{p_{50}(AA)}{p_{16}(AA)})] \tag{7.10}$$

If an additional rotation of the antennas occurs, then the distribution of the (adapted) antenna aperture (AA') will change, and likewise the 68% confidence interval will change to:

$$[\frac{P_r}{p_{84}(AA')}, \frac{P_r}{p_{16}(AA')}] \tag{7.11}$$

Note that during the measurements, the incident power density is determined using the median antenna aperture obtained using the calibration procedure and not the (unknown) median AA'; therefore, the relative 68% confidence interval has to be expressed using:

$$[u_{low,br}, u_{up,br}] = [10 \times log_{10}(\frac{p_{50}(AA)}{p_{84}(AA')}), 10 \times log_{10}(\frac{p_{50}(AA)}{p_{16}(AA')})] \tag{7.12}$$

In this approach, we assumed the uncertainty caused by the rotation to be independent of the uncertainty caused by translation of the nodes, see the following paragraphs.

In order to approximate the effect of a rotation of the antenna, we have assumed that the effect is the same as a constant rotation of the polarization by γ in Equation 6.11. This assumption holds if the influence of the body shape on the antenna's directive gain is smaller than the effect of the polarization loss. In order to quantify the variation due to rotation, a distribution of 1000 (ψ, γ) couples is used to determine the antenna aperture of each antenna using Eq. 6.11. The γ-samples are chosen uniformly in the interval $[-20°, 20°]$. The γ-samples are different for each antenna, while the ψ samples are the same in each exposure situation. A larger deviation than 20° is considered as unrealistic. $u_{br,low}$ and $u_{br,up}$ are determined in the same way as described in Section 6.6.1 for the single antenna and the PDE, listed in Table 7.1. $u'_{low/up}$ are determined using the uncertainties caused by the presence of the human body, determined in the previous paragraph.

7.2.2 Methodology for Estimating the SAR_{wb} from PDE Measurements

Simulated Whole-Body Averaged SAR in Realistic Environments The SAR_{wb} of the VFM can be determined in different realistic environment, using the stochastic multi-path exposure (SME) method described in [2]. This method relies on the linearity of Maxwells equations to determine the electric and magnetic fields on a closed surface around the VFM by combining the fields obtained for single plane waves incident from different directions [2].

First, Finite-difference time-domain (FDTD) simulations of single plane-wave exposures are executed at 950 MHz using the Virtual Family Male (VFM) [12]. The VFM is a heterogeneous phantom of an adult male with a BMI equal to 22.3 kg/m^2 (± 0.5 kg/m^2 difference compared to the BMI of the subject used for the measurements). From the results of each of these FDTD simulations the electric and magnetic fields on a closed surface around the VFM can be extracted. These are called the basic field distributions (BFDs). The electric and magnetic fields can be used to calculate the Poynting vector in each point on the closed surface around the VFM at which the fields are extracted. This Poynting vector can be integrated over the closed surface in order to determine the absorbed power within the surface. In this case this is the absorbed power in the VFM, which can be divided by the mass of the VFM to obtain the SAR_{wb}.

The BFDs only provide the electric and magnetic fields under single plane wave exposure. In a realistic environment a subject will be under multi-path exposure, which is a collection of plane-waves if only far-field exposure is considered. Due to the linearity of Maxwells equations the electric and magnetic fields on the closed surface around the VFM under multi-path exposure, can be obtained by adding the BFDs resulting from the plane-wave exposure that constitute the multi-path exposure. A real environment is also constantly changing. In order to correctly model the exposure in a certain environment, a large number of exposure samples has to be considered ($\geq$ 1000 exposure samples [2, 13]).

In this Chapter, the SAR_{wb} is calculated in 5000 multi-path exposure samples in the 'Urban Macro-cell' environment. The characteristics of this environment are described in Table 3.3 in Chapter 3. This environment is chosen because it corresponds best to the measurements, outlined in the next section. From these 5000 SAR_{wb} samples, a distribution $Prob(SAR_{wb} \leq Y | S_{inc} = 1\ W/m^2)$ is determined [2].

Whole-Body Averaged Specific Absorption Rate Estimation using a Personal, Distributed Exposimeter From the calibration measurements, a distribution of the antenna aperture $Prob(AA_{geom,PDE} \leq Z)$, with a Z surface between 0 and $\infty\ m^2$, is obtained, while from the numerical simulations and the method used in [2], a distribution of the SAR_{wb} for a constant incident power density is determined. These two distributions can be combined to calculate the distribution of the SAR_{wb} for a constant received power on the antennas, once the distribution of

$AA_{geom,PDE}$ is inverted, using the definition of the antenna aperture:

$$S_{inc} = \frac{P_{geom,PDE}}{AA_{geom,PDE}} \tag{7.13}$$

For a constant $P_{geom,PDE} = 1\ W$, a distribution $Prob(S_{inc} \leq X | P_{geom,PDE} = 1\ W)$ can be obtained using Equation 7.13. An expression for $Prob(SAR_{wb} \leq Y | P_{geom,PDE} = 1\ W)$ can be found using the law of total probability:

$$\begin{aligned} Prob(SAR_{wb} \leq Y | P_{geom,PDE} = 1\ W) = \\ \int_0^\infty Prob(SAR_{wb} \leq Y | S_{inc} = X) \\ \times \frac{dProb}{dX}(S_{inc} \leq X | P_{geom,PDE} = 1\ W) dX \end{aligned} \tag{7.14}$$

The $p_{50}(SAR_{wb} | P_{geom,PDE} = 1\ W)$ and $PI_{50}(SAR_{wb} | P_{geom,PDE} = 1\ W)$ are determined for this distribution.

7.2.3 Measurements using a PDE in a Real Environment

Measurements are executed using two PDEs. First, the methodology of the measurements of WiFi 2G using a PDE based on a design of diametrically opposite locations is presented. Second, measurements in the GSM 900 DL band, using a PDE based on a design using calibration measurements are presented.

7.2.3.1 Human subject

The subject that wears the PDE during the measurements is a 26 year old male with body mass 82 kg and a height of 1.91 m and thus a body mass index (BMI) of 22.5 kg/m^2. The two different PDEs are first calibrated on the body of the subject, using the methods outlined in the previous chapter, and are then used for outdoor measurements.

7.2.3.2 Measurements of WiFi 2G

Measurements are executed using a PDE tuned to the WiFi 2G band. The calibration of the PDE is presented and discussed in Section 6.5 of the previous chapter.

The subject is equipped with a PDE, consisting of two dual-polarized antennas, described in section 6.2.1.7, worn on the positions shown in Figure 6.7. He follows a predefined walk in Ghent, Belgium, shown in Fig. 7.3. The walk is performed on a weekday during business hours in the afternoon (12h-16h) and is approximately 1.9 km long. The buildings along the route are mainly residential buildings of 3 to 4 stories high, some of the ground floors are used for commercial purposes. The PDE records received powers with a sample rate of 2 Hz. The same path

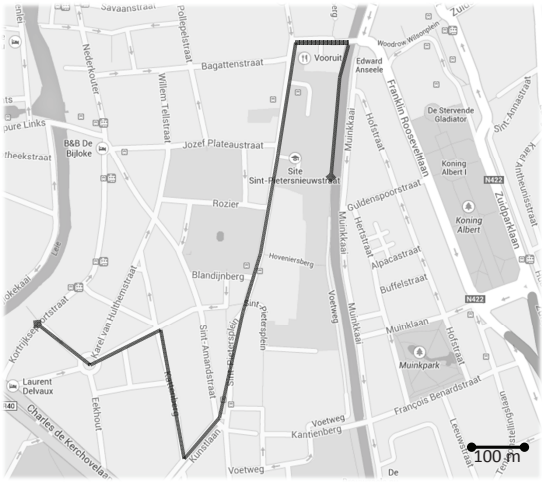

Figure 7.3: Trajectory followed by the subject wearing the PDE in Ghent, Belgium (from Google maps, CA USA). The black line indicates the trajectory.

is followed twice during the same afternoon, in order to increase the number of measured samples.

The RF nodes, described in Section 6.5.1 of Chapter 6, connected to the antennas record the received power on the antennas. These nodes have a detection limit (-90.5 ± 0.5 dBm) in terms of received power and thus power density, which implies that if a received power, equal to this detection limit is registered, the actual received power might be lower than or equal to this value. This left-censored data might lead to an overestimation of summary statistics of RF power densities [14, 15]. A commonly used technique to process left-censored data is Robust Regression on Order Statistics (ROS) in which a log-normal distribution is fitted to the (probability) of the data above the detection limit. Censored data are then replaced by data lower or equal to the detection limit from the same log-normal distribution [15–17]. This technique can only be applied if a sufficient amount ($> 20\%$) of data is recorded above the detection limit [14, 15]. When necessary, the same technique is used to process the data measured in this study. For the dual-polarized WiFi antennas, ROS has to be applied to the separate data registered for each polarization of the antennas. If ROS has to be applied, it has to be applied before any averaging over the nodes is executed.

During the walk, 2 EME SPY 140 (Satimo, Brest, France) PEMs are worn on both hips of the subject. These PEMs measure with a sample rate of 0.25 Hz. The values measured by the PEMs can be used for comparison with the values measured with the PDE. The data measured using the PEMs is first processed using

ROS and then averaged over both hips using eqn 6.12 with w_i=1/2. The data is also corrected for the presence of the human body using the techniques described in [18] and applied in Chapter 4 for a combination of 2 PEMs and realistic polarizations.

7.2.3.3 Measurements in the GSM 900 DL band

Similarly, on-body RF nodes tuned to the GSM 900 DL band are placed on the positions listed in Table 7.1 on the same subject.

Calibration Measurements in the Anechoic Chamber The PDE consists of four RF acquisition nodes tuned to the GSM 900 DL band, described in Section 6.6.1. Every node is a combination of a textile antenna and receiver electronics tuned to the GSM 900 DL band, as shown in Figure 6.9. The RF receiver electronics record the power $P_{r,i}$ received by textile antenna i ($i = 1..4$). They provide the geometrically averaged received power for every sample interval of 1 s. This result is stored with a resolution of 1 dB and a sensitivity of -72 dBm. The integrated receiver electronics are positioned on the antenna feed plane.

The PDE is calibrated on the body of a subject in an anechoic chamber. The subject is a 26-year-old male with a BMI of 22.5 kg/m^2. A calibration procedure is proposed to determine the effective on-body AA of a set of RF nodes placed on the subject's body and to select the positions of those nodes in order to minimize the measurement uncertainty. The RF nodes are placed on the torso of the subject in order not to impede the subject's movements. The RF nodes are placed on 4 locations on the front and back sections of the subject's torso, see Table 7.1. The linearly polarized RF nodes are placed either horizontally (H), parallel to the subject's transverse plane, or vertically (V), orthogonal to the subject's transverse plane.

The distribution $Prob(AA_{geom,PDE} \leq Z)$, with a Z surface between 0 and ∞ m^2, of the PDE's antenna aperture is determined in the 'Urban Macro-cell' scenario, using the procedure described in Section 6.6.1 of Chapter 6. This distribution is characterized by its median value $p_{50}(AA_{geom,PDE})$ and the 50% prediction interval $PI_{50}(AA_{geom,PDE})$.

Measurements in Ghent, Belgium After the calibration in the anechoic chamber, see Section 6.6.1 of Chapter 6, the textile antennas and receivers remain on the subject, who follows a predefined walk in Ghent, Belgium, shown in Figure 7.4. The walk is 3 km long and takes 2250 s to complete; leading to the same amount of measured average received powers. These powers are converted to incident power densities using Equations 6.14 and 6.15 and the effective AA determined during the calibration, described in Section 6.6.1 and listed in Table 7.1. Summary

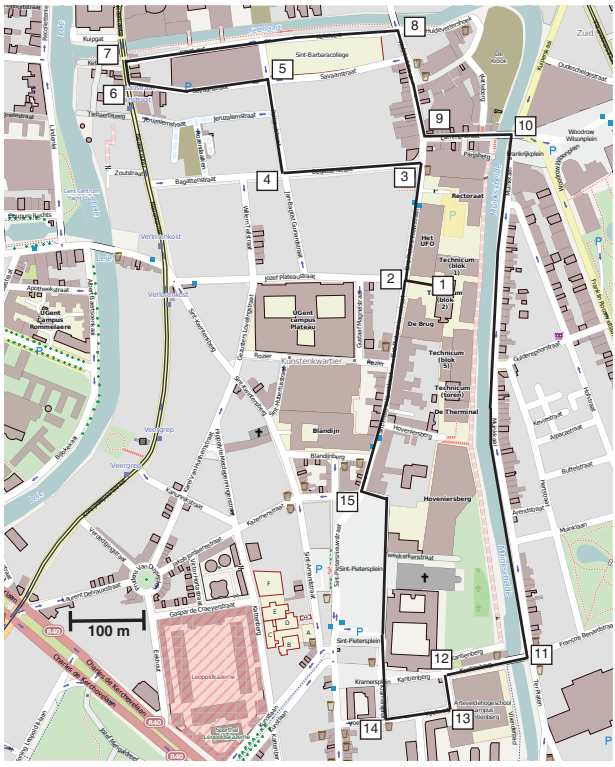

Figure 7.4: Second trajectory followed in Ghent, Belgium, during measurements (source: http://www.openstreetmap.org, 2014). Fifteen locations are indicated with white rectangles.

statistics are provided for these power densities and compared to the ICNIRP reference levels [1]. Robust Regression Order Statistics (ROS) [15] is not applied to this data, since no censoring occurs because of the low detection limits of the PDE. The SAR_{wb} values can be determined from the measured powers, using the method described in the previous paragraph.

Figure 7.5 (a) shows a frontal and rear view of the subject wearing the four RF nodes. The nodes are placed on the positions and according to the polarizations listed in Table 7.1. It is clear that this setup will not be usable for measurements in a real environment, since the antennas are visible for the public and might attract unwanted attention, thus altering the exposure of the subject. Therefore, a coat is used to cover the antennas during the measurements, see Figure 7.5 (b).

(a) Setup with Antennas (b) Covered Antennas

Figure 7.5: Setup of the antennas on the body (a) front and rear view of the subject wearing the antennas and (b) subject during measurements.

The values for the measurement uncertainties presented in Table 7.5 and the performance characteristics presented in Table 7.1 are determined for a calibration measurement, while the subject is wearing the same coat and can thus be used for these antennas. The influence of the coat on the antenna aperture of the antennas is small. The median antenna apertures of the single antennas show deviations between 9×10^{-4} and 2.4 dB, while the PI_{50} on these antenna apertures might deviate between 0.2 and 1.7 dB. For the PDE, we measure a deviation of 0.22 dB in terms of the median antenna aperture and 0.4 dB in terms of PI_{50}. In a previous study, the same antennas were worn underneath a solar panel [19], which resulted in an influence of the solar cells on the directive gain smaller than 1 dB and an almost identical free-space power reflection coefficient [19]. However, the influence on the antenna's total efficiency (and thus the antenna aperture) is not mentioned in [19].

7.3 Results

7.3.1 Extended Measurement Uncertainty during Personal Exposure Assessment

7.3.1.1 Standard Measurement Uncertainties

The standard measurement uncertainties of the different contributors to the combined measurement uncertainty, listed in Section 7.2.1 are presented in this section.

Uncertainty on the measurements of received power The log-normal standard deviation measured on the received power on the RF node is 0.19 dB, averaged over the full dynamic range of the RF node. It should be noted that no deviations higher than the accuracy of the device are measured between +5 dBm and -45 dBm input power. For a combination of 4 nodes, this uncertainty is a factor 4 lower when compared to a single exposimeter with one antenna: 0.048 dB.

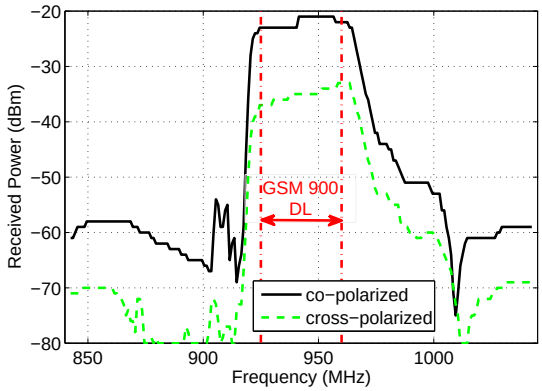

Figure 7.6: Co- and cross-polarized received power on a V-polarized RF node for an input power of 10 mW on the TX. Courtesy of Peter Van Veerdeghem.

Uncertainty caused by out-of-band Signals Figure 7.6 shows the co- and cross-polarized frequency dependence of the received power on a vertically polarized RF node placed at 4.34 m from the TX fed by a CW source generating 10 mW in the anechoic chamber. The differences between the received power in the GSM 900 DL and the GSM 900 UL band is at least 21 dB. Since there are some (small) differences in propagation losses and reflection coefficient of the TX between the GSM 900 DL and UL bands, the AA's are calculated with different incident power densities. In this setup, the H-polarized incident power densities are 160 and 180 $\mu W/m^2$ in the GSM UL and DL band, respectively, while the V-polarized incident power densities are 140 and 170 $\mu W/m^2$ in the GSM UL and DL band, respectively. The resulting H and V polarized antenna apertures are 18 cm^2 and 370 cm^2 in the GSM 900 DL band, and 1.1×10^{-3} cm^2 and 5.6×10^{-2} cm^2 in the GSM 900 UL band. Given these antenna apertures, the incident power density in the GSM 900 UL band has to be of the order of $O(10^4)\times$ higher than that received in the GSM 900 DL band, in order to cause comparable received powers on the RF node. Since the subject is not allowed to wear a mobile device in this study, this contribution to the uncertainty is very low. Therefore, this uncertainty is considered to be negligible.

The 1000 S_{inc} samples are drawn from a log-normal distribution with mean value 6.9×10^{-8} W/m^2 and a standard deviation of 9.6 dB in the GSM 900 UL band and a log-normal distribution with mean value 5.2×10^{-5} W/m^2 and a standard deviation of 6.6 dB in the GSM 900 DL band. This analysis resulted in a distribution of δ with a mean value of $-2.1 \times 10^{-5} \pm 1.4 \times 10^{-5}$ dB and a standard deviation of $2.6 \times 10^{-4} \pm 4.3 \times 10^{-4}$ dB. Both values are negligible. No compensation for out-of-band signals is needed and no significant uncertainty is estimated. Note that if the subject is allowed to wear a mobile device, the out-of-band received powers will be higher.

In [20], the whole-body dose is compared for a mobile device that emits in the GSM 900 UL band near the head of a numerical phantom at typical output power and far-field exposure in the GM 900 DL band. The whole-body averaged dose can be up to a factor 5 dB higher in the GSM 900 UL band, compared to the GSM 900 DL band. The organ-specific dose for organs or tissues located in the head can be more than 10 dB higher. This indicates that for antennas located near the position where the device is used, the received power in the GSM 900 DL band caused by radiation emitted in the GSM 900 UL band might become more relevant.

The model we used for the up-link from other users assumes a mean value, which is about 30 dB lower in the GSM 900 UL band than that measured in the GSM 900 DL band. Consequently, the received out-of-band power is very low as well. In [16] some environments were found where the GSM UL signals are more than 10 dB higher than those registered in the GSM 900 DL band. The largest difference was measured in a 'train' scenario, where the mean GSM 900 UL value was 0.23 mW/m^2 and the mean GSM 900 DL value is 0.01 mW/m^2. This difference would still be insufficient to compensate for the out-of-band attenuation of more than 10^4 obtained by the combination of the antenna and the SAW filter. However, [16] mentions contrasts up to a factor of 6.5×10^5 (up to 1.2×10^4 during outdoor activities) when personal up-link values are in- or excluded in the total exposure. These differences might be able to lead to out-of-band powers that are of the same order of magnitude as the in-band registered powers.

Uncertainty on the incident power density The standard uncertainty of $N = 2 \times 7 \times 11 = 154$ measured samples of the incident power density for 2 incident polarizations, 7 different heights along the rotational axis, and 11 samples for every step in height and polarization, is $u_{up/low}$= 0.73 dB. This uncertainty is equal for the single node and the PDE, because the same measurement of S_{inc} is used in both cases.

The value found here (0.73 dB) is lower than the values estimated in [8], where values are used between 1.4 and 1.75 dB. However, the values used in [8] are for measurements in a real environment, whereas the standard deviation reported in this paragraph is based on measurements in an anechoic chamber and is thus

expected to be lower.

Uncertainty due to the Measurement Equipment used during the Calibration All the listed uncertainty values in the data sheet of the used isotropic field probe (the Narda NBM 550 in combination with a EF 0391 probe [9]) are assumed to be worst cases of a rectangular distribution (a^- and a^+). Therefore, a correction factor of $2\sqrt{3}$ is applied to reduce these values to the standard uncertainty for a rectangular distribution: $u = (a^+ - a^-)/2\sqrt{3}$. Table 7.2 lists the different contributors to the uncertainty and the used values:

Contributor	a^- (dB)	a^+ (dB)	u_i (dB)
linearity	-0.5	+0.5	0.29
Frequency Sensitivity	-1.4	+1.4	0.81
Isotropic Response	-1	+1	0.58
Thermal Response	-1	+0.2	0.35
combined standard uncertainty (dB)			1.1

Table 7.2: Standard uncertainty on the registered power densities using a Narda NBM 550 in combination with a EF 0391 probe.

The combined standard uncertainty on the measurements using the isotropic field probe is 1.1 dB. In [8], an expanded uncertainty (k = 2) of 1.2 dB is found for a setup using a spectrum analyzer and an isotropic antenna, which corresponds to a standard uncertainty of 0.6 dB. A higher value was expected for the broadband probe. These values are the same for the single antenna and the PDE, since the same device was used in both calibrations.

In [21] the measurement uncertainty of a portable and stationary isotropic field probe is calculated. 4 different contributions to the combined standard measurement uncertainty of the portable probe are studied in [21]: the isotropy of the probe, linearity of the probe, flatness of the probe's response, and a calibration uncertainty, with values of 1.8 dB, 1.5 dB, 2.6 dB, and 2 dB, respectively. This results in a combined standard uncertainty of 4 dB (and an extended measurement uncertainty of 8 dB). These values are much higher than those found for the Narda NBM 550, but the individual components listed for the probe used in our measurements, see Table 7.2 are much smaller than those used for the (older) probe in [21].

Uncertainty due to the processing method The processing of the calibration measurements is repeated a 100 times in order to evaluate the variation caused by the used processing method. The standard uncertainties on the antenna aperture of the best single antenna are $u_{up/low} = \pm 0.10$ dB. For the geometric average

of the four antennas listed in Table 7.1, the standard uncertainties are $u_{up/low} = \pm 0.04$ dB.

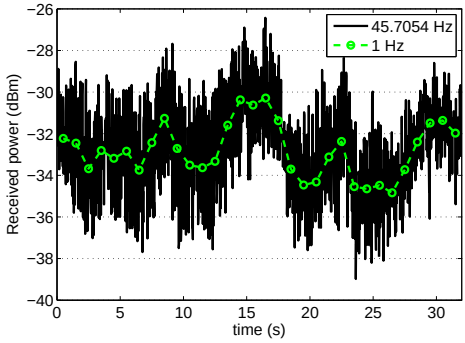

Figure 7.7: Received power in the GSM 900 DL band as a function of time for a stationary node. The black curve indicates measurements with the spectrum analyzer at 46 Hz, while the grey markers indicate the same measurements averaged over a 1 s period (what would be measured by the nodes).

Uncertainty due to Small Scale Fading Figure 7.7 shows the total received power in the GSM 900 DL band for a stationary antenna using the measurement setup described in Section 7.2.1.3, measured with a sample rate of 46 Hz (fastest sample rate obtainable using the spectrum analyzer) and using a geometric averaging over 1 s (the same averaging scheme and sample interval used in the measurements). This figure illustrates the effect of temporal fading. The variation on the received powers measured with a sample interval of 1 s, is much smaller than the variation when measured with a larger sample frequency. For example, between the 13^{th} and 14^{th} second, a geometric average received power of -32 dBm is measured (value calculated by taking the time-average of the spectrum analyzer measurements), while in the same interval (1 s) values between -36 and -28 dBm are measured by the spectrum analyzer. This additional variation is not measured by the RF nodes and is therefore treated as an uncertainty. The measurements shown in Figure 7.7 are for a stationary node and thus only temporal fading is measured. In reality the subject will also move during the measurements, which causes an additional variation due to the changing propagation paths of the incident electromagnetic fields. Therefore, 150 received powers are measured in each of the 50 steps of a translation of the antenna over 1 m ($\approx 3.\lambda$ at 942.5 MHz), according to the method described in paragraph 7.2.1.3. The relative standard deviation is calculated for each of these 50 steps. This procedure is repeated for 3 different orientations of the measurement system in the same 3×3 m^2 area and

for 3 positions in the same environment in Ghent, Belgium.

σ (dB)	Orientation		
	1	2	3
Position 1	1.9	1.5	1.6
Position 2	1.6	1.6	1.3
Position 3	1.7	1.7	1.8

Table 7.3: Average (log-normal) standard deviation for small-scale fading (of a single antenna) in the GSM 900 DL band in Ghent, Belgium.

Table 7.3 lists the averaged measured standard deviations for 3 orientations on 3 positions in Ghent, Belgium in the GSM 900 DL band. The maximal average standard deviation is 1.9 dB (the maximal measured value on any of the considered positions of the antenna is 3.8 dB, while the minimal value is 0.8 dB). For a geometric averaging over 4 antennas, the standard deviation caused by small-scale fading is a factor of 4 lower, since the fading is uncorrelated for the 4 antennas, this corresponds to a worst-case average standard deviation of 0.48 dB.

The standard uncertainties listed in Table 7.3, between 1.3 and 1.9 dB corresponds to the values used in [8]. In this standard, an expanded uncertainty (k = 2) between 0.9 and 4.5 dB is used, corresponding to a standard uncertainty between 0.45 and 2.25 dB. However, the standard recommends to use values around 1 dB [8].

Note that the combined standard uncertainty caused by small-scale fading and averaging used in [8] (1 dB (fading) and 1.75 dB (averaging)) is 2.0 dB, while using our values (1.9 dB and 0.73 dB) we also obtain a value of 2.0 dB. The additional variation due to fading that is taken into account in this chapter, is compensated by a smaller variation on the averaging method in the anechoic chamber.

Uncertainty due to translation of the nodes on the body In order to quantify the uncertainty caused by the translation of an RF node on the body, an RF node is placed H-polarized centered on position D on the body and in each of the four corners of position D. A larger translation is assumed to be unrealistic. The median antenna aperture in an 'Urban Macro-cell' scenario is then determined for each of the 5 configurations using the previously described calibration procedure. The difference between the maximal and minimal median AA ($b^+ - b^-$) is 3.6 dB, which corresponds to a standard measurement uncertainty of 1.0 dB, if a rectangular distribution of the median AA is assumed. In case of the PDE, the translation of the nodes on the body can be considered uncorrelated and therefore, the uncertainty is a factor 4 lower: 0.25 dB. In this approach, the uncertainty of a translation on the body is assumed to be uncorrelated with the other uncertainties and is assumed to have no effect on the uncertainty caused by the presence of the body.

Uncertainty due to translation of the nodes away from the body Equation 7.15 shows how the antenna aperture is related to the antenna's performance characteristics.

$$AA(\phi,\theta) = \eta_{rad}(1-|S_{11}|^2)D(\phi,\theta)\frac{\lambda^2}{4\pi} \tag{7.15}$$

with AA the antenna aperture, η_{rad} the radiation efficiency, $|S_{11}|^2$ the *power* reflection coefficient, $\eta_{mis} = (1-|S_{11}|^2)$ the mismatch efficiency, D the directive gain, λ the wavelength, and (ϕ,θ) spherical coordinates. In this paragraph we describe the uncertainties on: the radiation and mismatch efficiencies and the maximal directive gain for a H-polarized antenna on position A on the body which is translated orthogonally to the body towards a position 20 mm further in the positive X direction, with steps of 5 mm. The minimal and maximal deviations are then used to determine a standard uncertainty, assuming a rectangular distribution.

Contributor	a^- (dB)	a^+ (dB)	u_i (dB)
η_{rad}	-0.52	0.46	0.28
η_{mis}	-0.012	0.016	0.0080
Directive Gain	-0.23	0.35	0.17
Combined Uncertainty (dB)			0.33

Table 7.4: Standard uncertainty due to a potential translation of an RF node 2 cm away from the body.

The standard uncertainty due to the orthogonal translation of one of the RF nodes is 0.33 dB. For a combination of 4 nodes the uncertainty is a factor 4 lower, if the movement of the nodes are considered to be uncorrelated: 0.083 dB. This approach to calculate the uncertainty, assumes that the effect of the orthogonal translation is uncorrelated with the other sources of uncertainty. It also assumes that the translation of the node has the same effect on the full distribution of antenna apertures as it has on the maximum antenna aperture, obtained using the maximum directive gain. Future research has to be carried out in order to quantify the mutual influence of both translations, the rotation on the body, the absence of the polar angle during the measurements, and the presence of the body.

Uncertainty due to the presence of the body This uncertainty is studied in Section 6.6.1. In order to quantify the standard uncertainty, the PI_{68} is used here instead of the PI_{50}. The PI_{68} is 9.5 dB with an u_{low} = -6.0 dB and an u_{up} = 3.5 dB for the best single antenna (G^H) and a PI_{68} = 5.0 dB for the PDE used in the measurements (B^H,D^V,G^H,I^V), with an u_{low} = -2.6 dB and an u_{up} = 2.4 dB. The median values of the antenna apertures used to calculate these standard uncertainties are listed in Table 7.1.

Uncertainty due to rotation of the nodes In order to quantify this uncertainty, first the distribution of the antenna aperture is determined without any rotation of the nodes (approximated by a rotation of the polarization of the incident plane waves). From this distribution the median value $p_{50}(AA)$ and the 16% and 84% percentiles are determined. These are used to calculate $u_{low/up,body}$, see the previous paragraph and Table 7.5.

A second processing of the calibration data is then used, to determine the distribution of the antenna aperture (AA') when also a potential rotation $\gamma \in [-20°, 20°]$ is considered. The 16%, 50%, and 84% percentiles are extracted from this distribution and used in Equation 7.12 to calculate $u_{low/up,br}$. This results in an $[u_{low,br}, u_{up,br}]$ = [−6.6 dB,+3.2 dB] for the single antenna and [−2.9 dB,+2.2 dB] for the PDE. The PI_{68} values are 9.8 dB for the single antenna and 5.1 dB for the PDE. These are (slightly) larger than those determined using only the presence of the body: 9.5 and 5.0 dB. The inclusion of a potential rotation thus increases the uncertainty, as expected.

7.3.1.2 Expanded Measurement Uncertainty

Cause of uncertainty	$u_{low,i}$ (dB)		$u_{up,i}$ (dB)	
	SA[a]	PDE[b]	SA[a]	PDE[b]
Received Power	-0.19	-0.048	+0.19	+0.048
Out-of-band Signals	≈ 0	≈ 0	≈ 0	≈ 0
Incident S_{inc}	-0.73	-0.73	+0.73	+0.73
Measurement Equipment	-1.1	-1.1	+1.1	+1.1
Processing	-0.10	-0.040	+0.10	+0.040
Small-scale Fading	-1.9	-0.48	+1.9	+0.48
On-Body Translation	-1	-0.25	+1	+0.25
Off-Body Translation	-0.33	-0.083	+0.33	+0.083
Body, Rotation	-6.6	-2.9	+3.2	+2.2
Presence of the body	-6.0	-2.6	+3.5	+2.4
Combined Standard uncertainty (dB)	**-7.1**	**-3.2**	**+4.1**	**+2.6**
Expanded uncertainty (k=2) (dB)	**-14**	**-6.4**	**+8.2**	**+5.2**

[a] SA: single antenna
[b] PDE: Personal Distributed Exposimeter, with the configuration listed in Table 7.1.

Table 7.5: Expanded uncertainty assessment of the PDE and the best single antenna in the GSM 900 DL band.

Table 7.5 lists all the studied contributions to the measurement uncertainty considered in this chapter and the combined standard uncertainty calculated using Equation 7.1. The expanded measurement uncertainty is obtained by multiplying the combined standard uncertainty with a coverage factor of 2 and is listed in Table 7.5 as well. The expanded measurement uncertainty corresponds to a 95% confidence interval and is twice as large as the standard (combined) uncertainty.

The total combined standard uncertainties for the single antenna amount to a 68% confidence interval of 11.2 dB (-7.1 dB to 4.1 dB), while for the expanded uncertainties the 95% confidence interval is 22.2 dB (-14 dB to 8.2 dB). The uncertainty caused by the presence of the body is clearly the dominant factor for the single antenna. The other factors only amount to a value of 2.6 dB, which only increases the lower uncertainty by 0.5 dB and the upper uncertainty by 0.9 dB, due to the quadratic summation. The total combined standard uncertainty for the PDE is indeed much smaller and amounts to a 68% confidence interval of 5.8 dB (-3.2 dB to 2.6 dB), while the expanded uncertainty is 11.6 dB (-6.4 dB to 5.2 dB). These values are 5.4 dB and 10.6 dB lower than those obtained for the best single antenna. A large reduction can thus also be obtained in terms of the expanded uncertainty, due to the dominance of the uncertainty caused by the presence of the body in the combined uncertainty.

7.3.2 Measurement Results in the WiFi 2G band

Node	Averaging	Censored data (%)	u_{low} (%)	u_{up} (%)	$\mu(S_{inc})$ ($\mu W/m^2$)	$p_{25}(S_{inc})$ ($\mu W/m^2$)	$p_{50}(S_{inc})$ ($\mu W/m^2$)	$p_{75}(S_{inc})$ ($\mu W/m^2$)
1		0.8 and 0.0	94	190	0.094	0.033	0.065	0.18
2		0.0 and 0.0	94	1200	0.057	0.034	0.040	0.061
(1,2)	geom		32	43	0.059	0.027	0.042	0.079
2 x PEM	arith	19 and 22	33	77	0.52	0.16	0.52	1.7

*$\mu(S_{inc})$, $p_{25}(S_{inc})$, $p_{50}(S_{inc})$, and $p_{75}(S_{inc})$ are the mean, 25%, 50%, and 75% percentiles of the incident power densities measured during the walk.

Table 7.6: Summary statistics of the measured power density in the WiFi 2G band after ROS and percentage of censored power densities measured in Ghent along the trajectory shown in Fig. 7.3, together with the upper and lower limit of the interval of the uncertainty on the measured values in which 50% of the estimates are located.

Table 7.6 lists the summary statistics of the measurements during a walk in Ghent, described in Figure 7.3. Due to the low detection limit of the RF nodes, the number of censored samples is relatively low (up to 0.8% in Table 7.6), compared to those of commercial exposimeters, which may be higher than 80% [15]. Table 7.6 lists (for WiFi 2G) the mean value and the quartiles measured by the individual nodes, and the combination of two antennas with the smallest interquartile distance, found in the calibration (geometric averaging, Fig. 6.8), using the weights listed in Table 6.2.

Table 7.6 shows that the amount of censored data recorded by the PDE is negligible (0% for the 2nd node and $< 1\%$ for the first node), which means that on every instance during the measurements an exposure value was measured. The

PEMs show relatively high percentages of censored data (19% and 20%). Using the PDE a mean value of 0.059 $\mu W/m^2$ was measured during the walk, with 75% of samples below 0.079 $\mu W/m^2$, whereas the values recorded by the pair of PEMs are higher with a mean value of 0.52 $\mu W/m^2$ and 75% of all value lower than 1.7 $\mu W/m^2$.

7.3.3 Measurement Results in the GSM 900 DL band

In this section, first the results of the calibration and numerical simulations are presented and discussed. Second, the results of our measurements performed in Ghent, using the PDE, are outlined.

Calibration and Numerical Simulations A geometric averaging of the received power over four RF nodes placed horizontally on position B, vertically on D, horizontally on G, and vertically on I (see Figure 6.9), respectively, is found to produce the lowest 50% prediction interval (PI_{50}) on the S_{inc}. The isolation between the two antennas is larger than 27 dB averaged over the GSM 900 DL band. Table 7.1 lists the median AA of the PDE after the calibration procedure. Using this median AA of 6.1 cm^2 listed in Table 7.1, a detection limit of 0.104 $\mu W/m^2$ can be obtained from the sensitivity of -72 dBm. Commercial PEMs have a detection limit of 0.07 $\mu W/m^2$, which is a factor of 1.5 lower than our detection limit. However, single PEMs tend to underestimate the incident power density by a factor larger than 1.5, see Chapter 3 and [13].

The PI_{50} on the S_{inc} equals 3.1 dB. This value is a measure for the uncertainty caused by the human body and is low compared to the minimal and median values of 7.1 and 12 dB, respectively, which are found for the single antennas, polarized either along H or V directions on positions $A - L$.

Figure 7.8 shows the distribution $Prob(SAR_{wb} \leq Y | P_{geom,PDE} = 1\ W)$, obtained using Equation 7.14 for this configuration of RF nodes placed on the body. The SAR_{wb} will be lower than 8.7 W/kg in 50% of the cases, if a geometrically averaged power of 1 W is received on the antennas, see Fig. 7.8. Note that a received power of 1 W on the antennas is relatively high, given the antenna aperture of 6 cm^2 (see Table 6.3). The PI_{50} on the SAR_{wb} distribution of 3.3 dB is also relatively low compared to the minimal and median values of 5 and 10 dB, respectively, found for the single antennas placed on positions $A - L$. However, it should be noted that there is an additional uncertainty (50% prediction interval of 1.64 dB) on the numerically obtained SAR_{wb} values [22].

Measurements in Ghent, Belgium Figure 7.9 shows the S_{inc} (left vertical axis) and SAR_{wb} (right vertical axis) values that are obtained by geometrical averaging

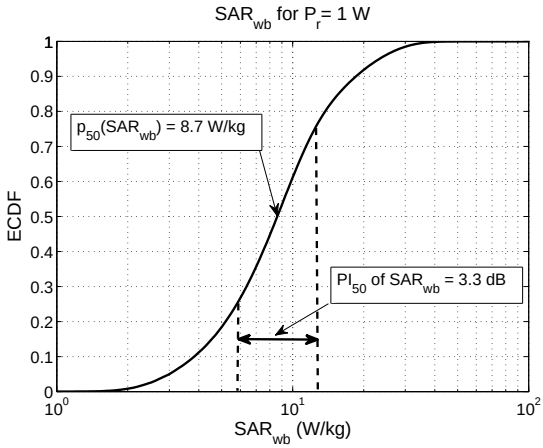

Figure 7.8: Experimental cumulative distribution function (ECDF) of the SAR_{wb} in the 'Urban Macro-cell' scenario, for a constant received power of 1 W on the antenna.

of the received powers over the 4 textile antennas with a sample rate of 1 Hz (black curve) and the same power densities averaged over 6 minutes (red curve), in order to enable a comparison with the ICNIRP 1998 guidelines [1]. The lower horizontal axis shows the measured time, while the upper horizontal axis shows the same checkpoints as shown in Figure 7.4. All measured data are above the detection limit. Note that even with the conventional PEMs, a relatively small amount of non-detects was measured in the same environment in the same frequency band, see Table 4.3 in Chapter 4.

Table 7.7 lists the summary statistics of the S_{inc} and SAR_{wb} measurements shown in Figure 7.9. A median S_{inc} of 47 $\mu W/m^2$ and a median SAR_{wb} = 0.25 $\mu W/kg$ are measured along the full trajectory using the PDE. The maximally registered values are $S_{inc} = 4.9\ mW/m^2$ and SAR_{wb} = 26 $\mu W/kg$, while the smallest registered values are $S_{inc} = 2.6\ \mu W/m^2$ and SAR_{wb}= 0.014 $\mu W/kg$. All the measured values, and thus also the values averaged over 6 minutes, are lower than the ICNIRP reference levels and basic restrictions, which are $4.6 \times 10^6 \mu W/m^2$ and 0.08 W/kg for the general public at the lowest frequency in the GSM 900 DL band (925 MHz).

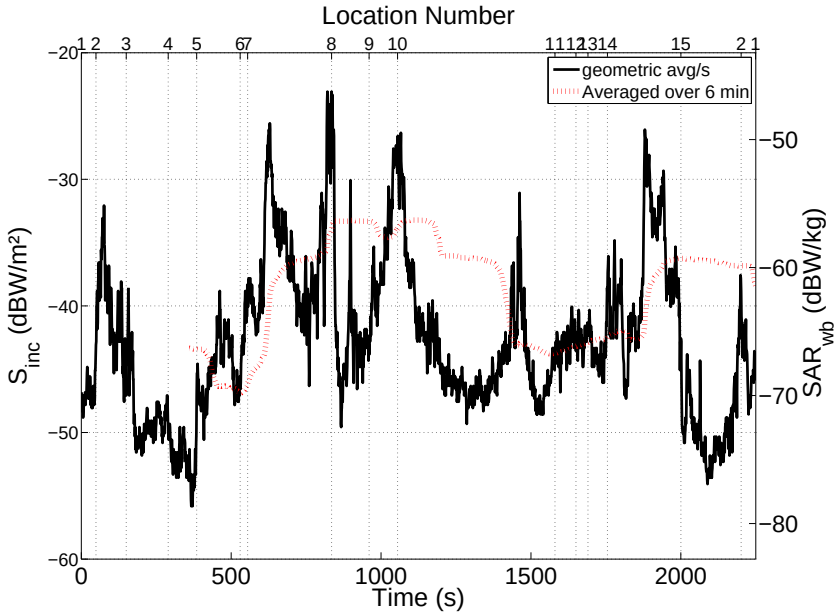

Figure 7.9: Measured power density and whole-body averaged SAR in the GSM 900 DL band along the trajectory shown in Fig. 7.4. The lower horizontal axis shows the measured time and the upper axis shows the corresponding checkpoints shown in Fig. 7.4. The black curve shows the measured results with a sample rate of 1 Hz, while the red curve shows the results averaged over 6 min according to [1].

7.4 Discussion

7.4.1 Extended Measurement Uncertainty

Table 7.5 lists the extended measurement uncertainties for both the best single antenna and the PDE. The values for the PDE are smaller than those found for the single antenna, due to a reduced influence of the presence of the body. The used broadband field meter (NARDA NBM 550) has a combined standard uncertainty of $\sqrt{0.73^2 + 1.1^2 + 1.9^2} = 2.3$ dB, which corresponds to an expanded uncertainty of ± 4.6 dB. The expanded uncertainty of the single antenna is much larger than this value, but the upper expanded uncertainty of the PDE is closer to that of the Narda probe, mainly because the upper uncertainty caused by the presence of the body is comparable to the uncertainty caused by small-scale fading in case of a PDE. The fact that the PDE uses multiple measurements of the same incident power density allows for a reduction in uncertainty that cannot be obtained with single off- or on-body antennas.

		p_{25}	p_{50}	p_{75}	p_{90}	p_{95}	$u_{low,body}$ (dB)	$u_{up,body}$ (dB)	$u_{low,exp}$ (dB)	$u_{up,exp}$ (dB)
SAR_{wb} ($\mu W/kg$)	PDE (1 Hz)	0.11	0.25	0.62	2.2	4.4	-2.7	+2.5	-	-
S_{inc} ($\mu W/m^2$)	PDE (1 Hz)	21	47	120	410	830	-2.6	+2.4	-6.4	5.2
	2 x PEM (0.25 Hz)	19	68	180	340	-	-1.7	+4.6	-	-

Table 7.7: Summary Statistics of the measured S_{inc} (in $\mu W/m^2$) and SAR_{wb} (in $\mu W/kg$) using a PDE during the walk shown in Fig. 7.4 for a 1 Hz sampling frequency. The summary statistics are compared with those obtained from measurements using a combination of two PEMs in the same environment, see Chapter 4, Table 4.3. $u_{low,body}$ and $u_{up,body}$ are the lower and upper limits, respectively, of the 68% prediction interval on the S_{inc} caused by the presence of the subject's body. $u_{low,exp}$ and $u_{up,exp}$ are the lower and upper expanded measurement uncertainties, respectively.

Note that the broadband probe has to be wielded by a person as well, so there will be a (smaller) influence of the body that is now not accounted for in the probe's specifications. Moreover, the probe is not frequency selective and cannot distinguish between the GSM 900 DL band and other bands. Note that the probe used in our calibrations has a relatively low measurement uncertainty in comparison to the probe used in [21], which has an expanded measurement uncertainty of ± 8 dB. The PDE already outperforms this (free-space) device in terms of expanded measurement uncertainty.

According to [8] a narrow-band, isotropic measurement of the exposure to a GSM signal is faced with an expanded uncertainty caused by the measurement equipment between 0.8 and 1.2 dB, an uncertainty caused by 'physical parameters' (predominantly small-scale fading) of 1 dB, and an uncertainty caused by 'Post-processing' between 2.8-3.5 dB. If these uncertainties are combined, one can obtain an expanded uncertainty between 3.1 dB and 3.8 dB. These values are smaller than the expanded uncertainties obtained for the PDE, but in order to translate measured values using a free-space measurement to actual personal exposure values, an additional uncertainty should be taken into account.

7.4.2 Measurements in the WiFi 2G band

Measurements of the WiFi signals are executed along an outdoor trajectory in the city center of Ghent (Belgium, Fig. 7.3). These measurements are performed by a subject who is simultaneously equipped with the PDE described in this manuscript and a combination of 2 (commercial) PEMs (Satimo, Brest, France) worn on both hips of the subject.

Table 7.6 lists the power densities measured using the PDE and those measured

by the pair of PEMs described in Chapter 4. All values measured are lower than the reference levels issued by the international commission on non-ionizing radiation protection (ICNIRP) [1]. An average power density of 59 nW/m^2 is registered for WiFi signals with a 50% prediction interval defined by u_{low} = 32%, and u_{up} = 43%. This power density value is relatively low, compared to values measured indoors [23]: 38 $\mu W/m^2$ on average measured in an office environment. WiFi is predominantly emitted indoors and thus much weaker when measured outdoors due to penetration (and propagation) losses. Moreover, the measurements perfomed indoors in [23] are performed for Wifi signals with a relatively high duty cycle of 86% in order to obtain worst-case results. The power density values measured in the WiFi band are lower than those measured by the combination of 2 PEMs. This difference is attributed to the averaging scheme used by the EME SPY 140, where the maximum value is registered only every 4 seconds. If the maximum of the data found in this study is calculated every 8 samples (4 s), then the values measured by the PDE become comparable to those measured by the commercial exposimeters: for example, the mean values are 0.35, 0.14, and 0.52 $\mu W/m^2$ for node 1, node 2, and the combination of the 2 nodes after calculating the maximum over 4 s. This is in excellent agreement with the measurements done with the PEMs, given the uncertainties listed in Table 7.6.

The lower measurement uncertainty of the PDE and the pair of PEMs are similar, -32% for the PDE and -33% for the couple of PEMs. The upper uncertainty on the PEM measurements is higher, given our calibration measurements, 77% compared to 43% for the PDE. Logarithmically this corresponds to PI_{50} values of 3.2 dB and 4.2 dB for the PDE and the pair of PEMs, respectively.

7.4.3 Measurements in the GSM 900 DL band

The PI_{50} on the measured S_{inc} when using the PDE is 3.1 dB. Previous studies using PEMs found values for the PI_{50} on the measured S_{inc} of 8.0 dB [24], using numerical simulations. For a PEM worn on the hips, 6.5 and 16 dB, for H- and V-polarized incident fields, respectively, are recorded [18]. A calibration of a couple of simultaneously worn PEMs on both hips of a subject, described in Chapter 4, showed a PI_{50} of 8.2 and 9.5 dB for the individual PEMs on the two hips and 4.8 dB for the combination of the two PEMs in a realistic environment. For a previous prototype of the PDE using three RF nodes, we obtained a PI_{50} of 4.5 dB, see Chapter 6. The PI_{50} found in this chapter is lower than all these values. This indicates that the PDE, presented here, can be used for measurements of S_{inc} with less uncertainty.

The measured power densities for GSM 900 DL are comparable to those measured in previous studies in Ghent. In [17] a 95% percentile of 0.34 mW/m^2 was measured in Ghent in the GSM DL band. In this study the 95% percentile of S_{inc} = 0.83 mW/m^2. A higher value was expected since the PDE does not

underestimate S_{inc} ,which is the case for the PEM used in [17], and has a higher sampling frequency, which commonly increases the percentiles higher than the median if a time averaging during the sampling period is used.

In [3] a p_{95} and p_{99} of 0.34 and 0.86 $\mu W/m^2$ were reported in the same city. In this study, these values are 0.83 and 2.2 mW/m^2. These values are higher, probably due to the sampling rate that is 10 times higher in this study than in [3], which usually increases percentiles higher than the median if an averaging within the sampling period is used.

In [16] a mean value of 0.022 mW/m^2 is measured in the GSM 900 DL band in the Netherlands using an on-body worn conventional PEM. The corresponding mean value during outdoor walking was 0.023 mW/m^2 in the GSM 900 DL band. The values are corrected for the presence of the human body, but are lower than the (log-normal) mean of 0.053 mW/m^2 measured in this study.

Using a combination of 2 PEMs, a median value of 68 $\mu W/m^2$ was measured in the same area in Ghent in the GSM DL band, which is in agreement with the measurements in this study, given the uncertainties (caused by the presence of the body) on the measured percentiles. When averaged over 4 seconds the p_{25}, p_{50}, p_{75}, and p_{90} of the measured S_{inc} using the PDE are 21, 46, 120, and 410 $\mu W/m^2$. For these percentiles, the averaging over a larger sampling interval has little influence, since only the median value changed slightly. The p_{95} value averaged over 4 s, 800 $\mu W/m^2$, is lower than the one found for the data measured with a sampling frequency of 1 Hz. The corresponding values using the average over two PEMs are within the uncertainty on the measured values.

In [25] different contributors to the variance of the mean value of measured incident electric field values are investigated. The mean values of the incident electric fields are found to be highly reproducible in the same areas on different days and times of the day if measurements of approximately 30 minutes are used. The measurements presented in this chapter and Chapter 4 fulfill that requirement and the median values (which should be the same as the mean values if the data are (log-)normally distributed) are indeed in agreement. However, the other percentiles show larger differences. These could be expected since the walks performed during both measurements are not executed at the same moment, nor are the measurements executed along the same trajectory. In order to characterize a particular urban environment and to obtain reproducible summary statistics, multiple, repeated measurements have to be carried out along several trajectories on fixed dates and times of the week [26]. The measurements presented in this chapter and Chapter 4 might not be relevant to determine a typical exposure in Ghent, but can be used to express statistics for the actual exposure of the subject that performed the measurements. In future studies, a more extensive and orchestrated measurement campaign can be executed with the PDE in order to obtain characteristic exposure values in a certain environment, that are not biased by the

shielding of the body or an uncertainty on the position of the antennas.

7.5 Conclusions

The measurement uncertainty caused by the presence of the human body on measurements of the incident power density, which is determined in the previous chapter, is used to determine the expanded measurement uncertainty for a PDE and the best single antenna in that PDE. The resulting expanded lower measurement uncertainty is -14 dB for the single antenna, while the expanded upper measurement uncertainty is +8.2 dB. The PDE has a smaller expanded measurement uncertainty with a lower value of -6.4 dB and a higher value of +5.2 dB. The reduction is mainly obtained by reducing the dominant uncertainty caused by the presence of the body.

The on-body antenna aperture of the weighted average of the different radio frequency nodes that form a PDE for the registration of the personal exposure in the WiFi 2G band, is determined using an on-body calibration in the previous chapter. These calibration results are used to process received powers on those RF nodes registered during a walk in Ghent, Belgium. An average incident power density of 59 nW/m^2 is registered for RF fields originating from WiFi outdoors in an urban environment, recorded with a sample frequency of 2 Hz. All measured power densities are lower than the reference levels issued by ICNIRP.

Similarly, we have presented a calibration method of a PDE, which measures the incident power density (S_{inc}) and, for the first time, real-life whole-body averaged specific absorption rate (SAR_{wb}) in the GSM 900 DL band using four RF power detection nodes integrated on four textile antennas. This device can thus be used both as a personal exposimeter and a SAR_{wb}-meter. The PDE has a relatively low measurement uncertainty caused by the human body: 50% prediction intervals (PI_{50}) of 3.1 dB on the S_{inc} and 3.3 dB on the SAR_{wb} were measured for the PDE, whereas the best single textile antenna in our measurements exhibits a PI_{50} of 7.1 dB on S_{inc} and 5 dB on SAR_{wb}. The measurement uncertainty is also low compared to existing solutions in literature. The PDE is used for real measurements in Ghent, Belgium, where a median S_{inc} of 47 $\mu W/m^2$ and $SAR_{wb} = 0.25\mu W/kg$ were measured. All measured S_{inc} and SAR_{wb} values are in compliance with the reference levels issued by ICNIRP even when the expanded measurement uncertainty on the results is taken into account.

Other factors that (potentially) contribute to the measurement uncertainty such as the uncertainty due to the morphology of different subjects, the uncertainty caused by the absence of different polar angles during the calibration measurements, and an uncertainty caused by the posture of the subjects, are to be studied in future research. A future version of the PDE should be unobtrusively integrated into a garment, since this could reduce some uncertainties such as the uncertainty

caused by translations of the nodes.

References

[1] ICNIRP International Commission on Non-Ionizing Radiation Protection. *Guidelines for limiting exposure to time-varying electric, magnetic, and electromagnetic fields (up to 300 GHz).* Health physics, 74:494–522, 1998.

[2] G Vermeeren, W Joseph, and L Martens. *Whole-body SAR in spheroidal adult and child phantoms in realistic exposure environment*. Health Physics, 94(June):345–354, 2008.

[3] W Joseph, G Vermeeren, L Verloock, M Masache Heredia, and L Martens. *Characterization of personal RF electromagnetic field exposure and actual absorption for the general public.* Health physics, 95(3):317–30, September 2008.

[4] E Brillaud, A Piotrowski, and R de Seze. *Effect of an acute 900 MHz GSM exposure on glia in the rat brain: A time-dependent study*. Toxicology, 238(1):23–33, August 2007.

[5] Q Balzano, CK Chou, R Cicchetti, A Faraone, and RYS Tay. *An efficient RF exposure system with precise whole-body average SAR determination for in vivo animal studies at 900 MHz*. IEEE Transactions on Microwave Theory and Techniques, 48(11, 2):2040–2049, NOV 2000.

[6] B N Taylor and C E Kuyatt. *Guidelines for Evaluating and Expressing the Uncertainty of NIST Measurement Results.* NIST Technical note 1297, 1994.

[7] Joint Comittee for Guides in Metrology (JCGM). *Evaluation of measurement data - Guide to the Expression of uncertainty in Measurement.* 2008.

[8] CENELEC (European Committee for Electrotechnical Standardization). *Basic standard for the in-situ measurement of electromagnetic field strength related to human exposure in the vicinity of base stations.* 20.

[9] Narda Safety Test Solutions. *Electric and Magnetic Field Measurement,NBM Series Probes*. NBM-Probes: DataSheet, 2014.

[10] S R Saunders. *Antennas and Propagation for Wireless Communication Systems.* TJ Wiley and Sons Ltd, 1999.

[11] C A Balanis. *Antenna Theory: Analysis and Design*. 1982.

[12] A Christ, W Kainz, E G Hahn, K Honegger, M Zefferer, E Neufeld, R Rascher, W Janka, W Bautz, J Chen, B Kiefer, P Schmitt, H P Hollenbach, J Shen, M Oberle, D Szczerba, A Kam, J W Guag, and N Kuster. *The Virtual Family–development of surface-based anatomical models of two adults and two children for dosimetric simulations.* Physics in medicine and biology, 55(2):N23–38, January 2010.

[13] S Iskra, R McKenzie, and I Cosic. *Monte Carlo simulations of the electric field close to the body in realistic environments for application in personal radiofrequency dosimetry.* Radiation Protection Dosimetry, 147(4):517–27, 2011.

[14] DR Helsel. *In: Nondetects and Data Analysis.* Scott, M. and Barnett, V.,Eds. JohnWiley & Sons Inc., 2005.

[15] M Röösli, P Frei, E Mohler, C Braun-Fahrländer, A Bürgi, J Fröhlich, G Neubauer, G Theis, and M Egger. *Statistical analysis of personal radiofrequency electromagnetic field measurements with nondetects.* Bioelectromagnetics, 29(6):471–8, September 2008.

[16] J F B Bolte and T Eikelboom. *Personal radiofrequency electromagnetic field measurements in The Netherlands: exposure level and variability for everyday activities, times of day and types of area.* Environment international, 48:133–42, November 2012.

[17] W Joseph, P Frei, M Roösli, G Thuróczy, P Gajsek, T Trcek, J Bolte, G Vermeeren, E Mohler, P Juhász, V Finta, and L Martens. *Comparison of personal radio frequency electromagnetic field exposure in different urban areas across Europe.* Environmental research, 110(7):658–63, October 2010.

[18] J F B Bolte, G van der Zande, and J Kamer. *Calibration and uncertainties in personal exposure measurements of radiofrequency electromagnetic fields.* Bioelectromagnetics, 32(8):652–63, December 2011.

[19] F Declerq, A Georgadis, and H Rogier. *Wearable aperturecoupled shorted solar patch antenna for remote tracking and monitoring applications.* Proceedings of the 5th European Conference on Antennas and Propagation (EUCAP). Rome, Italy., 2011.

[20] O Lauer, P Frei, M-C Gosselin, W Joseph, M Röösli, and J Fröhlich. *Combining Near- and Far-Field Exposure for an Organ-Specific and Whole-Body RF-EMF Proxy for Epidemiological Research: A Reference Case.* Bioelectromagnetics, 34:366–374, 2013.

[21] C Oliveira, D Sebastio, G Carpinteiro, L M Correia, C A Fernandes, A Serralha, and N Marques. *The moniT Project: Electromagnetic Radiation Exposure Assessment in Mobile Communications.* IEEE Antennas and Propagation Magazine, 49(1):44–53, 2007.

[22] J F Bakker, M M Paulides, A Christ, N Kuster, and G C van Rhoon. *Assessment of induced SAR in children exposed to electromagnetic plane waves between 10 MHz and 5.6 GHz.* Physics in medicine and biology, 55(11):3115–3130, 2010.

[23] L Verloock, W Joseph, G Vermeeren, and L Martens. *Procedure for assessment of general public exposure from WLAN in offices and in wireless sensor network testbed.* Health Phys., 98(4):628–638, 2010.

[24] G Neubauer, S Cecil, W Giczi, P Preiner, J Frölich, and Martin Röösli. *The Association Between Exposure Determined by Radiofrequency Personal Exposimeters and Human Exposure: A Simulation Study.* Bioelectromagnetics, 31(7):535–45, 2010.

[25] D Urbinello, A Huss, J Beekhuizen, R Vermeulen, and M Röösli. *Use of portable exposure meters for comparing mobile phone base station radiation in different types of areas in the cities of Basel and Amsterdam.* Science of the Total Environment, 468–469:1028–1033, 2014.

[26] D Urbinello, W Joseph, A Huss, L Verloock, J Beekhuizen, R Vermeulen, L Martens, and M Röösli. *Radio-frequency electromagnetic field (RF-EMF) exposure levels in different European outdoor urban environments in comparison with regulatory limits.* Environment International, 68:49–54, 2014.

8

Measuring the Organ-Specific Averaged Specific Absorption Rate in Realistic Environments

8.1 Introduction

Absorption of radio frequency (RF) electromagnetic radiation in the human body can be described using the specific absorption rate (SAR). The International Commission on Non-Ionizing Radiation Protection (ICNIRP) and the Institute of Electrical and Electronics Engineers (IEEE) have defined basic restrictions (or limits) on different averaged SAR values [1, 2]. These averaged values are the whole-body averaged SAR (SAR_{wb}) and the peak 10 and 1 g averaged SAR (SAR_{10g}, SAR_{1g}), where the maximum value of the SAR averaged over 10 and 1 g cubes is considered. From these basic restrictions, reference levels for incident electromagnetic fields (EMFs) or incident power density (S_{inc}) are extracted [1, 2].

The aforementioned SAR quantities are determined based on the thermal effect of RF radiation and do not provide detailed information about absorption in the body. However, differences in the SAR are expected to occur in different organs due to anatomical and dielectric differences [3, 4]. This should be investigated using an organ-specific quantity. Therefore, the organ-specific averaged SAR (SAR_{osa}) is introduced in this chapter in order to study the localization of absorption of the energy of EMFs in the body and as an important input for epidemiological and clinical research of RF radiation. The effects that are investigated

in these studies can be localized [5, 6]. Effects of RF radiation on the central nervous system are investigated in particular [7–11]. The SAR_{osa} provides a mass averaged SAR value for every organ or tissue in the body and is related to the SAR_{wb} since a mass average of all SAR_{osa} values equals the SAR_{wb}.

The SAR_{osa} in realistic human body phantoms has already been studied in the vicinity of a base station antenna [3], determined for near-field (NF) exposure conditions [4], and more specifically for different brain regions [7, 8, 12], but has not yet been studied in a stochastic manner, nor in realistic environments. This chapter aims at developing a finite-difference time domain (FDTD)-based method for determining the SAR_{osa} under realistic far-field (FF) exposure conditions, and investigates the dependence of the SAR_{osa} on the environment.

In the past, a deterministic approach has been used to estimate the SAR in heterogeneous phantoms, both for NF and FF exposure conditions [13–23]. More specifically, in order to estimate FF exposure, the SAR is calculated for different single plane-wave (SPW) exposure conditions [20, 23] or worst-case plane wave exposure [21]. More recent studies on FF exposure aim at determining the SAR for realistic environments. In a realistic environment however, SPW exposures almost never occur [24, 25]. The power absorbed in a realistically exposed organ can only be assessed using a stochastic approach. To estimate the SAR_{osa} of a certain organ, a statistically relevant number of exposure conditions have to be considered. To do this numerically would take thousands of time-consuming FDTD simulations and hundreds of terabytes of storage space.

Therefore, a fast stochastic method is used to avoid executing a large number of FDTD simulations. This method is based on statistical models of realistic exposure conditions [24, 25] and uses a set of EMFs induced by plane waves coming from some basic directions. These EMFs are combined to estimate the effect of a random plane wave or an exposure condition constituted by multiple plane waves, for which a new FDTD simulation would normally be executed. This approach has already been demonstrated for the SAR_{wb} in spheroidal human body models [24] and for heterogeneous human body models [26, 27].

The first objective of this chapter is to develop a stochastic method to determine the SAR in the organs of heterogeneous human body phantoms in realistic exposure conditions. This SAR_{osa} in realistic environments is compared with the SAR_{osa} induced by SPWs. A complementary investigation of two different contributors to the SAR_{osa}: the conductivity-density ratio, and the distance of an organ's center of gravity to the environment, is carried out.

A second objective of this chapter is to investigate whether the distributions of the SAR_{osa}, determined in realistic environments, can be used to estimate the SAR_{osa} during measurements with a PDE in the GSM 900 DL band. In the previous chapter, a technique to estimate the SAR_{wb} from measurements using a personal, distributed exposimeter (PDE) is introduced, where calibration measure-

ments of a PDE and numerical simulations of the SAR_{wb} are combined. The same technique can also be applied to the SAR_{osa}, if this quantity can be assessed in a realistic environment.

8.2 Materials and Methods

The SAR_{osa} is investigated numerically for realistic FF exposure conditions. The five different exposure scenarios that are introduced in Chapter 3 in Table 3.3 are investigated at 950 MHz. The used method will be demonstrated using some selected organs. Once the method to determine the SAR_{osa} under realistic exposure conditions is established and validated, it is used to estimate the SAR_{osa} during the measurements presented in the previous chapter.

8.2.1 Anatomical Human Body Models

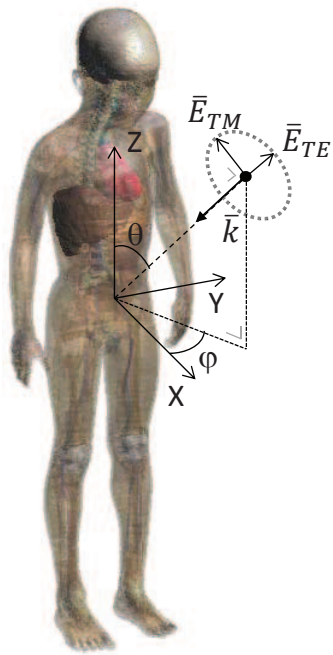

Figure 8.1: The Virtual Family Boy with an illustration of the spherical coordinates (ϕ, θ) and two orthogonally polarized plane waves ($\overline{E}_{TE}$ and $\overline{E}_{TM}$, with propagation vector $\overline{k}$) used to determine the basic fields.

The Virtual Family Boy (VFB) [28] is selected as the human body model (or phantom) to demonstrate the used methodology. This model is shown in Figure 8.1 and has been created using magnetic resonance imaging (MRI) of a 6-year-old male. The boy is 1.10 m tall and has a mass of 16.6 kg. The Gabriel database provides the dielectric properties of the phantom's different tissues [29]. The model consists of 75 predefined tissues, and from these, 38 have been selected to demonstrate the used method: the different tissues of the central nervous system (the brain can be influenced by RF radiation on a physiological level [7, 8, 12]), tissues of the peripheral nervous system, and other vital organs and glands in the body. Parts of the gastrointestinal system are not studied in this chapter, because the absorption in these organs depends on their contents. Simulations at 950 MHz, using various components of the gastrointestinal system (e.g., air, muscle tissue, and surrounding tissue) with frontally incident plane waves have been performed and showed that a variation up to 86% in SAR_{osa} can exist within the organs of the gastrointestinal system. A SAR_{osa} value is not determined for parts of the skeleton, the skin, fat, and connective tissues in this study, since the SAR_{osa} will not be an appropriate quantity to study localized absorption in these larger organs or tissues.

The same method is then applied to the corresponding organs of the Virtual Family Male (VFM) [28], in order to relate SAR_{osa} values to measurements of the RF exposure of an adult subject using a PDE. The VFM is used because of his morphological resemblance to the adult performing the measurements (see Section 7.2.3 in Chapter 7). The differences in body mass index (BMI) between the VFM and the subject are smaller than $0.3\ kg/m^2$. The VFM has a smaller mass (about 10 kg less) and height (11 cm less), so there is no exact correspondence between the used phantom and subject. However, from the available heterogeneous numerical phantoms that are compatible with the used FDTD software, the VFM corresponds best to the real adult [28].

8.2.2 Finite-Difference Time-Domain Simulations

The EMFs inside the phantoms, which are necessary to calculate the SAR_{osa}, are estimated using the FDTD method. A simulation domain is defined around the phantoms and is bounded by perfectly matched layers (PML). This simulation domain is then discretized using a rectilinear grid. As a rule of thumb, the grid step should be smaller than $\lambda/10$, with λ the shortest wavelength in the simulation domain for a stable simulation [30]. A small grid step is preferred because it will lead to a better spatial resolution and thus accuracy, but is accompanied by a small time step due to the Courant limit for stability. A shorter time step will give rise to longer simulations before reaching a steady-state solution and more data processing. The Global System for Mobile Communications (GSM) downlink frequency of 950 MHz has been chosen to demonstrate our method, since

our measurements are also executed in the same frequency band. For 950 MHz, a grid step of 2 mm has been used in the VFB [27] and a grid step of 1.5 mm has been used in the VFM. These correspond to a time steps of 3.8×10^{-12} s for simulations using the VFB and 2.9×10^{-12} s for simulations using the VFM. The grid steps of 1.5 and 2 mm allow the skin of the models to be resolved appropriately [31]. This resulted in a total number of 19.2×10^6 cells for simulations using the VFB and 128×10^6 cells for simulations using the VFM. The simulations are terminated after 12 periods for the simulations using the VFB and after 20 periods for the simulations with the VFM, when a steady state is reached. The commercial tool SEMCAD-X (Schmid & Partner Engineering (SPEAG), Zürich, Switzerland) is selected for the FDTD simulations. The simulations are accelerated using a Graphics Processing Unit (GPU)-based computing provided by SPEAG.

8.2.3 Methodology

The method used to determine the SAR_{osa} in the realistic environments listed in Table 3.3 is similar to the method used to determine the electric fields near the body of the VFM, outlined in Section 3.4.2 in Chapter 3. However, instead of the electric fields surrounding a phantom, the electric fields inside a phantom are determined.

After obtaining the electric fields ($\overline{E}(\overline{r})$) in every point of a particular organ of the phantoms in a particular exposure sample, using the method outlined in Section 3.4.2 and Equation 3.13, the SAR can be calculated in every point $\overline{r}$ of the organ:

$$SAR(\overline{r}) = \frac{\sigma(\overline{r})|\overline{E}(\overline{r})|^2}{2\rho(\overline{r})} \tag{8.1}$$

where $\overline{E}(\overline{r})$ is the vectorial electric field in each point, $\sigma(\overline{r})$ is the conductivity in each point, and $\rho(\overline{r})$ the mass density in each point. The SAR_{osa} is a mass average over the cells of the organ:

$$SAR_{osa} = \frac{1}{M_{organ}} \int_{V_{organ}} SAR(\overline{r})\rho(\overline{r})dV \tag{8.2}$$

with M_{organ} the organ's mass and V_{organ} the organ's volume. As the organ is discretized in space for the FDTD simulations, this becomes:

$$SAR_{osa} = \frac{\sum_{k=1}^{N_{cells}} SAR_k V_k \rho_k}{M_{organ}} \tag{8.3}$$

where N_{cells} is the number of cells in the organ, M_{organ} is the organ's mass, SAR_k is the SAR in grid cell *k* of the organ, V_k is the volume of that grid cell, and ρ_k is its density. The absorbed power in the organ ($P_{abs,organ}$) can then be calculated from the SAR_{osa}:

$$P_{abs,organ} = SAR_{osa}.M_{organ} \tag{8.4}$$

In order to obtain a SAR_{osa} value for a realistic exposure sample, $\overline{E}_{TE,l}$ and $\overline{E}_{TM,l}$ in Equation 3.13 have to be approximated using the BFDs. We propose two methods for this: vectorial cell-wise spline interpolation and organ-specific averaged scalar linear interpolation.

Vectorial Spline Interpolation in Every Grid Cell. In this first method, a cubic spline interpolation is performed over the different $\overline{E}_{TE}(\phi_i, \theta_j, \overline{r})$ and $\overline{E}_{TM}(\phi_i, \theta_j, \overline{r})$ to approximate the fields $\overline{E}_{TE}(\phi, \theta, \overline{r})$ and $\overline{E}_{TM}(\phi, \theta, \overline{r})$ in each point $\overline{r}$ of the organ under consideration. A different interpolation scheme is used for the two coordinates ϕ and θ, see section 3.4.2 in Chapter 3. The ϕ coordinate is periodic and extends over a domain that is twice as large as the θ domain. Therefore, first an interpolation is performed in the ϕ-dimension, followed by an interpolation in θ. The coefficients for the interpolation in the ϕ direction can be calculated in advance using a cyclic scheme and using all ϕ_i for every θ_j. They can thus be stored and loaded whenever necessary, speeding up the calculations. Unfortunately, the coefficients for the interpolation for the θ coordinate depend on ϕ and cannot be calculated in advance. A cubic spline interpolation using the fields calculated for the six nearest θ_j has been chosen. Both interpolations have to be carried out for every vectorial component of the electric field. The advantage of this scheme is its accuracy. The large tensors of interpolation coefficients that have to be loaded into random-access memory (RAM) are a major disadvantage.

Organ-Specific Averaged Scalar Linear Interpolation. The vectorial spline interpolation in each grid cell can very accurately calculate individual SAR_{osa} values for a random exposure sample. However, it provides an accuracy that is unnecessary for a statistical analysis of SAR_{osa}. Moreover, the method developed in this chapter also aims at being accessible for third-party users that do not normally possess the RAM memory required to upload all the BFDs. Therefore, a faster, but less accurate, method which requires less computational demands is proposed. The method consists of a linear interpolation of organ-specific averaged products of all combinations of two BFDs.

In this method, an organ-specific averaging of the BFDs is performed. This is possible since there are only a limited number of multiplications between two BFDs in a certain point. When Equation 3.13 is substituted in Equations 8.1 and 8.2, this will lead to:

$$
\begin{aligned}
SAR_{osa} = \sum_{k=1}^{N_s} \sum_{m=1}^{N_s} A_k \, A_m [\\
(Re(S_1\gamma) - Im(S_1)\chi) \, sin\psi_k \, sin\psi_m \\
+(Re(S_2\gamma) - Im(S_2)\chi) \, cos\psi_k \, cos\psi_m \\
+(Re(S_3\gamma) - Im(S_3)\chi) \, cos\psi_k \, sin\psi_m \\
+(Re(S_3\gamma) + Im(S_3)\chi) \, sin\psi_k \, cos\psi_m]
\end{aligned} \tag{8.5}
$$

with $\gamma = Re(e^{\alpha_k - \alpha_m})$ and $\chi = Im(e^{\alpha_k - \alpha_m})$. The coefficients S_1-S_3 have the following form:

$$S_1 = \frac{1}{M_{organ}} \int_{V_{organ}} \frac{\sigma}{2} \overline{E}_{TE,k} . \overline{E}^*_{TE,m} dV \tag{8.6}$$

$$S_2 = \frac{1}{M_{organ}} \int_{V_{organ}} \frac{\sigma}{2} \overline{E}_{TM,k} . \overline{E}^*_{TM,m} dV \tag{8.7}$$

$$S_3 = \frac{1}{M_{organ}} \int_{V_{organ}} \frac{\sigma}{2} \overline{E}_{TE,k} . \overline{E}^*_{TM,m} dV \tag{8.8}$$

where V_{organ} and M_{organ} are the volume and mass of the studied organ, respectively, and σ is the conductivity in every grid cell. The coefficients S_1-S_3 can be calculated for every combination of two BFDs and thus for every combination of pairs (ϕ_i, θ_j). These organ-specific averaged BFDs (scalars) can then be used for an interpolation in order to determine the coefficients S_1-S_3 for any ϕ and θ. A linear interpolation is chosen because it provides a good trade-off between accuracy and execution time. The method is considerably faster and has lower memory requirements. Instead of loading $18 \times N_\phi \times N_{cells}$ data points for every exposure sample (the 18 coming from the three components of the E-field loaded for the six nearest θ_j), now only $6 \times N_\phi \times N_{theta}$ data points have to be loaded. This seriously reduces RAM memory requirements for the user, especially for organs that consist of over 10^6 cells ($N_{cells} > 10^6$).

In this method, the SAR_{osa} is approximated using S_i coefficients that are calculated using the BFDs and then interpolated over the different incident angles. In an exact solution the S_i values should be calculated with the electric fields obtained from FDTD simulations of plane-wave exposure of the VFB, incident from the actual (ϕ_k, θ_k) angles.

8.2.4 Estimating the SAR_{osa} from measurements using a PDE

A personal distributed exposimeter (PDE) is a measurement device consisting of multiple body-worn antennas, in this case tuned to the GSM 900 DL band, that

is primarily used to measure one's personal exposure to RF EMFs in terms of incident power density (S_{inc}). The calibration and usage of this device have been discussed in Chapters 6 and 7. A method to estimate the SAR_{wb} from PDE measurements has been described in Chapter 7. This method requires a relationship between the SAR_{wb} distribution in a realistic environment [24] and the (geometrically averaged) received power on the PDE ($P_{geom,PDE}$). The goal of this chapter is to establish a similar relationship between a distribution of the SAR_{osa} in the 'Urban Macro-cell' scenario at 950 MHz and the received power on the PDE during measurements in the same environment, see Chapter 7.

The method outlined in the previous paragraphs provides us with a probability distribution of the SAR_{osa} for a certain organ or tissue for a constant incident power density (S_{inc}): $Prob(SAR_{osa} \leq Y|S_{inc} = 1\,W/m^2)$ with Y an SAR value $\in [0, \infty[\ W/kg$ at 950 MHz. From our calibration measurements, presented in Chapter 6, a probability distribution $Prob(AA_{geom,PDE} \leq Z)$ with $AA_{geom,PDE}$ the antenna aperture of the PDE worn by a subject and Z a surface $\in [0, \infty[\ m^2$ can be obtained. This distribution can be inverted using Equation 7.13 in order to obtain a distribution $Prob(S_{inc} \leq X|P_{geom,PDE} = 1\ W)$. A relationship between the SAR_{osa} and the received power on the PDE can then be established using the law of total probability:

$$\begin{aligned} &Prob(SAR_{osa} \leq Y|P_{geom,PDE} = 1\,W) = \\ &\qquad \int_0^\infty Prob(SAR_{osa} \leq Y|S_{inc} = X) \\ &\times \frac{dProb}{dX}(S_{inc} \leq X|P_{geom,PDE} = 1\,W)dX \end{aligned} \tag{8.9}$$

with $Prob(SAR_{osa} \leq Y|P_{geom,PDE} = 1\ W)$ the probability distribution of the SAR_{osa} of a certain organ for a fixed received power (of 1 W) on the PDE. The median value of this distribution multiplied by the received power during measurements, is used as an estimator of the SAR_{osa}. The 50% and 68% prediction intervals, denoted as PI_{50} and PI_{68} can be obtained from the distribution as well:

$$PI_{50} = \frac{p_{75}(SAR_{osa}|P_{geom,PDE} = 1\,W)}{p_{25}(SAR_{osa}|P_{geom,PDE} = 1\,W)} \tag{8.10}$$

$$PI_{68} = \frac{p_{84}(SAR_{osa}|P_{geom,PDE} = 1\,W)}{p_{16}(SAR_{osa}|P_{geom,PDE} = 1\,W)} \tag{8.11}$$

with $p_x()$ the x% percentile of the distribution on which it operates. The PI_{50} corresponds to half of the distribution and the PI_{68} corresponds to the interval covered by two standard deviations, if the distribution is (log-)normal. This median value and prediction intervals are used to estimate the SAR_{osa} from the recieved powers during the measurements described in Section 7.2.3.3 along the trajectory shown in Figure 7.4.

8.3 Results

8.3.1 Validation of the SAR_{osa} Calculation Methods

The goal of our method is to avoid executing an FDTD simulation for every exposure sample. Since the proposed method serves as a substitute for FDTD simulations, the results of the method have to be compared to the results obtained from FDTD simulations. The relative error on SAR_{osa} is defined as:

$$err = 100 \times \frac{|SAR_{osa,method} - SAR_{osa,FDTD}|}{SAR_{osa,FDTD}}(\%) \tag{8.12}$$

The comparison will be made for a number of exposure samples (N_{smp}) in a certain environment, giving rise to an average (err_{av}) error and maximal (err_{max}) error, as well as a standard deviation (SD) of the average error.

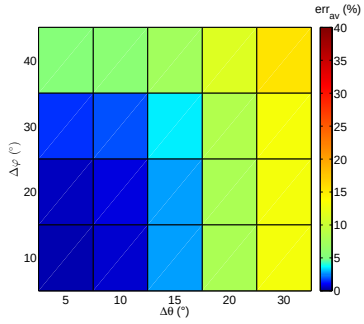

(a) err_{av} using spline interpolation

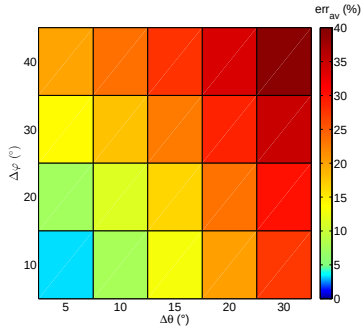

(b) err_{av} using linear interpolation

Figure 8.2: The err_{av} on the SAR_{osa} in the cortex of the VFB's kidney at 950 MHz for 100 samples.

Both interpolation schemes will approximate the actual SAR_{osa} with certain

accuracy. To validate the performance of our method, the results using an interpolation scheme are compared to the results obtained from 100 FDTD-simulated samples in the 'Urban Macro-cell' environment. The electric fields are extracted in all the grid cells of the organs under consideration, and $SAR_{osa,FDTD}$ is calculated using these fields. Simultaneously, the $SAR_{osa,method}$ is calculated using the aforementioned methods.

Figure 8.2 shows the err_{av} for the cortex of the VFB's kidneys at 950 MHz for both the vectorial spline (Fig. 8.2 (a)) and scalar linear (Fig. 8.2 (b)) interpolation schemes. Both err_{av} are shown for different discretization steps: $\Delta\phi = 10^\circ - 40^\circ$, and $\Delta\theta = 5^\circ - 30^\circ$. Both interpolation schemes show the expected trend of increased accuracy with decreasing discretization steps for the BFDs. The spline interpolation scheme is able to accurately predict ($err_{av} < 1\%$) the absorbed power in the kidneys. Using $\Delta\phi = 10^\circ$ and $\Delta\theta = 5^\circ$, an $err_{av} = 0.46 \pm 0.42\%$ is obtained for the cortex of the kidneys. The same discretization step leads to an $err_{av} = 3.3 \pm 1.5\%$ for linear interpolation. For the smallest discretization steps ($\Delta\phi = 10^\circ$, $\Delta\theta = 5^\circ$), the cell-wise spline interpolation shows an $err_{max} = 2\%$ for the kidneys cortex. This err_{max} is 6% for the faster linear interpolation.

Table 8.1 lists the average errors (for $\Delta\phi = 10^\circ$, $\Delta\theta = 5^\circ$) for the different studied organs for the two interpolation methods. Spline interpolation is always more accurate ($err_{av} < 1.8\%$) but is computationally too demanding to be used for all organs, while linear interpolation has a higher average error ($err_{av} < 14.3\%$ for $\Delta\phi = 10^\circ$ and $\Delta\theta = 5^\circ$).

Organ/tissue	Spline interpolation[a] $err_{av} \pm SD$ (%)	Linear interpolation $err_{av} \pm SD$ (%)
Adrenal gland	1.8 ± 1.6	4.3 ± 2.3
Artery		6.6 ± 2.0
Bladder		2.1 ± 1.6
Brain grey matter		14.0 ± 4.5
Brain white matter		14.0 ± 4.5
Cerebellum		11.7 ± 4.1
Cerebrospinal fluid	2.6 ± 0.15	12.9 ± 4.1
Commissura anterior	0.57 ± 0.61	12.7 ± 5.1
Cornea	0.40 ± 0.55	11.4 ± 4.1
Epididymis	0.56 ± 0.56	1.9 ± 1.7
Eye lens	0.34 ± 0.47	11.3 ± 4.0
Eye sclera	0.30 ± 0.40	11.4 ± 4.0
Eye vitreous humor	0.27 ± 0.35	11.4 ± 4.1
Gallbladder		3.1 ± 2.3
Heart lumen		4.3 ± 2.3
Heart muscle		5.5 ± 2.3
Hippocampus	0.64 ± 0.47	13.3 ± 4.6
Hypophysis	1.10 ± 1.07	10.4 ± 4.2
Hypothalamus	0.60 ± 0.54	12.3 ± 4.7
Kidney cortex	0.46 ± 0.42	3.3 ± 1.5
Kidney medulla	071 ± 0.79	3.8 ± 2.1
Liver		3.7 ± 1.6
Lung		6.4 ± 2.0
Medulla oblongata	1.0 ± 0.95	10.5± 3.9
Midbrain	0.46 ± 0.41	13.5 ± 4.5
Nerve	0.55 ± 0.55	5.6 ± 2.8
Pancreas		2.8 ± 2.0
Penis	0.42 ± 0.42	1.7 ± 1.7
Pineal body	0.53 ± 0.45	14.3 ± 5.0
Pons	0.65± 0.52	11.7 ± 4.1
Prostate	0.90 ± 0.92	2.5 ± 2.2
Spinal cord		7.6 ± 3.1
Spleen		4.0 ± 1.9
Testis	0.44 ± 0.68	1.7 ± 2.0
Thalamus	0.38 ± 0.30	14.0 ± 4.5
Thymus		6.9 ± 2.9
Tongue		8.8 ± 3.2
Vein		6.1 ± 1.8

[a] This error has not been estimated for all tissues due to too high memory requirements.

Table 8.1: $err_{av} \pm SD$ (%) using the two interpolation schemes for the VFB's organs averaged over 100 exposure samples.

8.3.2 SAR_{osa} Distributions in Realistic Environments at 950 MHz

After extracting the BFDs, they are combined to calculate the SAR_{osa} for every sample. To study the SAR_{osa} in a realistic environment a large number of samples have to be taken into consideration, ideally an infinite number of samples. A sample size of 5000 is chosen for every tissue in every environment, providing good accuracy and an acceptable calculation time per environment. This sample

size has been studied for the 'Indoor Pico-cell' scenario and is associated with an average coefficient of variance smaller than 1% and an average value of the 95% confidence interval smaller than 6.5% for percentiles between 0.1 and 99.9.

The electric fields incident on the phantom can be normalized using different approaches: the total incident root-mean-squared electric field (E_{RMS}), the E_{RMS} averaged over a volume where the phantom should be positioned, or the E_{RMS} in a point near the phantom. In this section, the results are normalized to the E_{RMS} averaged over the volume of a box surrounding the phantom with dimensions $21 \times 37 \times 118$ cm^3, which are the largest dimensions of the phantom in each orthogonal direction. These E_{RMS} values are set to the ICNIRP reference level for incident electric fields at the frequency under consideration [1]; for 950 MHz, $E_{RMS} = 42.38$ V/m.

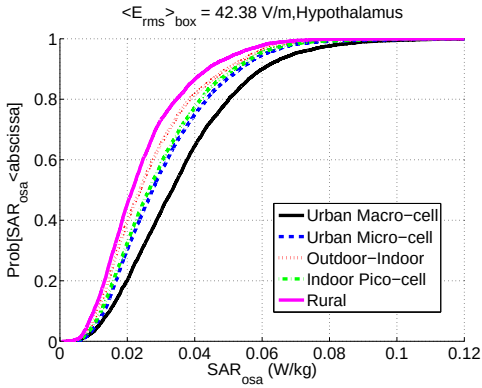

Figure 8.3: Cumulative distribution function of SAR_{osa} for different exposure conditions averaged over a box surrounding the phantom at 950 MHz for the VFB's hypothalamus using spline interpolation.

Figure 8.3 shows the cumulative distribution function for the VFB's hypothalamus for five different exposure scenarios. There is a dependence of SAR_{osa} on the environment. For the VFB's hypothalamus, the SAR_{osa} values are, on average, the highest in the 'Urban Macro-cell' scenario with a mean SAR_{osa} value of 0.036 W/kg, and lowest in the 'Rural' scenario with a mean value of 0.025 W/kg. The differences in SAR_{osa} distributions between the environments are due to differences in distributions for the polar angle in the different environments (see Section 8.4).

In Figure 8.4, the percentiles of the cumulative distribution function of the VFB's hypothalamus in the'Indoor Pico-cell' environment are compared for the two proposed methods: cell-wise spline interpolation and organ-specific averaged linear interpolation. Every marker on this quantile-quantile plot depicts a partic-

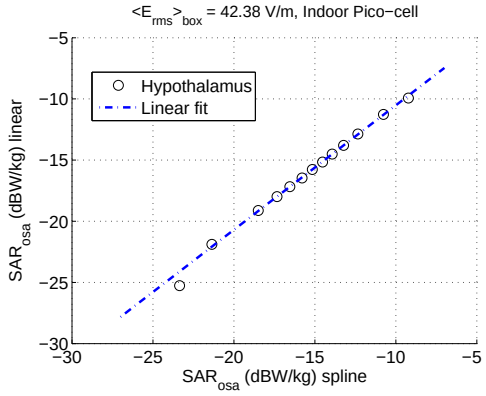

Figure 8.4: Quantile-quantile plot from 0.1^{th} to the 99.9^{th} percentile, comparing both SAR_{osa}-calculating methods for the VFB's hypothalamus in the 'Indoor Pico-cell' environment. The vertical axis shows the quantiles of the SAR_{osa} distribution using an organ-specific averaged linear interpolation, while the horizontal axis shows those using a vectorial spline interpolation. The markers follow a line parallel to the bisector (depicted by the dashed, linear fit).

ular percentile. The $10^{th} - 90^{th}$ percentiles in steps of 10%, complemented with the 0.1, 1, 99, and 99.9 percentiles are shown. The vertical axis shows the values of these percentiles using linear interpolation, while the horizontal axis shows the corresponding values for spline interpolation. Logarithmic axes are chosen in order to show high ($p_{99.9}$) and low ($p_{0.1}$) percentiles in one figure. Two identical distributions result in a line on the bisector in a quantile-quantile plot because their percentiles are identical. In Figure 8.4, the markers follow a line parallel to the bisector, indicating that both distributions have the same shape (between $p_{0.1}$ and $p_{99.9}$) but the linear interpolation slightly underestimates the SAR_{osa}. The same comparison between the two proposed methods is carried out for all studied organs or tissues in all studied environments. For some tissues, the linear organ-specific averaged interpolation introduces an overestimation while others show an underestimation. Considering all tissues for which a cell-wise spline interpolation has been executed (listed in Table 8.1), an average slope of the quantile quantile plots of 1.02 is found with an average offset of -4%, which is in agreement with [27]. The linear interpolation thus introduces a small average underestimation of SAR_{osa} of the different studied organs, but preserves the shape of the distribution. However, linear interpolation is an order of magnitude faster than spline interpolation and requires up to a factor of 200 less memory. Therefore the faster linear interpolation is used to obtain the further results presented in this chapter.

8.3.3 Comparing SAR_{osa} in Different Organs

Figure 8.5 shows the mean SAR_{osa} and the 90^{th} (p_{90}) and 95^{th} (p_{95}) percentiles of the cumulative distribution function for the different studied organs. Figure 8.5 (a) shows these values for the VFB's cerebral tissues, while Figure 8.5 (b) and (c) show the same values for the other studied organs and tissues. As Figure 8.5 shows, the 'Urban Macro-cell' environment accounts for the highest mean SAR_{osa}, p_{90}, and p_{95} for a majority of the studied organs. The VFB's pancreas has the lowest mean , p_{90}, and p_{95} of all the studied tissues in all scenarios (mean ≤ 0.009 W/kg, $p_{90} \leq 0.015$ W/kg, and $p_{95} \leq 0.018$ W/kg), except for the 'Rural' scenario where the hypophysis has the same mean (0.009 W/kg) and lower p_{90} and p_{95} values of 0.013 W/kg and 0.015 W/kg, respectively. The pancreas has an average conductivity to density ratio σ/ρ compared to the other studied organs, but is located relatively deep inside the body compared to the other studied organs. The tongue is the studied organ with the highest mean SAR_{osa} in all environments (mean $SAR_{osa} \geq 0.11$ W/kg and $p_{95} \geq 0.21$ W/kg). In the 'Rural' and 'Indoor Pico-cell' environments the cornea has the same high mean SAR_{osa} (0.11 W/kg) as the tongue. The cornea and penis do show higher p_{90} and p_{95} values ($p_{90} \geq 0.21$ W/kg and $p_{95} \geq 0.22$ W/kg). The three organs have medium conductivity to density ratios compared to the other studied organs, but are located very close to (tongue) or at the body's surface (cornea, penis). When only considering the cerebral tissues, shown in Figure 8.5 (a), the cerebrospinal fluid has the highest SAR_{osa} due to a high σ/ρ compared to the other studied organs, while the hypophysis has the lowest mean SAR_{osa}.

Figure 8.5 shows that large differences in SAR_{osa} can exist between different organs. Several factors will influence the SAR_{osa} in realistic environments. Two main contributors are studied in this paragraph: the ratio between electric conductivity and density (σ/ρ), and the distance (d) of the center of the mass of an organ to the body surface. SAR_{osa} should scale linearly with the ratio σ/ρ according to Equation 8.1. The internal electric field ($\overline{E}(\overline{r})$ in Equation 8.1) should decrease exponentially with the distance in the body due to the skin effect. However, the distance d of the center of the mass of an organ to the body's surface varies strongly in different directions.

The distance considered in this paragraph is the amplitude (d) of the spherical coordinates (d,ϕ,θ) of the phantom's surface in a spherical coordinate system, which is centered in the considered organ's center of mass. This distance is determined in the same directions (ϕ_i, θ_j) with $\Delta\phi = 10^\circ$ and $\Delta\theta = 5^\circ$) as the incident SPWs used for determining the BFDs. These SPWs are incident on the phantom at a field strength equal to the ICNIRP reference levels at 950 MHz and induce a $SAR_{osa,SPW}$ in the studied organs. Note that the $SAR_{osa,SPW}$ induced by these SPWs is not approximated by our method, but a direct result of the performed FDTD simulations. We have determined two distances: $d_{surf}(\phi, \theta)$

the in-body distance to the surface, and $d_{edge}(\phi, \theta)$ the distance to the phantom's edge. We consider two distances because it is possible that the line from the center of gravity of a certain organ in direction (ϕ, θ) intersects multiple times with the phantom's surface, for example, if the torso is shielded by an arm in a certain (ϕ, θ) direction. The distance of an organ's center of gravity to the first intersection is $d_{surf}(\phi, \theta)$, while the distance of an organ's center of gravity to the last intersection will be $d_{edge}(\phi, \theta)$; this last distance will take into account the limbs, head or torso, which can cause shadowing. Both contributors are investigated using a nonlinear regression of their mean values with the mean SAR_{osa} according to the following model:

$$\widehat{SAR}_{osa} = a_0 + a_1 \frac{\sigma}{\rho} + a_2 . e^{-a_3 . d} \tag{8.13}$$

where d can represent the mean d_{surf} or d_{edge}, and $\widehat{SAR}_{osa}$ is the estimated value determined by the regression model. The coefficient a_3 is included because d_{surf} and d_{edge} are physical distances and an attenuation coefficient (unit: 1/m) is thus required to account for the loss and reflections during the propagation.

Distance	a_0 (W/kg)	a_1 (V^2/m^2)	a_2 (W/kg)	a_3 (m^{-1})	r	P
$d_{surf,mean}$	-0.02	34	0.37	26	0.80	1.5×10^9
$d_{edge,mean}$	-0.03	35	0.40	18	0.73	1.8×10^7

Table 8.2: Coefficients (a_i), correlation coefficients (r), and the P-Value for these correlation coefficients for a fit using Equation 8.13.

Table 8.2 lists the estimates for the coefficients after a regression using all the studied organs, and the Pearson correlation between $\widehat{SAR}_{osa}$ and the mean $SAR_{osa,SPW}$, together with its P-value. We find good correlations of 0.73 and 0.80 between our proposed model in Equation 8.13 and the mean $SAR_{osa,SPW}$, respectively. There are other factors influencing the SAR_{osa}, for example, the volume, shape of an organ and dielectric properties of the surrounding tissues. A future study should include these factors and look for a combined regression model.

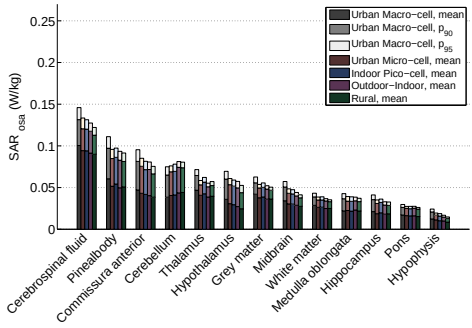

(a) Cerebral regions in descending order of the max p_{95}.

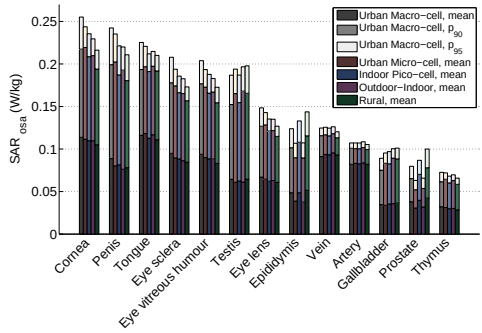

(b) Other studied tissues in descending order of the max p_{95}.

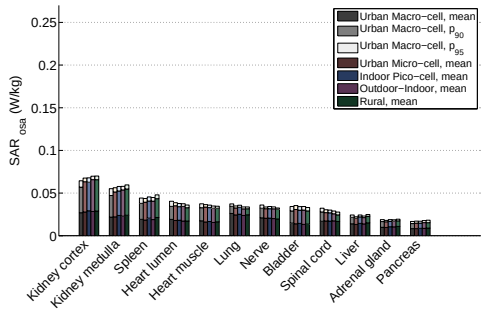

(c) Other studied tissues in descending order of the max p_{95}.

Figure 8.5: Mean SAR_{osa}, 90^{th}, and 95^{th} SAR_{osa} percentiles (W/kg) normalized to $E_{rms} = 42.38$ V/m over a box surrounding the VFB, for different exposure scenarios. The 5 columns represent the different environments for every organ of the VFB. Each column is divided in 3 parts: the lowest division indicates values that are lower than the mean SAR_{osa}, the middle one indicates the values between the mean and the p_{90}, and the top of the bars corresponds to the p_{95}.

8.3.4 SAR_{osa} Under Single Plane-Wave Exposures

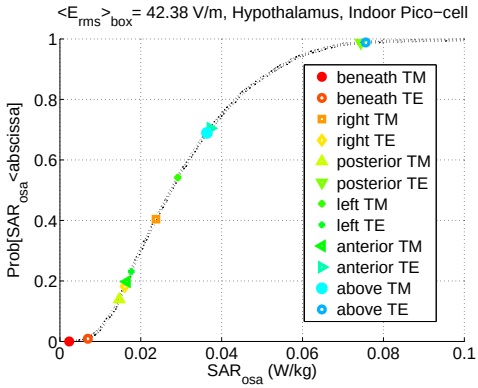

Figure 8.6: Cumulative distribution function of SAR_{osa} in the 'Indoor Pico-cell' environment, averaged over a box surrounding the phantom at 950 MHz for the VFB's hypothalamus, including 12 SPWs incident from the phantom's main axes.

It is plausible that for a certain organ, a quick, worst-case estimation of the exposure can be made using a SPW. The SAR_{wb} and peak SAR_{10g} have been studied deterministically in literature, using SPWs incident from the body's main axes [19–21]. Moreover, the ICNIRP calculates its basic restrictions and reference levels based on SPW-exposure [1]. To investigate whether a single plane wave incident from one of the main axes can be used as a(n) (worst-case) estimation for SAR_{osa}, we have calculated the $SAR_{osa,SPW}$ values for the organs under consideration in this study for both TE- and TM-polarization. The six directions of incidence are: from above, beneath, the anterior side, the posterior side, and both lateral sides of the phantom. After proper renormalization, the values for the SAR_{osa} can be compared to the values that were obtained for the cumulative distribution functions for the different environments. Figure 8.6 shows an example of how these 12 SPW exposure conditions correspond to the cumulative distribution functions for the VFB's hypothalamus in the 'Indoor Pico-cell' environment. The TE polarized plane wave incident from above could be used as a worst-case estimation for the SAR_{osa} of the hypothalamus since it is located at the 99^{th} percentile.

Organ	(ϕ_j, θ_i) (°)	Pol	$min(q_{SPW})$	$max(q_{SPW})$
Adrenal gland	(210,115)	TM	0.988	0.993
Artery	(0,105)	TM	0.986	0.992
Bladder	(0,80)	TM	0.979	0.991
Brain grey matter	(350,25)	TM	0.933	0.984
Brain white matter	(340,25)	TM	0.914	0.983
Cerebellum	(180,120)	TM	0.983	0.988
Cerebrospinal fluid	(0,25)	TM	0.938	0.982
Commissura anterior	(0,80)	TM	0.954	0.990
Cornea	(350,80)	TM	0.977	0.994
Epididymis	(0,90)	TE	1	1
Eye lens	(350,80)	TM	0.975	0.993
Eye sclera	(0,60)	TM	0.972	0.993
Eye vitreous humor	(0,80)	TM	0.973	0.994
Gallbladder	(340,100)	TM	0.987	0.991
Heart lumen	(0,85)	TM	0.961	0.988
Heart muscle	(0,75)	TM	0.970	0.991
Hippocampus	(300,85)	TE	0.982	0.998
Hypophysis	(350,40)	TM	0.987	1
Hypothalamus	(0,35)	TM	0.997	0.999
Kidney cortex	(180,105)	TM	0.982	0.987
Kidney medulla	(180,95)	TE	0.980	0.985
Liver	(340,90)	TE	0.996	0.999
Lung	(210,80)	TE	0.984	0.997
Medulla oblongata	(90,65)	TM	0.935	0.969
Midbrain	(170,10)	TE	0.977	0.999
Nerve	(180,60)	TM	0.966	0.986
Pancreas	(330,100)	TM	0.981	0.991
Penis	(0,45)	TM	0.989	0.998
Pineal body	(80,20)	TE	0.997	1
Pons	(180,75)	TM	0.968	0.992
Prostate	(0,100)	TE	1	1
Spinal cord	(180,80)	TM	0.970	0.990
Spleen	(160,95)	TE	0.991	0.993
Testis	(0,105)	TM	0.990	0.996
Thalamus	(180,80)	TE	0.995	1
Thymus	(0,85)	TM	0.971	0.992
Tongue	(0,105)	TM	0.974	0.987
Vein	(0,115)	TM	0.962	0.979

Table 8.3: Worst-Case single plane-wave exposure with incident field strength $E_{RMS} = 42.38$ V/m for every studied organ. The corresponding incident angles, polarization and the minimum and maximum $q_{SPW} = P[SAR_{osa} \leq SAR_{osa,SPW}]$ in the 5 studied environments are listed.

We have extended this plane-wave study to all of the (ϕ_i, θ_j) directions for which we have extracted BFDs. The calculation of SAR_{osa} is exact at these angles. Table 8.3 lists the worst case (ϕ_i and θ_j for $\Delta\phi = 10°$ and $\Delta\theta = 5°$) and polarization for every environment and organ, as well as the minimal and maximal probability $q_{SPW} = P[SAR_{osa} \leq SAR_{osa,SPW}]$ for this worst-case SPW in the five studied environments.

8.3.5 Estimating the SAR_{osa} from measurements using a PDE

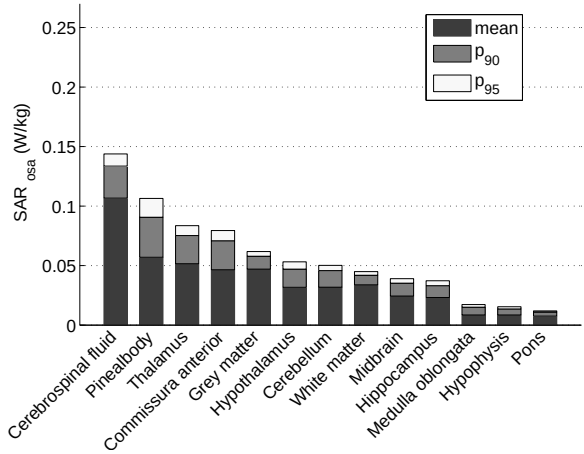

Figure 8.7: Mean SAR_{osa} and 90^{th} and 95^{th} SAR_{osa} percentiles (W/kg) of the VFM's cerebral tissues, normalized to $E_{rms} = 42.38$ V/m over a box (volume) surrounding the VFM, in the 'Urban Macro-cell' scenario at 950 MHz. The three divisions in each column indicate the values that are lower than the mean SAR_{osa} and the values that are lower than 90% and 95% of the studied samples.

Figure 8.7 shows the mean value, the p_{90}, and the p_{95} of the SAR_{osa} of the different cerebral tissues of the VFM at 950 MHz in the 'Urban Macro-cell' scenario. The organs are ranked from the highest to the lowest p_{95}. The commissura posterior is again not considered in this study, due to the low number of cells assigned to this tissue. The cerebrospinal fluid has the highest SAR_{osa}, with a mean value of 0.11 W/kg, a p_{90} value of 0.13 W/kg, and a p_{95} of 0.14 W/kg, for an incident, root-mean-squared electric field strength of 42.38 V/m. These relatively high values are explained by its location on the outer shell of the brain, in combination with a relatively high conductivity. The lowest SAR_{osa} is found for the pons, with a mean value of 7.6 mW/kg, a p_{90} value of 11 mW/kg, and a p_{95} of 12 mW/kg, for an incident electric field strength of 42.38 V/m. The location of this tissue is well-shielded from the environment by the other cerebral tissues and the other parts of the human head and neck.

The probability distributions obtained for the different cerebral tissues of the VFM are then normalized to an incident power density of 1 W/m^2. The incident power densities are averaged over a line (the main axis of the VFM) similar to the averaging used in the calibration of the PDE. These probability distribu-

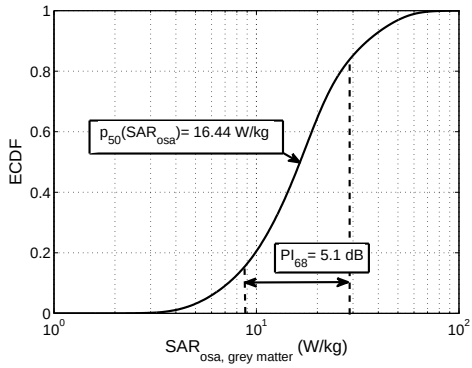

Figure 8.8: Experimental cumulative distribution function (ECDF) of the SAR_{osa} for the VFM's grey matter and a received power of 1 W on the PDE in the 'Urban Macro-cell' scenario.

tions are convoluted with the probability distribution of the S_{inc} for a fixed received power on the PDE, using Equation 8.9, in order to obtain a distribution $Prob(SAR_{osa} \leq Y | P_{geom,PDE} = 1\ W)$. Figure 8.8 shows this distribution for the grey matter of the VFM at 950 MHz in an 'Urban Macro-cell' scenario. The median value of the $SAR_{osa} = 18\ W/kg$, which is relatively high since received powers of 1 W are very uncommon (the upper detection limit of the RF nodes is only 0.01 W) in non-occupational exposure situations. The PI_{50} and PI_{68} on this median value are 3.7 dB and 5.6 dB, respectively. The median value of the distribution is used to rescale the received powers on the PDE during the walk presented in figure 7.4. The prediction intervals serve as a measure of uncertainty on the measured SAR_{osa} values.

Organ	$p_{50}(SAR_{osa}\|P_r = 1\,W)$ (W/kg)	PI_{50} (dB)	PI_{68} (dB)	$p_{50}(SAR_{osa,walk})$ ($\mu W/kg$)	$p_{95}(SAR_{osa,walk})$ ($\mu W/kg$)
Cerebellum	11	4.2	6.3	0.32	5.8
Cerebrospinal fluid	40	3.7	5.7	1.1	20
Commissura anterior	17	4.2	6.3	0.47	8.3
Grey matter	18	3.7	5.6	0.50	8.8
Hippocampus	8.4	4.1	6.1	0.24	4.2
Hypophysis	3.0	4.5	6.6	0.084	1.5
Hypothalamus	11	4.2	6.3	0.32	5.7
Medulla oblongata	2.8	4.8	7.1	0.080	1.4
Midbrain	8.8	4.0	6.0	0.25	4.4
Pineal body	20	4.3	6.4	0.56	10
Pons	2.7	4.1	6.1	0.077	1.4
Thalamus	19	4.1	6.1	0.52	9.3
White matter	13	3.7	5.6	0.36	6.4

Table 8.4: The first column list median values of the SAR_{osa} of the VFM's cerebral tissues at 950 MHz for a received power of 1 W on the PDE. The next two columns list the PI_{50} and PI_{68} of the distribution $Prob(SAR_{osa} \leq Y|P_{geom,PDE} = 1\,W)$ for the same tissues. The final two columns list p_{50} and p_{95} of SAR_{osa} measured during the walk shown in Fig. 7.4

Table 8.4 lists the median value of the SAR_{osa} for the different cerebral tissues of the VFM in the 'Urban Macro-cell' scenario for a geometrically averaged received power of 1 W on the PDE. The median values follow the same order as shown in Figure 8.8 and are relatively high, since a received power of 1 W also corresponds to a relatively high incident power density (1.7 kW/m^2), and range from 2.7 W/kg for the pons of the VFM to 40 W/kg for the cerebrospinal fluid. The corresponding PI_{50} and PI_{68} values of the distributions range from 3.7 dB (white and grey matter) to 4.8 dB (medulla oblongata) in case of the PI_{50} and from 5.6 dB to 7.1 dB in case of the PI_{68} for the same tissues.

The powers received during the walk shown in Figure 7.4 are translated into SAR_{osa} values using the p_{50} values listed in the first column. The median value and the p_{95} of these measurements are listed in the fourth and fifth column in Table 8.4. The median values range from 77 nW/kg (for the pons) to 1.1 $\mu W/kg$ (for the cerebrospinal fluid). The $p_{95}(SAR_{osa})$ values range from 1.4 $\mu W/kg$ to 20 $\mu W/kg$. There are no basic restrictions defined on the SAR_{osa}, so a comparison with the ICNIRP guidelines [1] cannot be made.

8.4 Discussion

8.4.1 SAR_{osa} in Different Realistic Environments at 950 MHz

In this chapter, we demonstrate that we can determine the SAR_{osa} for the VFB's organs in five different realistic environments. To this aim we have proposed two

methods: a method to calculate the SAR_{osa}, using a spline interpolation in every grid cell and an organ-specific averaged scalar linear interpolation. The err_{av} listed in Table 8.1 demonstrate that both methods are accurate, as the maximal err_{av} of 1.8% (spline interpolation) and 14.3% (linear interpolation) are acceptable, particularly since they are smaller than (or comparable to) the uncertainties that are associated with FDTD simulations using the Virtual Family (21% and 23% expanded uncorrelated uncertainty ($k = 2$) of SAR_{wb} and SAR_{10g}, respectively, associated with the FDTD simulations) [20, 21, 27]. Based on the preferred accuracy and calculation time, a choice has to be made between the different interpolation methods and discretization steps of the incident angles.

The properties (mean value, p_{90}, and p_{95}) of SAR_{osa} distributions in different environments are shown in Figure 8.5. An environmental dependence exists for all the studied organs or tissues, although this dependence is relatively small. The maximal difference between the mean SAR_{osa} value in two environments is 46% (59% for the p_{90} and 64% for the p_{95}), which is small compared to the differences in SAR_{osa} that can exist between two distinct organs; a factor of 14.3 between the mean SAR_{osa} for the tongue and pancreas in the 'Urban Macro-cell' environment is the largest difference that occurs. Note that when only studying the SAR_{wb} or peak SAR_{10g}, these differences in absorption between different organs would not become apparent since only one value would be obtained to describe the absorption in the human body. When the distribution of the SAR across the body is of interest, the SAR_{osa} obviously provides more information.

A regression model is introduced to explain these differences between SAR_{osa} values and provides good correlations using only two factors: the conductivity over density ratio, and the distance of an organ's center of gravity to the body's surface and edge of the phantom.

8.4.2 SAR_{osa} under Single Plane-Wave Exposures

A SPW study has been executed for comparison with the existing literature and for a further study of SAR_{osa}. The results are listed in Table 8.3 and demonstrate that it is possible to find a SPW for every studied organ that induces a SAR_{osa} that is larger than 91% of the samples in the studied environments. For certain organs (e.g., the VFB's prostate), a dominant path exists and the worst-case SPW exposure conditions will exceed all samples in every studied environment. However, not all SPW exposure conditions are realistic and should only be used as a worst-case approximation for a certain environment after comparison with a distribution of multipath exposures.

Table 8.3 also shows that only for the VFB's epididymis, the worst-case SPW condition is one of the 12 incident SPWs studied in [19], and [20, 21]. Moreover, the TM polarized SPW with $\phi = 0°$ and $\theta = 90°$, used to establish the ICNIRP [1] guidelines, is never found as a worst-case incident SPW for these studied organs.

Therefore, studying the SAR_{osa} deterministically with SPW exposures considering only the SPW incident from the phantoms main axis will thus not suffice for a conservative estimation of SAR_{osa}, and thus the power absorbed in a certain organ.

In previous studies, the TM polarization was found to be a worst-case SPW exposure for the SAR_{wb} [19, 23, 27]. However, as Table 8.3 shows, the dominant polarization is not the same for all organs. Two orthogonal polarizations should thus be considered when studying the worst-case SAR_{osa} for all organs.

The worst-case SPW angles provide more insight into the differences that exist between the SAR_{osa} distributions for different environments. A majority of the studied organs (87%) will exhibit their maximal mean SAR_{osa} in the environment where the average polar angle is closest to the worst-case spw polar angle, for example, the kindey's medulla with a worst case $\theta = 95°$, exhibits its maximal mean SAR_{osa} in the 'Rural' scenario with a median polar angle of $\theta_0 = 90°$. Another example is shown in Figure 8.3; the hypothalamus exhibits its highest average SAR_{osa} in the 'Urban Macro-cell' scenario, where the average polar angle is closest to the worst-case $\theta = 35°$. The opposite is also true for the hypothalamus; the average SAR_{osa} is lowest in the 'Rural' scenario, which has the highest average polar angle ($\theta = 94°$). When the worst-case SPW polar angle is closer to the average polar angle in a certain environment, it is more likely for this worst-case SPW, and plane waves close to this worst-case SPW, to be part of an exposure sample and thus induce a higher SAR_{osa} for the same incident field strength. This will then result in a larger mean SAR_{osa}.

8.4.3 Estimating the SAR_{osa} from measurements using a PDE

Table 8.4 lists the PI_{50} and PI_{68} values of the SAR_{osa} distribution for a constant received power on the PDE. These are relatively small compared to those found for the single antenna with the lowest PI_{50} and PI_{68} on the incident power density (G^H, see Table 7.1). For the single antenna, PI_{50} values on the SAR_{osa} between 6.6 and 7.3 dB are found for the different organs. The PI_{68} values for SAR_{osa} estimation using the single antenna range from 9.9 to 11 dB for the different organs. The prediction intervals on the incident power density are already relatively large for the single antenna ($9.5\ dB$), so the SAR_{osa} distribution (with a smaller variation) cannot contribute that much to the resulting uncertainty. The PDE thus also provides a lower uncertainty on the estimated SAR_{osa} values. It should be noted that there is an additional numerical uncertainty that is associated with FDTD simulations using the Virtual Family (21% and 23% expanded uncorrelated uncertainty ($k = 2$) of SAR_{wb} and SAR_{10g}, respectively, associated with the FDTD simulations) [20, 21, 27]. The uncertainty on the SAR_{osa} is expected to be in between these values, since the SAR_{osa} should have a similar uncertainty contribution by the chosen dielectric values, but an uncertainty in between the

SAR_{wb} and the SAR_{10g} caused by the discretization of the models.

The median SAR_{osa} values measured in this chapter are higher than the mean values estimated in [32]. For example, in [32] for a mean incident power density of 35 $\mu W/m^2$, a mean $SAR_{osa} = 0.24\ \mu W/kg$ is estimated for the grey matter of the VFM's brain, while, during our walk, we found a median value of 0.50 μW/kg for the grey matter, corresponding to a median power density value of 0.33 $\mu W/m^2$. Note that the median SAR_{osa} values estimated in [32] for a constant incident power density are also lower than those found in our study. Potentially due to a different placement of the plane wave source in [32].

In [3] SAR_{osa} value 0.63 mW/kg is reported for the brain of the visible human [33] at 30 m in front of a base station antenna (BSA) emitting 30 W at 947.5 MHz. We found a median value of 0.50 μW/kg for the grey matter of the VFM, using the measured powers on the PDE during our walk. This median value is a factor 1.3×10^3 smaller than the value found in [3]. The simulated SAR_{wb} value is 0.46 mW/kg in [3], which is a factor 1.8×10^3 higher than the median SAR_{wb} value of 0.25 μW/kg shown in Table 7.7. The absorption in the phantom is thus higher in front of a BSA than during a walk in the city, as expected.

8.5 Conclusions

We introduced, for the first time, a method to numerically investigate the organ-specific averaged SAR (SAR_{osa}) in heterogeneous phantoms in realistic environments. A stochastic method based on a plane-wave approximation of FF exposure, environmentally dependent distributions for these plane-wave exposure conditions and the linearity of Maxwell's equations, is extended in order to determine the SAR_{osa} in the Virtual Family Boy at 950 MHz. We proposed two different methods, which can both be used to estimate the SAR_{osa} for an arbitrary organ and environment. The SAR_{osa} can be estimated with an average error $< 2.6\%$ using the spline interpolation scheme of basic field distributions with angular resolutions of 10° in the azimuth angle (ϕ) and 5° in the polar angle (θ). Using a linear organ-specific averaged interpolation, a maximal average error of 14.3% can occur. Both methods provide the same shape of the distribution for SAR_{osa} in realistic environments. The SAR_{osa} in a particular environment has been studied by generating cumulative distribution functions for several organs. These distributions are dependent on the considered organs or tissues and on the studied environment. Both the dielectric properties and location in the phantom of the studied organ influence SAR_{osa} values. A good correlation using non-linear regression, including the conductivity to density ratio (σ/ρ) and the location of the center of gravity of the studied organs with the SAR_{osa}, has been found: 0.73 for the distance to the edge of the phantom, and 0.80 for the distance to the surface of the phantom.

Single plane-wave exposures can be used as a worst-case approximation for

some of the studied organs at 950 MHz, and a single plane-wave exposure condition exceeding 91% of the exposure samples could be found for all studied organs. The polarization of this worst-case single plane-wave exposure is dependent on the considered organ.

The methods, that are developed and validated in this chapter for the VFB, are then used to determine the SAR_{osa} of the virtual family male (VFM) in the 'Urban Macro-cell' scenario at the same frequency. These SAR_{osa} values are then used to determine the SAR_{osa} during measurements using a personal, distributed exposimeter, converting it to a SAR_{osa}*-meter*.

Future research can consist of extending the proposed method to other frequencies and phantoms. A further analysis of the factors influencing the SAR_{osa} has to be executed and current state-of-the-art propagation models for the incident fields will be implemented in the future.

References

[1] ICNIRP International Commission on Non-Ionizing Radiation Protection. *Guidelines for limiting exposure to time-varying electric, magnetic, and electromagnetic fields (up to 300 GHz).* Health physics, 74:494–522, 1998.

[2] IEEE Institute of Electrical and Electronics Engineers. *IEEE Standard for safety levels with respect to human exposure to radio frequency electromagnetic fields, 3 kHz to 300 GHz Std C95.1*. New York: IEEE, 2005.

[3] Paolo Bernardi, Marta Cavagnaro, Stefano Pisa, and Emanuele Piuzzi. *Human Exposure to Radio Base-Station Antennas in Urban Environment*. IEEE Trans Microw Theory Tech, 48:1996–2002, November 2000.

[4] A Christ, MC Gosselin, M Christopoulou, S Kühn, and N Küster. *Age-dependent tissue-specific exposure of cell phone users.* Physics in Medicine and Biology, 55:1767–1783, 2010.

[5] E Valentini, G Curcio, F Moroni, M Ferrara, L De Gennaro, and M Bertini. *Neurophysiological effects of mobile phone electromagnetic fields on humans: A comprehensive review.* Bioelectromagnetics, 28:415–432, 2007.

[6] V Baste, T Riise, and BE Moen. *Radiofrequency electromagnetic fields; male infertility and sex ratio of offspring.* Eur J Epidemiol, 23:369–377, 2008.

[7] R Huber, J Schuderer, T Graf, K Jütz, AA Borbly, N Küster, and Achermann P. *Radio frequency electromagnetic field exposure in humans: Estimation of SAR distribution in the brain, effects on sleep and heart rate.* Bioelectromagnetics, 24:262–276, 2003.

[8] d Tinguely G Regel, S J a, J Schuderer, M Adam, N Küster, H P Landolt, and P. Achermann. *Pulsed radio-frequency electromagnetic fields: Dose-dependent effects on sleep, the sleep EEG and cognitive performance.* J Sleep Res, 16:253–258, 2007.

[9] INTERPHONE Study Group. *Brain tumour risk in relation to mobile telephone use: Results of the INTERPHONE international casecontrol study.* Int J Epidemiol, 39:675–694, 2010.

[10] D Aydin, M Feychting, J Schüz, T Tynes, TV Andersen, LS Schmidt, AH Poulsen, C Johansen, M Prochazka, B Lannering, L Klboe, T Eggen, D Jenni, M Grotzer, N Von der Weid, CE Kuehni, and M. Röösli. *Mobile phone use and brain tumors in children and adolescents: A multicenter case control study.* J Natl Cancer Inst, 103:1264–1276, 2011.

[11] S Larjavaara, J Schüz, A Swerdlow, M Feychting, C Johansen, S Lagorio, T Tynes, L Klaeboe, SR Tonjer, M Blettner, G Berg-Beckhoff, B Schlehofer, M Schoemaker, J Britton, R Mäntylä, S Lönn, A Ahlbom, O Flodmark, A Lilja, S Martini, E Rastelli, A Vidiri, V Kähärä, J Raitanen, S Heinävaara, and A. Auvinen. *Location of gliomas in relation to mobile telephone use: A casecase and casespecular analysis.* Am J Epidemiol, 174:2–11, 2011.

[12] P Crespo-Valero, M Christopoulou, M Zefferer, A Christ, P Achermann, K S Nikita, and N Küster. *Novel methodology to characterize electromagnetic exposure of the brain.* Physics in Medicine and Biology, 56:383–396, 2011.

[13] Akimasa Hirata, Sachiko Kodera, Jianqing Wang, and Osamu Fujiwara. *Dominant factors influencing whole-body average SAR due to far-field exposure in whole-body resonance frequency and GHz regions.* Bioelectromagnetics, 28(6):484–7, September 2007.

[14] Akimasa Hirata, Naoki Ito, and Osamu Fujiwara. *Influence of electromagnetic polarization on the whole-body averaged SAR in children for plane-wave exposures.* Physics in medicine and biology, 54(4):N59–65, February 2009.

[15] R P Findlay and P J Dimbylow. *Calculated SAR distributions in a human voxel phantom due to the reflection of electromagnetic fields from a ground plane between 65 MHz and 2 GHz.* Physics in medicine and biology, 53(9):2277–89, May 2008.

[16] Peter J Dimbylow, Tomoaki Nagaoka, and X George Xu. *A comparison of foetal SAR in three sets of pregnant female models.* Physics in medicine and biology, 54(9):2755–67, May 2009.

[17] Peter Dimbylow, Wesley Bolch, and Choonsik Lee. *SAR calculations from 20 MHz to 6 GHz in the University of Florida newborn voxel phantom and their implications for dosimetry*. Phys Med Biol., 55(5):1519–1530, 2010.

[18] R P Findlay, A-K Lee, and P J Dimbylow. *FDTD calculations of SAR for child voxel models in different postures between 10 MHz and 3 GHz.* Radiation protection dosimetry, 135(4):226–31, August 2009.

[19] Sven Kühn, Wayne Jennings, Andreas Christ, and Niels Kuster. *Assessment of induced radio-frequency electromagnetic fields in various anatomical human body models.* Physics in medicine and biology, 54(4):875–90, February 2009.

[20] J F Bakker, M M Paulides, A Christ, N Kuster, and G C van Rhoon. *Assessment of induced SAR in children exposed to electromagnetic plane waves between 10 MHz and 5.6 GHz.* Physics in medicine and biology, 55(11):3115–3130, 2010.

[21] J F Bakker, M M Paulides, E Neufeld, A Christ, N Küster, and G C van Rhoon. *Children and adults exposed to electromagnetic fields at the ICNIRP reference levels: Theoretical assessment of the induced peek temperature increase.* Physics in medicine and biology, 56:4967–4989, 2011.

[22] T Uusitupa, I Laakso, S Ilvonen, and K Nikoskinen. *SAR variation study from 300 to 5000 MHz for 15 voxel models including different postures.* Physics in medicine and biology, 55(4):1157–76, February 2010.

[23] Emmanuelle Conil, Abdelhamid Hadjem, Azeddine Gati, Associate Member, and A Human Model. *Influence of Plane-Wave Incidence Angle on Whole Body and Local Exposure at 2100 MHz.* (February):48–52, 2011.

[24] G Vermeeren, W Joseph, and L Martens. *Whole-body SAR in spheroidal adult and child phantoms in realistic exposure environment*. Health Physics, 94(June):345–354, 2008.

[25] K Kalliola, K Sulonen, H Laitinen, J Krogerus, and P Vainikainen. *Angular Power Distribution and Mean Effective Gain of Mobile Antenna in Different Propagation*. (September):823–838, 2002.

[26] S Iskra, R McKenzie, and I Cosic. *Monte Carlo simulations of the electric field close to the body in realistic environments for application in personal radiofrequency dosimetry.* Radiation Protection Dosimetry, 147(4):517–527, 2011.

[27] G Vermeeren, W Joseph, and L Martens. *Statistical multi-path exposure method for assessing the whole-body SAR in a heterogeneous human body model in a realistic environment.* Bioelectromagnetics, 34(3):240–51, April 2013.

[28] A Christ, W Kainz, E G Hahn, K Honegger, M Zefferer, E Neufeld, R Rascher, W Janka, W Bautz, J Chen, B Kiefer, P Schmitt, H P Hollenbach, J Shen, M Oberle, D Szczerba, A Kam, J W Guag, and N Kuster. *The Virtual Family–development of surface-based anatomical models of two adults and two children for dosimetric simulations.* Physics in medicine and biology, 55(2):N23–38, January 2010.

[29] C Gabriel, S Gabriel, and E Corthout. *The dielectric properties of biological tissues: I. Literature survey.* Physics in medicine and biology, 41(11):2231–49, November 1996.

[30] J W Hand. *Modelling the interaction of electromagnetic fields (10 MHz-10 GHz) with the human body: methods and applications.* Physics in medicine and biology, 53(16):R243–86, August 2008.

[31] A Christ, T Samaras, A Klingenböck, and N Küster. *Characterization of the electromagnetic near-field absorption in layered biological tissue in the frequency range from 30 MHz to 6,000 MHz.* Physics in Medicine and Biology, 51:4951–4965, May 2006.

[32] Oliver Lauer, Patrizia Frei, Marie-Christine Gosselin, Wout Joseph, Martin Röösli, and Jürg Fröhlich. *Combining near- and far-field exposure for an organ-specific and whole-body RF-EMF proxy for epidemiological research: a reference case.* Bioelectromagnetics, 34(5):366–74, July 2013.

[33] S J Allen, E R Adair, K S Mylacraine, W Hurt, and J Ziriax. *Empirical and theoretical dosimetry in support of whole body resonant RF exposure (100 MHz) in human volunteers.* Bioelectromagnetics, 24:502–509, 2003.

9

Conclusions and future research

In the first section of this chapter, a summary of the conclusions obtained in the chapters 2 to 8 is presented. Potential areas of future research are also presented in the second section of this chapter.

9.1 Conclusions

Several topics related to personal exposure assessment to radio-frequency (RF) electromagnetic fields (EMFs) were studied in this dissertation. These are the main conclusions of the research presented in the previous chapters.

In Chapter 2, compliance boundaries around multi-band base station antennas (BSAs) were determined numerically, based on the International Commission on Non-Ionizing Radiation Protection's (ICNIRP) basic restrictions and reference levels for the general public and occupational exposure on the whole-body averaged specific absorption rate (SAR_{wb}), peak 10 g averaged SAR (SAR_{10g}) in head and trunk or in the limbs, and on the root-mean-squared electric field (E_{rms}). Two different approaches were followed: first, a compliance assessment using a realistic phantom and detailed models of the studied multi-band BSAs was executed. Second, a compliance assessment was executed using standardized procedures, in front of a generic model for one of the multi-band antennas. This study resulted in the first compliance boundaries for the (multi-band) Long-Term Evolution (LTE) antennas with corresponding numerical uncertainties on the compliance distances. The simulations showed that the ICNIRP reference levels are not always conser-

vative and electric field measurements or SAR simulations only are insufficient to obtain the actual compliance boundary of the studied antennas. The two modeling approaches were also compared to one another.

In Chapter 3, the response of a personal exposimeter (PEM) was studied in different exposure situations. First, the response of a body-worn PEM near a multiband, base station antenna was determined. Second, numerical simulations were executed to determine a PEM's response in five realistic, far-field environments. This response is the quadratic ratio of the electrical field strengths measured by a PEM and the incident field strengths. The response of a PEM should ideally be a constant, but has a certain statistical distribution in reality. Prediction intervals on PEM measurements of the incident field strengths can be obtained from this distribution. These prediction intervals contribute to a PEM's measurement uncertainty. Besides the simulation results, an overview of literature that studied a PEM's response was presented. All studies concluded that PEMs underestimate the incident fields and that their prediction intervals are relatively large. PEM measurements are consequently confronted with unacceptably large measurement uncertainties on the incident electric field strength.

Calibration measurements were used in Chapter 4 to study the response of conventional PEMs. A pair of RF PEMs worn simultaneously on both hips of a male human subject was calibrated from 880 MHz to 5.58 GHz in an anechoic chamber. The calibration measurements showed that single PEMs generally underestimate the incident electric field and show a relatively large variation on their response. This variation can be reduced when an average over the two PEMs is used. The PEM's crosstalk was determined during the calibration as well. Significant crosstalk was measured, indicating that measurements in the individual bands with the PEMs will be obfuscated by crosstalk. The calibration data were used to correct PEM measurement data for the influence on the body and to determine the uncertainty on the summary statistics of these data. Measurements were carried out in Ghent, Belgium, for which summary statistics of the measured electric fields were provided.

A personal, distributed exposimeter (PDE) is a device, consisting of multiple on-body RF sensors, which has a potential for the reduction of the measurement uncertainty caused by the influence of the presence of the human body on the incident power density. To this end, different design approaches of a PDE were investigated using numerical simulations in Chapter 5. In a first approach, a regression analysis between on-body electric fields and incident electric fields was used to simultaneously determine locations on the body to employ antennas and the error-on-prediction on the incident field strength. This approach proved that is it possible to reduce the error-on-prediction when multiple sensors on the body are used. In a second approach, two sensors were placed on the front and back of a heterogeneous phantom, the virtual family male (VFM) [1]. Using this approach,

we proved that any combination of an RF sensor placed on the front and the back of the VFM will cause a reduction in the 50% prediction interval on the PDE's response, due to the negative correlation between the responses on the front and the back. A third approach divided the torso of the VFM in 12 zones: six at the front and six at the back, in order to have a more reproducible setup on the body. This approach showed that the 50% prediction interval on the response can be reduced using multiple antennas placed on the body. In a fourth approach, numerical simulations of on-body textile antennas were used to determine the antennas' on-body antenna aperture (AA). This AA can be determined for multi-path exposure and will have a certain distribution, which is characterized by its 50% prediction interval. This 50% prediction interval showed a similar reduction when multiple antennas were used than obtained using the previous approach. All the studied approaches showed that using multiple RF sensors placed on the human torso can reduce the 50% prediction interval on the measurements of the incident power density.

Chapter 6 presented calibration measurements of PDEs. In a first section of this chapter, it was demonstrated that a PDE for measurements with good accuracy and low uncertainty in the GSM 900 down-link (DL) band can be constructed using a limited number of antennas. In the second part of the chapter, a PDE for the detection of Wireless Fidelity (WiFi) around 2450 MHz was calibrated. Calibration of the PDE showed that the uncertainty in terms of the 50% prediction interval of the measured incident electric-field strength can be significantly reduced to a minimal value of 3.2 dB for WiFi signals, respectively. In a third section of this chapter, a PDE for measurements in the GSM 900 DL band was designed based on calibration measurements of textile antennas on 12 potential location on the torso of a human subject in an anechoic chamber. The calibration measurements were processed in order to determine the (averaged) AA in a real environment. The calibration measurements showed that the variation on the AA, in terms of the PI_{50}, can be reduced when multiple antennas are worn on the body. The calibration measurements corresponded well with numerical simulations that were processed in the same way. In a final part of this chapter, a multi-band PDE, consisting of six types of antennas that measure in eleven frequency bands, was calibrated in an anechoic chamber. The calibration measurements showed that the measurement uncertainty in the different frequency bands, in terms of the 68% prediction interval, can be reduced when multiple antennas are placed on the body. An optimal placement to measure simultaneously on the 12 potential locations on the body in the eleven different frequency bands was determined. A combination of two antennas in each frequency band lead to the lowest combined 68% prediction interval.

In Chapter 7, measurements were executed with the PDE in a real environment. Measurements using a PDE in the GSM 900 DL band and the WiFi 2G band were

executed and summary statistics were provided for the measured power densities. A study to determine the combined measurement uncertainty on these power densities was executed. Nine factors that contribute to the combined measurement uncertainty were investigated. This resulted in expanded lower and upper measurement uncertainties of -7.6 dB and +4.2 dB, respectively, in the GSM 900 DL band. In a final part of the chapter, a method, based on calibration measurements and numerical simulations, to estimate the SAR_{wb} from PDE measurements was presented and applied.

A method to numerically investigate the organ-specific averaged SAR (SAR_{osa}) in heterogeneous phantoms in realistic environments was presented in Chapter 8. A stochastic method based on a plane-wave approximation of far-field exposure, environmentally dependent distributions for these plane-wave exposure conditions, and the linearity of Maxwell's equations, was used to determine the SAR_{osa} in the Virtual Family Boy at 950 MHz. The SAR_{osa} in a particular environment was studied by generating cumulative distribution functions for several organs. These distributions are dependent on the considered organs or tissues and on the studied environment. Both the dielectric properties and location in the phantom of the studied organ influence SAR_{osa} values. The same methods were then used to determine the SAR_{osa} of the VFM in the 'Urban Macro-cell' scenario at the same frequency. These SAR_{osa} values were then used to determine the SAR_{osa} during measurements using a PDE, converting it to an SAR_{osa}-meter.

9.2 Future research

9.2.1 Compliance Boundaries of Base Station Antennas

In Chapter 2, compliance distances near BSAs are determined using numerical simulations of a heterogeneous phantom of an adult male near the considered BSAs. The results could be expanded with simulations using different phantoms for the same antenna models [1]. This would allow one to determine compliance distances that are valid for a larger fraction of the population. The studied BSAs are used for Long Term Evolution (LTE) telecommunication. Nowadays, operators are investigating the potential of using 5th generation (5G) communication technologies in frequency bands around 28-30 GHz [2, 3] and 60 GHz [3, 4]. These communication technologies will use new antenna arrays, for which new compliance distances have to be determined, but will also be faced with larger path loss values do to the high carrier frequencies [2]. This might cause an increase in the number of required BSAs and of their emitted powers for sufficient coverage. Moreover, larger arrays with more focused antenna beams might be employed [5]. All these aspects are worthwhile investigating from a compliance assessment perspective.

Compliance boundaries are determined in three directions with respect to the BSA in most of the current studies [6, 7]. However, in reality there will be a compliance surface surrounding the BSA in three-dimensional space at which the basic restrictions or reference levels are met [8]. There are methods available to obtain these for comparison with the reference levels [8], but to our knowledge there exist no studies that determine compliance surfaces based on the basic restrictions, as this would require a very large set of simulations (or measurements) with a phantom placed near a BSA. A potential technique to assess these compliance surfaces is the use of surrogate modeling and sequential design [9]. A surrogate model provides a relationship between spatial coordinates and an investigated quantity, in this case the SAR in a human phantom. The model can be built using a limited set of simulations and is then refined using sequential design. This model has already been successfully used to determine RF exposure maps in large areas [10] and could be adapted to investigate the space surrounding a BSA.

9.2.2 Numerical Dosimetry

A method to study the SAR_{wb} due to RF exposure in realistic environments has been presented and applied in [11–13], while in a subsequent study [14] the same model is adapted to study the SAR_{osa} in the same environments. This method could be extended in order to determine the SAR_{10g} in a realistic environment. The main challenge in this research will be the combination of the basic field distributions, which are simulation results that are stored and combined in order to emulate the effect of multi-path exposure. In the procedure to determine the peak SAR_{10g} [15] a 10 g cube is assigned to every cell assigned by the FDTD algorithm to the numerical phantom, which results in more than 10^6 potential locations of the peak SAR_{10g} in a heterogeneous phantom if the current grid settings are used. Therefore, the storage of the basic field distributions will require several Terrabytes of available memory and combining them would require a large number of slow load and write steps to and from the Random-Acces Memory (RAM). High-Performance Computing (HPC) might provide a way of speeding up this process by parallelizing the necessary computations and providing enough RAM for the storage and usage of multiple basic field distributions at the same time.

An option to reduce the required RAM might be to only investigate the outer layers of a phantom in order to find the peak SAR_{10g}. The amplitude of the incident electric fields, at the frequency studied in this dissertation, will decrease as the fields propagate in the (conductive) body [16]. The maximal field values are therefore expected at the surface of the phantom. Consequently, the peak SAR_{10g} should be located in one of the outer layers of the phantom. Once the basic field distributions are determined for a full phantom, they could be stored and combined into realistic exposures, only for the outer layers of the phantom. This would reduce the memory requirements and would speed up the necessary calculations.

However, some validation samples with the full phantom should be run as well.

The propagation models used to emulate realistic exposure conditions in [11–14] are already a decade old and can be updated using more recent propagation models such as the WINNER II channel model [17], the 3GPP Spatial Channel model for Multiple Input Multiple Output (MIMO) [18], or the COST IC 2100 Channel Model [19]. These models take into account aspects of multi-path propagation that are not included in the currently used models, such as a relationship between time-of-arrival (delay) and phase, multi-path clustering, and improved estimations of the distributions for the amplitude and angle-of-arrival.

The current dosimetric studies focus mainly on the SAR for RF radiation below 6 GHz, while it seems that the future 5G networks might also operate at higher frequencies: around 28-30 GHz [2, 3] and 60 GHz [3, 4]. At these higher frequencies (> 10 GHz), the basic restrictions are incident power densities instead of SAR values. These power densities are limited in order to "prevent excessive tissue heating at or near the body surface" [20]. Finite-Difference Time-Domain (FDTD) simulations in combination with thermal solvers [21] should be executed in order to validate whether the basic restriction on the incident power density indeed protects from excessive tissue heating, in particular for multi-path exposure of heterogeneous phantoms. A challenge in the FDTD simulations will be the fact that the required spatial steps might become comparable to or even smaller than the resolution of the current models [1]. In particular the skin of the current phantoms will have to be refined in order to correctly determine the absorption and heating. Appropriate channel models are already under investigation [22–24] and should be implemented as well.

The diffuse multi-path component (DMC) is a particular part of the RF exposure, which has only been studied in the last years. The part of the incident RF EMFs that can not be attributed to a particular specular component are called DMC [25–27]. The propagation of the DMC can (approximately) be described using concepts taken from acoustics using a theory named 'Room Electromagnetics' [25, 26]. This theory has successfully been used to measure the SAR_{wb} in diffuse fields, using measurements of the reverberation time [26, 28, 29]. Recently some models have been proposed to numerically simulate the SAR_{wb} under DMC exposure [29, 30]. Future research can be executed to investigate the influence of the chosen polarization model on the obtained results and to determine the SAR_{osa} and peak SAR_{10g} under DMC exposure.

9.2.3 Conventional Personal Exposimeters

Conventional, single personal exposimeters (PEMs) have a larger measurement uncertainty than a PDE, but (currently) have the advantage that they contain a multi-band antenna, which can register in a relatively broad band (≈ 5 GHz). Therefore, these devices will probably still be used in exposure studies in the near

future. These studies should preferably be carried out using a combination of multiple PEMs on the body, as this reduces the measurement uncertainty and the percentage of censored data. At least a correction for the human body, using an on-body calibration, has to be taken into account as this can influence the summary statistics. Potentially a review of existing exposure assessment studies could be carried out in order to estimate the corrected results when the influence of the body is taken into account.

The use of a multi-band antenna is also a disadvantage of the conventional PEMs, as this causes an unwanted cross talk between the different bands. A future study has to be carried out in which this cross talk is estimated using real modulation schemes for the calibration signals and a processing method, which emulates a realistic, multi-path environment. The cross talk can partially be detected in the covariance of the measurement results. By comparing the covariances of measurements in different frequency bands using measurement devices with minimal cross talk, a method can be established to remove the cross talk from the measurement results obtained using PEMs.

9.2.4 Personal, Distributed Exposimeter

This subsection lists some potential improvements that can be made on the PDE and the calibration method used to characterize the PDE.

Uncertainty due to morphology Once the PDE is calibrated on a single subject, it could be worn by a different subject without recalibrating the device, thus using the same antenna aperture determined for the original subject. However, due to morphological differences the effective antenna aperture will be different for other subjects. The difference between the unknown antenna aperture of the subject wearing the device and the predetermined antenna aperture is an additional uncertainty that arises only when the device is not calibrated on the actual subject wearing the device. In order to quantify this, a measurement campaign should be executed where a fixed PDE integrated into clothing is calibrated on a large set of subjects chosen in order to morphologically resemble the general population.

Uncertainty due to posture The calibrations of the PDE assume an upright position of the subject wearing the PDE. During the measurements executed in this dissertation, the subject was indeed walking in an upright position, but during other activities a subject might have another posture. A study thus has to be carried out that calibrates a PDE in a setup where a known incident field can be combined with a subject that can assume different postures.

Uncertainty due to the absence of a polar angle In the current calibration method the dependence of the PDE's antenna aperture on the polar angle is not

investigated. Numerical simulations have shown that this can have an influence on the effective antenna aperture and the measurement uncertainty. Anechoic chambers where a spherical or rotating circular array of antennas can be placed around a subject exist and can be used to improve the current calibration measurements. Another interesting potential way of including the polar angle in the calibration is the use of reverberation chambers.

Calibration in a reverberation chamber A reverberation chamber [31] is a closed metal cavity (or room) which includes (at least) a transmitting antenna (TX) and one or more electromagnetic stirrers. The TX emits RF signals which will reverberate in the room, while the stirrers rotate and excite different modes of the cavity. Scattering of the RF EMFs occurs due to the stirrer and the positioning of the TX in the room, which in its turn causes the fields in a certain volume of the room, depending on the used wavelength to excite the room, to be approximately diffuse. The incident power density in this volume of the chamber is equally distributed over all polar angles (usually when averaged over all stirrer positions) and can thus be used to determine the antenna aperture of an on-body antenna including the effect of the polarization angle. It has the advantage that with relatively little effort all the angular channels that are incident on a subject can be excited, but, in contrast to an anechoic chamber, all angular information about the signal is lost. The calibration in a reverberation room has the additional advantage that using 'Room Electromagnetics' a simultaneous estimation can be made of the SAR_{wb} [26, 28–30] and the PDE's response. A correspondence in morphology and pose that can never be obtained using a combination of numerical simulations and calibration measurements.

Registration of the uplink exposure generated by the subject Subjects that participate in exposure assessment studies are sometimes requested not to use personal devices during the measurements or a correction factor is applied to remove measurement data caused by mobile phone use of the subjects [32]. Further studies have to be executed in order to determine an on-body antenna's response to the use of a personal device in the vicinity of the body.

A large reduction in the uncertainty on a subject's uplink exposure could be obtained by registering the location, the emitted power, and frequency of the personal device. Many personal devices already contain some inertial sensors such as accelerometers, gyroscopes, and compasses, which can help in estimating the device's location near the body. This uncertainty can be reduced even further when the potential trajectories of personal devices are restricted to those governed by the potential movements of a subject's arms and hands.

When there is no access to the subject's personal device, a reduction in uncertainty could be obtained by not only using the multiple nodes placed on the body

to estimate exposure, but to simultaneously make an estimation of the location of the device near the body, based on the received powers on the nodes.

Integration of more frequency bands The current multi-band PDE measures in eleven frequency bands above 700 MHz, while commercial PEMs usually also cover frequency bands lower than 700 MHz. In our design, these frequency bands are not included, because they cannot properly be measured in the used calibration setup and development of textile antennas with wearable dimensions is difficult. A potential idea would be to use wire antennas, as these could be integrated into clothing, but would be difficult to calibrate on the body since small antenna movements with relation to the body might have a large influence on the antenna's characteristics. Future research has to determine which antenna type is most suitable to measure these relatively low frequencies on the body. A calibration in an anechoic chamber will probably be unrealistic at these frequencies since a relatively large room is necessary to ensure far-field exposure and provide enough damping of potential reflection. A calibration in an open area test-site will be more suitable. However, this calibration method has the disadvantage that there might be background signals that have to be removed from the calibration data and will cause more uncertainty on the registered powers on the antennas.

It is expected that other frequency bands will be used in the future at the other end of the RF frequency spectrum 28-30 GHz [2, 3] and 60 GHz [3, 4]. The development of antennas to register these frequency bands will be less problematic, due to the high frequencies and thus options to miniaturize the antennas. Note that at these higher frequencies (> 10 GHz), the basic restrictions are incident power densities instead of SAR values [20]. It should thus be investigated how the received powers of body-worn antennas can be used to estimate these power densities, which may vary locally on the body due to the relatively narrow beams emitted by the antenna arrays used for these technologies [2].

Integration of the PDE During the measurements presented in this dissertation, the PDE is worn underneath a coat. This already provides a solution to make the PDE invisible for other people. However, the PDE has not yet been integrated into a garment. This could reduce some of the measurement uncertainties (the translations on and off the body) and is necessary in order to obtain a reproducible link between calibration and measurements.

Measurements In future studies, a more extensive and orchestrated measurement campaign can be executed with the PDE in order to obtain characteristic exposure values in a certain environment, that are not biased by the shielding of the body or a large uncertainty on the position of the antennas.

References

[1] A Christ, W Kainz, E G Hahn, K Honegger, M Zefferer, E Neufeld, W Rascher, R Janka, W Bautz, J Chen, B Kiefer, P Schmitt, H Hollenbach, J Shen, M Oberle, D Szczerba, A Kam, J W Guag, and N Kuster. *The Virtual Family–development of surface-based anatomical models of two adults and two children for dosimetric simulations.* Physics in medicine and biology, 55(2):N23–38, January 2010.

[2] W Roh, J-Y Seol, J Park, B Lee, J Lee, Y Kim, J Cho, K Cheun, and F Aryanfar. *Millimeter-wave beamforming as an enabling technology for 5G cellular communications: theoretical feasibility and prototype results*. Communications Magazine, IEEE, 52(2):106–113, February 2014.

[3] TS Rappaport, S Sun, R Mayzus, H Zhao, Y Azar, K Wang, GN Wong, JK Schulz, M Samimi, and F Gutierrez. *Millimeter Wave Mobile Communications for 5G Cellular: It Will Work!* Access, IEEE, 1:335–349, 2013.

[4] RC Daniels and RW Heath. *60 GHz wireless communications: emerging requirements and design recommendations.* Vehicular Technology Magazine, IEEE, 2(3):41–50, Sept 2007.

[5] EG Larsson, O Edfors, F Tufvesson, and TL Marzetta. *Massive MIMO for Next Generation Wireless Systems.* IEEE Communications Magazine, 52(3):186–195, February 2014.

[6] B Thors, M L Strydom, F J C Meyer, and K Kimmo. *On the Estimation of SAR and Compliance Distance Related to RF Exposure From Mobile Communication Base Station Antennas*. IEEE Trans Electromagn Compat, 50(4):837–848, November 2008.

[7] B Kos, B Valič, T Kotnik, and P Gajšek. *Exposure assessment in front of a multi-band base station antenna.* Bioelectromagnetics, 32(3):234–42, April 2011.

[8] B Thors, A Thielens, J Friden, D Colombi, C Tornevik, G Vermeeren, L Martens, and W Joseph. *Radio frequency electromagnetic field compliance assessment of multi-band and MIMO equipped radio base stations.* Bioelectromagnetics, 35(4):296–308, May 2014.

[9] K Crombecq, D Gorissen, D Deschrijver, and T Dhaene. *A novel hybrid sequential design strategy for global surrogate modeling of computer experiments.* SIAM J Sci Com- put, 33(4):19481974, 2011.

[10] S Aerts, D Deschrijver, W Joseph, L Verloock, F Goeminne, L Martens, and T Dhaene. *Exposure assessment of mobile phone base station radiation in an outdoor environment using sequential surrogate modeling.* Bioelectromagnetics, 34(4):300–311, May 2013.

[11] G Vermeeren, W Joseph, and L Martens. *Whole-body SAR in spheroidal adult and child phantoms in realistic exposure environment*. Health Physics, 94(June):345–354, 2008.

[12] G Vermeeren, W Joseph, and L Martens. *Statistical multi-path exposure method for assessing the whole-body SAR in a heterogeneous human body model in a realistic environment.* Bioelectromagnetics, 34(3):240–51, April 2013.

[13] S Iskra, R McKenzie, and I Cosic. *Monte Carlo simulations of the electric field close to the body in realistic environments for application in personal radiofrequency dosimetry.* Radiation Protection Dosimetry, 147(4):517–527, 2011.

[14] A Thielens, G Vermeeren, W Joseph, and L Martens. *Stochastic Method for the Determination of the Organ-specific Averages SAR in Realistic Environments at 950 MHz.* Bioelectromagnetics, 34(7):549–562, 2013.

[15] IEEE and IEC. *62704-1 Recommended Practice for Determining the Peak Spatial-Average Specific Absorption Rate (SAR) in the Human Body from Wireless Communications Devices, 30 MHz - 6 GHz: General Requirements for using the Finite Difference Time Domain (FDTD) Method for SAR Calculations.* 2011.

[16] T Uusitupa, I Laakso, S Ilvonen, and K Nikoskinen. *SAR variation study from 300 to 5000 MHz for 15 voxel models including different postures.* Physics in medicine and biology, 55(4):1157–76, February 2010.

[17] L L Hentilla, P Kyosti, M Kaske, M Narandzic, and M Alatossava. *MATLAB implementation of the WINNER Phase II Channel Model ver1.1.* 2007.

[18] 3 GPP 3rd Generation Partnership Project; Technical Specification Group Radio Access Network. *Spatial channel model for Multiple Input Multiple Output (MIMO) simulations.* 2008.

[19] R Verdone and A Zanella. *Pervasive Mobile and Ambient Wireless Communications. COST Action 2100.* Springer-Verlag London, 2012.

[20] ICNIRP International Commission on Non-Ionizing Radiation Protection. *Guidelines for limiting exposure to time-varying electric, magnetic, and electromagnetic fields (up to 300 GHz).* Health physics, 74:494–522, 1998.

[21] JF Bakker, MM Paulides, E Neufeld, a Christ, N Kuster, and G C van Rhoon. *Children and adults exposed to electromagnetic fields at the ICNIRP reference levels: theoretical assessment of the induced peak temperature increase.* Physics in medicine and biology, 56(15):4967–89, August 2011.

[22] MR Akdeniz, Y Liu, MK Samimi, S Sun, S Rangan, TS Rappaport, and E Erkip. *Millimeter Wave Channel Modeling and Cellular Capacity Evaluation.* IEEE Journal on Selected Areas in Communications, 32(6):1164–1179, 2014.

[23] Millimetre-Wave Evolution for Backhaul, Antennas Access (MiWeba). WP5: Propagation, and Multi-Antenna Techniques. *Deliverable FP7-ICT 368721/D5.1*. 2014.

[24] M Kyro, V Kolmonen, and P Vainikainen. *Experimental Propagation Channel Characterization of mm-Wave Radio Links in Urban Scenarios*. IEEE Antennas and Wireless Propagation Letters, 11:865–868, 2012.

[25] JB Andersen, JO Nielsen, GF Pedersen, G Bauch, and M Herdin. *Room Electromagnetics*. IEEE Antennas and Propagation Magazine, 49(2):27–33, April 2007.

[26] JB Andersen, KL Chee, M Jacob, GF Pedersen, and T Kurner. *Reverberation and Absorption in an Aircraft Cabin With the Impact of Passengers*. IEEE Transactions on Antennas and Propagation, 60(5):2472–2480, May 2012.

[27] J Poutanen, J Salmi, K Haneda, V M Kolmonen, and P Vainikainen. *Angular and Shadowing Characteristics of Dense Multipath Components in Indoor Radio Channels*. IEEE Trans. Antennas Propag., 59:245–253, 2011.

[28] A Bamba, W Joseph, JB Andersen, E Tanghe, G Vermeeren, D Plets, JO Nielsen, and L Martens. *Experimental Assessment of Specific Absorption Rate Using Room Electromagnetics*. IEEE Transactions on Electromagnetic Compatibility, 54(4):747–757, Aug 2012.

[29] A Bamba, W Joseph, G Vermeeren, E Tanghe, DP Gaillot, JB Andersen, JO Nielsen, M Lienard, and L Martens. *Validation of experimental whole-body SAR assessment method in a complex indoor environment.* Bioelectromagnetics, 34(2):122–32, February 2013.

[30] A Bamba, W Joseph, G Vermeeren, A Thielens, E Tanghe, and L Martens. *A formula for human average whole-body SARwb under diffuse fields exposure in the GHz region.* Physics in medicine and biology, 59(23):7435–56, December 2014.

[31] P Besnier and B Demoulin. *Electromagnetic Reverberation Chambers.* J Wiley & Sons, 2011.

[32] J F B Bolte and T Eikelboom. *Personal radiofrequency electromagnetic field measurements in The Netherlands: exposure level and variability for everyday activities, times of day and types of area.* Environment international, 48:133–42, November 2012.